Mechanics and Thermal Transport in Low-Dimensional Heterostructures and Applications to Sensors

A Dissertation Submitted to the Faculty of
School of Engineering and Applied Science,
University of Virginia

In Partial Fulfillment of the
Requirements for the Degree of
Doctor of Philosophy
in Mechanical and Aerospace Engineering

By
Yuan Gao
March 2019

Abstract

The immense growth of skin-like electronic devices based on two-dimensional (2D) heterostructures is considered to revolutionize technologies of communication, health, and fitness for grand applications in healthcare monitoring and human-machine interfaces. The large deformation exerted to the devices that are required to accommodate the complex human motions while maintaining a conformal attachment to human skin is a current bottleneck in thermal management. Understanding of fundamental thermal transport in response to large mechanical loading conditions is expected to lay the foundation for controllable thermal management in these devices.

This dissertation presents the fundamental understanding of thermal transport in 2D nanomaterials and heterostructures in response to an externally large mechanical loading and proposes a novel measuring principle for mechanical sensors based on the mechanics-thermal coupling.

Specifically, in Chapter 2 the thermal responses in 2D materials and their corresponding heterostructures subjected to loadings are systematically introduced. A small mechanical loading within the stretchability of materials can alter the geometric features, influence the heat transfer path and the effective conducting area of the material, leading to the change in thermal transport. A large external mechanical stimulation beyond the stretchability can intrigue lattice deformation and thus directly coordinate with the phonon properties, intriguing dramatic

variation in thermal transport capabilities. Extensive calculations on mechanical, thermal transport and phonon properties support these findings.

To elucidate the competition mechanism of thermal transport under intrinsically small mismatch-induced strain and externally applied mechanical loads, several types of heterostructures with either covalent bonded or van der Waals (vdW) heterojunctions, are discussed in Chapter 3 and 4, supported by extensive analyses of stress, deformation, geometric morphology, phonon activities and atomic interactions. Generalized models that take into account structural features, mechanical deformation and thermal activities in heterostructures were proposed to quality thermal properties.

In Chapter 5 and 6, two types of mechanical sensors that both rely on thermal responses to mechanical loading were proposed and exemplified: a pressure sensor capable of sensing, locating and mapping pressure loadings; a multifunctional sensor capable of sensing and differentiating modes of mechanical stimuli, including tension, compression, bending and external pressure.

These results and new findings provide a firsthand fundamental understanding of thermal transport in deformed nanomaterials and immediate guidance to the development of stretchable devices whose thermal management could be mechanically tunable. Besides, they will help open a new route for the exploration of future devices by leveraging unique thermal properties of materials, thereby strategically extending design solutions of mechanical sensors from electrical resistance to thermal transport-based responses.

Table of Contents

List of Figures

Figure 1.1. Electric wearable sensors and their functional principle and limitations. (**a**) Wearable sensors on an athlete. The top left graph shows the chemical sensor that measures blood glucose by analyzing sweat. The bottom left graph shows the electrical sensor that measures the heart rate based on the electrical impedance of the skin. The top right graph shows the optical sensor that measures oxygenation based on light absorption and diffraction. The bottom right graph shows the mechanical sensor that measures the breath rate based on the strain. The measuring mechanisms of all types of wearable sensors are based on the change in the electrical resistance in the functional circuit. (**b**) The electric resistance response $\Delta R/R_0$ in a wearable mechanical sensor (bottom right scheme in (a)) to external tensile strain. The external strain changes the contact of the materials in the functional circuit and increases the electrical resistance. (**c**) Electric signal noise caused by the electrical interference in the measurement of electromyography signals. (**d**) The Relationship between the breakdown power and the root square of the foot print of device. The break down power corresponds to the minimum electric power that can lead to the break down of the device owing to the temperature rise. The self-heating is more severe in smaller devices, indicated by the lower break down power.

Figure 1.2. The atomistic model and transmission electron microscopy (TEM) images of representative candidates of low-dimensional materials. (**a**) A 1-D carbon nanotube with 1 dimension reaching macroscale. (**b**) A 2-D graphene with 2 dimensions reaching macroscale.

Figure 1.3. The atomistic schematic of examples of (**a**) a vertical heterostructure with a vdW interface between components and (**b**) a lateral heterostructure with a bonded interface between components.

Figure 1.4. A typical setup of NEMD approach for thermal conductivity calculation and result (**a**) Hot and cold reservoirs are set to generate a temperature gradient and heat flow in a 1D CNT (**b**) Temperature distribution along the direction of heat transport. The temperature is almost linear, based on which Fourier’s law is directly applied to obtain the thermal conductivity.

Figure 1.5. The experimental setup and result of Raman thermometry method in the measurement of the thermal conductivity of a single layer graphene (**a**) A schematic of experimental setup in Raman thermometry measurement. The focused laser light creates a local hot spot and generates a heat wave inside SLG propagating toward heat sinks. (**b**) G peak in Raman spectra of graphene at two different lase power level. A higher power level can enhance

the magnitude and shift of G peak. (**c**) Based on the slope of the linear relationship between G peak shift and power on the sample, the value of thermal conductivity can be obtained.

Figure 1.6. Thermal transport in representative 1D-2D heterostructures. (**a**) Atomistic schematic of 1D CNT-2D graphene architecture heterostructure with (**b**) thermal transport depending on the sizes of components. (**c**) Design of 1D-2D heterostructure enabled thermal diode with (**d**) thermal rectification ratio optimized by the geometric size of CNT and graphene. (**e**) 1D-2D vdW heterostructures composed of graphene and CNT whose thermal conductance at the junction is dependent on the effective contact between 1D and 2D components.

Figure 2.1. Computational models of serpentine graphene nanoribbons (SGNRs) with **(a)** the same length in the $\boldsymbol{x}$-direction and **(b)** the same total number of carbon atoms. A periodic boundary condition is applied in the $\boldsymbol{x}$-direction and non-periodic boundary conditions are applied in the y and z-direction in MD simulations. l_0 and b are the length and width of projection of the structure in the $\boldsymbol{x}$ and y-direction, respectively, w and a are the width and length of nanoribbons, respectively, and α is the angle of serration. When α=180^o, it corresponds to a regular pristine GNR. The length l_0 is 33.95nm for all structures in the model (a), and in the model (b) the length l_0 is 33.95nm, 58.73 nm, and 67.90 nm for SGNRs with α=60^o and α=120^o, and regular GNRs, respectively. The width of all nanoribbons w in both groups is the same and is 1.897nm.

Figure 2.2. Uniaxial nominal stress-strain curves of regular graphene nanoribbons (GNRs, $\boldsymbol{\alpha}$=180^o) and serpentine graphene nanoribbons (SGNRs) with **(a)** the same initial length and **(b)** the same number of carbon atoms in tension.

Figure 2.3. Snapshots of von Mises stress distribution of SGNRs with the angle of serration $\boldsymbol{\alpha}$ (a) 180^o (regular GNRs), **(b)** 60^o and **(c)** 120^o under different tensile strain ε

Figure 2.4. Temperature profile in SGNRs with the angle of serration $\boldsymbol{\alpha}$ (a) 180^o (regular GNRs) and **(b)** 60^o. The insets illustrate the computational model and linear region of temperature profiles, respectively. In the computational model, both ends and the middle of SGNRs are set as cold and hot reservoirs, respectively to construct a periodic boundary condition in the heat flow $\boldsymbol{x}$-direction. The heat flow is imposed by scaling energy of atoms in reservoirs at a rate of 0.3 eV/ps. The temperature gradient is extracted by fitting the linear regions of temperature profiles of group atoms.

Figure 2.5. Effect of tensile strain on thermal conductivity of the **(a)** regular GNR, κ_g, and **(b)** SGNR60 (α=60^o), κ_{sg}. The errors arise from the uncertainty of fitting the linear region of temperature profiles in SGNRs.

Figure 2.6. Effect of nanoribbons size, $\boldsymbol{w/a}$, on thermal conductivity of the **(a)** regular GNR , κ_g, and **(b)** SGNR60 (α=60^o), κ_{sg}, under different tensile strains. The errors arise from the uncertainty for fitting the linear region of temperature profiles.

Figure 2.7. Phonon spectra of SGNRs with different angles of serration, α, and nanoribbon sizes, w/a, at tensile strain. **(a)** α=180° (regular GNR), w/a=0.157, **(b)** α=180° (regular GNR), w/a=0.352, **(c)** α=60°, w/a=0.157.

Figure 2.8. Computational model of auxetic graphene (AG), contractile graphene (CG) and their enabled heterostructures (AC1-6). (a), (b) and (c) Molecular modeling of auxetic graphene (AG), contractile graphene (CG) and their enabled heterostructures (AC1-6), respectively. A uniform displacement loading is applied in the *x*-direction to obtain a uniaxial tensile strain ε_x. Parallel to the strain loading *x*-direction, both ends are chosen to be the hot and cold reservoir, respectively and are fixed in the study of thermal transport properties. Non-periodic periodic boundary condition was set in *x*, *y* and *z*-direction. The modeling length for all AG, CG, and AC1-6 is the same and l_m=59.03 nm and width w_m=54.53 nm. (**d**) Structures and dimensions of unit cells in auxetic graphene and contractile graphene. $l_m = 9.84$ nm, $w_m = 13.63$ nm. The aspect ratio is defined as p/q as marked in the figure. For AG unit cell, $p = 3.74$ nm and $q = 7.66$ nm. For CG unit cell, $p = 3.74$ nm and $q = 7.10$ nm.

Figure 2.9. Schematic illustration of AG and CG unit cells enabled heterostructures. The horizontal interface I_H and the vertical interface coefficient I_V are defined as $I_H = \frac{N_H}{mn}$ and $I_V = \frac{N_V}{mn}$, respectively, where N_H and N_V are the total number of AG and CG unit cells that are employed to construct the horizontal interfaces and the vertical interfaces, respectively, and m and n are the numbers of unit cells in a row and in a column of the heterostructure, respectively. The total number of unit cells associated with horizontal and vertical interfaces is referred to as N_I, the average number of pure columns of AG and CG cells without either type of interfaces is referred to as N_{AN}, the number of pure columns of AG and CG cells are referred to as N_{PAC} and N_{PCC}, respectively, and the number of types of cell patterns in the heterostructures is referred to as N_{TP}.

Figure 2.10. Mechanical properties of auxetic graphene (AG), contractile graphene (CG) and their enabled heterostructures (AC1-6). (**a**) Nominal stress-strain curves of auxetic graphene (AG), contractile graphene (AG) and heterostructures (AC 1-6). (**b**) Comparison of Poisson's ratio of heterostructures (AC 1-6) at different tensile strains between simulation results and theoretical predictions.

Figure 2.11. Comparison of theoretical predictions and simulation results on Poisson's ratio of AG and CG unit cells enabled heterostructures with different patterns and volume fractions c_A. (**a**) Molecular model of AG and CG unit cells enabled heterostructures with simplex repeating and complex patterns. **(b)** and **(c)** Variation of Poisson's ratio of heterostructures with simplex repeating and complex patterns with the uniaxial tensile strain, respectively.

Figure 2.12. The thermal conductivity of the auxetic graphene (AG), contractile graphene (CG) and heterostructures (AC 1-6) in tension. (**a**) Variation of thermal conductivity of the auxetic graphene (AG), contractile graphene (CG), the representative heterostructure (AC1-3) with the applied uniaxial tensile strain ε_x. (**b**) Variation of thermal conductivity of auxetic graphene (AG), contractile graphene (CG), the heterostructure (AC1-6) with their Poisson's ratios at $\varepsilon_x = 10\%$ and $\varepsilon_x = 20\%$ and their comparison with theoretical predictions. (**c**) and (**d**) Variation of thermal conductivity of heterostructures (AC1-6) with the horizontal interface coefficient I_H and the vertical interface coefficient I_V at $\varepsilon_x = 10\%$ and $\varepsilon_x = 20\%$ and their comparison with theoretical predictions. k_0 is the thermal conductivity in the absence of tensile strain.

Figure 2.13. **Mechanical deformation features of the auxetic graphene (AG), contractile graphene (CG) and heterostructures in tension**. Von Mises stress distribution of auxetic graphene (AG), contractile graphene (CG) and heterostructure under different tensile strains.

Figure 2.14. **Stress in the auxetic graphene (AG), contractile graphene (CG) and heterostructures in tension**. (**a**) Variation of averaged von Mises stress in horizontal and vertical ribbons auxetic graphene (AG), contractile graphene (CG) and heterostructure AC3 with tensile strain. (**b**) Variation of averaged von Mises stress in horizontal ribbons of heterostructures AC1-6 with the horizontal interface coefficient I_H at the tensile strain of 20%. (**c**) Variation of averaged von Mises stress in vertical ribbons of heterostructures AC1-6 with the vertical interface coefficient I_V at the tensile strain of 20%.

Figure 2.15. **Vibrational spectra of the auxetic graphene (AG), contractile graphene (CG) and heterostructures in tension**. Total vibrational spectra, horizontal ribbon spectra and vertical ribbon spectra of (**a**) auxetic graphene (AG), (**b**) contractile graphene (CG), and (**c**) heterostructure AC3 at the uniaxial strain of 0%, 10% and 20%. (**d**) Comparison of horizontal ribbon spectra of heterostructures AC2 and AC3 at the strain of 0% and 20%. **(e)** Comparison of horizontal ribbon spectra of heterostructures AC1, AC4, AC5 and AC6 at the tensile strain of 20%. **(f)** Comparison of vertical ribbon spectra of heterostructures AC1-6 at the tensile strain of 20%.

Figure 2.16. Semi-auxetic graphene, the combination of its unit cell with AG and CG unit cell enabled heterostructures AS and SC and their mechanical properties. (**a**) Molecular model of semi-auxetic graphene unit cell. The aspect ratio is defined as p/q as marked in the figure. For SG unit cell, $p = 3.00$ nm and $q =$ 6.39 nm. (**b**) The heterostructures AS and SC. (**c**) Nominal stress-strain of semi-auxetic graphene, heterostructures AS1-3, CS1-3. (**d**) Variation of Poisson's ratio with the applied uniaxial strain.

Figure 2.17. Verification and prediction of thermal conductivity on heterostructures in tension. (**a**) Comparison of the thermal conductivity of heterostructures AC 1-6, heterostructures AS1-3 and heterostructures CS1-3 between theoretical predictions and simulation results at the strain of 10%. **(b)** Improved theoretical prediction on the thermal conductivity of heterostructures AC 1-6, heterostructures AS1-3 and heterostructures CS1-3 at

the strain of 20%. The error bar arises from the small uncertainty of fitting the linear region of temperature gradient profiles.

Figure 3.1. Atomic model of GBN heterostructures (left) and highlighted structures in interface junctions (right).

Figure 3.2. Asymmetric thermal transport in graphene-boron nitride (GBN) heterostructures with controlled interface junctions. (**a**) Comparison of heat flow J in heterostructures along both directions as functions of tensile strain ε. (**b**) Thermal conductivity κ of pure graphene and boron nitride as a function of tensile strain, where the graphene (G) and boron nitride (BN) have the same dimension as when they are in GBN heterostructures. (**c**) The temperature profile in GBN heterostructure with α=3/7 at two opposite directions of heat flow. The black solid lines illustrate the linear regions. (**d**) Comparison of heat flow J in heterostructures along both directions as functions of junction parameter α.

Figure 3.3. Thermal rectification in graphene-boron nitride (GBN) heterostructures with controlled interface junctions. (a) and **(b)** Variation of thermal rectification η as tensile strain ε, and heterojunction parameter α. (**c**) Thermal rectification ratio as a function of temperature difference between hot and cold reservoirs

Figure 3.4. Stress analysis in graphene-boron nitride (GBN) heterostructures. (a) Snapshots of von Mises stress distribution near the interface. (**b**) Variation of stress concentration K_t in graphene and boron nitride domains as tensile strain ε, and heterojunction parameter α. (**c**) Comparison of relative stress concentration P in different heterostructures as functions of tensile strain ε.

Figure 3.5. Heat flow distribution in GBN heterostructures with (a) $\alpha = 0$, **(b)** $\boldsymbol{\alpha} = 1/7$, **(c)** $\alpha = 3/7$, **(d)** $\alpha = 5/7$ and **(e)** $\alpha = 1$ before and after the reverse of heat flow direction at different tensile strains.

Figure 3.6. Out-of-plane Vibrational spectra of graphene and boron nitride domain in graphene-boron nitride (GBN) heterostructures. (a), (b) and **(c)** Out-of-plane vibrational spectra G_o of graphene and boron nitride in the heterostructure with $\alpha = 3/7$ at the tensile strain of $\varepsilon = 0$, 5% and 10%.

Figure 3.7. In-plane Vibrational spectra of graphene and boron nitride domain in graphene-boron nitride (GBN) heterostructures. (a), (b) and **(c)** In-plane vibrational spectra G_o of graphene and boron nitride in the heterostructure with $\alpha = 3/7$ at the tensile strain of $\varepsilon = 0$, 5% and 10%.

Figure 3.8. (a) Relative overlap H_o in the heterostructure with $\alpha = 3/7$ at different strains. (**b**) Variation of relative overlap of out-of-plane phonon spectra H_o as functions of junction parameter α.

Figure 3.9. Phonon participation ratio in heterostructures with α =0, $3/7$ and 1 at the tensile strain (**a**) $\varepsilon = 0$, (**b**) 5% and (**c**) 10%

Figure 3.10. Energy distribution of localized out-of-plane phonon modes (top) and the averaged plots as y-axis with x-position normalized by the length l (bottom) in the heterostructure with $\alpha = 3/7$ in both directions of heat flow at different tensile strains.

Figure 3.11. Demonstration applications of controllable thermal transport paths in the heterostructure systems with selective interface junctions. (a) Atomic structure of GBN heterostructure system composed of alternatively arranged graphene and boron nitride sheets with parallel interfaces but different junction parameters α (=0, 1), referred to as a thermal antiparallel shunt. **(b)** Comparison of heat flux in the "thermal antiparallel shunt" system at 0% and 10% tensile strain.

Figure 3.12. Demonstration applications of controllable thermal transport paths in the heterostructure systems with selective interface junctions. Atomic structure of GBN heterostructure system with an equally shared interface but different junction parameters (α=0, 1), referred to as a thermal parallel shunt. **(d)** Comparison of heat flux in both directions in the "thermal parallel shunt" system at 0% and 10% tensile strain.

Figure 4.1. Computational model of the bilayer graphene-MoS_2 heterostructure (a) Molecular modeling of the graphene-MoS_2 heterostructure. Heat flow is achieved along the *x*-direction, in parallel to the interface of the heterostructure, and a uniaxial tensile strain ε is applied in the *x*-direction. The ends are set to the hot and cold region, respectively and are fixed in simulations. A periodic boundary condition is applied to the *y*-direction and other two directions (i.e. *x*- and *z*-directions) are non-periodic boundary conditions.

Figure 4.2. Temperature profiles in the graphene-MoS_2 heterostructure and individual layer components. (a) The temperature profile in the graphene-MoS_2 heterostructure, where the cold and hot ends are set to the ends of the heterostructure, respectively and controlled by Langevin thermostats. The linear region is employed to extract the temperature gradient for use in the determination of thermal conductivity. **(b)** Comparison of temperature profiles of individual layers of graphene (GE-in-GM), and MoS_2 (MS-in-GM) in heterostructure and graphene-MoS_2 heterostructure (GM). The temperature profiles of individual layer components are obtained by assigning the hot and cold reservoir separately to graphene and MoS_2 layers.

Figure 4.3. Mechanical properties of the Graphene-MoS2 bilayer heterostructure. (b) Nominal stress-strain curve of the graphene-MoS_2 heterostructure, bilayer graphene and bilayer MoS_2. **(c)** Lattice mismatch-induced out-of-plane displacement, d_o, of atomic positions in graphene and MoS_2 layer in the heterostructure at equilibrium under the tensile strain of 0% and 15%, and it is calculated by comparing positions of atoms in heterostructures and their corresponding bilayer structures.

Figure 4.4. The thermal conductivity of the graphene-MoS_2 heterostructure. **(a)** The thermal conductivity of the graphene-MoS_2 (GM) heterostructure, bilayer graphene (BGE) and bilayer MoS_2 (BMS) as a function of the applied tensile strain ε. **(b)** The thermal conductivity of individual graphene (GE-in-GM) and MoS_2 (MS-in-GM) components in the heterostructure, and comparison of thermal conductivity under different tensile strains between the theoretical predictions **(c)** The ratio of thermal conductivity of graphene in the heterostructure to that in bilayer graphene in tension, $\kappa_{GE-in-GM}$. **(d)** The ratio of thermal conductivity of MoS_2 in the heterostructure to that in bilayer MoS_2 in tension, $\kappa_{MS-in-GM}$. The error bar arises from the small uncertainty of determining the temperature gradient by fitting the linear region of temperature profiles.

Figure 4.5. Total, in-plane and out-of-plane phonon spectra of (a)-(c) graphene and **(d)-(f)** MoS2 at tensile strain of 0, 5% and 15%

Figure 4.6. (**a**) and (**b**) Comparison of in-plane phonon spectrum $G_i(\omega)$ of graphene in heterostructure and in bilayer graphene at the tensile strain of 0 and 15%. (**c**) and (**d**) Comparison of out-of-plane phonon spectrum $G_o(\omega)$ of graphene in heterostructure and in bilayer graphene at the tensile strain of 0 and 15%.

Figure 4.7. (**a**) and (**b**) Comparison of in-plane phonon spectrum $G_i(\omega)$ of MoS_2 in heterostructure and in bilayer MoS_2 at the tensile strain of 0 and 15%. (**c**) and (**d**) Comparison of out-of-plane phonon spectrum $G_o(\omega)$ of MoS_2 in heterostructure and in bilayer MoS_2 at the tensile strain of 0 and 15%.

Figure 4.8. Comparison of theoretical predictions with simulations on the thermal conductivity in the graphene-MoS_2 heterostructure in tension. The error bar arises from the small uncertainty of determining the temperature gradient by fitting the linear region of temperature profiles.

Figure 4.9. Molecular structures of 2D materials black phosphorus (BP) (left) and hexagonal boron nitride (hBN) (right). The first lattice constant of black phosphorus and hexagonal boron nitride is used to define the lattice mismatch when they are stacked with other 2D materials in heterostructures, and is 0.331 nm and 0.251 nm, respectively.

Figure 4.10. Verification of the lattice mismatch-integrated thermal theory on bilayer heterostructures. (a) Comparison of theoretical predictions and simulations on thermal conductivity of five bilayer heterostructures (graphene-hBN, hBN-black phosphorus (BP), hBN-MoS_2, graphene-MoS_2 and graphene-black phosphorus (BP) heterostructures) with different lattice mismatch parameters. **(b)** Variation of the ratio of thermal conductivity δ with the lattice mismatch.

Figure 4.11. Modeling of van der Waals graphene kirigami heterostructure. (**a**) Atomistic modeling of graphene kirigami bilayer heterostructure (left) and individual kirigami layer components with U and I cut patterns (right). In the heterostructure, its dimension size is

l=27.55 nm in length and w=30.67 nm in width. The external tensile strain ε is applied in the x-direction on both layers as marked in the black arrows, and the heat flow q is transferred from the upper layer to the lower layer along the z-direction as marked in the yellow arrow. (**b**) The individual kirigami layer unit. The length and width are a=6.89 nm and b=10.22 nm, respectively, the cut length is d=8.09 nm and the cut width c changes with cut patterns.

Figure 4.12. (a) and (b) Variations of nominal stress σ with tensile strain ε in graphene heterostructure, where homobilayers are composed of the same two pristine graphene, or kirigami layers U1, U2, U3, or I1, I2, I3, and heterobilayers are composed of one layer with cut pattern U (U1) and the other with cut pattern I (I1, I2 and I3).

Figure 4.13. (a) and (b) Variations of thermal conductance G with tensile strain ε in graphene heterostructure.

Figure 4.14. Generalized functions of thermal conductance G of kirigami heterostructure as thermal transparency O. O=1 for bilayer pristine graphene, and $O=1-\phi$ and $O=\sqrt{(1-\phi_{upper})(1-\phi_{lower})}$ for homobilayers and heterobilayers, respectively. Homobilayers: U1/U1 (red circles), U2/U2 (red squares), U3/U3 (red triangles), I1/I1 (blue circles), I2/I2 (blue squares), I3/I3 (blue triangles); Heterobilayers: U1/I1 (green circles), U1/I2 (green squares), U1/I3 (green triangles), U2/I1 (cyan circles), U2/I2 (cyan squares), U2/I3 (cyan triangles), U3/I1 (purple circles), U3/I2 (purple squares), U3/I3 (purple triangles), U1/U3 (orange circles) and I1/I3 (orange squares).

Figure 4.15. Vibrational spectra of graphene kirigami heterostructures. (**a**) Vibrational spectra $PS(\omega)$ of kirigami layer in the cut pattern I under different porosity ϕ. (**b**) Effect of tensile strain. As tensile strain ε increases, the cut expands, leading to lower thermal transparency. The high frequency peak at 55 THz and the low frequency peaks at 13 and 18 THz are slightly suppressed, indicating more inconsistent motion of atoms owing to the expanded cuts in the kirigami layer and a lower thermal conductance. The same conclusion can be drawn when increasing the size of cuts, as shown by (**c**). The same statement still holds true when making comparisons between different basic patterns, demonstrated by (**d**).

Figure 4.16. Unified relationship between density of interaction per unit area $\bar{N}$ and thermal transparency O. Same legends as those in Figure 4.14 are applied.

Figure 4.17. (**a**) Distribution of interaction N in kirigami layer with cut pattern U1 in homobilayers U1/U1 and heterobilayers U1/I3. (**b**) Distribution of interaction N in kirigami layer I3 in homobilayers I3/I3 and heterobilayers U1/I3.

Figure 4.18. Thermal conductance G as functions of the density of interactions $\bar{N}$. While sharing the same slope with the linear function of homobilayers, the relationship between the thermal conductance and density of interactions is down shifted, which indicate the quality of each interaction is reduced in heterobilayers. Same legends as those in Figure 4.14 are applied.

Figure 4.19. (**a**) Phonon participation ratio (PPR) of eigenmodes at different frequency f in pristine graphene, kirigami layers with cut patterns U1 and I1. As the sizes of cuts increase, the phonon participation ratio slightly reduces in pattern U (**b**) and pattern I (**c**).

Figure 4.20. Distribution of normalized energy of delocalized phonon ($\boldsymbol{PPR > 0.4}$) in the unit cell of pristine graphene, kirigami layer with cut patterns U1-3 and I1-3.

Figure 4.21. The difference in the distribution of delocalized phonon energy in four bilayer systems. Top left: homobilayers U1/U1 composed of layers with the same porosity $\phi = 0.14$ and the same cut pattern. Top right: heterobilayers U1/U3 composed of layers with different porosity $\phi_{upper} = 0.14$ and $\phi_{lower} = 0.36$ but the same cut pattern. Bottom left: heterobilayers U3/I2 composed of layers with different porosity $\phi_{upper} = 0.36$ and $\phi_{lower} = 0.37$ but the same cut pattern. Bottom right: homobilayers U1/I1 composed of layers with different porosity $\phi_{upper} = 0.14$ and $\phi_{lower} = 0.26$ but the same cut pattern.

Figure 4.22. The overall difference of the coefficient $\boldsymbol{D}$ as a function of thermal transparency $\boldsymbol{O}$

Figure 4.23. Application demonstration of strain-controlled heat flow in van der Waals graphene kirigami heterostructures. (**a**) The unified relationship between the tuning ratio of thermal conductance and performance governing coefficient η. (**b**) Schematic illustration of the bilayer van der Waals graphene kirigami system capable of being controlled in heat flow across the out-of-plane interface. (**c**) Distribution of local density of interaction $\overline{N}_{local}$ in the homobilayer at $\varepsilon = 0$ (left) and $\varepsilon = 55\%$ (right), indicating a clear change of thermal transparency O from initial O_0=0.86 (left) to O=0.64 (right).

Figure 5.1. Computational model of 1D-2D van der Waals (vdW) heterostructures Molecular modeling of the 1D-2D heterostructure with a monolayer 2D materials (left: perspective view; right: side view). The 2D layer is sandwiched between the same two orthotropic 1D carbon nanotubes (CNTs), forming a 1D-2D heterostructure through non-covalent vdW interactions. Hot and cold reservoirs are assigned to the two ends of upper and lower nanotubes, generating a heat flow across the heterojunctions.

Figure 5.2. Thermal conductance of 1D-2D vdW heterostructures (a) Thermal conductance of heterostructures G as a function of relative bending stiffness between 1D and 2D materials B_{CNT}/B_{2D} for monolayer and multiple layer 2D materials. G: graphene, hBN: hexagonal boron nitride, BP: black phosphorus (BP), and MoS_2: molybdenum disulfide. **(b)** Thermal conductance of heterostructures G as a function of the proposed dimensionless coefficient η ($=\frac{B_{CNT}}{B_{2D}} \cdot \frac{d}{a_{2D}} \cdot \frac{1}{l} \cdot N^2$)

Figure 5.3. Out-of-plane mechanical deformation (*d*₀) and Gaussian curvature (*g*) distribution in 2D layers in heterostructures. (**a**) Monolayer graphene (G) with CNTs of 1.085 nm in diameter. (**b**) Monolayer graphene (G) with CNTs of 2.170 nm in diameter. (**c**)

Monolayer boron nitride (BN) with CNTs of 1.085 nm in diameter. (**d**) Monolayer molybdenum disulfide (MoS_2) with CNTs of 1.085 nm in diameter. (**e**) Trilayer graphene (G) with CNTs of 2.170 nm in diameter. (**f**) Pentalayer graphene (G) with CNTs of 2.170 nm in diameter.

Figure 5.4. Out-of-plane mechanical deformation (*d*o) and Gaussian curvature (*g*) distribution in 2D layers in heterostructures. 2D monolayer black phosphorus (BP) in heterostructures with CNT in diameter of (**a**) 1.085 nm and (**b**) 2.170 nm. 2D monolayer (**c**) hexagonal boron nitride (hBN) and (**d**) molybdenum disulfide (MoS_2) in heterostructures. The diameter of CNT is 2.170 nm. (**e**) bilayer graphene and (**f**) quadralayer graphene in heterostructures. The diameter of CNT is 2.170 nm.

Figure 5.5. (**a**) Schematic illustration of atom pairs at two heterojunctions in 1D-2D heterostructure. i, j, k and l illustrate the atomic positions in the upper CNT, 2D layer, and lower CNT at the heterojunctions, respectively and form two atom pairs (i, j) and (k, *l*), and d_{ij} and d_{kl} are the equilibrium distance of atoms for the atom pairs (i, j) and (k, *l*). (**b**) The effective contribution of the cumulated pairwise interactions N_{eff} at upper and lower interfaces in heterostructures as a function of CNT diameter d.

Figure 5.6. (**a**) Thermal conductance G as a function of the pairwise interaction contribution factor of atoms at heterojunctions C $(= N_{eff\_up}N_{eff\_low})$. (**b**) Contribution factor C as a function of the proposed dimensionless coefficient η

Figure 5.7. Thermal response of 1D-2D heterostructures to external pressure. (**a**) Schematic illustration of a 1D-2D heterostructure subjected to external pressure (P) at the heterojunction via the upper CNT. (**b**) Normalized thermal conductance $(G - G_0)/G_0$ of heterostructures composed of multilayer graphene as a function of external pressure $\boldsymbol{P}$. G_0 is the thermal conductance at P=0. (**c**) Response sensitivity S of the heterostructure with multilayered graphene (layer number: N) to the pressure P. (**d**) Normalized pairwise interaction contribution factor of atoms $(C - C_0)/C_0$ at heterojunctions in heterostructures with multilayer graphene.

Figure 5.8. Stress distribution in graphene (a) in the absence of external pressure **(b)** at the pressure P_1=2GPa. (**c**) Stress change in monolayer graphene in the heterostructure at P=2 GPa in comparison with that of in absence of pressure

Figure 5.9. Conceptual design and demonstration application of 1D-2D heterostructure enabled pressure sensor. (**a**) Schematic illustrations of the heterostructure-pressure sensor array with monolayer graphene sandwiched between three pairs of CNTs with the same length but different diameters. The applied external pressure loadings are P_1=2GPa. (**b**) Stress change in graphene layers due to the external pressure loading. (**c**) The pressure change in graphene in the heterostructure-pressure sensor. (**d**) Pressure mapping demonstration through the total local pairwise interaction contribution factor of atoms at heterojunctions $\sum C'$ in heterostructures.

Figure 5.10. Conceptual design and demonstration application of 1D-2D heterostructure enabled pressure sensor. (**a**) Schematic illustrations of the heterostructure-pressure sensor array with monolayer graphene sandwiched between three pairs of CNTs with the same length but different diameters. The applied external pressure loadings are P_2=1.5 GPa, P_3=1 GPa and P_4= 0.67 GPa. (**b**) The stress change in graphene layers due to the external pressure loading. (**c**) Pressure change in graphene in the heterostructure-pressure sensor. (**d**) Pressure mapping demonstration through the total local pairwise interaction contribution factor of atoms at heterojunctions $\sum C'$ in heterostructures.

Figure 6.1. Atomistic modeling of the graphene oxide (GO)-confined water heterostructures with the size of $l =$ 6.15 nm and $w =$ 6.39 nm. The surface of both GO layers that is decorated with epoxy and hydroxyl functional groups reflects the oxidation. The heat is transferred from upper graphene oxide to the lower one.

Figure 6.2. Thermal conductance G of the heterostructures with degrees of oxidation p =0.4 and 0.5 as functions of confined water content.

Figure 6.3. Schematic of the hydrogen bonds-featured interactions between graphene oxide layers (GO-GO) and between graphene oxide and water molecules (GO-W) (left) and their correspondence to a circuit model consisting of the two heat transfer paths with thermal conductance of $G_{\mathrm{GO-GO}}$ and $G_{\mathrm{GO-W}}$, respectively (right).

Figure 6.4. Variation of $G_{\mathrm{GO-GO}}$ and $G_{\mathrm{GO-W}}$ as functions of water content in the heterostructure with degrees of oxidation $p =$ 0.4 and 0.5.

Figure 6.5. Responses of thermal conductance in graphene oxide (GO)-confined water heterostructures to different mechanical loading modes. The thermal conductance G in the heterostructure with degree of oxidation $\mathrm{p} =$ 0.5 and water content of 0, 10% and 25% as functions of (**a**) in-plane tensile strain ε_{t}, (**b**) in-plane compressive strain ε_{c}, (**c**) cross-plane pressure P and (**d**) cross-plane bending curvature κ.

Figure 6.6. Phonon spectra of graphene oxide under mechanical loadings. No obvious difference is observed under the influence of (**a**) tensile strain ε_{t}, (**b**) compressive strain ε_{c}, (**c**) pressure P and (**d**) bending curvature κ.

Figure 6.7. Thermal conductance G versus interfacial interaction energyE_{int} at (**a**) $\mathrm{p} =$ 0.5 and (**b**) $\mathrm{p} =$ 0.4. Compared to the $G - E_{\mathrm{int}}$ relationships obtained at $\mathrm{p} =$ 0.5, the slopes of linear fittings decrease due to the reduction in the number of functional groups and atomic density at the solid-liquid interface.

Figure 6.8. The number of hydrogen (H)-bonds between graphene oxides (GO-GO H-bonds) and graphene oxides and water (GO-W H-bonds) as functions of (**a**) water content,

(**b**) tensile strain ε_{t}, (**c**) compressive strain ε_{c}, (**d**) external pressure P, and (**e**) bending curvature κ.

Figure 6.9. Decoupled thermal conductance along two heat transfer paths. The partial contribution to the thermal conductance from the interaction between graphene oxide layers $G_{\mathrm{GO-GO}}$ and the interaction between graphene oxide and water molecule $G_{\mathrm{GO-W}}$ at different water weight ratio $wt =$ 0, 10% and 25%. Partial contributions as functions of (**a**) tensile strain ε_{t}, (**b**) compressive strain ε_{c}, (**c**) pressure P and (**d**) bending curvature κ.

Figure 6.10. Decoupled contribution of GO-GO H-bonds to thermal conductance $G_{\mathrm{GO-GO}}$ and GO-W H-bonds to thermal conductance $G_{\mathrm{GO-W}}$ at (**a**) $\mathrm{p} =$ 0.5 and (**b**) $\mathrm{p} =$ 0.4.

Figure 6.11. Planar distribution and occupation of hydrogen (H)-bonds in the interlayer of confined water and graphene oxides. The density ρ_{HB} and planar occupation rate ϕ of hydrogen bonds in the interlayer of heterostructures with degree of oxidation $p =$ 0.5 and water weight ratio $wt =$ 10% (**a**) in the absence of loading, under (**b**) tensile strain ε_{t}, (**c**) compressive strain ε_{c}, (**d**) external pressure P, and (**e**) bending curvature κ. The H-bonds formed between graphene oxide layers (GO-GO) and between graphene oxide and water molecules (GO-W) are represented by red and blue dots, respectively.

Figure 6.12. Deformation snapshots of the heterostructure with $p = 0.5$ and $wt = 10\%$ (**a**) tensile strain ε_{t}, (**b**) compressive strain ε_{c}, (**c**) pressure P and (**d**) bending curvature κ.

Figure 6.13. Design and demonstration application of mechanical sensor enabled by graphene oxide-confined water heterostructure. (a) Schematic of mechanical sensor design, where a constant heat flow q is applied to generate a temperature difference ΔT between the graphene oxides in the heterostructure. Measurement of relative temperature $(\Delta T - \Delta T_0)/T_0$ with respect to external mechanical loading of (**b**) tension ε_{t}, (**c**) compression ε_{c}, (**d**) pressure P and (**e**) bending curvature κ. ΔT (~60 K) is the temperature difference in the absence of mechanical loading.

Figure 6.14. Measurement of relative temperature $(\Delta T - \Delta T_0)/\Delta T_0$ with respect to external mechanical loading of (**a**) tensile strain ε_{t}, (**b**) compressive strain ε_{c}, (**c**) pressure P and (**d**) bending curvature κ. ΔT_0 (~30 K) is the temperature difference in the absence of mechanical loading.

List of Tables

Acknowledgements

My sincere and deep gratitude goes and foremost to my advisor Professor Baoxing Xu for his insightful academic guidance, persuasive encouragement as well as inspiring criticisms. To me, he has always been a perfect example demonstrating how a self-motivated person could dedicate himself to his beloved career with love and joy. His enthusiastic and rigorous attitude would continue to inspire and encourage me in my future career, no matter whether I am still in his group. It is such a great fortune to have an advisor like him in the pursuit of education and research.

I would appreciate my thesis committee members, Professor Xiaodong (Chris) Li, Professor Gaurav Giri, Professor Osman E. Ozbulut and Professor Lin Ma, for their time to read my thesis and publications, for their kindness to serve in my thesis defense, and for their inspiring sharing to support my research.

I would also thank the current and former members in Professor Xu's research group for their long-term supports, friendship, encouragements, helpful suggestions and thoughtful discussions, including Prof. Zongzhan Gao, Dr. Weizhu Yang, Mr. Qingchang Liu, Mr. Yue Zhang, Mr. Haozhe Zhang, Mr. Mengtian Yin, Mr. Zachary Massey, Mr. Yize Dong and Ms. Songwei Li.

Last but not least, my deep thanks go to my parents, my beloved girlfriend and my family members for their supports, encouragements, understandings, and blessings.

Chapter 1 Introduction and Motivation

1.1 Challenges in Wearable Mechanical Sensors

The emerging wearable electronic devices have received increasing attention during recent years[14, 15] and are expected to cause a significant impact on our daily activities in the future, especially in the aspects of fitness, health, and communication[16, 17]. The wearable electronic sensors[18, 19] that are capable of monitoring body information are of critical importance (**Figure 1.1a**). Generally, the measuring principle of these sensors relies on sensing the response of electrical resistance in the functional circuit to the external signals[20-22]. Take wearable mechanical sensor (bottom right scheme in Figure 1a) as an example, the external strain will change the contact of conducting materials in the functional circuit and increase the electrical resistance, based on which the external strain can be detected and measured (**Figure 1.1b**).

However, the widely adopted method, which requires continuous electric power input, is limited by the mutual electrical interference when sensing bioelectrical and magnetic signals[23-25]. For example, the electric signal in the muscle can influence the electric current in the functional circuit and challenge the measurement of electromyography signal in biomedical systems[24] (**Figure 1.1c**). On the other hand, thermal management issues are also one limitation[26, 27], especially in wearable devices with nanoscale chips[28-30]. The heat generated by electricity can cause severe temperature rise. In smaller devices, the lower heat dissipation rate usually leads to more severe temperature rise and self-heating effects (**Figure 1.1d**). Without control, the increasing temperature can influence the functionality and reduce the durability and lifetime of devices[31]. More importantly, the increasing temperature of devices attached to human skin is one potential danger.

To address these challenges, the fundamental of thermal transport subjected to large mechanical deformation should be understood. Furthermore, a novel measuring principle for mechanical sensors relying on unique responses to external mechanical stimuli need to be developed.

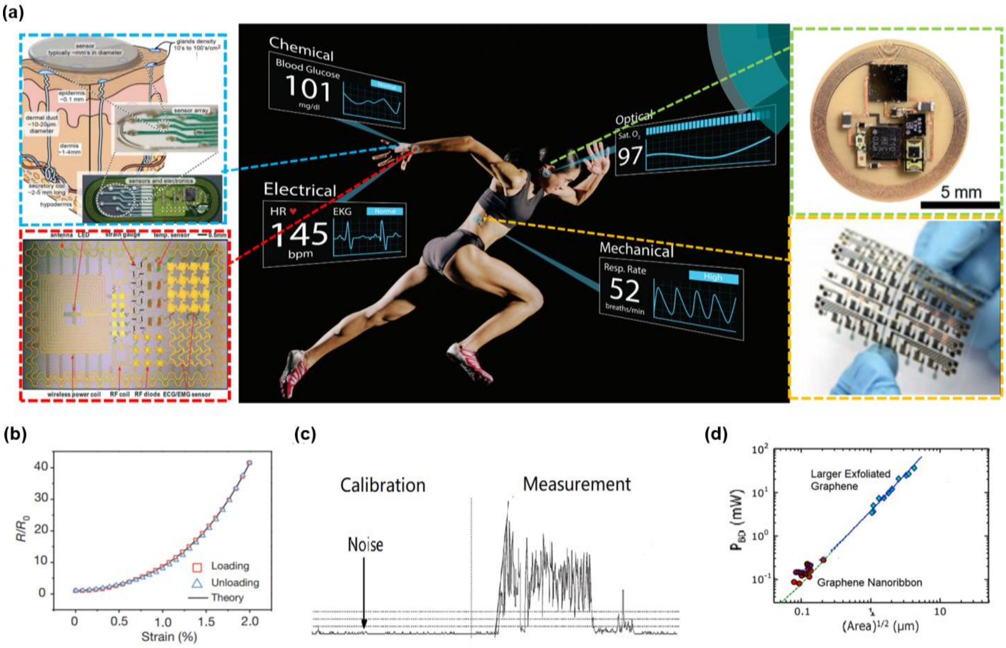

Figure 1.1. Electric wearable sensors and their functional principle and limitations. (**a**) Wearable sensors on an athlete[1-4]. The top left graph shows the chemical sensor that measures blood glucose by analyzing sweat. The bottom left graph shows the electrical sensor that measures the heart rate based on the electrical impedance of the skin. The top right graph shows the optical sensor that measures oxygenation based on light absorption and diffraction. The bottom right graph shows the mechanical sensor that measures the breath rate based on the strain. The measuring mechanisms of all types of wearable sensors are based on the change in the electrical resistance in the functional circuit. (**b**) The electric resistance response ΔR/R_0 in a wearable mechanical sensor (bottom right scheme in (a)) to external tensile strain. The external strain changes the contact of the materials in the functional circuit and increases the electrical resistance. (**c**) Electric signal noise caused by the electrical interference in the measurement of electromyography signals[10]. (**d**) The Relationship between the breakdown power and the root square of the foot print of device. The break down power corresponds to the minimum electric power that can lead to the break down of the device owing to the temperature rise. The self-heating is more severe in smaller devices, indicated by the lower break down power[13].

1.2 Advantages of Low-Dimensional Materials and Heterostructures in Wearable Electronics

The term “low-dimensional materials” refers to those have at least one dimension at the nanoscale, which usually results in novel properties from their bulk counterparts[32-34] such as 1D nanorods with 1 dimension reaching the macroscale like carbon nanotubes (CNTs) and 2D nanolayers with 2 dimensions reaching the macroscale such as graphene (**Figure 1.2**).

These emerging low-dimensional materials are popular for their novel mechanical[35-38], electronic[39-44] and thermal properties[45-47] as well as the broad applications in related fields[33, 48]. In particular, the extremely high Young’s modulus of 1 TPa in 2D graphene has been explored in both experimental measurement[36] and theoretical computation[49]. The outstanding stiffness (~100 GPa) and strength (~10 GPa) have also been confirmed in other 2D materials such as hexagonal boron nitride (hBN)[50], MoS_2 and $MoSe_2$[51] as well as the 1D carbon nanotube[52]. On the other hand, reduction in the thickness dimension of 2D materials results in atomically thin

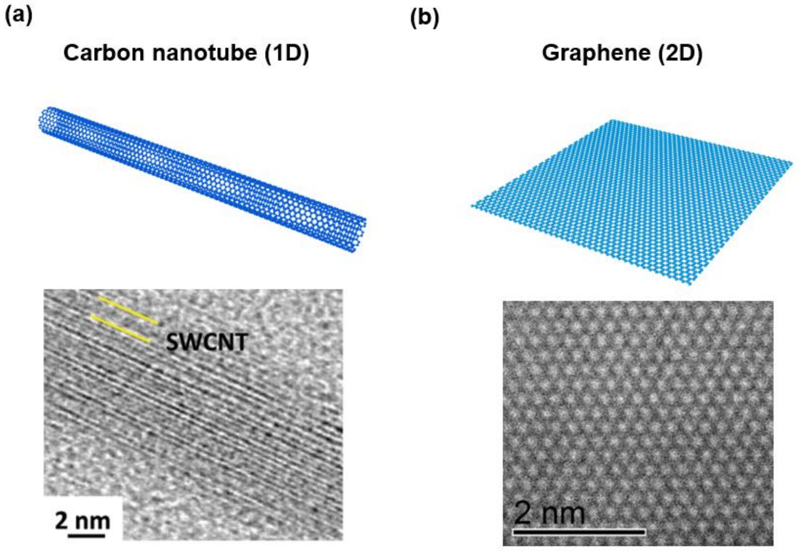

Figure 1.2. The atomistic model and transmission electron microscopy (TEM) images of representative candidates of low-dimensional materials. (**a**) A 1D carbon nanotube with 1 dimension reaching macroscale[8]. (**b**) A 2-D graphene with 2 dimensions reaching macroscale[11].

features, leading to restricted flexural rigidity (~10^{-19} to ~10^{-18} Nm in graphene[53], hBN[54], phosphorene[55] and, MoS_2[56]), which enables significant non-planar deformation and geometries that are not allowed in their bulk crystals[57]. Consequently, extraordinary mechanical stability, durability as well as flexibility are highly recommended in wearable electronics. Meanwhile, low-dimensional carbon-based materials with intrinsically remarkable carrier mobility (~10^6 cm^2 V^{-1} S^{-1}) and electrical conductivities (10^4 S/cm) are ideal and widely applied in flexible and wearable electronics[58].

Assembling two or more types of low-dimensional materials with either vdW or covalently bonded junction to create lateral (**Figure 1.3a**) and vertical (**Figure 1.3b**) heterostructures can harness drawbacks of the single materials, and to achieve unprecedented properties beyond that of individual components[59-68]. For example, the intrinsic weak absorption characteristics in graphene can be improved by assembling a vdW heterostructure with 2D molybdenum disulfide (MoS_2) materials that possess a strong optical absorption and visible-range bandgap[69, 70]. In the graphene-hBN vdW heterostructure, the presence of hBN layer minimizes the carrier scattering, leading to an order of magnitude higher in electronic quality of graphene than that of single isolated graphene sheet[71]. A remarkable tunability in the

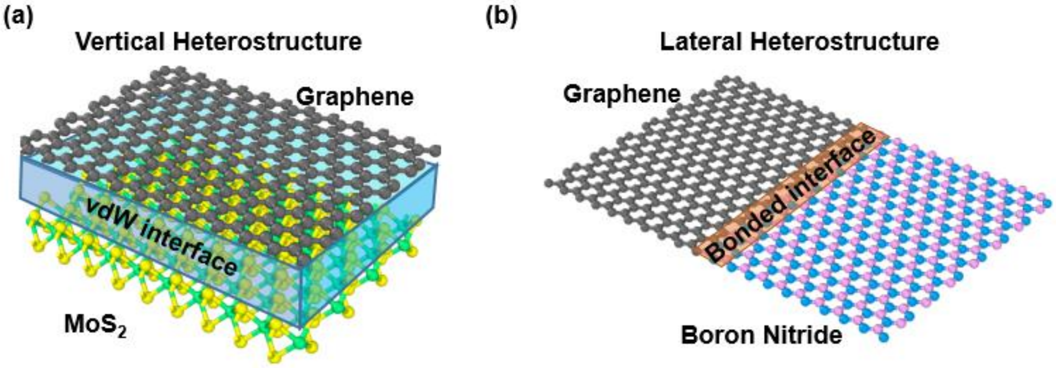

Figure 1.3. The atomistic schematic of examples of (**a**) a vertical heterostructure with a vdW interface between components and (**b**) a lateral heterostructure with a bonded interface between components.

rectification ratio, as high as five orders of magnitude, has been achieved in 1D carbon nanotubes-2D MoS_2 p-n diode[72]. Tilting the covalent heterojunctions in polycrystalline graphene could manipulate its mechanical stress to match the requirement of biological and electronic applications[73]. Creating selective covalent heterojunctions in hexagonal-boron nitride would introduce net charges and leads to a significant reduction of bandgap[74]. These novel properties enabled by the introduction of heterojunctions lead to broad applications such as semiconductors[75], sensors[76] energy harvesting[77] and memory devices[78] and broaden the functionality of wearable electronic devices.

1.3 Opportunity for Thermal Transport in Low-Dimensional Materials and Heterostructures

As another fundamental property of materials, thermal transport is reported to have unique behavior under the influence of applied external field such as mechanical strain[17, 79-82], especially for the low-dimensional materials and their heterostructures[61, 80, 83] that have been widely involved in electronic devices, leading to the potential of creating mechanical sensors with thermal responses. This section will serve as an introduction of the fundamental of thermal transport, the thermal responses in these structures to mechanical stimuli and the theoretical possibility of creating thermal based mechanical sensors.

1.3.1 Brief Overview of Intrinsic Thermal Transport in Low-Dimensional Materials and Heterostructures

Essentially, nanoscale thermal transport is the redistribution of kinetic energy[84] and is critical to the application of thermal management[30], thermal-based calculation[85]. and energy harvesting[86]. The phononic thermal transport and has been extensively investigated in 1D and

2D materials with both computational and experimental approaches. A brief overview will be given to discuss the fundamental of thermal transport and its response to mechanical loadings.

1.3.1.1 Fundamental of Nanoscale Phononic Thermal Transport

The Fourier's Law is widely adopted to describe the heat conduction at macroscale, which states that

$$q = -\kappa \nabla T A, \tag{1.1}$$

In this expression, q is the heat flow, κ is thermal conductivity, ∇T is the temperature gradient and A is the cross-sectional area of the material. The thermal conductivity of either a certain material or composite should be intensive and independent of geometry and size[87]. However, at the nanoscale, the heat conduction in electric insulator or semiconductor is ballistic, and does not follow the diffusive Fourier Law, which was referred to the "breakdown of Fourier's Law" by Chang *et al*[88]. On the other hand, in low-dimensional materials at the nanoscale, the ballistic thermal transport is dominated by phonons, which are quanta of crystal lattice vibrations and can carry a specific amount of heat[32], traveling at the speed of $\boldsymbol{v}_g$. Similar to photons, the transport properties of phonons are believed to follow the Boltzmann transport equation[89]:

$$\frac{\partial f_\lambda}{\partial t} + \boldsymbol{v}_{g,\lambda} \cdot \nabla f_\lambda = \left(\frac{\partial f_\lambda}{\partial \mathrm{t}}\right)_{\mathrm{scattering}} \tag{1.2}$$

Where t is time, f_λ and $\boldsymbol{v}_{g,\lambda}$ are the probability distribution function and phonon group velocity of the λ^{th} phonon mode, respectively. Under small perturbation, f_λ can be decomposed as $f_\lambda = f_\lambda^0 + f_\lambda'$, where f_λ^0 and f_λ' are equilibrium phonon distribution function and temperature-independent perturbation term, respectively. At small temperature gradient ∇T,

$$\nabla f_\lambda = \nabla T \cdot \left(\frac{\partial f_\lambda}{\partial \mathrm{T}}\right) \tag{1.3}$$

At a steady state, $\frac{\partial f_\lambda}{\partial \mathrm{t}} = 0$, equation (1.1) becomes

$$\boldsymbol{v}_{g,\lambda} \cdot \nabla T \left(\frac{\partial f_\lambda}{\partial \mathrm{T}}\right) = \left(\frac{\partial f_\lambda}{\partial \mathrm{t}}\right)_{\mathrm{scattering}}. \tag{1.4}$$

By using single-mode relaxation time approximation, the scattering term can be expressed as

$$\left(\frac{\partial f_\lambda}{\partial \mathrm{t}}\right)_{\mathrm{scattering}} = -\frac{f_\lambda - f_\lambda^0}{\tau_\lambda}, \tag{1.5}$$

where τ_λ is the relaxation time of λ^{th} phonon mode and is determined by combining different phonon scattering mechanisms, such as the intrinsic phonon-phonon scattering time $\tau_{\mathrm{p-p}}$, size effect related phonon-boundary term $\tau_{\mathrm{p-b}}$ and impurity/defect term τ_{defect} via Matthiessen's rule:

$$\frac{1}{\tau_\lambda} = \frac{1}{\tau_{\mathrm{p-p}}} + \frac{1}{\tau_{\mathrm{p-b}}} + \frac{1}{\tau_{\mathrm{defect}}} \tag{1.6}$$

The phononic thermal conductivity can be obtained by summarizing the contribution from each phonon mode via:

$$\kappa = \frac{1}{3}\sum_\lambda c_\lambda v_{g,\lambda} v_{g,\lambda} \tau_\lambda, \tag{1.7}$$

where c_λ is the is phonon specific heat. Considering the phonon mean free path l_λ as $l_\lambda = v_{g,\lambda} l_\lambda$, equation (1.7) can be written as

$$\kappa = \frac{1}{3}\sum_\lambda c_\lambda v_{g,\lambda} l_\lambda, \tag{1.8}$$

in which the phonon mean free path is a very important characteristic length associated with the competition between ballistic and diffusive regimes as well as the size effect of thermal conductivity[90].

To investigate thermal transport in low-dimensional materials, different approaches, including both computational and experimental methods, can be applied. Among the computational methods, molecular dynamics (MD) calculations are widely adopted, which

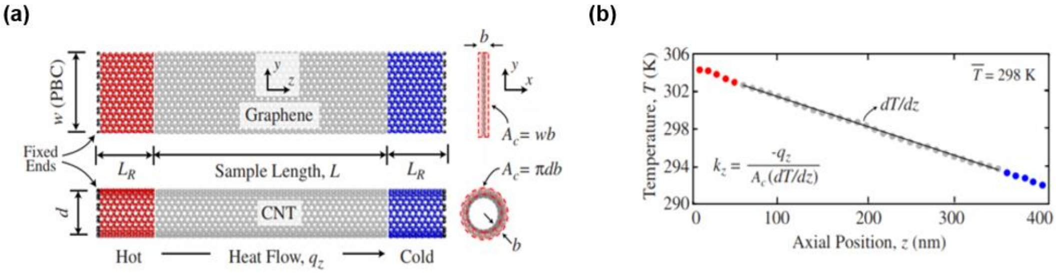

Figure 1.4. A typical setup of NEMD approach for thermal conductivity calculation and result[5] (**a**) Hot and cold reservoirs are set to generate a temperature gradient and heat flow in a 1D CNT (**b**) Temperature distribution along the direction of heat transport. The temperature is almost linear, based on which Fourier's law is directly applied to obtain the thermal conductivity.

includes nonequilibrium molecular dynamics simulation (NEMD) and equilibrium molecular dynamics (EMD) calculation. In NEMD (**Figure 1.4**), although the validity of Fourier's Law at the nanoscale is quite debatable, an "effective" thermal conductivity is evaluated by directly applying Fourier's Law (Equation 1.1)[84]. On the other hand, EMD is based on Green-Kubo formula:

$$\kappa = \frac{1}{Vk_BT^2}\int < J(t)\cdot J(0) > dt, \tag{1.8}$$

where V is the system volume, k_B is the Boltzmann constant, J is the heat flux and T is the system temperature. First principle calculations can provide more precise assessment of thermal conductivity with more accurate interatomic potential functions, yet for periodic systems with limited sizes[91]. Directly solving linearized Boltzmann transport equation (Equation 1.4) can provide more phonon information in addition to the value of thermal conductivity but is also limited by the system size leveraged by the computational cost[92].

Experimentally, Raman thermometry (**Figure 1.5**) based on the shift of excited Raman peaks is widely used[93], which has outstanding resolution for temperature measurement but requires considerable amount of instant heat when measuring materials with high thermal conductivity to generate notable temperature change. The method of microbridge relying on

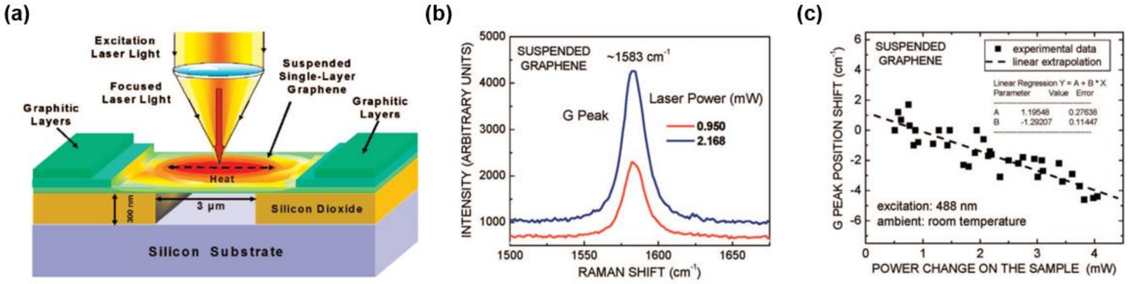

Figure 1.5. The experimental setup and result of Raman thermometry method in the measurement of the thermal conductivity of a single layer graphene (**a**) A schematic of experimental setup in Raman thermometry measurement. The focused laser light creates a local hot spot and generates a heat wave inside SLG propagating toward heat sinks. (**b**) G peak in Raman spectra of graphene at two different lase power level. A higher power level can enhance the magnitude and shift of G peak. (**c**) Based on the slope of the linear relationship between G peak shift and power on the sample, the value of thermal conductivity can be obtained.

measuring temperature rise with Pt electrode during heating is also widely adopted[94] yet challenged by limiting thermal/resistance at the contact of nanomaterials.

1.3.1.2 Material Factors that Influence Intrinsic Thermal Transport in Low-Dimensional Materials

With the methods discussed above, the phononic thermal conductivity in 1D and 2D materials have been extensively investigated and is reported to span a few orders of magnitudes (~1 to ~1000 W/mK)[32, 95]. In addition, according to equation 1.6, the material factors such as size[96], edge-chirality[97, 98], defect[99, 100], impurity[101, 102] edge roughness[103] can change the phonon scattering properties and are reported to cause the modification of thermal transport, which will be summarized briefly below.

In 1D materials, the size of materials usually has an impact on thermal conductivity[87]. Using NEMD simulation, Zhang and Li explored the length L dependence of the thermal conductivity in a (5,5) CNT as $\kappa \sim L^{\beta}$, where β decreases from 0.40 to 0.26 as temperature increases from 300 to 800 K. The reduction of β is caused by the strengthened interaction between the transverse and longitudinal modes given a larger vibration at a higher temperature.

The size dependence of thermal conductivity is also observed in CNTs with different diameter with NEMD simulation[104] and has been experimentally verified by Chang *et al*[88]. To understand the mechanism of the length dependent thermal transport, Li and Wang investigate the quantitative connection between two regimes of heat conduction and diffusion with fractional derivative and attribute the size effect to heat diffusion[105]. Similar finite-size effect of the thermal conductivity is also confirmed in 1D silicon nanowires with both NEMD and EMD. Liang and Li investigate the dependence of thermal conductivity on the diameter of silicon nanowires with theory development validated by experiments, in which size effects are well-explained by the phonon surface scattering and phonon confinement effects[106].

In addition to the size effect, Zhang and Li explore that the introduction of impurity with isotope can dramatically reduce the thermal conductivity of CNTs by more than half[107]. An exponential decrease of thermal conductivity with random isotopic doping is reported in silicon nanowires. At 50% doping, the thermal conductivity reaches only ~27% of the pristine silicon nanowire due to enhanced phonon scattering[108]. Introducing vacancy to silicon nanowire can cause reductions in phonon participation ratio and thermal conductivity, and a 1% decrease in cross-sectional area can dramatically decrease the thermal conductivity by 35%[109].

In 2D materials, the similar effects of size[110], defects[111], and doping[112] have also been reported. However, different from 1D materials, 2D materials demonstrate intrinsic planar anisotropic thermal conductivity. Contrasting behavior of thermal transport in zigzag and armchair direction has been found in graphene[113], boron nitride[114], black phosphorus[115], MoS_2[116] and arsenene[117]. Xu *et al* report that such size effect decreases with the increase of size and diminish as the width reaches 100 nm[113].

Moreover, the expansion in two directions of 2D materials enables the planar molecular morphological designs achieved by tailoring different shapes, which leads to novel properties of thermal transport. For example, Yang *et al*. tailors graphene into periodic T-shape and explores the edge phonon localization effect and resonant phonon peak splitting due to edge modes with non-equilibrium Green function (NEGF) method[118]. Tailoring graphene into an asymmetric shape such as trapezoidal and single T-shape can lead to thermal rectification (thermal diode, governing the heat flow across the structure and analogical to the function of electric diodes on electric current[119]) phenomenon: the thermal transport is usually higher from wider to narrower direction than in the opposite one[118]. Similar diode performance is also reported in triangle shaped graphene by Hu and Ruan with NEMD simulations[97]. The mechanism of thermal diode phenomenon in different asymmetric structures of graphene is thoroughly explained with contrasting phonon resonance and distribution of localized phonon modes under opposite temperature gradient obtained in extensive NEMD and lattice dynamics (LD) calculations by Wang *et al*[120]. Instead of tailoring, creating either regularly or randomly arranged pores in graphene layer to generate porosity can lead to phonon localization and reduction thermal transport. According to Feng and Ruan, at a higher porosity achieved by increasing number or sizes of pores, the localization and restriction in thermal transport is more severe[121]. By arranging the size and distribution of the pores to generate porosity gradient, thermal diode performance can be introduced to the structure[122], which has been experimentally verified by Wang *et al*[123]. Generating rectangular cuts in a graphene sheet to create a kirigami structure can lead to superior mechanical flexibility[124]. However, by using NEMD simulation, Wei *et al*. report that the thermal conductivity will be depressed by the extended heat transfer path[125].

1.3.1.3 Thermal Transport in Low-Dimensional Heterostructures Dominated by Heterojunctions

Unlike pristine low-dimensional materials, composing two or more intrinsic low-dimensional materials together to create low-dimensional heterostructures can leads to novel thermal transport either across or parallel to the interface dependent on the vdW or covalent bonded heterojunction between components, and will be summarized below based on the dimension of components, namely 0D-1D, 1D-1D, 1D-2D and 2D-2D.

According to Vavro *et al.*, encapsulating 1D CNT with 0D C_{60} fullerene to create peapod heterostructure can enhance the thermal transport compared to the empty CNT[126]. The same phenomenon is confirmed by Noya *et al.* with NEMD simulations in a carbon nanotube with the chirality of (10, 10) filled with C_{60}. The enhancement in thermal conductivity is attributed to the low-frequency radial vibration coupling between fullerenes and nanotube and the fullerene-fullerene collisions, which facilitate energy transfer[127]. However, the investigation by Kodama *et al.* with both experimental and computational approaches explore the opposite conclusion that the thermal conductivity of C_{60}-CNT heterostructure is suppressed by 35-55% given the elastic deformation and softened phonon modes at the vdW heterojunction [128]. Nevertheless, in either way, encapsulating 0D particles in 1D confinement environment provide a novel solution to alternate thermal transport properties for potential applications such as thermal management[129] or thermoelectric materials[33]. By arranging asymmetric distribution of 0D C_{60}s in 1D boron nitride nanotube (BNNT), a thermal diode performance in C_{60}-BNNT heterostructure is proposed with NEMD simulation by Loh and Baillargeat and understood with the contingency of the thermal flux on the conductance at the localized region around the heterojunction[130].

As for 1D-1D heterostructures, composing solid germanium nanowire and hollow silicon nanowire with a bonded interface to create core-shell structure can lead to a depression in thermal conductivity parallel to the interface of more than 25%, which is further dependent on the surface roughness. With NEMD simulation, Chen, Zhang, and Li demonstrate that the reduction is caused by the phonon localization [131]. Instead of a core-shell structure, arranging Si and Ge nanowires alternatively to create Si-Ge superlattice heterostructure can restrict thermal transport across bonded interfaces due to enhanced phonon scattering and reduced phonon group velocity at the junction[84], which have been extensively investigated with computations[132, 133], experiments[134] and theory developments[135]. A similar phenomenon is also found in similar superlattices composed of other 1D materials in experiments[136]. On the other hand, composing vdW junctions with 1D CNT and BNNT with different diameter can results in thermal rectification effect due to the phonon resonance at the heterojunction dependent on the temperature gradient[137]. Such thermal diode performance is expected to exist in other 1D-1D vdW heterostructures with different components[138].

Assembling heterostructures with 1D and 2D nanostructures with covalent junctions can achieve 3D architectures. One example is the pillared-graphene architecture composed of 1D CNTs and graphene layers (**Figure 1.6a**). Varshney *et al.* report the outstanding thermal conductivity along the CNT direction (up to ~500 W/mK) in this heterostructure with NEMD simulations, which originates from the intrinsically high thermal transport properties from its component. Nevertheless, the thermal transport is still limited by the phonon scattering at the junctions, leading to the size effects in thermal conductivity (**Figure 1.6b**)[7, 139]. Xu *et al.* report the size effects of thermal conductivity in the perpendicular direction, namely the graphene direction[140]. Similar findings are reported in 1D BNNT-2D boron nitride architectures[141]. Moreover, the geometry dependence and phonon scattering at the 1D-2D covalent junction (**Figure 1.6c**) can be used to design thermal diode with remarkable thermal rectification ratios (>1500%) (**Figure 1.6d**)[9, 142]. Replacing bonded junction with vdW junction reduces atomic interaction (**Figure 1.6e**), and impede thermal transport across the 1D-2D heterojunction[7]. In this case the interfacial thermal conductance depends on the effective contact between graphene and CNT, which determines the atomic interactions across the interface[12].

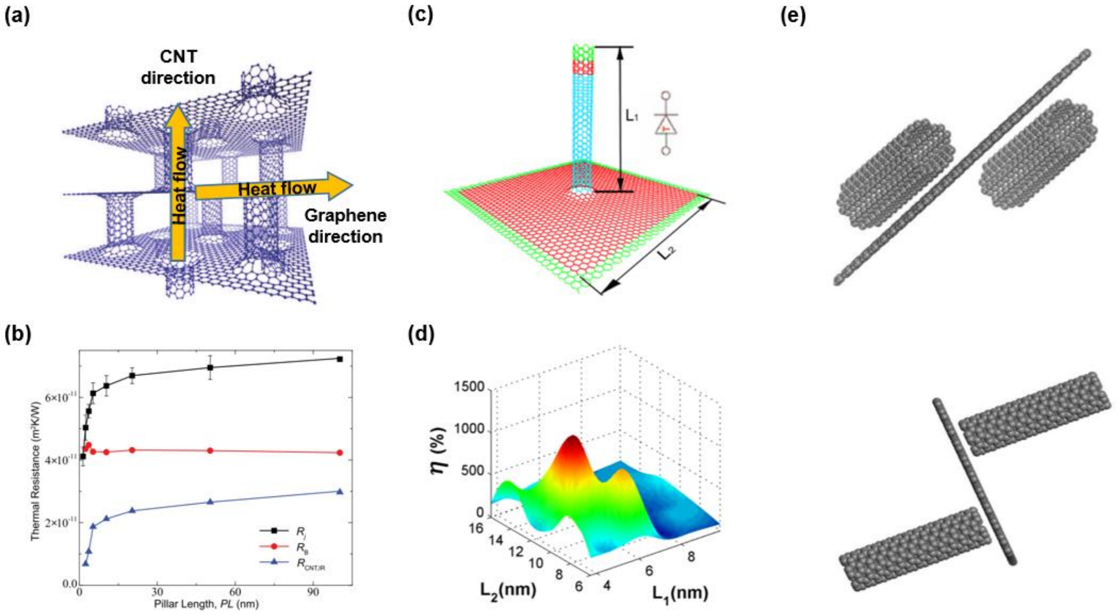

Figure 1.6. Thermal transport in representative 1D-2D heterostructures. (**a**) Atomistic schematic of 1D CNT-2D graphene architecture heterostructure with (**b**) thermal transport depending on the sizes of components[7]. (**c**) Design of 1D-2D heterostructure enabled thermal diode with (**d**) thermal rectification ratio optimized by the geometric size of CNT and graphene[9]. (**e**) 1D-2D vdW heterostructures composed of graphene and CNT whose thermal conductance at the junction is dependent on the effective contact between 1D and 2D components[12].

Introducing covalent heterojunction between two different 2D materials can form a lateral heterostructure. By using NEMD and LD calculations, Zhu and Ertekin report that the thermal transport across the 2D-2D bonded heterojunction of graphene-boron nitride lateral heterostructure is reduced by interface scattering, which further depends on the length of graphene and boron nitride in heat transport direction[143]. Moreover, reducing the length of graphene and boron nitride to the one of single unit and creating 2D superlattices can dramatically reduce the thermal transport. The associated phonon properties are theoretically modeled by Ong and Zhang[144]. With NEMD, thermal rectification effect based on which the heat prefers to transport from boron nitride to graphene is explored by Chen et al[145], and similar investigations have been performed on other 2D-2D lateral heterostructures such as graphene-MoS_2[146] and graphene-silicene[147]. In addition, the thermal transport parallel to the interface is also hindered by phonon scattering, verified by Song and Medhekar with EMD simulation[148] In 2D-2D vdW heterostructure, due to the intrinsic geometric difference in the lattices of 2D components, mismatch strain will be introduced to the structure[149], which reduces the phonon lifetime and hinders thermal conductivity in the direction parallel to the vdW interface. The reduction in thermal conductivity has been found in other 2D-2D heterostructures composed of graphene-MoS_2[150, 151], MoS_2-$MoSe_2$[152] and graphene-black phosphorus[153]. According to *Ding et al*, the thermal transport across vdW interfaces in vertical heterostructures is poorly dependent on intralayer phonon modes, and the atomic interaction determines the phonon transmission behavior[154]. A similar conclusion has been drawn for the interfacial thermal transport of graphene-black phosphorus heterostructure[155]. With experiments, Chen *et al.* demonstrate that interactions limited by interface with low quality can impede interfacial thermal transport[156]. Nevertheless, the interfacial thermal rectification phenomena found in 2D heterostructures such as graphene-silicene[147] are attributed to the phonon resonance of intraplane modes.

To summarize, the thermal transport properties parallel or across the heterojunction of heterostructures composed of nanomaterials with different dimensions are largely dependent or influenced by the existence of interfaces. Although the phonon transport across vdW and bonded interfaces are different in mechanisms as discussed above, the interfaces generally cause negative impacts.

1.3.2 Response of Thermal Transport in Low-Dimensional Materials and Heterostructures to Mechanical Loadings

Compared to the impact of material factors on the intrinsically outstanding thermal transport ability of low-dimensional materials and heterostructures, the influence of mechanical stimuli such as strain and pressure is more important and it provides the opportunity to develop mechanical sensors based on the thermal response. For bulk materials such as diamonds, silicon, and argon, the thermal transport properties under mechanical strain has been reported[16, 17]. It is also confirmed that the thermal transport in low-dimensional materials and heterostructures is sensitive to mechanical loadings[32], which will be introduced in this section.

1.3.2.1 Thermal Transport in Low-Dimensional Materials Under Mechanical loadings

By using NEMD simulation, Ren *et al.* finds that either a tensile strain or compressive strain (<5%) will decrease the axial thermal conductivity of 1D CNT, which is attributed to the variation in phonon activities: a tensile and compressive strain will generate the red and blue shift of the high frequency phonon modes, corresponding to the bond stretching and compressing, respectively. Meanwhile, the magnitude of the primary peak in the phonon spectra is depressed, indicating lower phonon resonance[157]. While the same effect of tensile strain on thermal conductivity of CNT is reported by Xu and Buehler, they explore that higher compressive strain (>5%) will intrigue local mechanical instability such as buckling in CNT, which cause enhanced phonon scattering and suppress thermal conductivity[158]. For the strong phonon scattering, a similar reduction in thermal transport achieved by twisting[158] and bending[159] is found. Extensive investigations have been performed on other 1D nanomaterials such as silicon nanowire[17] and silicene nanotube[160] and confirm the mechanical effect on thermal conductivity.

As for 2D materials such as graphene, a tensile loading can reduce phonon group velocity and intrigue lattice anharmonicity, leading to the reduction in thermal conductivity, which is explored by Wei et al[80]. The same finding is also found by Li et al. with EMD[17]. Applying local strain instead of a global one in graphene, similar to the nano-indentation on materials, is found to generate a similar negative impact on thermal transport[161]. Similar phenomena and mechanisms have been confirmed in 2D materials including phosphorene[162], boron nitride[143], and MoS_2[163]. However, tailoring 2D materials to generate topological patterns with high mechanical flexibility and durability such as graphene kirigami can delay the negative response of thermal transport to tensile loading. Given the atomically thin feature and the ultralow flexural rigidity as discussed in 1.2, compressive strain in 2D graphene can lead to significant out-of-plane deformation and form a corrugated structure. However, no significant change is found in thermal conductivity due to the almost unchanged frequency and magnitude of phonon modes[80]. A twist in graphene will reduce the thermal conductivity owing to the strengthened confinement to the flexural modes[80].

In summary, for low-dimensional materials with different dimensions geometrics and material properties, the mechanical loading in different modes can directly coordinate with phonon modes and generate impact on thermal transport properties. Nevertheless, structural designs that can alter mechanical responses in terms of lattice structures to the original geometry can change the response.

1.3.2.2 Thermal Transport in Low-Dimensional Heterostructures Under Mechanical loadings

As discussed in 1.3.1.3, the thermal transport in low-dimensional heterostructure is closely related to the properties of the heterojunction. Therefore, the thermal response subjected to mechanical loading should depend on the behavior of heterojunction in addition to the individual response of the components, which is usually more sensitive to external loadings compared to pristine materials and will be introduced in this section.

As for thermal transport across a heterostructure with a bonded junction, the phonon transmission properties at the junction is the key and can be tuned by applying strain effect. For example, Ong, Zhang and, Zhang explore that in 2D graphene-2D boron nitride lateral heterostructure, the interfacial thermal conductance can be significantly improved (25%) by applying tensile strain (~7%) given the enhanced alignment between the phonon bands of graphene and boron nitride, which facilitate the phonon transport[164]. The same mechanism of strain-dependent phonon transmission is found in 2D graphene-2D silicene lateral heterostructure[147] and mix dimensional1D CNT-2D graphene heterojunction[165].

On the other hand, by applying external loading, the thermal transport across vdW junctions can be changed by the atomic interaction[166], which is usually associated with the morphology of the junction. With NEMD simulation, Ding *et al.* explored that the thermal transport across the vdW junction of graphene MoS_2 can be increased by twice or decreased to 50% of the initial value by the cross-planar compression or tension with small magnitude (~5%), respectively, which drastically decrease/increase the separation of graphene and MoS_2 at the junction and enhance the atomic interaction. The same mechanism is reported in graphene-black phosphorus vdW heterostructure[155].

Although the role of heterojunction in thermal transport parallel to either vdW or covalently bonded interfaces subjected to loadings has not been highlighted in current research, the sensitivity of thermal transport is confirmed in both bonded Si/Ge heterostructure[167].

1.4 Innovation of Present Research

Previous works have explored that the thermal transport properties in low-dimensional heterostructures can be influenced by mechanical effects. However, fundamental understandings of detailed coupling mechanisms are still lacking. For example, the difference between the mechanisms in phonon activities subjected to small loadings (<15%) and large loadings (>15%) has not been thoroughly discussed. In addition, current understandings of mechanism in thermal transport of heterostructures are usually limited to elucidate a specific heterostructure composed of certain materials, and a generalized theory to explain the mechanically responsive thermal transport in heterostructures with different combinations of materials has not been set up. As for application, the mechanically responsive thermal transport has only been proposed for thermal management, and the versatility needs to be broadened.

In this thesis, fundamentally, we build up the bridge connecting the thermal transport mechanisms under small and large loadings by introducing the concept of mechanical stretchability. In Chapter 2, *via* detailed discussion and extensive analyses of the behavior of mechanical stress and phonon activities, we demonstrate the contrasting mechanisms below mechanical stretchability (small loading) and beyond stretchability (large loading) and further incorporate them into a theoretical model for quantitative explanation of thermal transport covering the whole loading range. In Chapter 4 and 5, the barrier of materials is further broken by incorporating geometric and mechanical properties of component materials into the theoretical model. The strong robustness of models has been confirmed by extensive calculations.

In Section 1.1, we have introduced that the current mechanical sensors based on the response in electric resistance are limited by mutual electric signal interference and self-heating issues caused by the continuous electricity input. We propose that the quantitative relationship between mechanical loading and thermal transport can be utilized to develop a novel and analogical working mechanism for mechanical sensors to avoid these limitations, which broadens the applications of mechanics-thermal mechanisms. In Chapter 5 and 6, two types of mechanical sensors including pressure sensors and strain sensors that both rely on thermal responses to mechanical loading were proposed and exemplified. Their functionalities can be further improved by molecular design at their heterojunctions.

1.5 Methodology

Full-scale molecular dynamics (MD) simulations will be used in this research to understand the thermal transport mechanism subjected to mechanical loadings. In comparison with other popular methods such as density functional theory (DFT) calculations and solving Boltzmann transport equation (BTE) which are limited by system sizes numbers of atoms, usually less than 10000 atoms, and finite-difference time-domain (FDTD) method which fails to capture the atomic dynamics of materials at the nanoscale, MD simulation will overcome these limitations and has been proved to capture both mechanical deformation and thermal transports of low-dimensional materials of close relevance to atomic activities at the nanoscale in a low-cost manner.

In addition, to obtain the fundamental properties of phonons and explain the heat transport phenomenon in terms of lattice vibration, normal mode analysis (NMA) will be adopted in this research, which further relies on lattice dynamics (LD) calculation.

This section will briefly introduce the fundamental of MD and LD while the computational details will be given in the following chapters.

1.5.1 Fundamental of MD

As a simulation technique, MD was introduced by Alder and Wainwright[168] with the aim of building bridges between micro/nanoscopic length and time scale and between theory and experiment by using dynamics properties. MD simulations are based on stepwise and numerical solutions to the classical equation of motions:

$$m_i \frac{\mathrm{d}^2 r_i}{\mathrm{d}t^2} = -\frac{\partial U}{\partial r_i}, \tag{1.9}$$

where m_i and r_i are the mass and position of i$^{\text{th}}$ atom and U is the potential energy of the system, which is further determined by the potential functions. At each time step, the Verlet algorithm is adopted to integral the acceleration of each atom and update the atomic velocity and position to further reproduce the dynamic behavior of atomic systems[169]. In MD simulations, the proper selection of potential function is the key to the preciseness and reliability. Generally, the potential function is contributed by two parts, namely intramolecular $U_{intramolecular}$ and intermolecular potential $U_{intermolecular}$, which describes the bonded interaction within a molecule and non-bonded interactions between different molecules, respectively, will be simply introduced below.

1.4.1.1 Intramolecular Potential in MD Simulation

The intramolecular potential energy is usually contributed separately by bond stretch potential U_{bond}, bond bending potential U_{angle} and bond torsion potential $U_{dihedral}$ as:

$$U_{intramolecular} = U_{bond} + U_{angle} + U_{dihedral}. \tag{1.10}$$

The bond stretch term U_{bond} describes the potential energy associated with stretching or compressing an atomic bond with an equilibrium distance of r_0 and force constant k_{bond}, leading to the change of distance between two bonded atoms r, and for the popular harmonic expression:

$$U_{bond} = k_{bond}(r - r_0)^2 \tag{1.11}$$

The bond bending term U_{angle} refers to the potential energy associated with the change in the angle formed by two adjacent bonds. If the bond angle with angle force constant k_{angle} and an equilibrium value of θ_0 changed to θ, assuming harmonic expression,

$$U_{angle} = k_{angle}(\theta - \theta_0)^2 \tag{1.12}$$

The bond torsion term describes the potential energy results from displacing a planar groups of atoms with at least three covalent bonds from its equilibrium angle ϕ_0 (usually equals 0), and one of the popular form is:

$$U_{dihedral} = k_{dihedral}[1 + dcos(n\phi_0)], \tag{1.13}$$

where $k_{diheral}$ is the dihedral force constant, d and n are empirical parameters.

Note that for different systems, the expressions for U_{bond}, U_{angle} and $U_{dihedral}$ may vary to better fit the experimental behavior. Such as Morse style bond and 2-fold bond torsion terms in carbon-based low-dimensional materials[170]. In addition, for some newly developed empirical potential such as REBO[171] and Tersoff[172] potentials, multibody expressions will be adopted, in which the explicit expressions of bond stretch, bending or torsion is not available. Nevertheless, their working principle in MD simulation remains the same.

1.4.1.2 Intermolecular Potential in MD Simulation

Intermolecular potential governs the attractions and repulsion between non-bonded species, such as molecules, single atoms, and ions, which is generally weaker than the intramolecular interaction associated with the deformation of atomic bonds. Generally, the intermolecular potential is contributed by two parts, namely vdW potential U_{vdW} and electrostatic interaction $U_{coulomb}$:

$$U_{intermolecular} = U_{vdW} + U_{coulomb}. \tag{1.14}$$

The pair wise vdW potential depends on the separation distance r_{ij} between the ith and jth atoms and has the form of:

$$U_{vdW}(r_{ij}) = 4\varepsilon_{ij}[\left(\frac{\sigma_{ij}}{r_{ij}}\right)^{12} + \left(\frac{\sigma_{ij}}{r_{ij}}\right)^{6}], \tag{1.15}$$

where σ_{ij} is the equilibrium distance where the potential is zero and ε_{ij} is the depth of the potential depending on the species of atoms.

Electrostatic potential is based on the Coulomb Law:

$$U_{\mathrm{coulomb}}(r_{\mathrm{ij}}) = \frac{q_i q_j}{4\pi\varepsilon_0 r_{ij}} \tag{1.16}$$

where q_i and q_j are the charges on ith and jth atoms, respectively. ε_0 is the dielectric constant of vacuum. Given that the vdW interaction gets weaker with distance at the speed of r_{ij}^6, for a system with a considerable number of atoms, setting a truncation distance for vdW interaction (usually 1 nm) is widely adopted to save the computational cost. On the other hand, for electrostatic potential, the reduction with distance is not significant, specific summation techniques such as particle-particle particle-mesh (PPPM) is usually adopted[173].

1.5.2 Fundamental of LD

While MD focuses on the dynamic properties of atoms, the aim of LD is to obtain vibrations of atoms and the sound wave propagation in the system. The modern theory of lattice dynamics is based on the lattice dynamics model proposed by Born and von Karman in 1912[174], and further developed by Debye and Waller to become a technique for deducing atomic structures[175]. In this thesis research, the LD calculation is used to perform normal mode analysis (NMA) to calculate the mode vector and frequency of each vibration modes, based on which the phonon properties associated with thermal transport, such as phonon participation ratio, can be extracted.

To do this, based on the harmonic approximation, the force constant matrix can be obtained by taking the 2nd derivative of the potential energy of the atomic system U with respect to the position of atom:

$$\boldsymbol{\Phi}_{k,l}^{pq}(m,n) = \frac{\partial^2 U(\boldsymbol{x})}{\partial \boldsymbol{x}_{mk} \partial \boldsymbol{x}_{nl}}_{x=x^0, m\in B_p, n\in B_q, k=x,y,z, l=1,2} \tag{1.17}$$

where $\boldsymbol{x}_{mk}$ and $\boldsymbol{x}_{nl}$ are the *k*th and *l*th component of the position of atoms *m* and *n*, respectively. B_p and B_q are Bravais lattices i and j. Notice that U is determined by the potential function. The same potential function applied in MD calculation should be applied in

LD calculation to ensure consistency. Furthermore, the dynamic matrix $\boldsymbol{D}(\boldsymbol{k})$ of the wave vector $\boldsymbol{k}$ will be determined via:

$$\boldsymbol{D}(\boldsymbol{k}) = \frac{1}{M}\begin{bmatrix} \sum_n \boldsymbol{\Phi}_{\mathrm{k,l}}^{11}(m,n)e^{i\boldsymbol{k}\cdot(\boldsymbol{x}_n^0-\boldsymbol{x}_m^0)} & \sum_n \boldsymbol{\Phi}_{\mathrm{k,l}}^{12}(m,n)e^{i\boldsymbol{k}\cdot(\boldsymbol{x}_n^0-\boldsymbol{x}_m^0)} \\ \sum_n \boldsymbol{\Phi}_{\mathrm{k,l}}^{21}(m,n)e^{i\boldsymbol{k}\cdot(\boldsymbol{x}_n^0-\boldsymbol{x}_m^0)} & \sum_n \boldsymbol{\Phi}_{\mathrm{k,l}}^{22}(m,n)e^{i\boldsymbol{k}\cdot(\boldsymbol{x}_n^0-\boldsymbol{x}_m^0)} \end{bmatrix}, \tag{1.18}$$

where M is the atomic mass. The eigenvectors of the dynamic matrix are the mode vector of the system and the eigenvalue is the square of angular frequency of each mode ω^2.

1.6 Outline of Dissertation

The thermal transport properties in low-dimensional materials and heterostructure are sensitive to external loadings such as tension and external pressure owing to the direct coupling of mechanical effect and phonon activities. Through the present thesis, the thermal transport and the underlying mechanism in 2D low-dimensional materials, and their heterostructures subjected to external loadings is thoroughly investigated and explored, based on which mechanical sensors are designed *via* computational approach. The thesis consists of six chapters:

In Chapter 1, an introduction of the current challenges in wearable mechanical sensors, the fundamental and key factors in nanoscale thermal transport, the responsive thermal transport properties in low-dimensional materials and heterostructures subjected to external mechanical loadings and current research findings, mechanisms and probing methods, is briefly overviewed.

In Chapter 2, by using nonequilibrium molecular dynamics simulation, the thermal transport and phonon mechanism in serpentine graphene nanoribbon and auxetic (AG), contractile graphene (CG) and the heterostructures composed of their single units subjected to mechanical loading is systematically investigated. The key factor of mechanical stretchability is explored, which leads to different responsive mechanisms at high and low mechanical loadings. The stress level and phonon activities are further obtained to elucidate the findings.

In chapter 3, with molecular dynamics simulations, the mechanically responsive thermal transport in graphene-boron nitride lateral heterostructure with a material interface is investigated. The dependence of thermal transport on mechanical loading is understood *via* stress concentration, phonon resonance and localization at heterojunctions.

In chapter 4, the thermal response in two types of vdW heterostructures, Bilayer 2D vdW heterostructure and graphene kirigami vdW heterostructure, subjected to external tension is investigated. The mechanics-thermal coupling is thoroughly explained by the lattice mismatch effect and atomic interaction at the interface in response to the external tensile strain and verified by stress level and phonon properties.

In Chapter 5, with molecular dynamics simulations, the thermal conductance in 1D CNT-2D material-1D CNT is explored. Simulation analyses further reveal the strong dependence of thermal conductance on the location and magnitude of an external pressure loading applied to the local vdW heterojunctions. The underlying thermal transport mechanism is uncovered through the elucidation of the mechanical deformation. A proof-of-conceptual design of such a heterostructure-enabled pressure sensor is explored by utilizing the unique response of thermal transport to mechanical deformation at heterojunctions.

In Chapter 6, with molecular simulations, the thermal transport across solid-liquid interfaces of graphene oxide-water molecules heterostructure that is sensitive to loading modes is explored. The responsive thermal transport is attributed to the reversible response of hydrogen bonding networks between confined water molecules and graphene oxides, and quantitatively elucidate the thermal transport mechanism by correlating thermal conductance, number and distribution of hydrogen bonds and interfacial energy with mechanical loadings, based on which a mechanical sensor capable of load sensing and mode differentiating is proposed.

For heterostructures demonstrated in Chapter 2-6, theoretical models incorporating mechanical and geometric properties of materials are developed for the comprehensive understanding of the mechanics-thermal coupling. Moreover, by varying the material and geometric parameters in the model, the findings can be generalized to the same type of heterostructures composed of other potential components. The generalization may serve as the theoretical foundation guiding the design and improvement of the mechanical tunable thermal devices and mechanical thermal sensors with ideal mechanical durability and thermal sensitivity.

In Chapter 7, the major findings are summarized and future works in the relative fields are suggested.

Chapter 2 Thermal Transport of Two-Dimensional Structures under Mechanical Loadings

2.1 Overview of the Chapter

In this chapter, we report the mechanically responsive thermal transport in serpentine graphene nanoribbons and meshed graphene subjected to small and large mechanical loadings with full-scale molecular dynamics computational approach.

The thermal conductivity of graphene nanoribbons usually decreases quickly with the increase of tensile strain due to the softened phonon modes and increased lattice anharmonicities. We present a new design on graphene nanoribbon of serpentine graphene nanoribbons (SGNRs) and demonstrate that the thermal conductivity of SGNRs increases with the increase of tensile strain through nonequilibrium molecular dynamics (NEMD) simulations. This increase can be held till to as large as 54.7% stretchability of SGNRs. The unusual response of thermal conductivity results from the competition between the elongation of heat transfer path and stress distribution in nanoribbon structures under tension and is closely related with the maximum stretchability of serpentine structures. Both mechanical stress distribution and phonon spectra of SGNRs are examined to understand the underlying thermal transport mechanism and show good agreement with simulation findings.

Using computational simulations, we show that the thermal conductivity of meshed graphene can be regulated by patterning unit cells of auxetic graphene (AG) and contractile graphene (CG) with different interface properties under a uniaxial tensile strain. Analyses of both mechanical deformation and vibrational spectra indicate that the thermal transport properties of graphene heterostructures are highly dependent on their mechanical stress distribution, and also rely on the interfaces that are parallel with the directions of mechanical loadings. Theoretical models that integrate the contributions of mechanical loading and patterned-interfaces are developed to quantitatively describe the thermal conductivity of graphene heterostructures. Good agreement of thermal conductivity between theoretical predictions and extensive simulations is obtained. These designs and findings are expected to pave a new route to seek interface-mediated stretchable thermal electronics with mechanically controllable performance.

2.2Thermal Transport in Serpentine Graphene Nanoribbon Subjected to Tensile Loading

2.2.1 Computational Modeling and Method

Figure 2.1 depicts an SGNR with periodic serrated-edges. w and a are the width and length of nanoribbons, respectively, and α is the angle of serration. The initial length of the SGNR, l_0, is defined as the length of its projection in the *x*-direction and $l_0 = 6a\sin(\frac{1}{2}\alpha)$. The width of the SGNR in the *y*-direction is defined as b, and $w = bsin(\frac{1}{2}\alpha)$. Given the length l_0 and width w, by changing the angle of serration α, two groups of computational models are constructed. α is selected to be 60^{o} and 120^{o} to ensure zigzag edges in SGNRs. These zigzag edges will help to avoid employments of hydrogen atoms at the edge in the simulations [102].The first group is based on the same length l_0 (=33.95 nm) and a proper length of nanoribbons a, and is illustrated in Figure 2.1a. The second group has the same number of carbon atoms in SGNRs and is illustrated in Figure 2.1b. Calibrated by the number of carbon atoms in the SGNR with α of 60° (l_0=33.95 nm), the length of the SGNR with α of 120° can be calculated and is 58.73 nm. In each group, a regular pristine GNR counterpart (corresponding to α=180°) is employed for comparisons and its length is 67.90 nm in the second group (Figure 2.1b). The width of all nanoribbons w in both groups is the same and is 1.897nm, similar to the measurement in experiment[176].

All simulations were performed by using LAMMPS[177]. The AIREBO potential was employed to describe carbon-carbon interactions[178]. The cutoff radius for REBO and L-J potentials was set as 0.2 nm and 0.68 nm, respectively, to reproduce the reliable mechanical

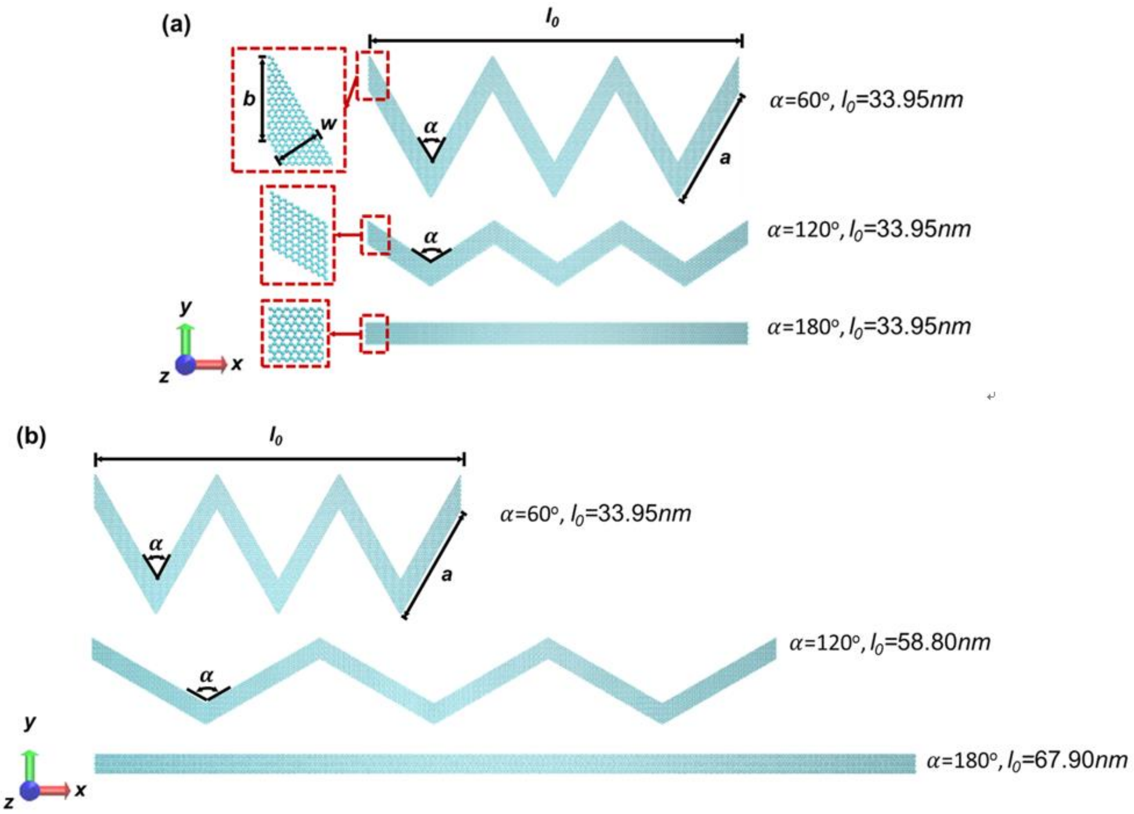

Figure 2.1. Computational models of serpentine graphene nanoribbons (SGNRs) with **(a)** the same length in the ***x***-direction and **(b)** the same total number of carbon atoms. A periodic boundary condition is applied in the ***x***-direction and non-periodic boundary conditions are applied in the *y* and *z*-direction in MD simulations. l_0 and b are the length and width of projection of the structure in the ***x*** and *y*-direction, respectively, w and a are the width and length of nanoribbons, respectively, and α is the angle of serration. When α=180°, it corresponds to a regular pristine GNR. The length l_0 is 33.95nm for all structures in the model (a), and in the model (b) the length l_0 is 33.95nm, 58.73 nm, and 67.90 nm for SGNRs with α=60° and α=120°, and regular GNRs, respectively. The width of all nanoribbons w in both groups is the same and is 1.897nm.

and thermal properties of graphene such as failure strain and thermal conductivity[49, 100]. The integration time step was 0.5 fs. A periodic boundary condition was applied to the $\boldsymbol{x}$-direction and a non-periodic boundary condition was used in the y and z–direction, through which a freestanding graphene structure was achieved to allow out-of-plane deformation.

To extract the thermal conductivity of SGNRs under tensile strain, the uniaxial tensile test is first performed to obtain strained SGNRs as follows. At initialization, SGNRs are equilibrated in canonical ensemble (NVT ensemble) for 0.5 ns at the temperature of 300 K with the help of Nosé-Hoover thermostat. Next, the SGNRs are uniformly stretched in NVT ensemble along the $\boldsymbol{x}$-direction under a quasi-static displacement loading to reach a desirable tensile strain. The nominal strain ε is used and defined as $= \frac{l-l_0}{l_0}$, where l is the total length of the SGNRs after tensile deformation. The resultant nominal stress σ is calculated via $\sigma = -(\frac{\sum_k^N m_k v_{kx} v_{kx}}{V_0} + \frac{\sum_k^N r_{kx} f_{kx}}{V_0})$, where N is the total number of carbon atoms, m_k is the mass of the k^{th} carbon atom, v_{kx}, r_{kx} and f_{kx} are the velocity, position, and total force in the x-direction of the k^{th} carbon atom, respectively. V_0 is the initial volume of the SGNRs and equals $l_0 bt$, where t is the thickness of graphene nanoribbons, and is taken to be 0.34nm[36].

Once the SGNRs are deformed to a desirable strain, non-equilibrium molecular dynamics (NEMD) simulations will then be carried out to extract the thermal conductivity of the strained SGNR by following the procedures, as described below. Equilibrium was run to the strained SGNRs in NVT ensemble for 0.5 ns at 300 K at the beginning. Afterward, a constant value of heat flow was imposed to the system along the x-direction in the microcanonical ensemble (NVE ensemble) for 1.5ns. The strained SGNR was divided into 40 slabs along the heat flow direction to extract their temperature profiles. The two slabs at both ends were selected as cold reservoirs, and the two slabs in the middle were used as the hot reservoir, through which a periodic boundary of thermal flow in the *x*-direction was applied. The constant heat flow was achieved by allowing hot/cold reservoirs to generate/dissipate heat at a rate of 0.3 eV/ps through the velocity scaling of atoms. This method is referred to as the reverse non-equilibrium molecular dynamics (RNEMD) simulation and has been widely acknowledged in the extraction of thermal conductivity because it helps to process data easily by imposing a constant value of quantity such as heat flow [179, 180]. Temperature distributions during the last 1.0 ns were collected to calculate thermal conductivity of the strained SGNR.

2.2.2 Uniaxial Nominal Stress-Strain of SGNRs in Tension

Figure 2.2a shows the nominal stress-strain curves of the SGNRs with the same initial length l_0. l_0 and w are 33.95 nm and 1.897nm, respectively. For the regular GNR (black line, α=180°), the stress increases linearly at a small strain, followed by a nonlinear variation. Then a sudden drop takes place, corresponding to the failure of carbon-carbon bonds, which is in good agreement with that of typical pristine zigzag GNRs under uniaxial tension[181]. The nominal failure strain of GNR is 32.6%, which is also close to reports in MD simulations on

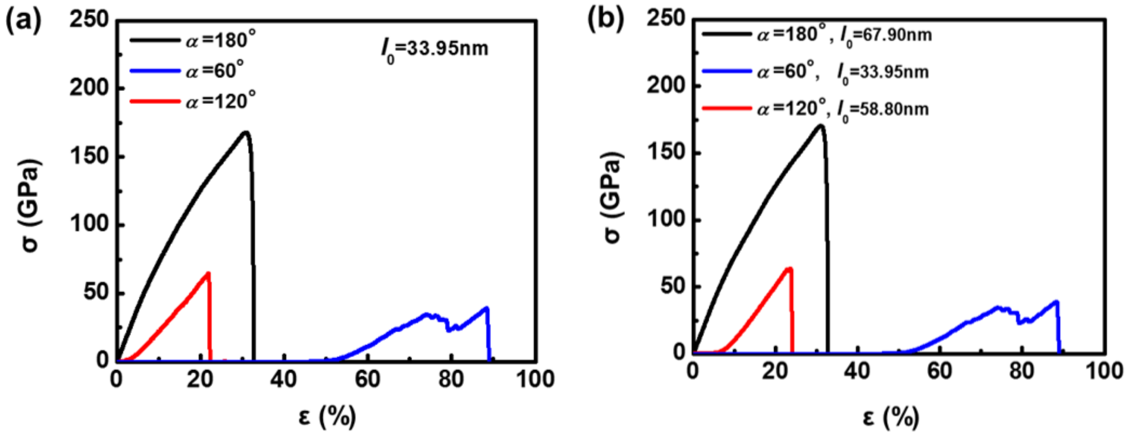

Figure 2.2. Uniaxial nominal stress-strain curves of regular graphene nanoribbons (GNRs, α=180°) and serpentine graphene nanoribbons (SGNRs) with **(a)** the same initial length and **(b)** the same number of carbon atoms in tension.

pristine zigzag GNRs (23%-35%) performed using the same force fields[181, 182]. In contrast, in the SGNR with α of 60^{o} (blue line), the nominal stress almost remains zero even if the applied strain is as large as 54.7%. After that, a linear increase of nominal stress with strain appears, followed by an approximate plateau of stress. Finally, the structure fails due to the failure of carbon-carbon bonds, which is indicated by a sudden drop of stress. The corresponding nominal failure strain is 89.1%, which is almost three times higher than that of the pristine GNRs, and also much higher than that of other designed structures of GNRs such as porous GNRs (<60%)[183, 184]. The fluctuations of stress in a range of nominal strain from 73% to 89.1% are caused by the local breaks of carbon-carbon bonds near the corners of serrations. For the SGNR with α of 120^{o} (red line), a nonlinear variation of nominal stress is also observed, but unexpectedly there is an obvious decrease under a smaller nominal failure strain (22.3%) in comparison with either GNR or SGNR with α of 60^{o}, which will be elucidated later.

In parallel, **Figure 2.2b** plots the nominal stress-strain curves of GNR and SGNRs for the second group models (Figure 2.1b) with the same carbon atoms and different length l_0. Similar with observations in Figure 2.2a, an enhanced failure strain in the SGNR with α of 60^{o} over that of the pristine GNR are observed, while the failure strain shows a decrease in the SGNR with α of 120^{o}, demonstrating that the deformation behavior of GNRs can be significantly changed through the introduction of serpentine structures without altering their inherent carbon-carbon bonding structures. In addition, for both GNRs and SGNRs with the same angle of serration, α, Figure 2.2a and b show almost the same maximum nominal failure strain and stress without obvious scaling effects. Since the thermal properties to be investigated below are strongly related with the number of atoms [5, 96], the SGNRs with the same number of carbon atoms (the second group model, Figure 2.1b) will be employed in the following study of thermal properties unless otherwise specified.

2.2.3 Stress Distribution in SGNRs Subjected to Tension

To uncover the difference in nominal failure strain of SGNRs and GNRs, von Mises stress is calculated to understand the stress distribution in the SGNRs and GNR counterparts under tension. **Figure 2.3a** gives snapshots of stress distribution in the GNR with the length of 67.90 GNR because the whole structure is too long to be viewed in details. When there is no external applied tensile strain (0%), after initial equilibrium in NVT ensemble, the GNR will twist spontaneously due to the edge effects for narrow pristine GNR, and a clear out-of-plane twisting deformation is observed. This twisting deformation is strongly dependent of the width

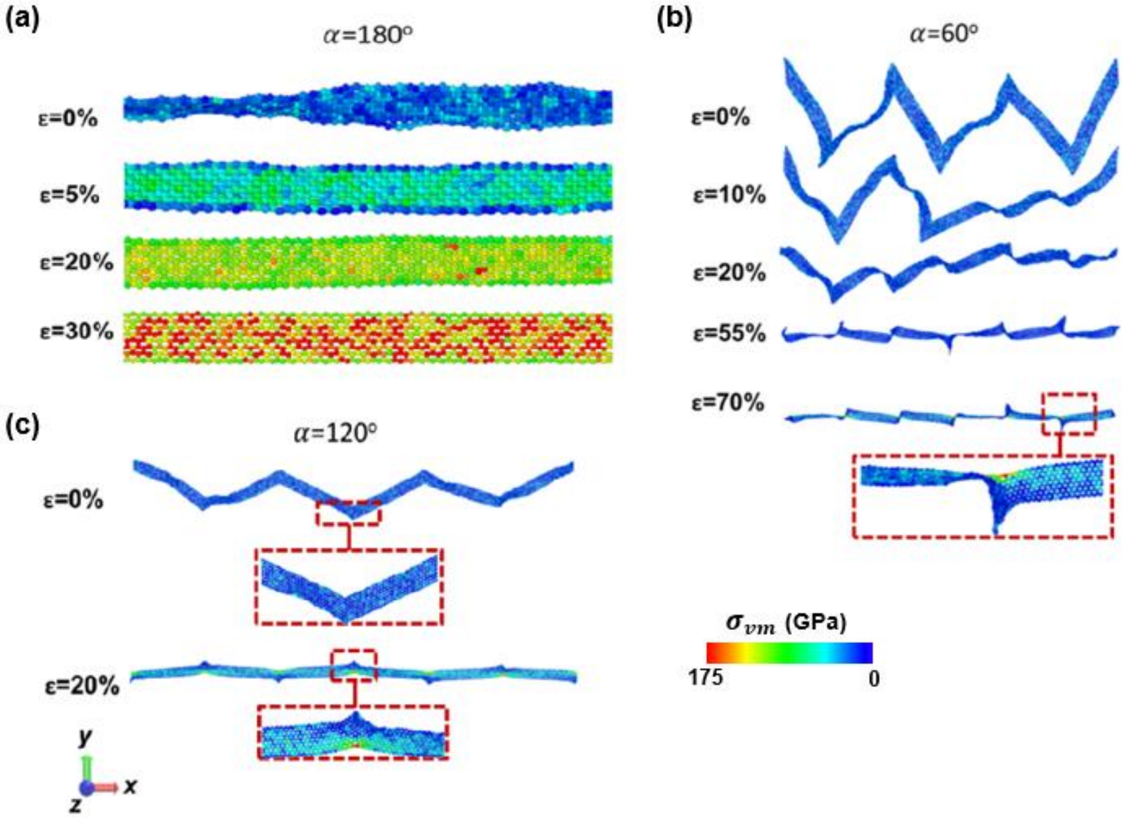

Figure 2.3. Snapshots of von Mises stress distribution of SGNRs with the angle of serration α (a) 180° (regular GNRs), **(b)** 60° and **(c)** 120° under different tensile strain ε

of GNR and boundary conditions, and will vanish if periodic boundary conditions is applied in both x and y-direction [185]. As the tensile strain increases to 5%, the torsion is significantly reduced due to the axial tensile constraint from the stretching deformation, and the deformation is dominated by tension in the x-y plane, showing an approximately uniform distribution of von Mises stress. We should note that the von Mises stress is a little bit lower on the edge atoms than that on central atoms due to edge effect in the current non-periodic boundary conditions applied in the $\boldsymbol{y}$-direction. As the strain goes to 30% and gets close to the failure strain (32.6%), von Mises stress of the whole structure increases but is still uniform except for the edges. Besides, the torsion seems to be insignificant.

Figure 2.3b shows the distribution of von Mises stress in the SGNR with α of 60^{o}. Similar with that in the GNR counterpart, a slight deformation in the $\boldsymbol{x}$-$\boldsymbol{y}$ plane is observed when no strain is applied after equilibrium in the NVT ensemble, and will remain throughout the whole tensile process. The applied tensile strain will tend to straighten the serrated-edges by intriguing rotation in the $\boldsymbol{x}$-$\boldsymbol{y}$ plane first, rather than leading to elastic deformation of the SGNR due to strong carbon-carbon bond interactions. Under a tensile strain of 20%, the deformation of the SGNR is elongated but the stress in the whole structure still remains zero. As the tensile strain rises to 30%, the rotation of serrated-edges becomes severe, elongating the SGNR further. Such rotations will remain until the tensile strain reaches 55% when all serration edges are approximately parallel with the tensile direction. Afterward, the tensile strain causes a high stress concentration at the corners of serrations, as shown in the snapshot at ε=70%, leading to breaks of carbon-carbon bonds.

The failure strain in the SGNRs depends on the competition of geometric rotations of serrated-edges and local breaks of carbon-carbon bonds. For instance, when the angle of serration is 60^o, the rotation of the serrated-edges can be as high as 60^o till to aligning with the axial tensile direction. This high rotation can lead to 50% deformation in theory, which is much higher than that of the failure strain of the pristine GNRs (33%), leading to a significant delay of localized elastic deformation in the SGNR, and thus enhancing the nominal failure strain of the SGNR with α of 60^o in comparison with that of GNRs. In contrast, in the SGNR with α of 120^o, the maximum rotation of the serrated-edges is only 30^o, corresponding to the maximum tensile strain of 13.4%, which is far less than the failure strain of pristine GNRs (33%). Therefore, after a quick rotation of the serrated-edges, the elastic deformation will begin and the early onset of stress concentration at the corners of serrations accelerates breaks of carbon-carbon bonds, thus decreasing the failure strain. To decrease the stress concentration at the corners and delay breaks of carbon-carbon bonds, rounded transitions among serrated-edges can be introduced to optimize SGNRs in practical applications.

2.2.4 Thermal Conductivity of SGNRs in Tension

Given the outstanding stretchability of the SGNR with α of 60^o (referred to as SGNR60 below), we will focus on the investigation of its thermal conductivity under a tensile strain. Its initial length l_0 is 33.95 nm. The thermal conductivity of the GNR with the same total number of carbon atoms yet length of 67.90 nm is also extracted under the tensile strain for comparisons. After the SGNR60 is stretched to a desirable strain by following above procedures in MD simulations, the strained SGNR60 is then equilibrated in NVT ensemble at 300K for 0.5 ns. Next, a heat flow J is applied for reaching a stable temperature distribution in the strained

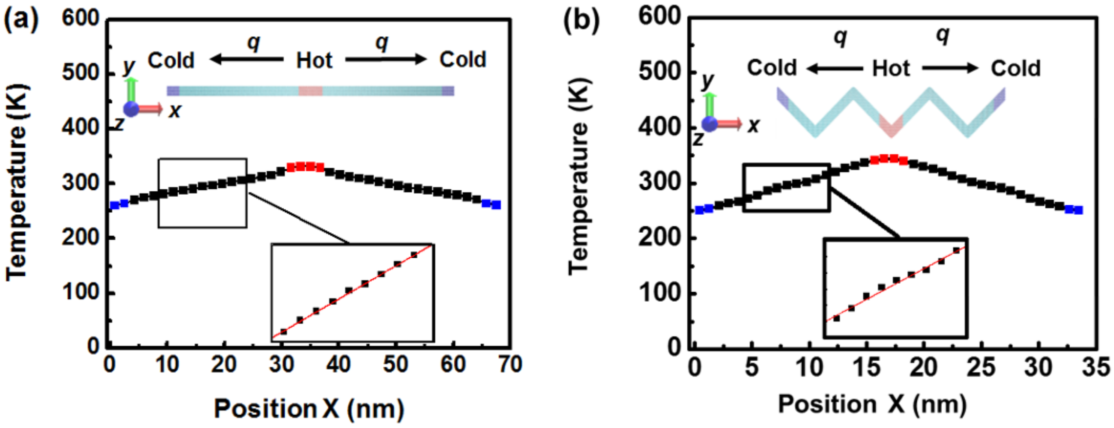

Figure 2.4. Temperature profile in SGNRs with the angle of serration α (a) 180° (regular GNRs) and **(b)** 60°. The insets illustrate the computational model and linear region of temperature profiles, respectively. In the computational model, both ends and the middle of SGNRs are set as cold and hot reservoirs, respectively to construct a periodic boundary condition in the heat flow $\boldsymbol{x}$-direction. The heat flow is imposed by scaling energy of atoms in reservoirs at a rate of 0.3 eV/ps. The temperature gradient is extracted by fitting the linear regions of temperature profiles of group atoms.

SGNR60 in NVE ensemble, as explained in the computational method in Section 2.3.1. According to Fourier's Law, thermal conductivity κ can be calculated via $\kappa = \frac{J}{2A(\partial T/\partial x)}$, where A is the cross-sectional area perpendicular to the heat flow direction and equals bt. Under a tensile strain, as shown in Figure 2.2b, since the rotation will occur in serrated-edges yet with a negligible change of strain on carbon-carbon bonds, one can have $A = tb/(1+\varepsilon)$ approximately. $(\partial T/\partial x)$ is the temperature gradient along the $\boldsymbol{x}$-direction. Since the heat is transferred from the central hot regions to the cold regions at both ends, the calculation of κ is divided by a factor of 2. Figure **2.4a and b** show the temperature distribution along the x-direction at a heat flow of 0.3 eV/ps in both GNR and SGNR60. The temperature gradient of the linear region is used to calculate the thermal conductivity by fitting temperature profiles.

Figure 2.5a shows the variation of thermal conductivity of the pristine GNR, κ_g, with tensile strain. The error bars result from uncertainties of the linear fitting to the temperature profiles. In the absence of tensile strain, κ_g is 84.02 W/mK, close to the previous findings

(77.3 Wm/K) of zigzag GNRs with a similar size[80]. With the increase of the applied strain, κ_g first shows a slight increase and then drops quickly. When no tensile strain is applied, since the out-of-plane twisting deformation in the GNR will occur as shown above, it will increase the interface phonon scattering, and weaken the ability of thermal transport[80]. Under a small applied strain (less than 5%), as evidenced by stress distribution in Figure 2.3a, the applied strain is balanced to minimize the out-of-plane torsion of the GNR. Consequently, a slightly higher κ_g is observed at a tensile strain of 5% than that without tensile strain. When the applied strain is beyond 5%, the stress distribution in the GNR increases, the out-of-plane deformation is maintained at the same level while the carbon-carbon bonds are highly stretched, resulting in an obvious decrease in κ_g due to softened phonon modes[80].

The variation of the measured thermal conductivity of the SGNR60, κ_{sg}, with applied tensile strain, ε, is plotted in **Figure 2.5b**. Similar to the observation in the pristine GNR in Figure 2.5a, a nonlinearity is observed for the SGNR60. However, κ_{sg} keeps increasing until the tensile strain reaches 55%. This unusual increase of thermal conductivity in tension depends on the stress distribution in the SGNR60. From the nominal stress-strain curve of the SGNR60

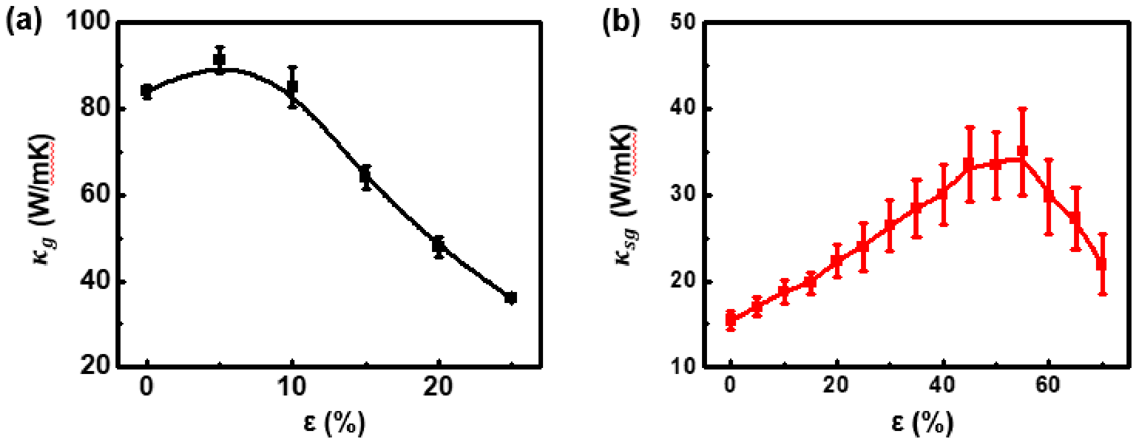

Figure 2.5. Effect of tensile strain on thermal conductivity of the **(a)** regular GNR, κ_g, and **(b)** SGNR60 (α=60°), κ_{sg}. The errors arise from the uncertainty of fitting the linear region of temperature profiles in SGNRs.

(Figure 2.2b), when the strain is less than 54.7%, the nominal stress remains zero and the deformation of the SGNR60 is dominated by the rotation of serrated-edges in the ***x*-*y*** plane without obvious elastic deformation. These rotations of serrated-edges will tend to align the SGNR in the tensile ***x***-direction, and promote longitudinal phonon transports, thus enhancing thermal transport properties. Once the elastic deformation dominates the tensile process with an obvious increase of stress in the SGNR60 (Figure 2.3b), the thermal conductivity will decrease due to the softening of phonon modes and increasing of lattice anharmonicities, similar with the mechanism of GNR in tension, and will lead to significant reductions in the thermal conductivity.

This unusual behavior of thermal conductivity in the SGNR60 under tension is also expected to exist in SGNRs with different angles of serrations and orientations such as the SGNR120 and armchair SGNRs. The critical turning point from the initial increase to later decrease of thermal conductivity with tensile strain will depend on the maximum stretchability associated with approximate zero stress over the entire structures. We should note that the thermal conductivity of GNRs and SGNRs is different at a tensile strain of zero because of their difference in geometric shapes.

2.2.5 Effect of Nanoribbons Size in SGNRs on Thermal Conductivity in Tension

Following the similar procedures, we further investigate the variation of thermal conductivity with the size of GNR and SGNR60 by considering the ratio of width to length of nanoribbons, w/a. **Figure 2.6a** shows that κ_g increases with w/a in the GNRs. Generally, the edge-phonon scattering effect will reduce at a higher w/a, promoting the ability of heat

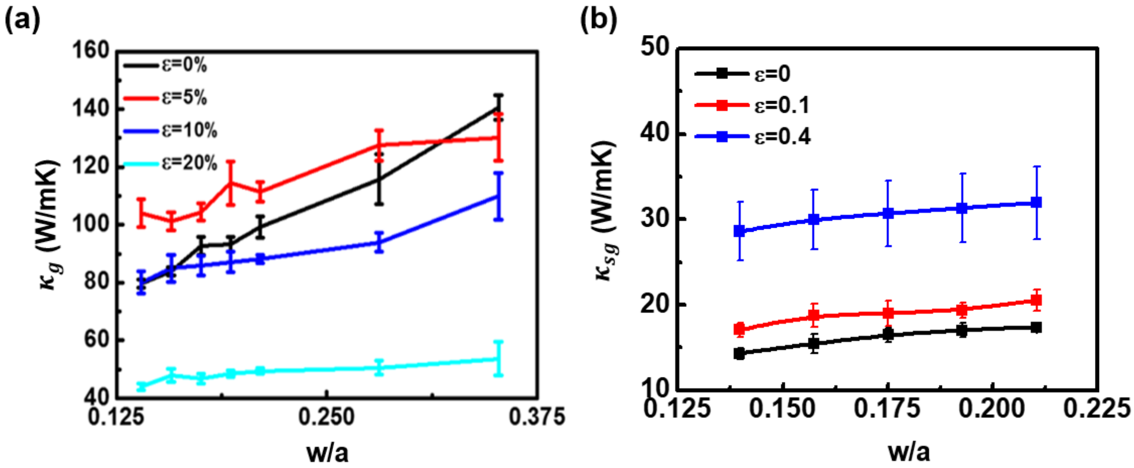

Figure 2.6. Effect of nanoribbons size, w/a, on thermal conductivity of the **(a)** regular GNR , κ_g, and **(b)** SGNR60 (α=60°), κ_{sg}, under different tensile strains. The errors arise from the uncertainty for fitting the linear region of temperature profiles.

conduction of the overall structure, and leading to a higher κ_g[96, 110]. Besides, in the absence of external tensile strain (0%), a larger w/a will minimize the out-of-plane twisting deformation due to the decreased edge effects[185]. When the graphene ribbon is wide enough such as w/a=0.352 employed in our current simulations, the effect of the out-of-plane deformation on thermal conductivity can be neglected and κ_g will decrease monotonously with the applied strain. The monotonous decrease of thermal conductivity for a wide enough GNRs resembles the deformation of GNRs under a periodic boundary constraint in both *x* and *y*-direction[96, 110, 185].

Similar to that in the GNR, an increase in the thermal conductivity κ_{sg} with w/a is also observed in the SGNR60, as shown in **Figure 2.6b**. However, since the increase of κ_{sg} is caused by geometric rotations of serrated-edges, this increase is expected to be held with the increase of applied strain until the carbon-carbon bonds are deformed. Therefore, the slight increase of κ_g in the GNRs at a relatively small tensile strain is different from the increase of κ_{sg} in the SGNR60 with the tensile strain. The κ_g is strongly dependent of w/a; while the unusual thermal response in the SGNR60, κ_{sg}, to tensile strain remains even at a larger w/a, and is highly related with geometric shapes of the serpentine structures associated with maximum stretchability.

2.2.6 Phonon Spectra of SGNRs in Uniaxial Tension

To study the effect of tensile strain on the unusual thermal conductivity of the SGNR60, the most popular phonon frequency spectrum $G(\omega)$ that represents vibrational energy of atoms per unit frequency is employed to unveil thermal transport mechanism of the SGNR60. The phonon spectrum is calculated through performing Fourier transform on the velocity autocorrelation function via $G(\omega) = \int_0^\infty e^{-i\omega t} \frac{<v(t)\cdot v(0)>}{<v(0)\cdot v(0)>}$. The $G(\omega)$ of the narrow GNR (w/a=0.157) under a tensile strain is first examined and plotted in **Figure 2.7a**. Generally, the edge phonon of GNRs will reduce phonon thermal conduction, and the peak at 14.4 THz (the inset in Figure 2.7a) is a typical edge phonon mode[186]. Under 5% small strain, its peak is lower than that without tensile strain (0%), indicating that a small tensile strain attenuates edge phonon mode by alleviating the out-of-plane torsion, and promotes the thermal transport of the narrow GNR. On the other hand, the phonon mode at the high frequency close to 52 THz is slightly softened due to a small shift to low frequency, suggesting a decreased phonon group velocity and attenuation of thermal conduction. The slight increase of thermal conductivity κ_g at 5% tensile strain in comparison with that without tension (Figure 2.5a) indicates that the attenuation of edge phonon modes associated with the out-of-plane deformation will dominate the thermal conductivity of the narrow GNR. Besides, from a mechanical point of view, the out-of-plane torsion at equilibrium restricts the phonon transport[80], and its reduction at a small strain will relax the GNR and facilitate the phonon thermal transport. With further increase of tensile strain (>5%), an obvious shift of phonon modes from high to low frequency is observed, softening high frequency modes (> 50 THz). Such a strong softening is expected to be led by tensile deformation of carbon-carbon bonds and suggests a reduced phonon group velocity and attenuated thermal transport, thus leading to a decreased thermal conductivity. At the same time, at a large deformation with an obvious tension on carbon-carbon bonds, the out-of-plane torsion nearly dies out, and the vibration of carbon atoms is only affected by lattice anharmonicity[80, 187]. As a result, κ_g shows a rapid decrease after a slight increase in the narrow GNR.

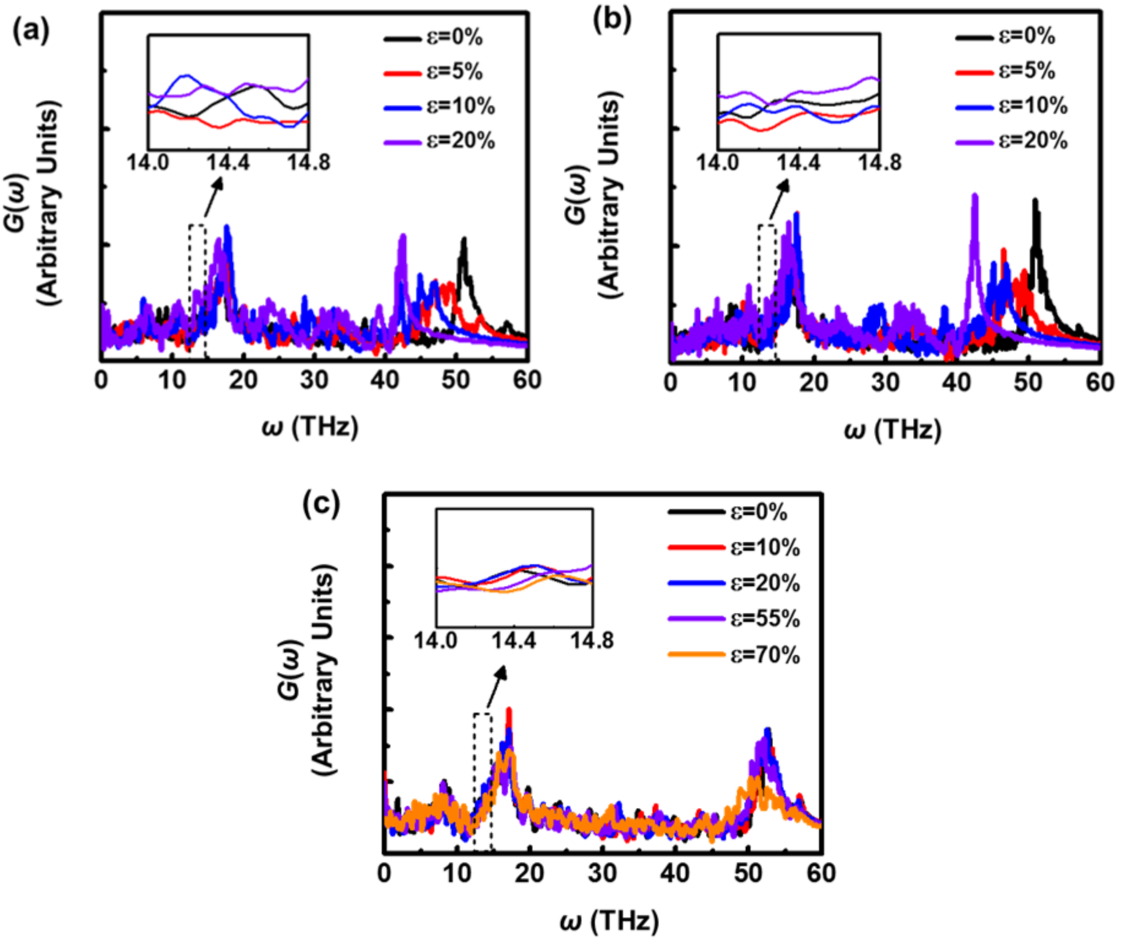

Figure 2.7. Phonon spectra of SGNRs with different angles of serration, α, and nanoribbon sizes, w/a, at tensile strain. **(a)** α=180° (regular GNR), w/a=0.157, **(b)** α=180° (regular GNR), w/a=0.352, **(c)** α=60°, w/a=0.157.

The phonon modes of a wide GNR (w/a=0.352) under different tensile strains are shown in **Figure 2.7b**. In comparison with observations in Figure 2.7a, the peak difference of the typical edge phonon mode at 14.4THz under the strain 0% and 5% (the inset in Figure 2.7b) is much smaller than that of the narrow GNR; while high frequency modes (such as the one near 52 THz) are largely softened with obvious shifts towards low frequency, suggesting that phonon group velocity is constrained. Under this circumstance, the softening of high frequency modes dominates the thermal transport and decreases thermal conductivity even under a small strain 5%. The increase of tensile strain will further soften high frequency modes, reducing the frequency from 52THz to as low as 42 THz. Thus, the thermal conductivity is decreased, which is consistent with the monotonous decrease of thermal conductivity in the wide GNR (Figure 6a).

Figure 2.7c shows $G(\omega)$ of the SGNR60 under a tensile strain of 0%, 10%, 20%, 55% and 70%. As shown in the inset, almost no difference in both frequency and magnitude of phonon modes is found in low frequency range, especially for the case with tensile strain smaller than 55%, indicating that the effect of edge phonon mode is not sensitive to tensile strain in the SGNR60 throughout the tensile process[186]. In high frequency ranges, there is also no significant difference in $G(\omega)$ under the tensile strains of 0%, 10% and 20%, and most of the phonon modes are activated at almost the same frequencies, suggesting that phonon modes are not softened by elastic deformation, and echoing well with zero nominal stress in SGNR60 (Figure 2.2b). With approximately the same $G(\omega)$, the geometric change of the SGNR60 alters the heat transfer path from serpentine to nearly straight route, leading to an enhancement of κ_{sg}. Under the strain of 55%, the stress shows a slight increase in comparison with zero under strain of 54.7% (Figure 2.2b), and the elastic deformation in serrated-edges, especially at the corners of serrated-edges, becomes crucial. As a result, a very small shift in the phonon mode from frequency 53THz to 52THz is observed. Beyond the 55% strain, the stress in the SGNR60 increases rapidly and the SGNR60 experiences severe localized deformation. Considering the SGNR 60 in the strain of 70% as a representative, Figure 2.7c shows that the phonon modes at high frequency are significantly softened and shift to low frequency (<50 THz), similar to the phonon behavior of GNRs under tensile strain (Figures 2.7a and b). Consequently, a decreased κ_{sg} is obtained when the tensile strain is beyond 55% (Figure 2.5b).

2.2.7 Summary

A class of graphene nanoribbons with a serpentine structure, namely serpentine graphene nanoribbons (SGNRs), is designed and investigated through comprehensive nonequilibrium molecular dynamics (NEMD) simulations. Simulations indicate that the thermal conductivity of SGNRs increases with the increase of tensile strain till to a significant appearance of localized stress in the structures. For the SGNRs with the angle of serration of 60^{o}, the simulations show that the stress remains an approximate zero until the tensile strain reaches 54.7%, and this large deformation without the increase in localized stress is dominated by the alignment effect of serrated-edges to the direction of the tensile strain. This straightening deformation mechanism of SGNRs in tension does not change the phonon modes while extensively extends the effective length of thermal transport and enhances the thermal conductivity. Therefore, the thermal transport mechanism of SGNRs in tension is different from that of GNRs. Beyond a critical strain, the carbon-carbon bonds will experience stretching deformation, which leads to elastic deformation of SGNRs till to the failure of structures with a sudden drop in stress. The localized elastic deformation softens the phonon modes, leading to a reduced thermal conductivity. The unusual thermal behavior depends on the mechanical stretchability of SGNRs, and a large stretchability will promote the unusual thermal behavior in tension.

Our findings provide a new guideline for designing materials and structures that have an elevated thermal conductivity subjected to uniaxial tensile deformation and simultaneously can sustain a large stretchability. For instance, the SGNRs may be used to design and optimize stretchability of graphene structures such as the recently developed graphene kirigami [188]. The SGNRs may also be employed to design stretchable graphene nanodevices, and the increase of thermal conductivity in tension will reduce the thermal energy dissipation and improve the thermal transport efficiency. In addition, the unusual thermal behavior of SGNRs in tension can be used in the next-generation circuit packaging systems, conducting nanocomposites and microelectronic circuits with unprecedented thermal properties.

2.3 Thermal Transport in Meshed Graphene Subjected to Tensile Loading

2.3.1 Computational Modeling and Method

Figure 2.8a and b presents the structures of auxetic graphene (AG) and contractile graphene (CG). Their unit cells-enabled graphene heterostructures (AC1-6) are shown in **Figure 2.8c**. Each unit cell of AG and CG has the same dimension in size (13.63 nm in length, 9.84 nm in width) (**Figure 2.8d**) and the same numbers of carbon atoms. The shapes and the aspect ratio (≈ 0.47 in AG unit cell, ≈ 0.53 in CG unit cell) of AG and CG unit cells were taken on the estimation of Poisson’s ratio of macro scale auxetic and contractile honeycombs

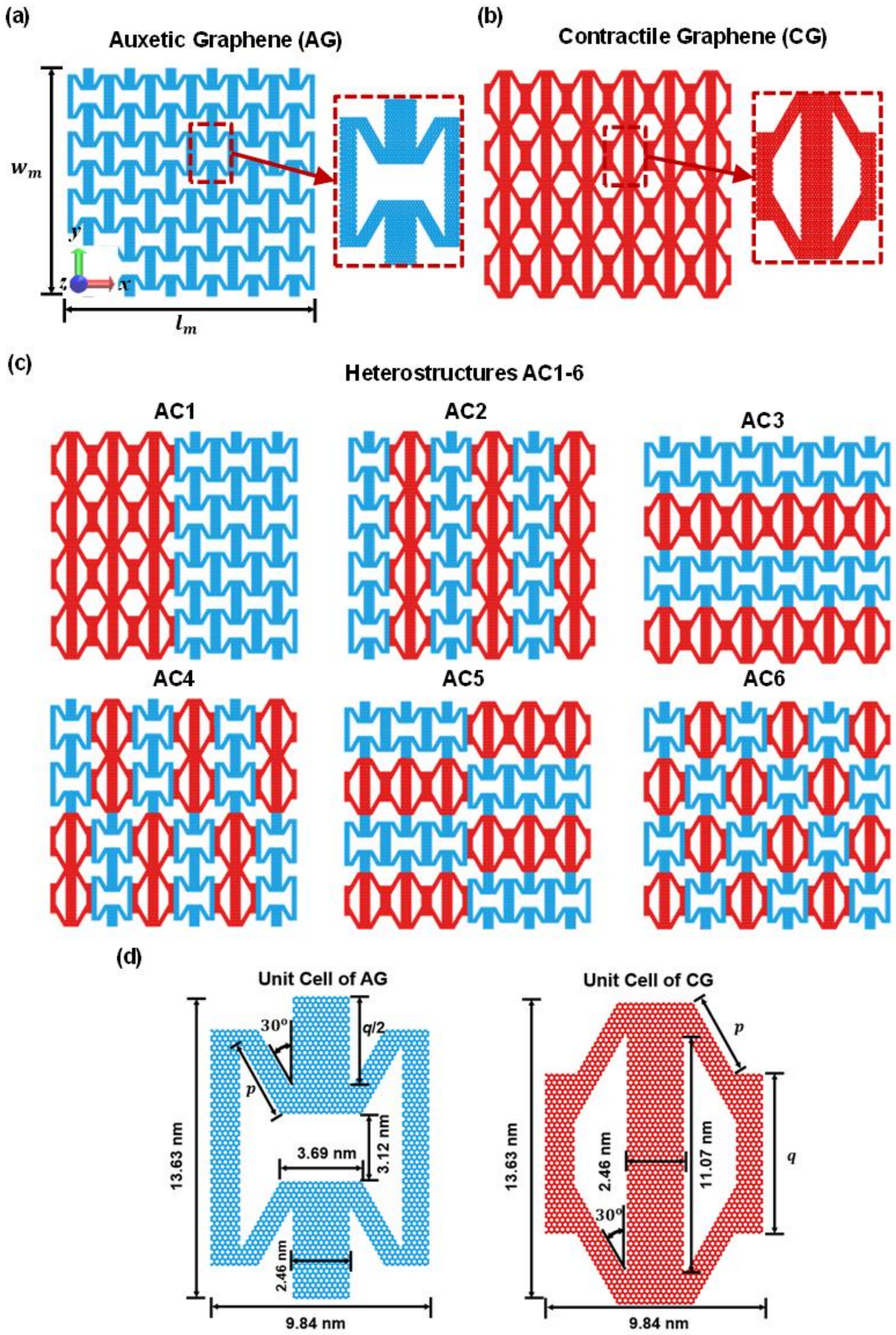

Figure 2.8. Computational model of auxetic graphene (AG), contractile graphene (CG) and their enabled heterostructures (AC1-6). (a), (b) and (c) Molecular modeling of auxetic graphene (AG), contractile graphene (CG) and their enabled heterostructures (AC1-6), respectively. A uniform displacement loading is applied in the x-direction to obtain a uniaxial tensile strain ε_x. Parallel to the strain loading x-direction, both ends are chosen to be the hot and cold reservoir, respectively and are fixed in the study of thermal transport properties. Non-periodic periodic boundary condition was set in x, y and z-direction. The modeling length for all AG, CG, and AC1-6 is the same and l_m=59.03 nm and width w_m=54.53 nm. (**d**) Structures and dimensions of unit cells in auxetic graphene and contractile graphene. $l_m = 9.84$ nm, $w_m = 13.63$ nm. The aspect ratio is defined as p/q as marked in the figure. For AG unit cell, $p = 3.74$ nm and $q = 7.66$ nm. For CG unit cell, $p = 3.74$ nm and $q = 7.10$ nm.

in tension [189-191]. The enabled heterostructures AC1-6 also have the same modeling length l_{m}(=59.03 nm) and width w_{m}(=54.53 nm), and consist of six unit cells in the x-direction and 4 unit cells in the y-direction. These periodic arrangements will ensure up to five horizontal interfaces and three vertical interfaces, and the variations will allow us to probe the role of interfaces in the thermal transport in tension. To highlight the difference of arrangements of unit cells in AC1-6, as schematized in **Figure 2.9**, we defined the horizontal interface

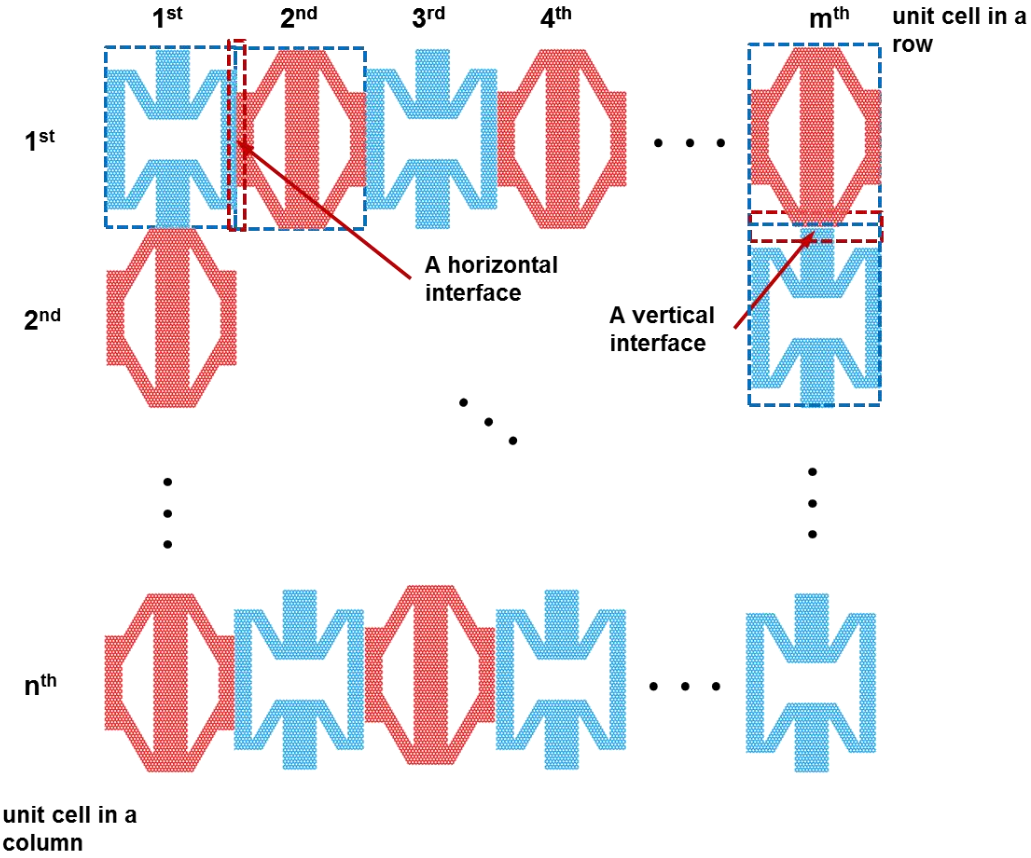

Figure 2.9. Schematic illustration of AG and CG unit cells enabled heterostructures. The horizontal interface I_H and the vertical interface coefficient I_V are defined as $I_H = \frac{N_H}{mn}$ and $I_V = \frac{N_V}{mn}$, respectively, where N_H and N_V are the total number of AG and CG unit cells that are employed to construct the horizontal interfaces and the vertical interfaces, respectively, and m and n are the numbers of unit cells in a row and in a column of the heterostructure, respectively. The total number of unit cells associated with horizontal and vertical interfaces is referred to as N_I, the average number of pure columns of AG and CG cells without either type of interfaces is referred to as N_{AN}, the number of pure columns of AG and CG cells are referred to as N_{PAC} and N_{PCC}, respectively, and the number of types of cell patterns in the heterostructures is referred to as N_{TP}.

coefficient I_H and the vertical interface coefficient I_V as $I_H = \frac{N_H}{mn}$ and $I_V = \frac{N_V}{mn}$, respectively, where N_H and N_V are the total number of AG and CG unit cells that are employed to construct the horizontal interfaces and the vertical interfaces, respectively, and m and n are the number of unit cells in a row and in a column of the heterostructure, respectively.

All molecular dynamics simulations were carried out by LAMMPS[177]. The time step was set as 0.5 fs. Non-periodic boundary condition was applied in *x*, *y* and *z*-direction. All structures were modeled by AIREBO potential[178]. Equilibrium was first performed in canonical ensemble (NVT ensemble) with Nose-Hoover thermostat at 300 K for 2 ns. And then, a uniform displacement elongation at a strain rate $\dot{\varepsilon_x} = 0.5$/ns (can be approximately considered a quasistatic manner) was introduced to the structures every 1000 time steps to achieve a uniaxial tensile strain in *x*-direction, ε_x, and $\varepsilon_x = \frac{l-l_0}{l_0}$, where l and l_0 are the elongated length and equilibrated length of structures, respectively. The nominal stress σ was calculated via $\sigma = \frac{F}{A_0}$, where F is the reactive force of boundary atoms at ε_x, $A_0 = w_0 t$ is the cross-sectional area at ε_x=0, and t (= 0.335 nm) is the thickness of 2D graphene[192]. F was recorded every 500 steps to obtain the stress-strain curves.

The Poisson's ratio was calculated through $\nu = -\frac{\varepsilon_y}{\varepsilon_x} = \frac{\frac{w-w_0}{w_0}}{\varepsilon_x}$, where w and w_0 are elongated width and equilibrated width at ε_x=0. The equilibrated width w_0 for all the structures can be found in Table 2.1.

Table. 2.1. The width (w_0) and length (l_0) of equilibrated structures and thermal conductivity (k_0) in the absence of tensile strain.

Structure	l_0=l_m (nm)	w_0 (nm)	k_0 (W/mK)
AG	59.03	53.92	3.32
CG	59.03	52.58	4.85
AC1	59.03	53.87	3.41
AC2	59.03	52.45	2.81
AC3	59.03	53.06	3.66
AC4	59.03	53.17	2.84
AC5	59.03	53.13	3.37
AC6	59.03	53.38	2.76
SG	59.03	52.80	3.52
AS1	59.03	53.68	3.08
AS2	59.03	53.20	3.11
AS3	59.03	53.14	3.26
CS1	59.03	52.89	3.43
CS2	59.03	52.06	2.86
CS3	59.03	52.78	3.83

Given the advantages of non-equilibrium molecular dynamics (NEMD) in the simulation of thermal properties to inhomogeneous systems, in particular, structures with boundaries and interfaces, we employed NEMD method in the study of thermal transport properties. To extract thermal conductivity of structures, the simulation box was divided into 100 slabs in the loading *x*-direction, the five slabs closest to the ends were selected as the hot and cold reservoirs. The heat flow was introduced by adding/subtracting kinetic energy of atoms in hot/cold reservoirs at a constant rate of 0.5 eV/ps every timestep. After 2 ns, a steady temperature gradient was obtained. The temperature data of 100 slabs in the following 4 ns were recorded to calculate thermal conductivity by utilizing the Fourier's Law $\kappa = \frac{\dot{J}}{A\frac{\partial T}{\partial x}}$, where $\dot{J}$, A and $\frac{\partial T}{\partial x}$ are the heat flow rate, current cross-sectional area and temperature gradient along the *x*-direction, respectively.

The vibrational spectra were calculated via $G(\omega) = \int_0^\infty e^{-i\omega t} \frac{<v(0)\cdot v(t)>}{<v(0)\cdot v(0)>} dt$, where ω is frequency, $v(t)$ is atomic velocity vector and $\cdot$ denotes average over atoms in specific group. The total spectra were extracted from all the atoms except for those at boundaries, and the spectra of horizontal/vertical ribbons only included the atoms in corresponding ribbons.

The atomic heat flux vector is defined as $q_{\mathrm{i}} = e_i v_i - S_i v_i$, where e, v and S are the energy, velocity vector and stress tensor, respectively, and the subscript i refers to the i^{th} atom. The results were obtained by averaging data for 4 ns after a steady temperature gradient was established.

2.3.2 Mechanical Properties of Auxetic and Contractile Graphene and Their Heterostructures

When subjected to a uniaxial tensile loading in the horizontal *x*-direction, their nominal stress-strain curves are plotted in **Figure 2.10a**. The nominal stress σ remains zero in all structures until the tensile strain ε_x reaches approximately 10% followed by a gradual increase. This critical strain of 10% depends on the deformation mechanism of nanoribbons in unit cells such as rotation, twisting and straightening and may change with the shape and dimension of nanoribbons[83]. The critical strain of 10% here is referred to as the stretchability, which is analogous to that in stretchable electronics[193, 194]. Afterward, σ increases linearly until the failure of the structure with a sudden drop of σ. Given the similarity of σ-ε_x curves, the structures can be categorized into three groups: AG, CG and AC3 (group 1), AC1 and AC5 (group 2), AC2, AC4 and AC6 (group 3). The similarity in each group is expected to result from the same N_H and I_H because a horizontal interface can reduce the stretching-induced rising of deformation stress in the horizontal *x*-direction. Besides, the higher I_H, the more reduction of stress, leading to a lower nominal stress σ at the same tensile strain ε_x (Figure 10a). During the stretching deformation, Poisson's ratio υ of structures will vary, and is plotted in **Figure 2.10b**. υ decreases quickly in AG structure at the beginning and then increases until failure. In contrast, υ of CG structure shows a rapid increase initially and then decrease until failure. Besides, υ of AG structure is negative while υ of CG structure is positive. This distinct difference results from their inherent structural features. At a small stretching load, the deformation is dominated by straightening horizontal serrated ribbons in both AG and CG structures and leads to an obvious variation of υ, which corresponds to approximate zero stresses in stress-strain curves (Figure 2.10a). When the stretching load is large enough, either the expansion in AG structure or the contraction in CG structure in the vertical *y*-direction is constrained, and υ shows a small change with ε_x and will eventually arrive at a stable state. This variation of Poisson's ratio with the applied strain ε_x in both AG and CG structures is well consistent with auxetic and contractile structures at the macroscale such as re-entrant structures[195, 196] and honeycomb structures[197].

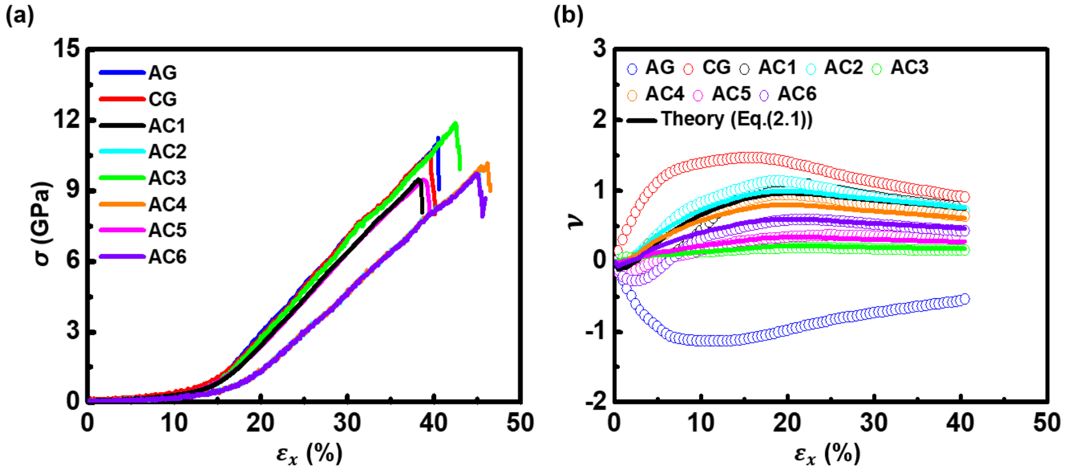

Figure 2.10. Mechanical properties of auxetic graphene (AG), contractile graphene (CG) and their enabled heterostructures (AC1-6). (**a**) Nominal stress-strain curves of auxetic graphene (AG), contractile graphene (AG) and heterostructures (AC 1-6). (**b**) Comparison of Poisson's ratio of heterostructures (AC 1-6) at different tensile strains between simulation results and theoretical predictions.

A similar variation of Poisson's ratio with the applied strain in the heterostructures AC1-6 is also found, beginning with an initial nonlinear change till to a stable state with the increase of ε_x. Among them, because there are only vertical interfaces in the heterostructure AC3, the interaction between auxetic and contractile cells can be neglected when subjected to mechanical loading in the horizontal x-direction, and its Poisson's ratio in theory is $\frac{1}{2}(\upsilon_A + \upsilon_C)$, in good agreement with simulations. Besides, the approximately stable υ with the increase of ε_x results from the absence of horizontal interfaces in the heterostructure AC3. Further analysis shows that Poisson's ratio of heterostructures AC1-6 is highly dominated by the deformation mismatch between AG and CG cells. For example, at a small ε_x, CG cells will contract and drive the buckling of the vertical ribbons, while AG cells can expand freely, leading to earlier and easier deformation of AG cells than that of CG cells, and thus an overall expansion in the heterostructures is obtained. As ε_x increases, the deformation of CG cells will mitigate the deformation mismatch, and at ε_x>10% the asynchronous deformation effect can be neglected because of an obvious increase of stress and deformation in both AG and CG cells and the entire structures (Figure 2.10a). By defining the stretchability of the heterostructures λ (=10%, Figure 2.10a) and the critical buckling strain of the vertical rectangular ribbons in AG and CG, $\varepsilon_{buck,crit}$ (=0.34% for current geometric ribbons of AG and CG[198]), the Poisson's ratio in the heterostructures can be estimated with the help of interface coefficients I_H and I_V as

$$\upsilon = \upsilon_A c_A + \upsilon_C c_C + \frac{1}{2}(\upsilon_C - \upsilon_A) I \left(\frac{\varepsilon_x - \lambda}{\varepsilon_x + \lambda} + 1\right) c_A c_C + \frac{\upsilon_A c_A I}{\frac{\varepsilon_x I_H}{\varepsilon_{buck,crit}} + 1} \tag{2.1}$$

Where $I = (I_H - I_V + I_R) I_C$ and $I_R = \frac{N_I}{mn}$. $I_C = \frac{(N_{AN}+1)\left(\frac{N_{PAC}}{N_{TP}}+1\right)}{\frac{n_{PCC}}{N_{TP}}+1}$ is the correction coefficient for complex and repeating cell patterns. N_I is the total number of unit cells

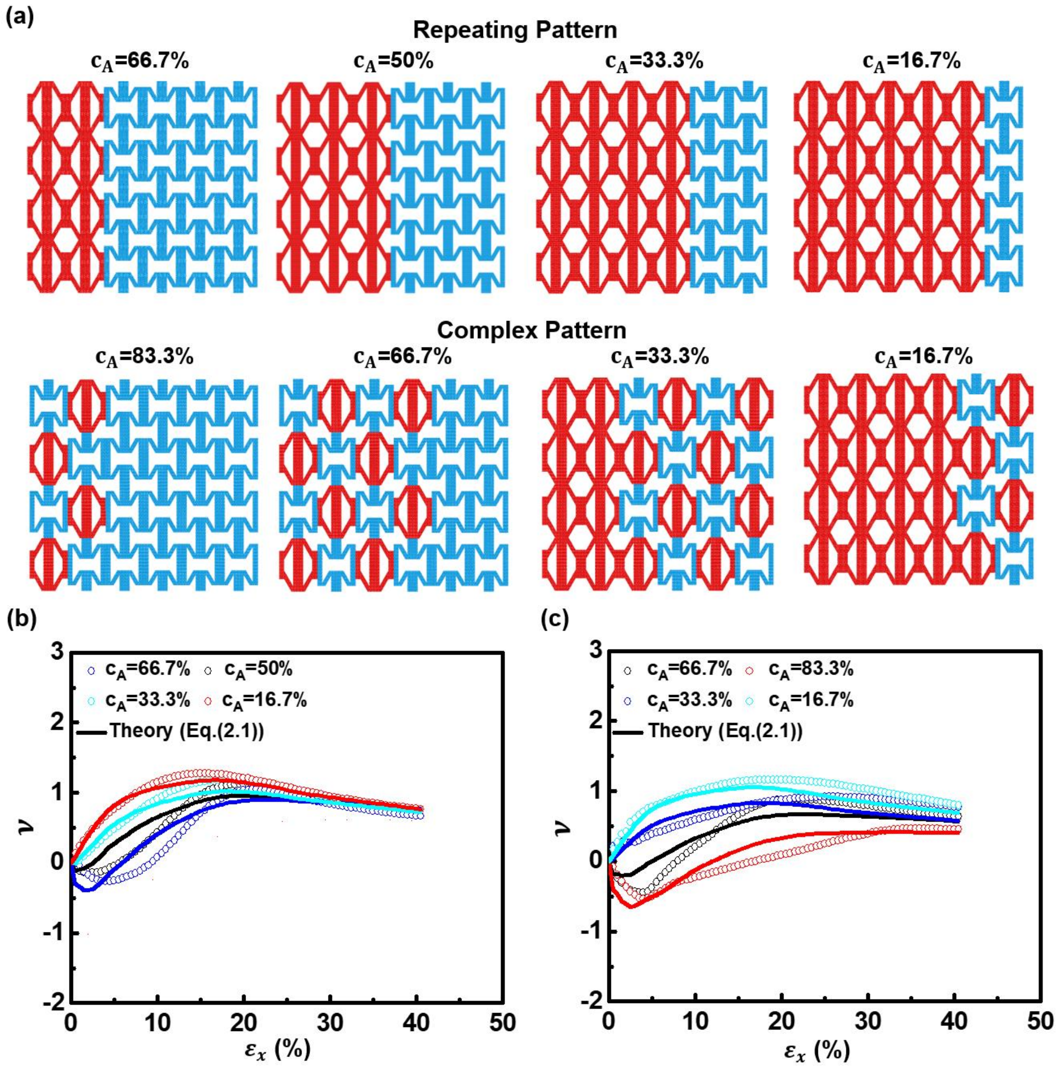

Figure 2.11. Comparison of theoretical predictions and simulation results on Poisson's ratio of AG and CG unit cells enabled heterostructures with different patterns and volume fractions c_A. (**a**) Molecular model of AG and CG unit cells enabled heterostructures with simplex repeating and complex patterns. **(b)** and **(c)** Variation of Poisson's ratio of heterostructures with simplex repeating and complex patterns with the uniaxial tensile strain, respectively.

associated with horizontal and vertical interfaces, N_{AN} is the average number of pure columns of AG and CG cells without either type of interfaces, N_{PAC} and N_{PCC} are the numbers of pure columns of AG and CG cells, respectively. N_{TP} is the number of types of cell patterns in the heterostructures (Figure 2.9). c_A and c_C are the volume fraction of AG cells and CG cells in the heterostructures, respectively, and $c_A + c_C = 1$. When $c_A = 1$, Equation 2.1 reduces to the Poisson's ratio of AG, and when $c_A = 0$, it stands for the pure CG. In particular, in the heterostructure AC3 with only vertical interfaces, Equation 2.1 will reduce to $\upsilon = \frac{1}{2}(\upsilon_A + \upsilon_C)$. Given the Poisson's ratio of AG and CG and the geometric features of their enabled heterostructures, Figure 2.10b shows that the Poisson's ratio of the heterostructures can be well predicted through Equation 2.1, where $c_A = 50\%$ otherwise specified. Besides, when the c_A or c_C varies, good agreement of Poisson's ratio between the predictions and the simulations holds, as shown in **Figure 2.11a-c**.

2.3.3 Thermal Transport Properties of Auxetic and Contractile Graphene and Their Heterostructures

Reverse non-equilibrium molecular dynamics method was performed to investigate the thermal transport properties of AG and CG structures and their enabled heterostructures under tensile strain. As representatives of heterostructures AC1-6, **Figure 2.12a** shows the normalized thermal conductivity $\frac{\kappa-\kappa_0}{\kappa_0}$ of AC1 and AC3 as ε_x increases, where k_0 is the thermal conductivity of the structure at ε_x=0. $\frac{\kappa-\kappa_0}{\kappa_0}$ shows an initial increase and then decreases with the increase of ε_x, and this nonlinear variation is governed by mechanical deformation. For example, when $\varepsilon_x \leq$10%, less than the stretchability of the structures λ, the stress can be negligible (Figure 2.10a), and the stretching will elongate the structures. At the same time, the structures will be expanded if Poisson's ratio υ is negative, or contracted if Poisson's ratio υ is negative. With the same thermal flux, the longer and narrower the path of thermal transport, the higher the thermal conductivity, and thus an initial increase and decrease of $\frac{\kappa-\kappa_0}{\kappa_0}$ observed in CG and AG structures and heterostructures AC1 and AC3, respectively. When ε_x>10%, the nominal stress will rise and deform atomic structures (Figure 2.10a), softening phonon modes and intriguing lattice anharmonicity[80, 83] and thus leading to a lower

$\frac{\kappa-\kappa_0}{\kappa_0}$ (Figure 2.12a). The similar mechanism of thermal transport is also observed in serpentine graphene structures subjected to a uniaxial tensile loading[83].

To quantitatively probe the thermal transport response of heterostructures to the tensile strain ε_x, we develop a model to correlate the thermal conductivity with ε_x. When the strain is less than the stretchability of the structures λ, i.e. $\varepsilon_x \leq 10\%$, because the nominal stress is

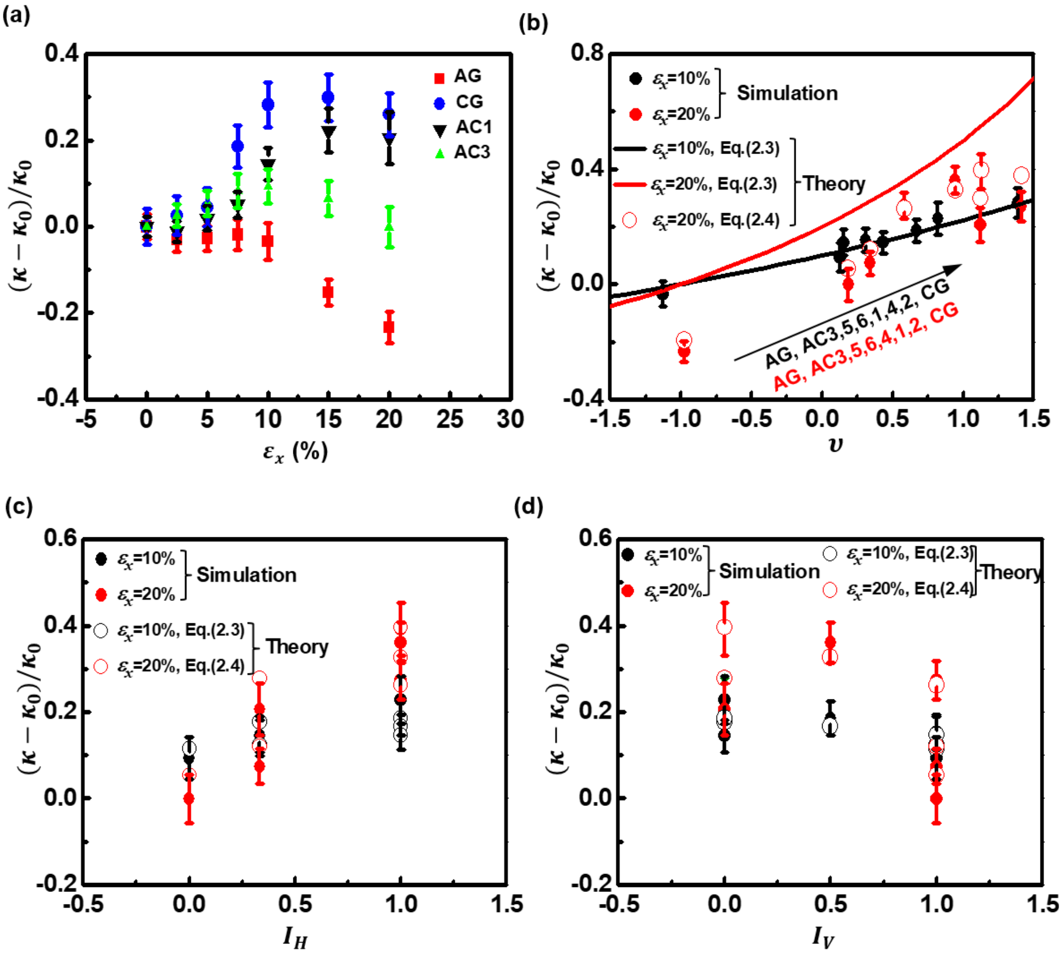

Figure 2.12. The thermal conductivity of the auxetic graphene (AG), contractile graphene (CG) and heterostructures (AC 1-6) in tension. (**a**) Variation of thermal conductivity of the auxetic graphene (AG), contractile graphene (CG), the representative heterostructure (AC1-3) with the applied uniaxial tensile strain ε_x. (**b**) Variation of thermal conductivity of auxetic graphene (AG), contractile graphene (CG), the heterostructure (AC1-6) with their Poisson's ratios at $\varepsilon_x = 10\%$ and $\varepsilon_x = 20\%$ and their comparison with theoretical predictions. (**c**) and (**d**) Variation of thermal conductivity of heterostructures (AC1-6) with the horizontal interface coefficient I_H and the vertical interface coefficient I_V at $\varepsilon_x = 10\%$ and $\varepsilon_x = 20\%$ and their comparison with theoretical predictions. k_0 is the thermal conductivity in the absence of tensile strain.

almost zero and its effect on phonon activity will be negligible, based on Fourier's law, we will have

$$\frac{\kappa-\kappa_0}{\kappa_0}=\frac{1+\varepsilon_x}{1-\varepsilon_x v}-1 \tag{2.2}$$

Further with Equation 2.1, Equation 2.2 can be rewritten as:

$$\frac{\kappa-\kappa_0}{\kappa_0}=\frac{1+\varepsilon_x}{1-\varepsilon_x\left[v_A c_A+v_C c_C+\frac{1}{2}(v_C-v_A)I\left(\frac{\varepsilon_x-\lambda}{\varepsilon_x+\lambda}+1\right)c_A c_C+\frac{v_A c_A I}{\frac{\varepsilon_x I_H}{\varepsilon_{buck,crit}}+1}\right]}-1 \tag{2.3}$$

Figure 2.12b gives a comparison between predictions and simulations, and good agreement is found. When the strain is beyond the stretchability of the structures λ, i.e. ε_x >10%, the atomic structures will experience significant deformation due to the obvious increase of nominal stress (Figure 2.10a), and the mechanical deformation of atomic structures will suppress phonon activity and enhance the thermal resistance[80]. As a consequence, an overestimation on $\frac{\kappa-\kappa_0}{\kappa_0}$ via Equation 2.3 at ε_x =20% is observed in Figure 2.12b. To integrate the effect of the mechanical stretching-induced stress, Equation.2.3 can be modified to

$$\frac{\kappa-\kappa_0}{\kappa_0}=\frac{1+\varepsilon_x}{1-\varepsilon_x\left[v_A c_A+v_C c_C+\frac{1}{2}(v_C-v_A)I\left(\frac{\varepsilon_x-\lambda}{\varepsilon_x+\lambda}+1\right)c_A c_C+\frac{v_A c_A I}{\frac{\varepsilon_x I_H}{\varepsilon_{buck,crit}}+1}\right]}-1-\beta(\varepsilon_x-I_H\lambda) \tag{2.4}$$

Where $\beta=0$ if $\varepsilon_x\leq\lambda$, and $\beta=1$ if $\varepsilon_x>\lambda$. With Equation 2.4, good agreement between the predictions and simulations at $\varepsilon_x=20\%$ is achieved and is also given in Figure 2.12b. Note that when $\varepsilon_x\leq\lambda$, $\beta=0$, i.e. there is no mechanical stretching-induced stress in the heterostructures, Equation 2.4 will reduce to Equation 2.3. The critical stretchability of the structures will be the principle of designing stretchable thermal devices, which is similar to that in stretchable electronics[199].

To highlight the importance of interfaces between AG and CG cells in heterostructures, we present the variation of $\frac{\kappa-\kappa_0}{\kappa_0}$ with the horizontal interface coefficient I_H and vertical horizontal interface coefficient I_V in **Figure 2.12c and d**, respectively. Generally, the horizontal interface will facilitate the interaction between AG and CG cells, and promotes the buckling of AG cells, leading to a higher Poisson's ratio of the heterostructures. Therefore, a lager I_H results in a larger $\frac{\kappa-\kappa_0}{\kappa_0}$, as shown in Figure 2.12c. On the other hand, the vertical interface will weaken the interaction between AG and CG cells and leads to a lower Poisson's ratio, and a lower value of $\frac{\kappa-\kappa_0}{\kappa_0}$ at a higher I_V is obtained in Figure 2.12d.

2.3.4 Mechanical Deformation Mechanism

Figure 2.13 presents the von Mises stress snapshots of heterostructures to help understanding the mechanical tunable thermal transport mechanism, and the deformation of AG and CG is also given for comparisons. In the AG structure, when ε_x rises from 0% to 5%, horizontal serrated ribbons are straightened toward parallel to the tensile *x*-direction and push the outward movement of vertical rectangular ribbons, leading to an expansion of the AG structure in the *y*-direction and a negative v. Serrated ribbons continue to be stretched until ε_x =10%, and the approximate zero von Mises stress remains. Afterward, i.e. $\varepsilon_x = 17.5\%$, 20%, obvious stress in the horizontal serrated ribbons (insets) is observed and increases with ε_x. Besides, the width of structures stays approximately the same, which corresponds well to the increase of v with ε_x in Figure 2.10b. In contrast, as the ε_x increases to 5%, the tensile stretch-induced straightening of the horizontal serrated ribbons in the CG structure squeezes the vertical rectangular ribbons, and shrinks the width of the structure, leading to a positive v. Similar to that in the AG structure, this squeezing will continue until $\varepsilon_x = 10\%$ while approximately keeping the initial zero von Mises stress. Besides, beyond $\varepsilon_x = 10\%$, i.e. $\varepsilon_x = 17.5\%$, 20%, the stretching-induced stress appears in the horizontal serrated ribbons, and the structure cannot sustain being further contracted, which also corresponds well to the decrease

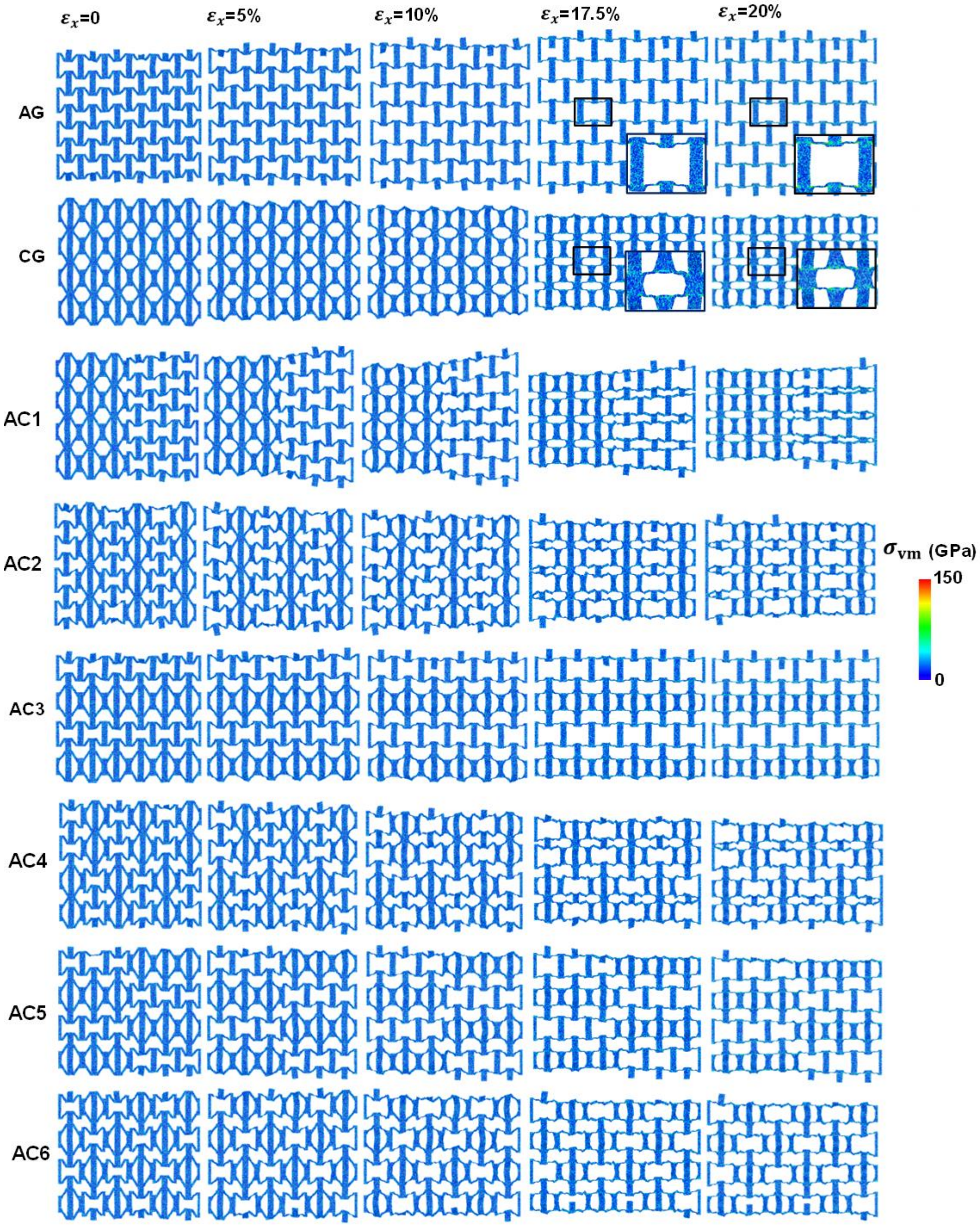

Figure 2.13. **Mechanical deformation features of the auxetic graphene (AG), contractile graphene (CG) and heterostructures in tension**. Von Mises stress distribution of auxetic graphene (AG), contractile graphene (CG) and heterostructure under different tensile strains.

of v with ε_x in Figure 2.10b. In the heterostructures AC1, 2 and 4-6, depending on the competition of the assembled AG and CG cells, the stretching-induced expansion and contraction of structures are also observed with clear elevated stress when $\varepsilon_x > 10\%$. In particular, in the heterostructure AC3 whose Poisson's ratio is $\frac{1}{2}(v_A + v_C)$ due to the lack of vertical interfaces, as the ε_x increases from 0 to 20%, the horizontal serrated ribbons in AG and CG cells are stretched and straightened in the same direction and their effects on the width nearly cancel each other, leading to no significant change in width.

Figure 2.14a further gives the averaged von Mises stress $\bar{\sigma}_{\mathrm{vm}}$ in horizontal ribbons and vertical ribbons for AG, CG and AC3. For all three structures, as the tensile strain increases, the stress in the vertical ribbons remains; while the stress in the horizontal ribbons starts to increase at ε_x>10%. In addition, the higher stress in the horizontal ribbons in AG structure than that in the CG structure is consistent with that of the nominal stress-strain curves due to the inherent difference of their structures. Given the absence of vertical interfaces in AC3, the horizontal ribbon stress in AC3 falls in between AG and CG structures. To further reveal the effect of horizontal interfaces in heterostructures, the variation of the averaged von Mises stress in horizontal ribbons with I_H at ε_x=20% is plotted in **Figure 2.14b**. The heterostructures with the same number of horizontal interfaces have a very close stress level in horizontal ribbons, and the heterostructures with more horizontal interfaces have a lower stress level. The lower stress will lead to a smaller reduction to its thermal conductivity, which is in good agreement with a larger $\frac{\kappa-\kappa_0}{\kappa_0}$ (Figure 2.12c). As for comparison, the number of vertical interfaces does not affect the averaged von Mises stress in horizontal ribbon (**Figure 2.14c**) and cannot be employed in the structures to tune the thermal transport properties by managing the stress level.

2.3.5 Thermal Transport Mechanism

Figure 2.15a shows the vibrational spectra of AG structure at different tensile strains. At ε_x=0, two main peaks are observed at 17.5 and 52.5 THz, respectively. When the ε_x increases to 10%, no obvious change is found, consistent with that of stress absence in AG structure (Figures 2.10a and 2.14a). As ε_x increases to 20%, the peak at the high frequency (52.5 THz)

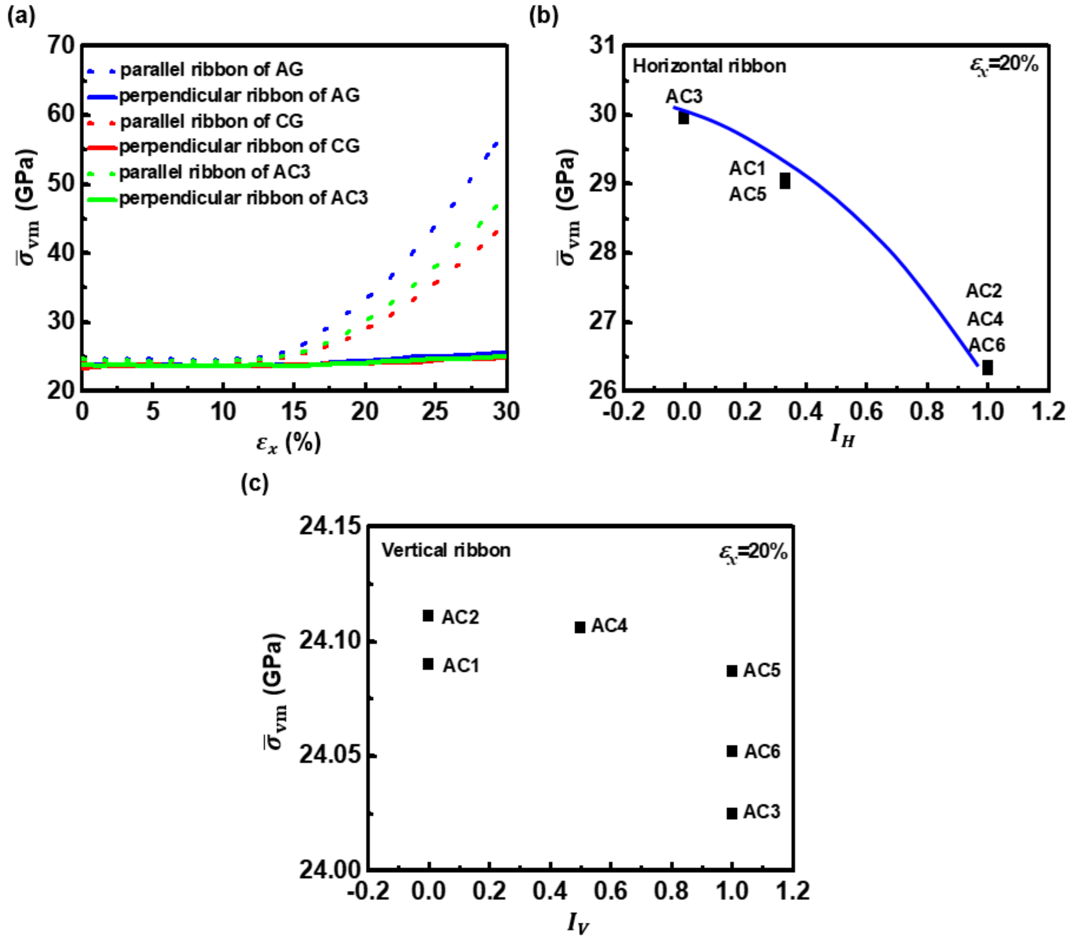

Figure 2.14. **Stress in the auxetic graphene (AG), contractile graphene (CG) and heterostructures in tension**. (**a**) Variation of averaged von Mises stress in horizontal and vertical ribbons auxetic graphene (AG), contractile graphene (CG) and heterostructure AC3 with tensile strain. (**b**) Variation of averaged von Mises stress in horizontal ribbons of heterostructures AC1-6 with the horizontal interface coefficient I_H at the tensile strain of 20%. (**c**) Variation of averaged von Mises stress in vertical ribbons of heterostructures AC1-6 with the vertical interface coefficient I_V at the tensile strain of 20%.

is depressed and slightly broadened, leading to a reduction of phonon lifetime,[192] and thus suppressing thermal conductivity, which agrees with observation in Figure 2.12a. Further analysis shows that the phonon spectra of vertical ribbons will not change with ε_x, and this independence agrees well with approximate maintenance of von Mises stress in vertical ribbons (Figure 2.14a). On the other hand, the spectrum of horizontal ribbons is broadened at the high frequency (52.5 THz) and shifts to a lower frequency when the strain ε_x increases from 10% to 20%, indicating that phonon mode is softened and phonon lifetime is reduced. The softening and reduction of phonon activities will weaken the heat transport, echoing with a decreased thermal conductivity in simulations (Figure 2.12a). No obvious change of spectra when the strain ε_x increases from 0 to 10% is consistent with the approximate zero von Mises stress in vertical ribbons (Figure 2.14a). The vibrational spectrum of CG structure exhibits similarity to those of AG structure (**Figure 2.15b**). No obvious change in total spectra until ε_x increases to 20%, and beyond 20% of tensile strain, depression to the high frequency peak (52.5 THz) is observed. Besides, spectra of vertical ribbons are also independent of ε_x, while the depression of spectra is found in horizontal ribbons when ε_x increases from 10% to 20%, which reduces phonon lifetime and heat transport, consistent with the stress distributions (Figure 2.14a) and the decreased thermal conductivity in theory and simulations (Figure 2.12a). Note that the shift of the high frequency peak in the CG structure is absent, which is different from that in the AG structure at the same strain of 20%. This difference is in good agreement with a lower von Mises stress in CG structure (Figure 2.14a). Similar phenomena on the variation of spectra with the tensile strain are also found in the heterostructures, as shown in **Figure 2.15c** for AC3 as a

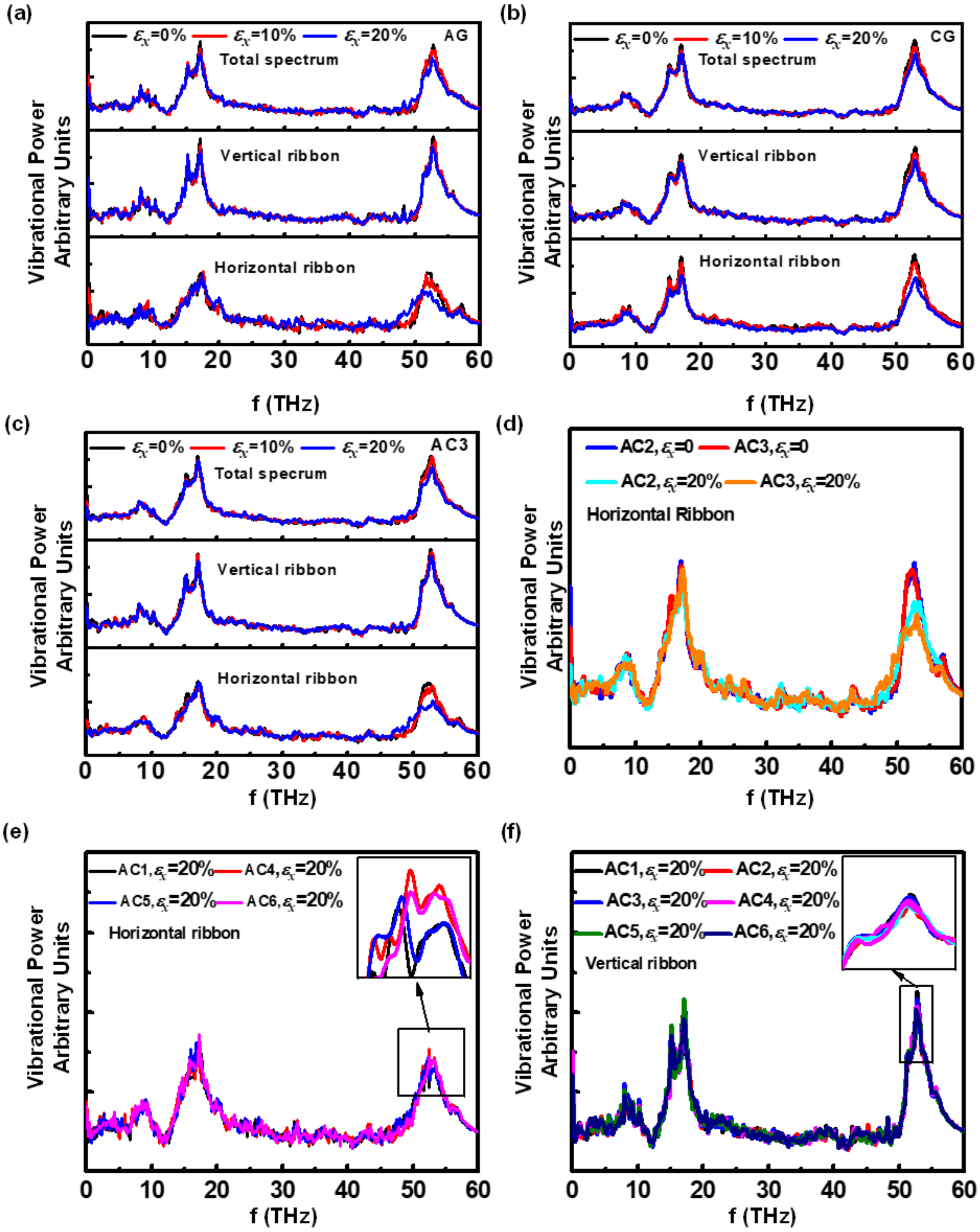

Figure 2.15. **Vibrational spectra of the auxetic graphene (AG), contractile graphene (CG) and heterostructures in tension**. Total vibrational spectra, horizontal ribbon spectra and vertical ribbon spectra of (**a**) auxetic graphene (AG), (**b**) contractile graphene (CG), and (**c**) heterostructure AC3 at the uniaxial strain of 0%, 10% and 20%. (**d**) Comparison of horizontal ribbon spectra of heterostructures AC2 and AC3 at the strain of 0% and 20%. **(e)** Comparison of horizontal ribbon spectra of heterostructures AC1, AC4, AC5 and AC6 at the tensile strain of 20%. **(f)** Comparison of vertical ribbon spectra of heterostructures AC1-6 at the tensile strain of 20%.

and broadened, and shifts to a lower frequency at 20% of tensile strain in AC3, but these events are not as obvious as those in AG due to the joint contribution of auxetic and contractile cells. For comparisons, **Figure 2.15d** shows the spectra of horizontal ribbons in heterostructures AC2 and AC3. When ε_x increases to 20%, both spectra of AC2 and AC3 are depressed and broadened, and shift to a lower frequency with more severity in AC2, indicating a lower thermal conductivity in AC2. Comparisons of horizontal ribbon phonon spectra for other heterostructures further (**Figure 2.15e**) suggest that the phonon activities highly depend on the number of horizontal interfaces. The more horizontal interfaces, the weaker suppression to the phonon activities, consistent well with theory and simulations (Figure 2.12d). Besides, no significant difference is observed in the spectra of vertical ribbons in all heterostructures (**Figure 2.15f**), which also agrees well with the irrelevance of stress level to the number of vertical interfaces (Figure 2.14c).

2.3.6 Application of the Theoretical model to Other Nanomeshed Heterostructures

To verify the robustness of the thermal transport theory (Equations 3.3 and 3.4), we constructed another graphene structure, semi-auxetic graphene (SG) (**Figure 2.16a**), inspired by the semi-re-entrant honeycomb structure at macroscale[200]. Its unit cell has the same dimension in size with that of auxetic graphene (AG) and contractile graphene (CG) unit cells and its aspect ratio (~0.47) is also close to the ones of AG and CG. The new heterostructures were designed by tailoring AG and SG, and CG and SG cells, respectively, referred to as AS1, AS2, AS3, CS1, CS2 and CS3 (**Figure 2.16b**). Similar to the heterostructures AC1-6, and no significant stress arises in their nominal stress-strain curves at $\varepsilon_x < 10\%$ (**Figure 2.16c**).

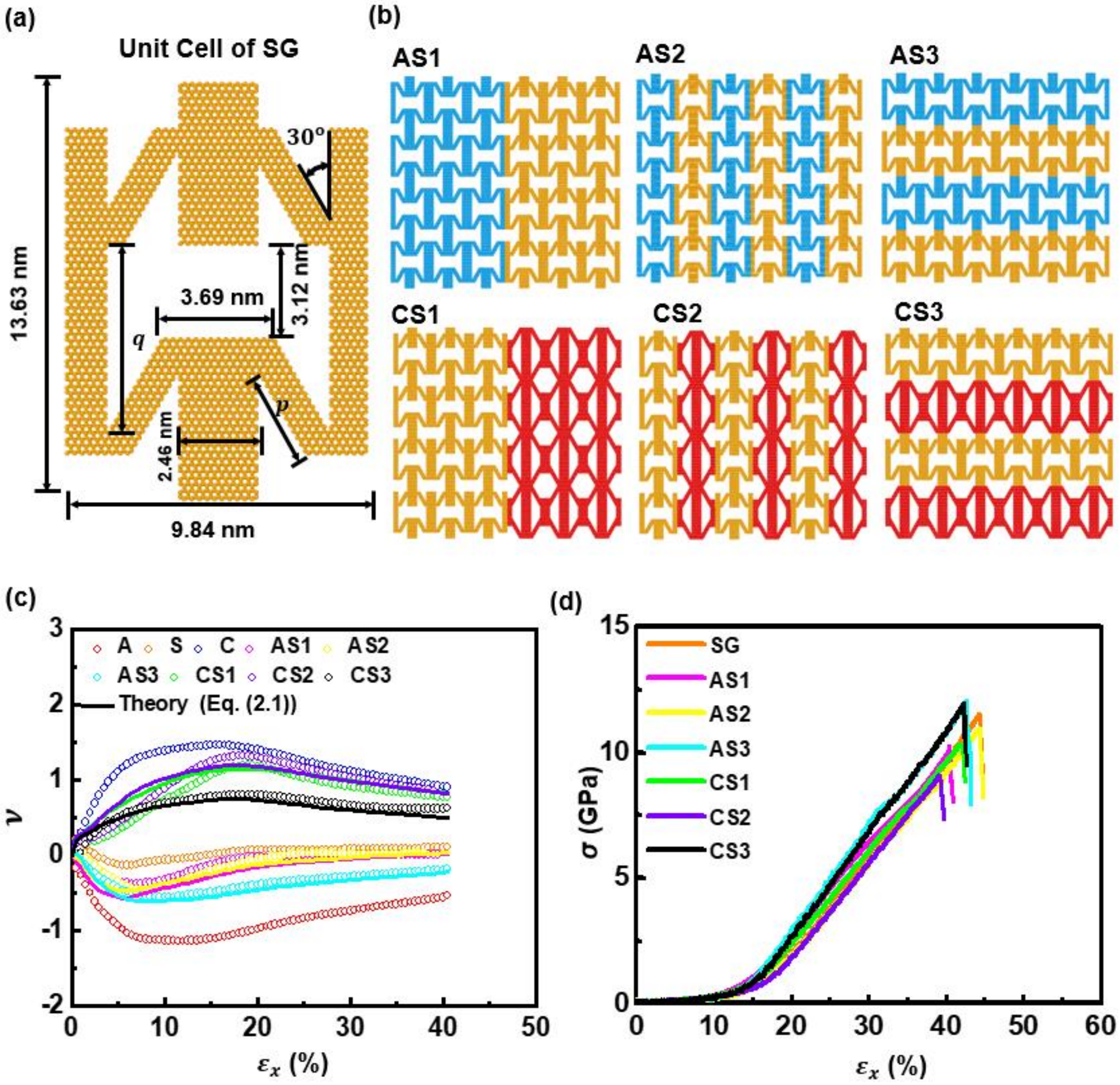

Figure 2.16. Semi-auxetic graphene, the combination of its unit cell with AG and CG unit cell enabled heterostructures AS and SC and their mechanical properties. (**a**) Molecular model of semi-auxetic graphene unit cell. The aspect ratio is defined as p/q as marked in the figure. For SG unit cell, $p = 3.00$ nm and $q = 6.39$ nm. (**b**) The heterostructures AS and SC. (**c**) Nominal stress-strain of semi-auxetic

When the Poisson's ratio of basic AG, CG, and SG structures are known at different strains, the Poisson's ratio of their cell assembled heterostructures can be obtained by using Equation 2.1. Good agreement between theoretical predictions and simulations are found (**Figure 2.16d**). After that, the thermal conductivity $\frac{\kappa-\kappa_0}{\kappa_0}$ can be predicted for both non-stressed and stressed heterostructures through Eqs. (3) and (4), respectively. **Figure 2.17a and b** gives a comparison of $\frac{\kappa-\kappa_0}{\kappa_0}$ for all AG, CG, SG cells-enabled heterostructures between predictions and simulations at ε_x=10% and ε_x=20%, respectively. The good agreement indicates that the mechanical tunable thermal transport properties in heterostructures can be predicted.

The unit cells of above AG, CG or SG are taken with the help of well-known mechanical properties of macroscale auxetic and contractile honeycombs in tension so as to find a stable structure in a low computational cost, and in theory they can be any stable structures at equilibrium. When their dimensions and shapes change, their mechanical properties such as stretchability may change[198, 201] and may also affect the thermal transport such as phonon scattering length [83, 202, 203], and either of them will lead to a variation of thermal properties. Besides, when more than two unit cells are involved in the heterostructures, the enhanced interfaces may increase both thermal and mechanical properties and further facilitate the controllability of thermal properties through mechanical loading. Nevertheless, given the integration of the thermal models with the stretchability and geometric features of heterostructures and the normalization by the thermal conductivity without tension, when the

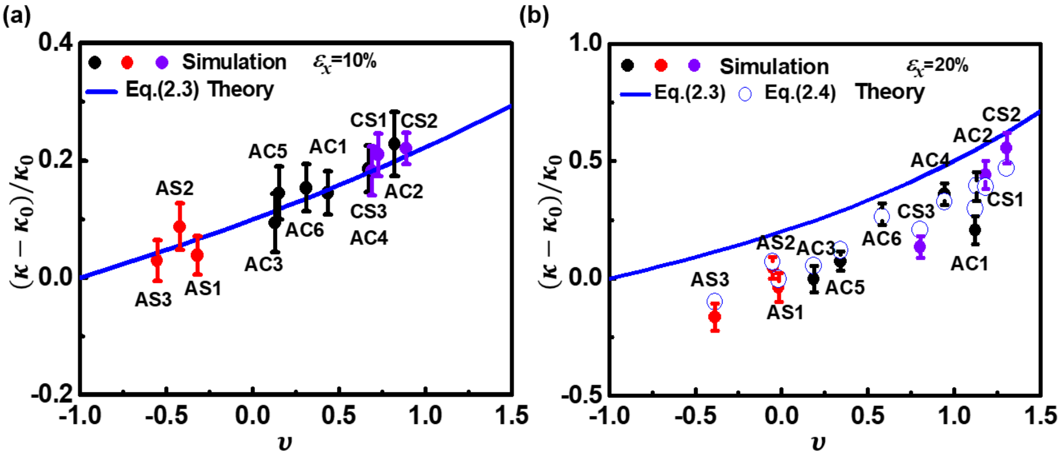

Figure 2.17. Verification and prediction of thermal conductivity on heterostructures in tension. (a) Comparison of the thermal conductivity of heterostructures AC 1-6, heterostructures AS1-3 and heterostructures CS1-3 between theoretical predictions and simulation results at the strain of 10%. **(b)** Improved theoretical prediction on the thermal conductivity of heterostructures AC 1-6, heterostructures AS1-3 and heterostructures CS1-3 at the strain of 20%. The error bar arises from the small uncertainty of fitting the linear region of temperature gradient profiles.

mechanical properties of the heterostructures such as υ and λ are determined in advance, they are expected to be useful in the predication of the thermal properties of other interface-dominated heterostructures, and guide the study of interface enabled 2-D structural designing in the future.

2.3.7 Summary

Using computational simulations, we show that the Poisson's ratio and thermal conductivity of the graphene heterostructures under tensile strain can be regulated by patterning AG and CG unit cells with different interface properties. Analyses of both mechanical deformation and vibrational spectra indicate that the thermal transport properties of graphene heterostructures are highly dependent on their stress distribution, and also rely on the interfaces that are parallel with the directions of mechanical loadings. Theoretical models are developed to quantitatively describe the thermal conductivity of graphene heterostructures in a uniaxial tensile loading and their robustness is verified by extensive simulations. In particular, when the mechanical deformation is less than the stretchability of heterostructures with negligible mechanical stress distribution, the theoretical model will reduce to an interface-dominated thermal model. These findings and models are expected to lay the groundwork for designing and manufacturing 2D materials-based interface-mediated functional devices with mechanically tunable thermal performance.

Chapter 3 Thermal Transport in Heterostructure with Bonded Interfaces under Mechanical Loading

3.1 Overview of the Chapter

Using non-equilibrium molecular dynamics simulation, we present an in-plane graphene-boron nitride heterostructure with a controlled interface junction and demonstrate that its thermal transport ability is asymmetric when reversing the direction of heat flow. Such thermal rectification performance can be further regulated by applying an external tensile loading due to the mitigation of stress concentration, phonon resonance, and phonon localization. The analyses on heat flow distribution, vibrational spectra, and phonon participation suggest that the out-of-plane phonon modes dominate thermal rectification at a small tensile strain, while the mechanical stress plays a dominant role in regulation at a large tensile strain due to the weakened localization of out-of-plane phonon modes. The effect of tensile loading on the thermal rectification is demonstrated by selective interface junction-enabled heterostructures, and the results indicate that both asymmetry and direction of thermal transport can be controlled by introducing defects to the interface junction and/or applying mechanical tensile strain. These findings and models are expected to provide immediate guidance for designing and manufacturing 2D material-based devices with mechanically tunable thermal management capabilities.

3.2 Computational Modeling and Method

Figure 3.1 presents the atomic model of GBN in-plane heterostructure with a size of 14.9 nm×6.0 nm. The interface is located in the middle and has a width of 0.5nm. SW-5577 defects that are formed by rotating two bonded carbon atoms 90 degrees about the midpoint of their pairwise bond,[204] and often used in structures with interfaces[205, 206], are selectively employed to achieve controlled interface junctions in GBN in-plane heterostructures, and the ratio of the number of implemented defect units to the maximum allowable number of defect units at the interface is defined as the interface junction parameter α. The atomic structures of interface junctions with α=0, $1/7$, $3/7$, $5/7$ and 1 are highlighted in Figure 3.1 and the GBN in-plane heterostructures with these interface junctions will be investigated as representatives in this work.

All molecular dynamics simulations were performed with LAMMPS[177]. Non-periodic boundary condition was applied in all directions. The boundary atoms at both ends in the *x*-direction were fixed. The time step was set as 0.5 fs. The atomistic interactions were described

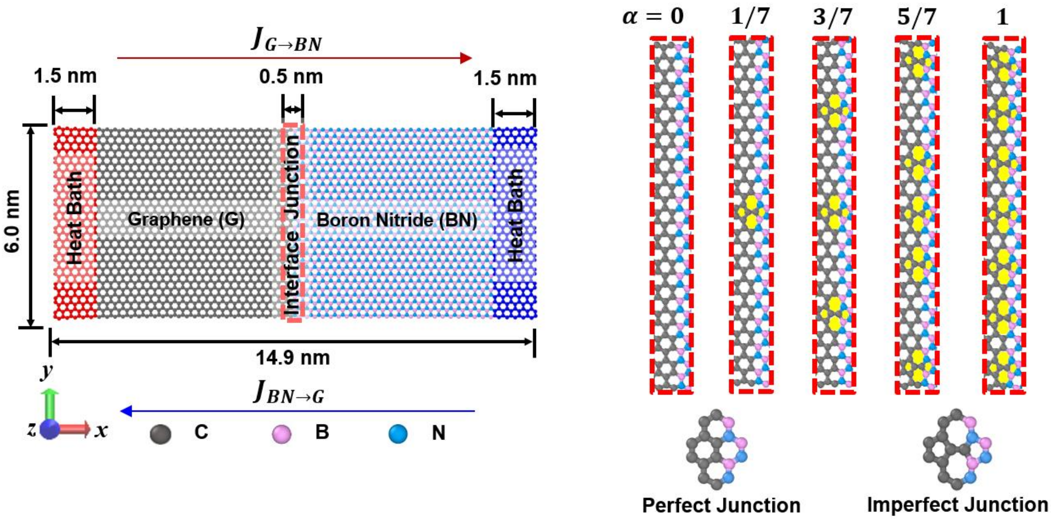

Figure 3.1. Atomic model of GBN heterostructures (left) and highlighted structures in interface junctions (right).

by Tersoff force field[207]. We should note that the Tersoff potential has been well-acknowledged in the studies of thermal transport in graphene-boron nitride systems[208, 209] and proves to accurately reproduce the tensile properties of graphene and boron nitride[210, 211], which are critical in our current study. The structure was first relaxed in canonical ensemble (NVT ensemble) with Nose-Hoover thermostat at 300 K for 1 ns. Next, a uniaxial quasistatic loading under the strain rate of $0.5\ \mathrm{ns}^{-1}$ was applied to heterostructures by uniformly projecting the coordinates of atoms in the x-direction every 1000 time steps. The nominal tensile strain was calculated via $\varepsilon = \frac{l-l_0}{l_0}$, where l and l_0 are the stretched and initial length of the structure, respectively, and l_0 =14.9 nm. The nominal tensile stress was calculated via $\sigma_N = \frac{F}{A}$, where F is the reactive force of the fixed boundary atoms, and $A = wt$ is the cross-sectional area. w=6.0 nm is the width of the structure. t is the thickness of the GBN heterostructure and is taken as 0.335 nm[192].

Afterward, to measure the heat transport of the GBN heterostructures, the atoms within 1.5 nm of both ends were selected as heat baths. In simulations, the two heat baths were maintained at 390 K and 210 K with the temperature difference of 180 K between them by the Nose-Hoover thermostat for 8.0 ns to reach a steady-state of thermal transport. We should note that a temperature difference of ~200 K is usually employed in numerical simulations to highlight the thermal rectification performance.[212, 213] In another 8.0 ns, the heat flow J was extracted from the slope of the linear regression curve by fitting the cumulative energy change in the heat baths with simulation time.

The vibrational spectra were calculated through $G(\omega) = \int_0^\infty e^{-i\omega t} \frac{<v(t)\cdot v(0)>}{<v(0)\cdot v(0)>} dt$, where ω is angular frequency and $v(t)$ is atomic velocity vector. The symbol · stands for dot product and the symbol < > denotes the average over atoms in specific groups. The atoms in both graphene and boron nitride domains, which are more than 1.6 nm (>1.5nm, the width of baths) away from the ends, were taken so as to avoid the effect of the boundary constraints and thermal reservoirs. The calculation of out-of-plane phonon spectra only involves the z component of velocity vectors, and the in-plane phonon spectra only consider the velocity of atoms in the *x* and *y*-directions. The overlap between spectra reflects the capability of phonon transport across the interface[209, 214], and can be determined through the mode matching theory $S = \frac{\int_0^\infty G_G(\omega)G_{BN}(\omega)d\omega}{\int_0^\infty G_G(\omega)d\omega \int_0^\infty G_{BN}(\omega)d\omega}$,[215] where G_G and G_{BN} are the spectra of graphene and boron nitride domain, respectively. Furthermore, the out-of-plane and in-plane spectra overlaps can be obtained to uncover the roles of in-plane and out-of-plane phonons in thermal rectification, and are defined as $S_o = \frac{\int_0^\infty G_{Go}(\omega)G_{BNo}(\omega)d\omega}{\int_0^\infty G_{Go}(\omega)d\omega \int_0^\infty G_{BNo}(\omega)d\omega}$ and $S_i = \frac{\int_0^\infty G_{Gi}(\omega)G_{BNi}(\omega)d\omega}{\int_0^\infty G_{Gi}(\omega)d\omega \int_0^\infty G_{BNi}(\omega)d\omega}$, respectively, where G_{Go} and G_{Gi} are the out-of-plane and in-plane phonon spectra of graphene, respectively, and G_{BNo} and G_{BNi} are the out-of-plane and in-plane phonon spectra of boron nitride, respectively.

The atomic heat flux vector is defined as $q_\mathrm{i} = \frac{1}{V}(e_i v_i - \sigma_i v_i)$, where V, e, v and σ are the atomic volume, energy, velocity vector and stress tensor, respectively, and the subscript i refers to the i^{th} atom. We should note that the stress tensor of an atom is calculated based on the atomic interaction and has the dimension of stress×volume with an energy unit. The heat flux vectors were obtained by averaging data for 8.0 ns after a steady state of thermal transport was reached.

3.3 Thermal Rectification Performance in GBN Heterostructure

When the heat flows from graphene to boron nitride region, **Figure 3.2a** shows that the heat flow J decreases at first at a small ε, and then increases as ε further increases. In contrast, J shows an opposite variation with ε when the direction of heat flow reverses. The simulations on the individual graphene and boron nitride nanoribbons, which have the same dimensions as when they are in the heterostructures, are also performed here as references (**Figure 3.2b**). The results suggest that both of their intrinsic thermal conductivities show an

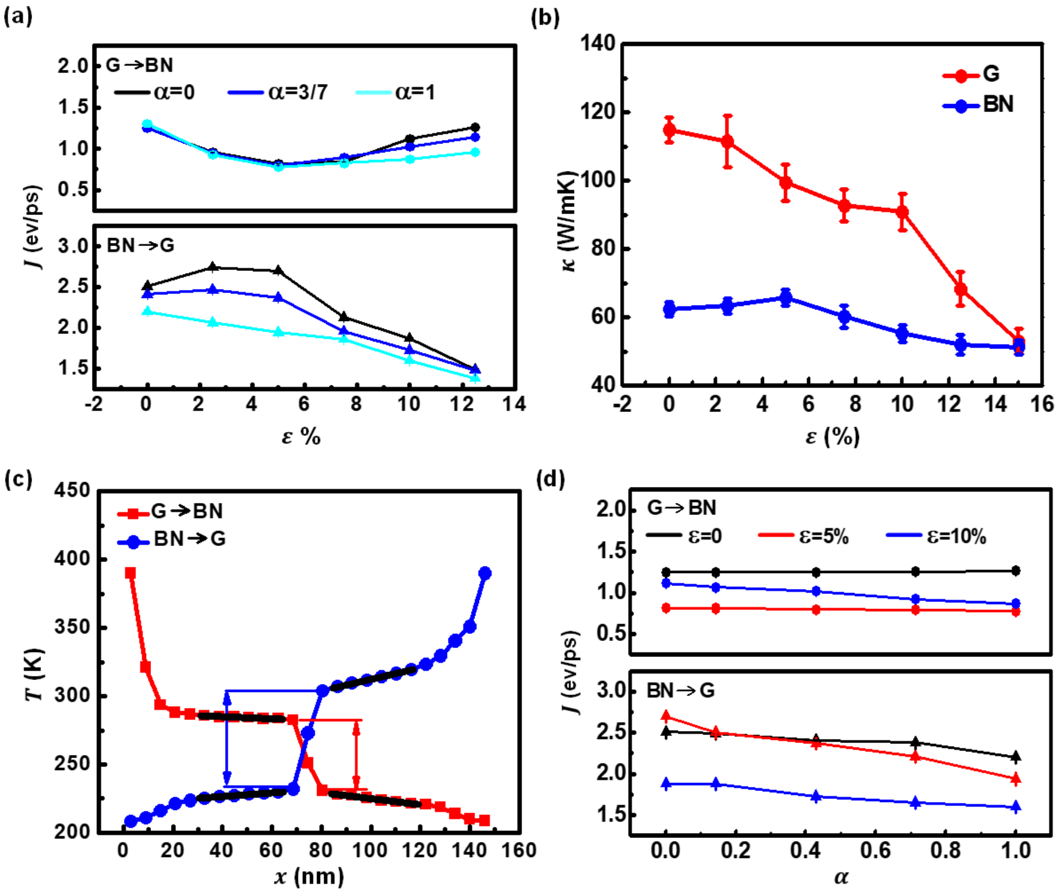

Figure 3.2. Asymmetric thermal transport in graphene-boron nitride (GBN) heterostructures with controlled interface junctions. (**a**) Comparison of heat flow J in heterostructures along both directions as functions of tensile strain ε. (**b**) Thermal conductivity κ of pure graphene and boron nitride as a function of tensile strain, where the graphene (G) and boron nitride (BN) have the same dimension as when they are in GBN heterostructures. (**c**) The temperature profile in GBN heterostructure with α=3/7 at two opposite directions of heat flow. The black solid lines illustrate the linear regions. (**d**) Comparison of heat flow J in heterostructures along both directions as functions of junction parameter α.

overall decrease with the increase of tensile strain. Therefore, the nonlinear variations in GBN heterostructures in the presence of interfaces are expected to be caused by the competition between phonon softening, phonon resonance and stress concentration at the interface, which will be illuminated in Section 3.4. Additionally, with the same temperature difference between hot and cold reservoirs, the magnitude of heat flow from boron nitride to graphene domain is higher than that in the opposite direction, indicating a clear thermal rectification performance in GBN heterostructures, analogous to the current flow in an electric diode. More importantly, with the increase of tensile strain ε, the difference between J in these two cases becomes smaller, suggesting the regulation on thermal rectification by an external mechanical strain. As an alternative proof, given the same magnitude of temperature difference between heat baths, a linear temperature profile is obtained in the graphene and boron nitride domains, but a clear temperature drop exists at the interface when heat transports in both directions, as shown in **Figure 3.2c**. A higher temperature drop across the interface is observed when heat transports from boron nitride to graphene domain, which further confirms the asymmetry of thermal transport in the GBN heterostructures. Note that the temperature drop near thermostats is caused by the local thermal conductivity and the phonon-boundary scattering[216-218]. Since the phonon-boundary scattering is independent of temperature while the local thermal conductivity decreases with the increase of temperature[219], a higher temperature drop is obtained near the hot thermostat than near the cold thermostat. Besides, as α increases, more defects will intensify the impediment to heat transport across the interface, leading to a decrease in J, as shown in **Figure 3.2d**. In particular, a clear decrease is observed when the heat flows from boron nitride to graphene domain.

We further define the thermal rectification ratio via $\eta = \frac{J_{BN\to G}-J_{G\to BN}}{J_{G\to BN}}$ to quantitatively characterize the thermal rectification performance, where $J_{G\to BN}$ and $J_{BN\to G}$ are the heat flow in the direction from graphene to boron nitride region and from boron nitride to graphene region, respectively. **Figure 3.3a** shows that η increases approximately by 100% at first before reaching a peak at $\varepsilon = 5\%$, and decreases with a further increase of ε, weakening the asymmetry of thermal transport. Besides, at a small ε (<5%), a smaller α leads to a larger η; At a large ε (>7.5%), a smaller α leads to a smaller η. The competing effects of ε and α on η are further confirmed in **Figure 3.3b**, and are expected to result from the mechanisms of stress, phonon resonance and phonon localization near the interfaces. In addition, it is

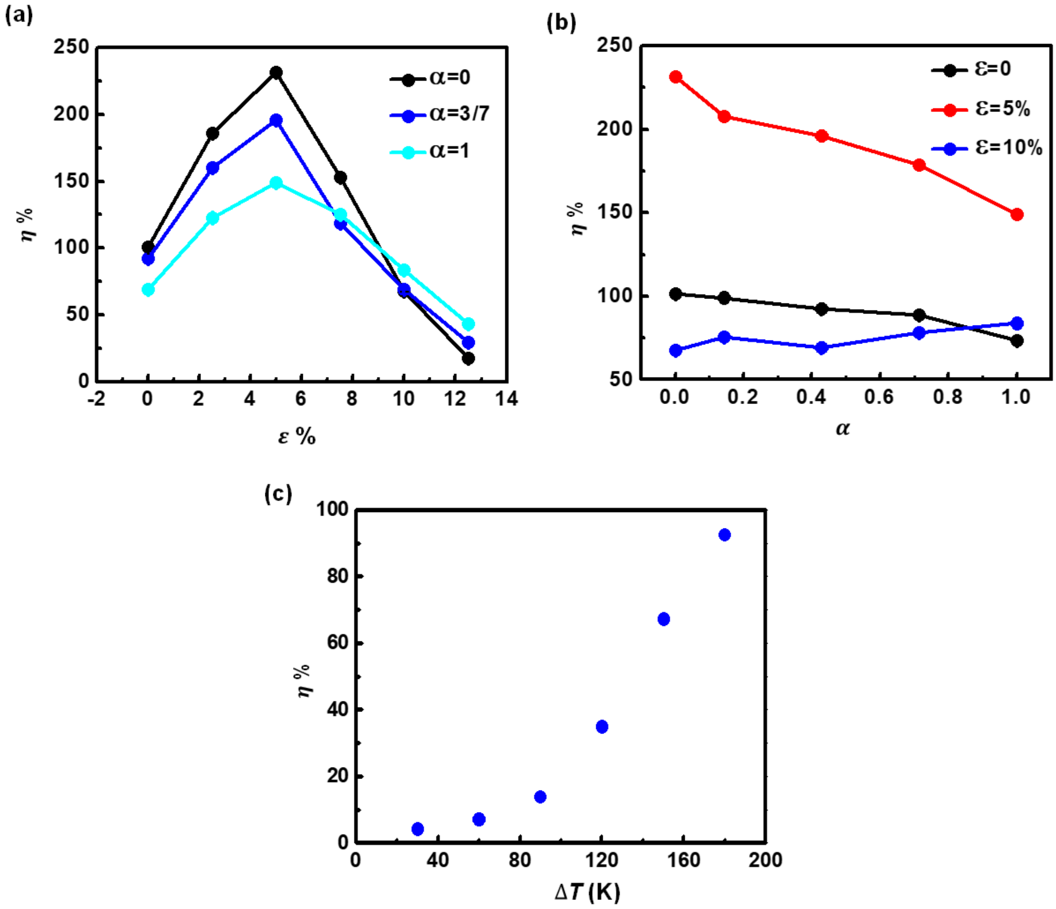

Figure 3.3. Thermal rectification in graphene-boron nitride (GBN) heterostructures with controlled interface junctions. (a) and **(b)** Variation of thermal rectification η as tensile strain ε, and heterojunction parameter α. (**c**) Thermal rectification ratio as a function of temperature difference between hot and cold reservoirs.

emphasized that a larger temperature difference between heat bathes or a smaller structure usually yields a higher thermal rectification ratio η. Nevertheless, the thermal rectification ratio η will not be zero as long as a temperature difference exists[220]. **Figure 3.3c** shows the effect of the temperature difference between heat bathes on the thermal rectification of the heterostructure with an imperfect junction ($\alpha = \frac{3}{7}$), and the thermal rectification still remains when the temperature difference is as low as 30 K, which is commonly employed in experiments[221, 222].

3.4 Mechanical Stress and Thermal Transport Analyses

Figure 3.4a presents the snapshots of von Mises stress distribution near the interfaces in the heterostructures. The von Mises stress is defined as $\sigma_{\mathrm{vm}} = \sqrt{\frac{1}{2}[(\sigma_{11} - \sigma_{22})^2 + [(\sigma_{22} - \sigma_{33})^2 + [(\sigma_{33} - \sigma_{11})^2 + 6(\sigma_{23}^2 + \sigma_{31}^2 + \sigma_{12}^2)]}$, where σ represents stress, and subscripts 1, 2, 3 are coordinate directions (i.e. *x*, *y* and *z* accordingly). For the heterostructure with a perfect interface junction (α=0), the stress gradient across the interface is very small due to the similar lattice structures of graphene and boron nitride. A clear stress concentration is observed when defects are introduced to the interfaces, and is more severe in the graphene domain because of its higher in-plane stiffness[223]. As the applied strain increases, the stress concentration becomes weaker.

To quantitatively describe the contribution of interfacial stress, the stress concentration factor, K_t , is extracted by taking the ratio of the averaged stress of carbon and boron nitride atoms at the interface (σ_{int}) to the far-field stress (σ_{ff}) in their corresponding graphene and boron nitride domains, i.e. $K_t = \sigma_{int}/\sigma_{ff}$. The far-field stress ($\sigma_{ff}$) in graphene and boron nitride domains is determined at the location where the effect of interfaces can be neglected[224].

Figure 3.4b shows a higher K_t in graphene than in boron nitride. Besides, a higher α leads to a higher K_t. K_t in both graphene and boron nitride domains decreases with the increase of ε, which is well consistent with von Mises stress distribution in Figure 3.4a. Usually, a higher K_t will constrain vibrations of atoms and weaken their thermal transport ability,[83, 209] thus leading to a lower J from graphene to boron nitride domain than from boron nitride to graphene domain. Moreover, an enhanced resistance against the heat transport across the interface at selective junctions at a higher K_t is consistent with a decreased J at a larger α in Figure 3.2d.

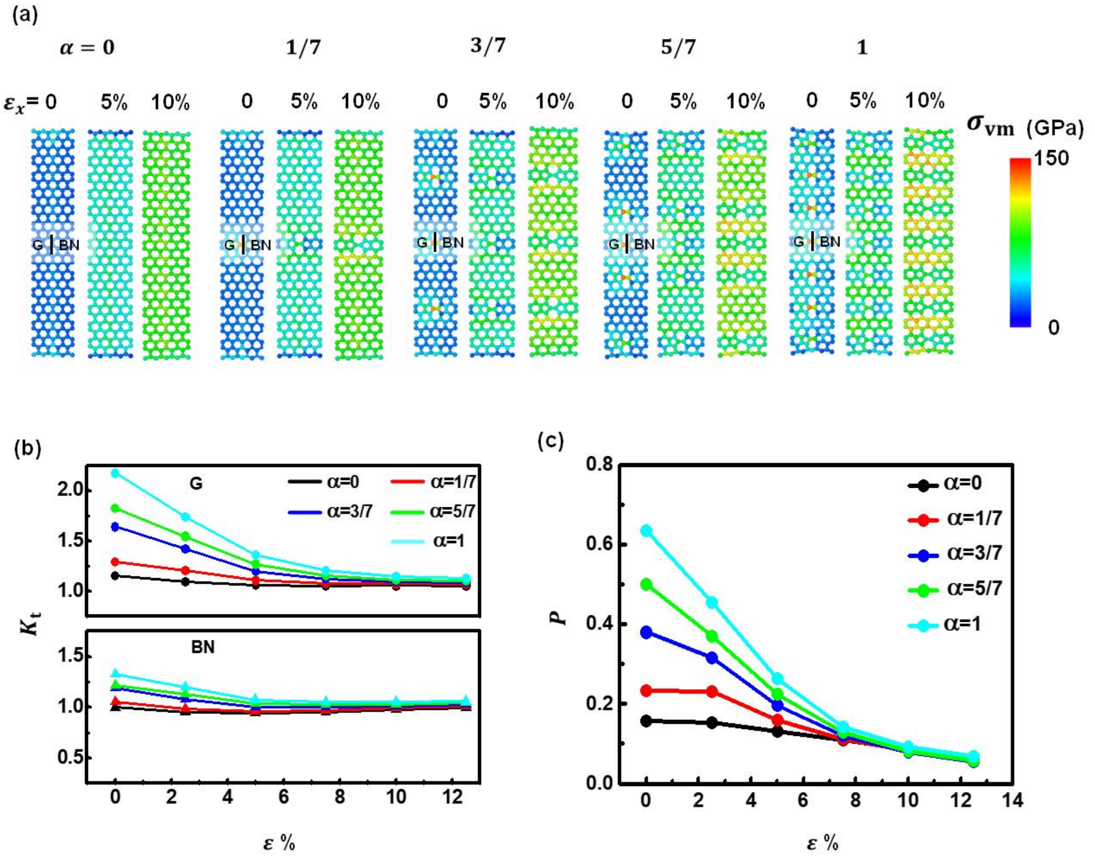

Figure 3.4. Stress analysis in graphene-boron nitride (GBN) heterostructures. (a) Snapshots of von Mises stress distribution near the interface. (**b**) Variation of stress concentration K_t in graphene and boron nitride domains as tensile strain ε, and heterojunction parameter α. (**c**) Comparison of relative stress concentration P in different heterostructures as functions of tensile strain ε.

Analogous to the thermal rectification ratio η, the stress concentration factor ratio P is also calculated to further characterize the effect of stress concentration on the thermal rectification, and is defined as $P = \frac{K_{tG} - K_{tBN}}{K_{tBN}}$, where K_{tG} and K_{tBN} are the stress concentration factors in the graphene domain and boron nitride domain, respectively. **Figure 3.4c** shows that P decreases monotonously with the increase of the tensile strain ε. In

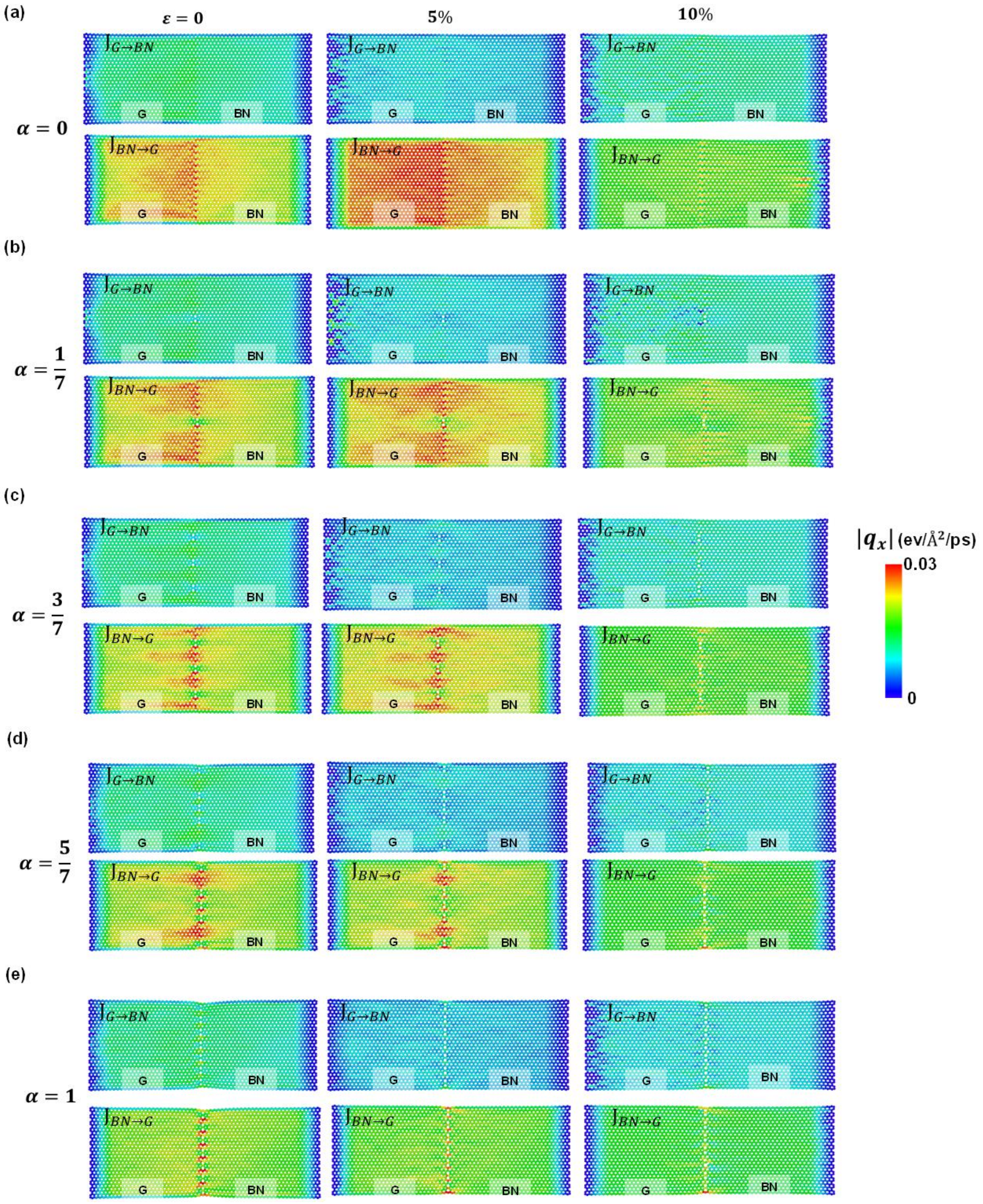

Figure 3.5. Heat flow distribution in GBN heterostructures with (a) $\alpha = 0$, **(b)** $\boldsymbol{\alpha} = 1/7$, **(c)** $\alpha = 3/7$, **(d)** $\alpha = 5/7$ and **(e)** $\alpha = 1$ before and after the reverse of heat flow direction at different tensile strains.

particular, at ε>7.5%, this monotonous decrease agrees well with the decrease of η in Figure 3.3a, indicating the dominant role of mechanical stress in the thermal rectification at a larger strain. As for comparison, the elevated η, despite reduced P, at a small strain implies the out-of-plane phonon resonance and phonon localization play a more important role, which also agrees well with the thermal transport mechanism of graphene nanoribbons in tension[83].

To further demonstrate the resistance effect of stress concentration on thermal transport at interface junctions, **Figure 3.5** gives the snapshots of atomic heat flux vectors in the heterostructures with different α at different tensile strains (see Section 3.2.1). Note that the summation of the heat flux vector over the atoms between the heat baths multiplied by the cross-sectional area will be the total heat flow J across the structures, which is consistent with steady heat conduction. Strong congestion (green region) is observed near the defects at the interface and is caused by in-plane phonon localization (will be discussed in details in Section 3.6) and stress concentration. In contrast, the perfect interface has lower stress, and higher heat flux (red region) is observed. When the heat flows from boron nitride to graphene domain, the magnitude of average heat flux is higher than that along the opposite direction, echoing well with the thermal rectification. At elevated strains, the effect of the interface becomes weak with a decreased congestion of heat flow, and the heat flow tends to be uniform. In addition, with more defects in the interfaces, the congestion of heat flow will be stronger because of the enhanced stress concentration. These snapshots indicate that the mechanical strain is capable of being used to tune thermal rectification performance in heterostructures by weakening the interface stress concentration.

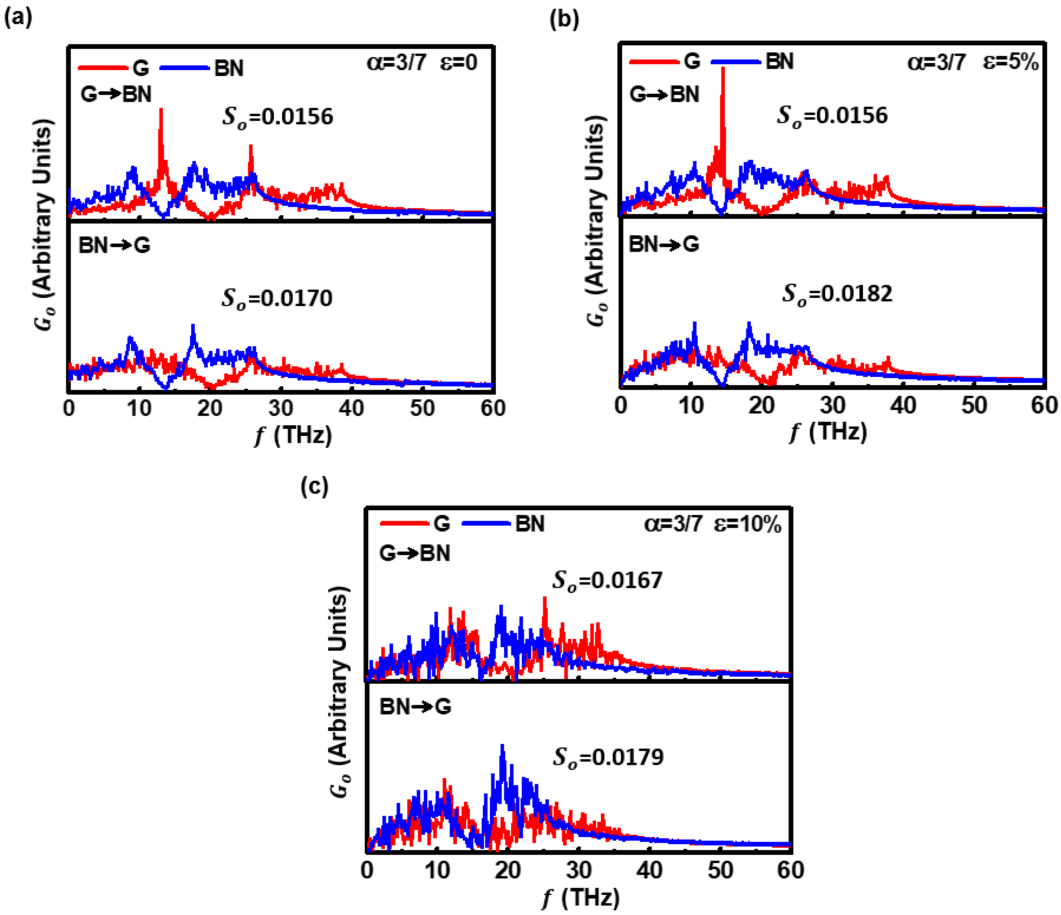

Figure 3.6. Out-of-plane Vibrational spectra of graphene and boron nitride domain in graphene-boron nitride (GBN) heterostructures. (a), (b) and **(c)** Out-of-plane vibrational spectra G_o of graphene and boron nitride in the heterostructure with $\alpha = 3/7$ at the tensile strain of $\varepsilon = 0$, 5% and 10%.

3.5 Vibrational Spectrum and Mode Matching Analyses

Figure 3.6a shows the out-of-plane vibrational spectra of graphene and boron nitride atoms in the heterostructure with $\alpha = \frac{3}{7}$, and a clear difference between them is observed. In particular, when the heat flows from graphene to boron nitride domain, the phonon modes in graphene distribute in the frequency ranges of 0-20 and 20-40 THz with a minimum magnitude at 20 THz. Considering the frequency range of intrinsic graphene out-of-plane phonon modes (0-30 THz)[225], the phonon modes with a frequency higher than 30 THz are contributed by the atoms near the interface[147]. In contrast, the spectrum of boron nitride is higher between 0 and 10 THz and between 15 and 30 THz. When the direction of heat flow reverses with the same temperature difference between heat baths, since a higher temperature will result in a higher phonon population in vibrational spectrum[145, 226], the phonon peak magnitudes in vibrational spectra of both graphene and boron nitride domains change. To reveal the mechanism of thermal rectification, the popular out-of-plane vibrational spectra overlap S_o is extracted. When heat flows from boron nitride to graphene domain in the absence of mechanical tensile strain ($\varepsilon = 0$), the peak at 13 THz in graphene spectrum broadens, leading to a significant increase of the overlap S_o in comparison with the spectrum obtained from the case with opposite heat transport direction. The enhancement of S_o leads to an increased heat flow from boron nitride to graphene domain, which is consistent with the calculations in Figure 3.2a and d. When heat transports from graphene to boron nitride domain at a small tensile strain (5%), the spectra of both graphene and boron nitride are similar to the ones at $\varepsilon = 0$ and the overlap of their spectra S_o approximately remains with the same value (**Figure 3.6b**). When heat transports from boron nitride to graphene domain, the small peak at 8 THz in the out-of-plane spectrum of boron nitride is broadened in comparison with the one at $\varepsilon = 0$, leading to a slight increase in the overlap. As the tensile strain further increases to 10% (**Figure 3.6c**), the overlap of S_o shows an increase when the heat flows from graphene to boron nitride domain. When the heat flow reverses its direction, S_o shows a slight decrease but is still larger than that in the absence of tensile strain, indicating the mitigation effect of a larger strain on the phonon localization and phonon resonance.

In comparison with the out-of-plane vibrational spectra and resulting spectra overlap, **Figure 3.7a** shows the in-plane vibrational spectra of graphene and boron nitride, and no obvious difference is observed. Besides, the overlap S_i is approximately the same before and

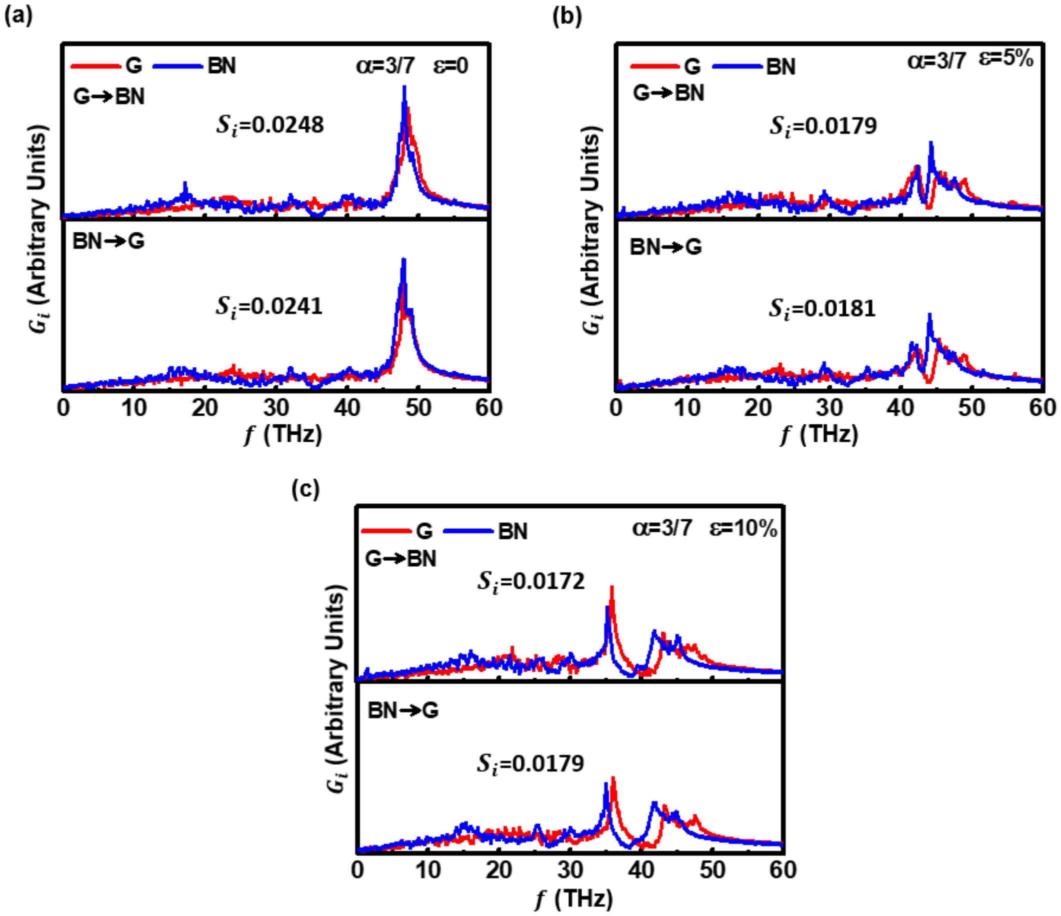

Figure 3.7. In-plane Vibrational spectra of graphene and boron nitride domain in graphene-boron nitride (GBN) heterostructures. (a), (b) and **(c)** In-plane vibrational spectra G_o of graphene and boron nitride in the heterostructure with $\alpha = 3/7$ at the tensile strain of $\varepsilon = 0$, 5% and 10%.

after the switch of heat flow directions. This negligible difference in S_i remains after applying 5% and 10% tensile strain to heterostructures, as shown in **Figure 3.7b and c**, which suggests that the thermal rectification should be contributed by the out-of-plane phonon resonance, and is independent of in-plane phonon resonance. We should note that once the heterostructure is stretched by the tensile loading, the resulting stress or strain in the graphene or boron nitride domain will constrain the lattice deformation and softens phonon modes, leading to lattice anharmonicity[80]. Consequently, a shift of high frequency peak (~48 THz in the absence of tensile strain in Figure 3.7a) to lower frequency (~46 THz at 5% and ~43 THz at 10% tensile strain in Figure 3.7b and c), often referred to as red shift, is observed in the spectra of both

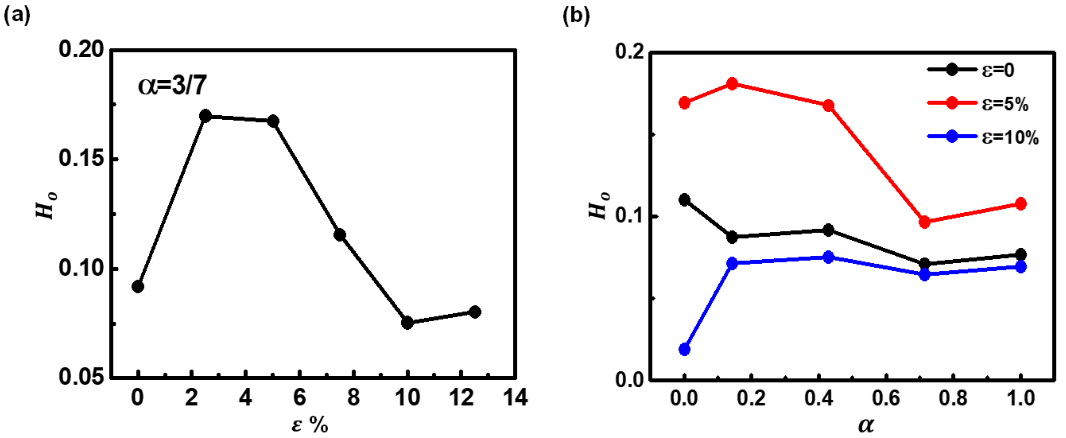

Figure 3.8. (a) Relative overlap H_o in the heterostructure with $\alpha = 3/7$ at different strains. (**b**) Variation of relative overlap of out-of-plane phonon spectra H_o as functions of junction parameter α.

graphene and boron nitride. In addition, at a higher strain, a larger red shift is observed in boron nitride than in graphene. These uneven shifts decrease the overlap of their spectra, and lead to a clear reduction in S_i at 5% and 10% tensile strain, as shown in Figure 3.7b and c. Nevertheless, S_i still remains approximately the same after reversing heat flow direction at the same tensile strain.

Furthermore, we calculate $H_o = \frac{S_{O(BN\to G)} - S_{O(G\to BN)}}{S_{O(G\to BN)}}$ to characterize the effect of out-of-plane phonon modes on thermal rectification, and its variation with ε is plotted in **Figure 3.8a**. H_o shows an increase initially and then decreases, which is in agreement with the variation of η, indicating the dominant role of out-of-plane phonon modes resonance in thermal rectification at a small tensile strain. **Figure 3.8b** presents the effect of α on H_o. When the tensile strain is small (< 5%), H_o decreases with the increase of α; At a high tensile strain (ε=10%), H_o increases with α.

3.6 Phonon Localization and Energy Distribution

To further probe the effect of the stress concentration and the out-of-plane phonon localization on thermal rectification, we calculate the phonon participation ratio of each phonon mode via $p_{\lambda}^{-1} = N\sum_{i}(\sum_{\beta}\epsilon_{i\beta,\lambda}^{*}\,\epsilon_{i\beta,\lambda})^{2}$, where N is the number of atoms, β is the polarization of interest (β= x, y or z), $\epsilon_{i\beta,\lambda}$ is the eigenvector component of i^{th} atom in the λ^{th} phonon mode in β direction. At the equilibrium position of atoms in both graphene and boron nitride domains, $\epsilon_{i\beta,\lambda}$ can be obtained by calculating the Hessian matrix with lattice dynamics simulation.[227] The calculation of p_{λ} indicates that the phonon participation ratio is independent of temperature and lies between $O(1)$ for completely delocalized modes and $O(1/N)$ for completely localized phonon modes[214]. Here $p_{\lambda} < 0.25$ is taken as the criterion to ensure the delocalization of most phonon modes. In the absence of tensile strain, **Figure 3.9a** shows that most localized modes (i.e. $p_{\lambda} < 0.25$) emerge in the frequency range of 0-30 THz,

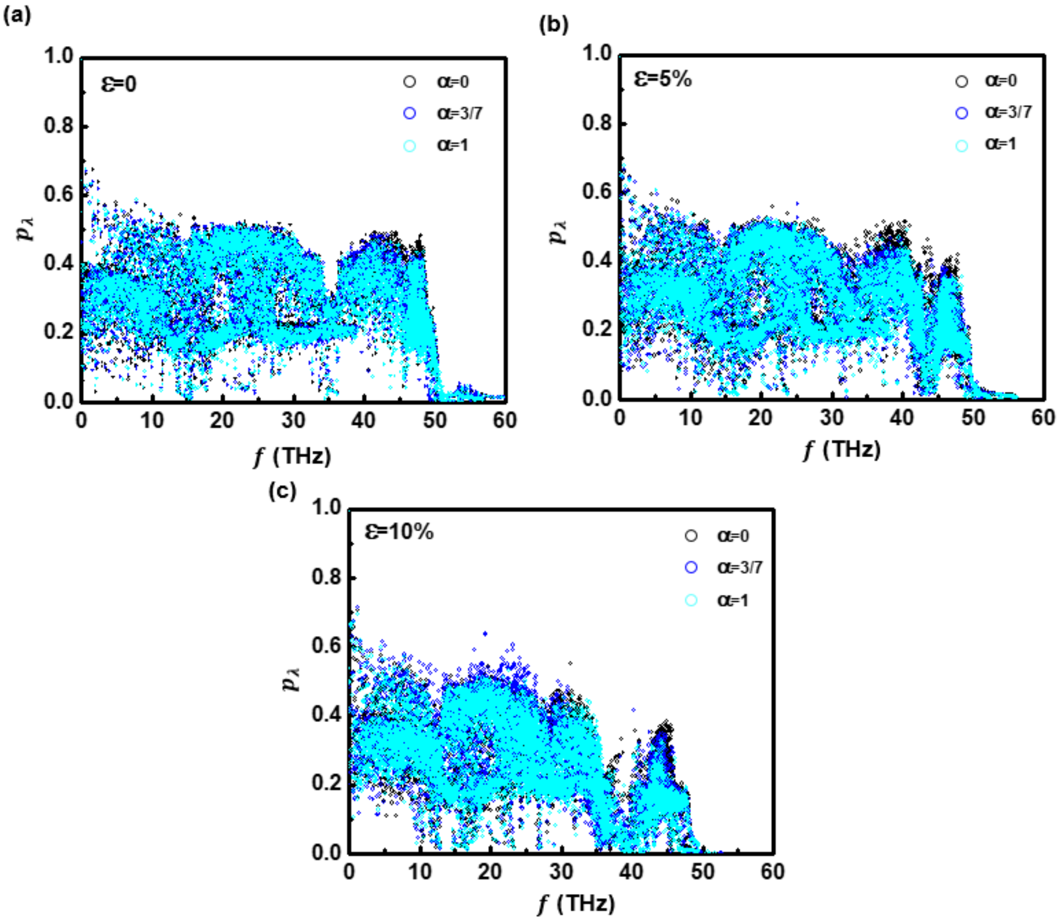

Figure 3.9. Phonon participation ratio in heterostructures with α =0, $3/7$ and 1 at the tensile strain (**a**) $\varepsilon = 0$, (**b**) 5% and (**c**) 10%

which corresponds well to the appearance of significant out-of-plane phonon modes in Figure 3.6a-c. With the increase of interface defects (i.e. larger α), lower phonon participation ratios are obtained in the high frequency range (>40 THz), which is dominated by in-plane phonon modes, indicating that the imperfect junctions will lead to in-plane phonon localization and reduction in thermal transport, consistent with Figure 3.2d. The similar observations are also obtained under tensile strain of 5% and 10% (**Figure 3.9b and c**).

To understand the evolution of in-plane and out-of-plane phonons, we investigate the energy spatial distribution of both localized in-plane and out-of-plane phonons in the heterostructure. The energy of the localized phonons at a location is calculated via $E = \sum_{\omega}(n+\frac{1}{2})\hbar\omega\, D_i$[228, 229], where $\hbar$ is the reduced Planck constant, ω is the angular frequency, n is the occupation number in the Bose-Einstein distribution and D_i is the local vibrational density of states. More specifically, $D_i = \sum_{\lambda}\sum_{\beta}\epsilon^{*}_{i\beta,\lambda}\,\epsilon_{i\beta,\lambda}\,\delta(\omega-\omega_{\lambda})$, where δ denotes Dirac delta function, and ω_{λ} is the angular frequency of the λth phonon mode. For in-plane phonon modes, β is x and y, and for out-of-plane modes, only β=z is counted. **Figure 3.10** shows the energy distribution of localized out-of-plane phonon modes in the heterostructure with $\alpha = \frac{3}{7}$. Higher energy of localized phonons exists in the graphene region and it corresponds well with the wider range of frequencies in out-of-plane spectra in graphene (Figure 3.6a-c). The concentration of localized phonon energy in graphene is more obvious when heat transfers from graphene to boron nitride domain, narrowing the propagation path of delocalized phonon modes and thus limiting the thermal conductance.[214] When heat transfers from boron nitride to graphene, the difference between average localized phonon energy in the domains of the two materials becomes smaller, which leads to an increased phonon resonance.

As a consequence, an enhanced thermal transport ability in the heterostructures is achieved, which further leads to the thermal rectification. At an external mechanical tensile strain, the energy of localized phonons becomes smaller in the entire structure, indicating its mitigation effect on out-of-plane phonon localization. To further reveal the regulatory role of tensile strain, the out-of-plane localized phonon energy along the *y*-axis is averaged and plotted with *x*-coordinates (i.e. the direction of heat transport) normalized by the length of structure x/l in Figure 3.10. It shows that when heat travels from graphene to boron nitride, the localized phonon energy is maintained at a higher magnitude of plateaus in the graphene domain than that in the boron nitride domain, associated with a clear drop near the interface; when the heat

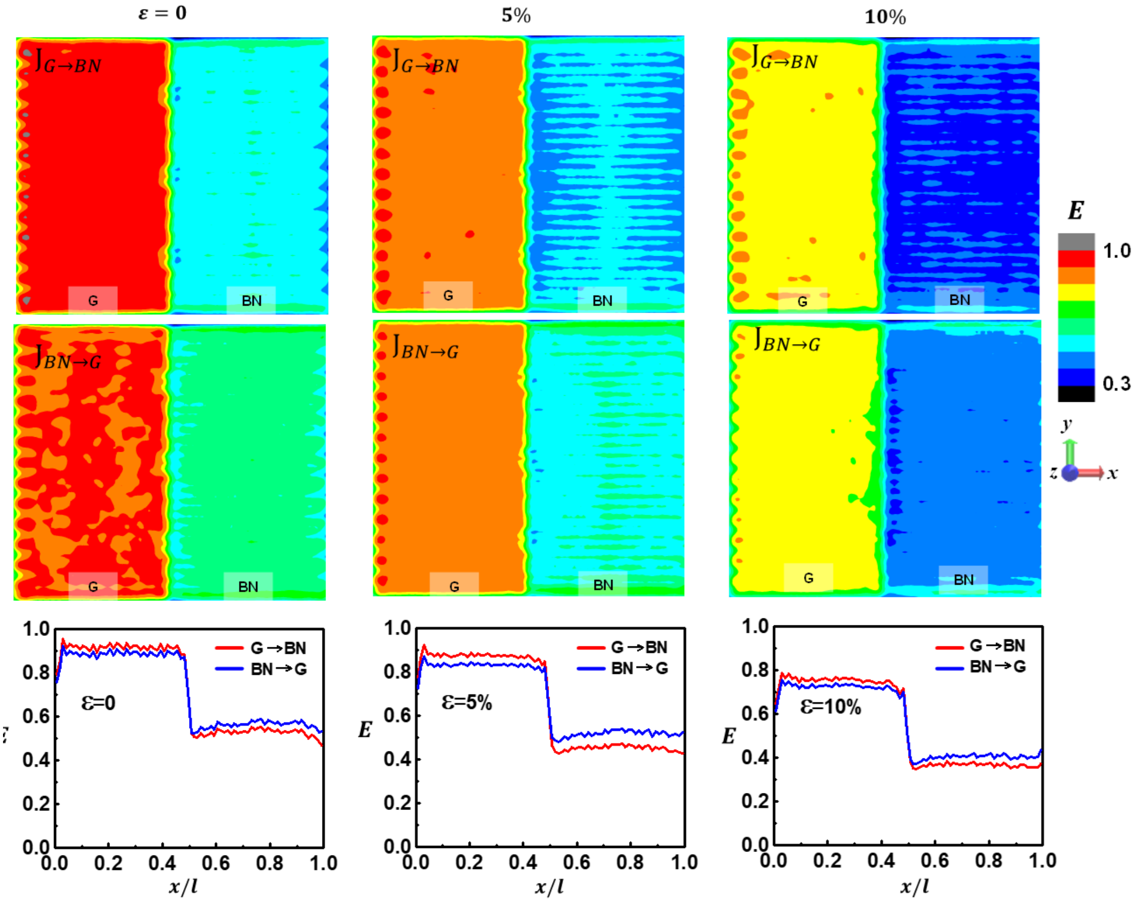

Figure 3.10. Energy distribution of localized out-of-plane phonon modes (top) and the averaged plots as *y*-axis with *x*-position normalized by the length *l* (bottom) in the heterostructure with $\alpha = 3/7$ in both directions of heat flow at different tensile strains.

flow reverses its direction, both plateaus shrink to the middle with a smaller drop between them, indicating a reduced difference of localized phonon energy distribution in both graphene and boron nitride. This reduction will lead to an enhanced phonon resonance of these localized phonons, and thus improve the thermal transport ability. The “shrink” becomes the most obvious at 5% tensile strain, which is consistent with the optimized thermal rectification ratio at 5% tensile strain shown in Figure 3.3a.

Moreover, the reduced overall energy of out-of-plane localized phonon modes echoes with the increased phonon participation ratio at a large strain in the frequencies 0-30 THz in Figure 3.10d. Besides, this finding further confirms that the effect of out-of-plane phonon mode localization is weak at large tensile strain, and the thermal rectification is dominated by the stress concentration near the interfaces, which is in agreement with a monotonous decrease of both η and P (ε>7.5%).

3.7 Conceptual Heterostructure Systems with Controllable Thermal Transport Paths

To demonstrate the potential applications of mechanical tensile strain and selective junction interfaces in the thermal transport of heterostructures, we present two conceptual designs of heterostructure systems. **Figure 3.11a** shows the atomic modeling of the first heterostructure system composed of alternatively arranged graphene and boron nitride sheets with parallel interfaces but different junction parameters α=0, 1, referred to as a thermal antiparallel shunt. In this system, both ends and middle regions were selected as heat baths to generate a temperature gradient. When the heat flows from the middle region with a high

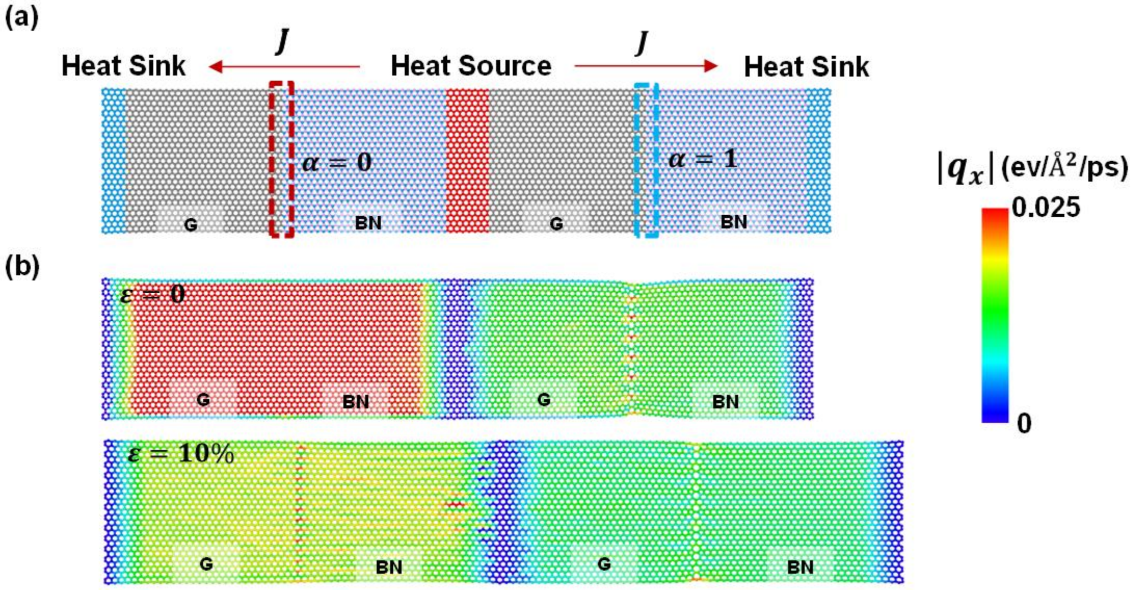

Figure 3.11. Demonstration applications of controllable thermal transport paths in the heterostructure systems with selective interface junctions. **(a)** Atomic structure of GBN heterostructure system composed of alternatively arranged graphene and boron nitride sheets with parallel interfaces but different junction parameters α (=0, 1), referred to as a thermal antiparallel shunt. **(b)** Comparison of heat flux in the "thermal antiparallel shunt" system at 0% and 10% tensile strain.

temperature (hot bath) to both ends with the same temperature (cold bath), **Figure 3.11b** shows a clear difference in the heat flows in the two directions.

Figure 3.12a presents a second graphene-boron nitride heterostructure system with one interface. Its interface consists of equal junctions but with different parameters (α=0, 1), referred to as a thermal parallel shunt. When the heat flows from boron nitride to graphene domain, **Figure 3.12b** shows that heat flow with greater magnitude is much easier to cross the interface with α=0 than with α=1. When the direction of the temperature gradient switches, the asymmetry of heat flow across the interfaces with both α=0 and α=1 decreases. Besides, upon applying a tensile strain, the dependence of heat flow in both directions on the interface parameter α becomes weak. The preference of heat flow in these two heterostructure systems indicates that the asymmetric thermal transport can be tuned by interface junctions, and more importantly, it can be reduced by an external mechanical strain.

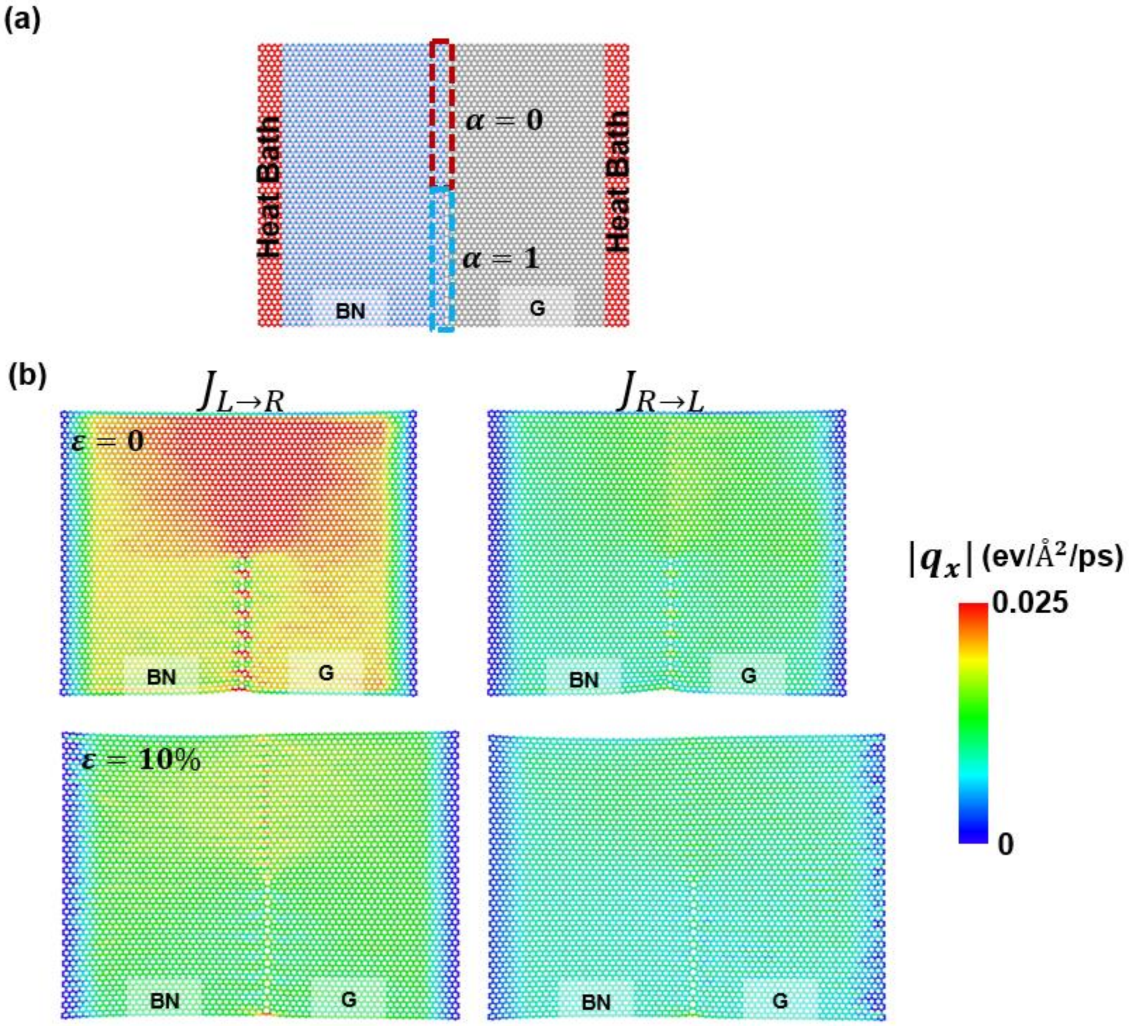

Figure 3.12. Demonstration applications of controllable thermal transport paths in the heterostructure systems with selective interface junctions. Atomic structure of GBN heterostructure system with an equally shared interface but different junction parameters (α=0, 1), referred to as a thermal parallel shunt. **(d)** Comparison of heat flux in both directions in the "thermal parallel shunt" system at 0% and 10% tensile strain.

3.8 Summary

In summary, we systematically investigate the thermal rectification in graphene-boron nitride (GBN) in-plane heterostructures with controlled interface junctions and their response to an external mechanical tensile strain. Using non-equilibrium molecular dynamics (NEMD) simulation, we show that the asymmetric heat transport decreases with the introduction of junction defects. Upon applying a mechanical deformation to GBN heterostructures, it will increase at a small tensile strain but decrease at a large tensile strain. This competing effect of heterojunction interfaces and mechanical tensile strain are probed through the stress analysis, vibrational spectra, phonon participation ratio, and heat flow distribution. At a small tensile strain, the thermal rectification is dominated by out-of-plane phonon mode resonance and localization, and with the increase of tensile strain, the mechanical stress concentration at the interface plays a dominant role.

Chapter 4 Thermal Transport in Heterostructures with van der Waals Interfaces under Mechanical Loadings

4.1 Overview of the Chapter

In this chapter, we report the thermal transport in vdW heterostructures subjected to mechanical tension loadings, including bilayer vdW heterostructures enabled by two different 2D materials, which are exerted with small loadings ($\varepsilon \leq 15\%$), and bilayer graphene kirigami heterostructures composed of two graphene kirigami with different cuts, which is durable to large loadings ($\varepsilon > 15\%$).

Using nonequilibrium molecular dynamics simulations, we show that the phonon thermal transport in the graphene-MoS_2 bilayer heterostructure is reduced by the lattice mismatch, and the reduction can be mitigated well by an external tension, weakening the effect of inherent mismatch-induced strain on thermal conductivity. Mechanical analyses in each layered component indicate that the external tension will alleviate the lattice mismatch-induced deformation. The phonon spectra are also softened by the applied tension with a significant shift of frequency from high to low modes. A universal theory is proposed to quantitatively predict the role of the lattice mismatch in thermal conductivity of various bilayer heterostructures and shows good agreement with simulations.

We report a van der Waals heterostructure that is composed of bilayer graphene kirigami with diverse layer cut patterns and assembly organizations and show that the thermal flow intensity across the van der Waals interfaces, named as thermal transparency, could be continuously regulated by applying an external in-plane tensile strain. The density of atomic interactions across the interfaces and the distribution of delocalized phonon modes in each graphene kirigami are elucidated to understand the underlying thermal transport mechanism and are also incorporated into a theoretical model for quantitative predictions of thermal conductance under mechanical strain. A proof-of-conceptual van der Waals graphene kirigami heterostructure by design is proposed and validated through extensive full-scale atomistic simulations on the feasibility and reliability of regulating the transparency ratio of thermal transport by mechanical strain, demonstrating its potential applications in thermal and electronic devices.

4.2 Thermal Transport in Bilayer van der Waals Heterostructures Subjected to Tensile Loading

4.2.1 Computational Modeling and Method

Figure 4.1 illustrates the computational model of a bilayer van der Waals heterostructure that consists of one pristine graphene layer and one pristine MoS_2 layer. The lattice mismatch ratio λ between them is defined as $\lambda = (a_1 - a_2)/a_2$, where a_1=0.312 nm and a_2=0.249 nm are the first lattice constants of MoS_2 and graphene,[230] respectively, and λ=0.253. The heat transfer is applied in parallel to the interface of heterostructures, and the external tensile strain ε is applied to the same direction as the heat flow.

Graphene-MoS_2 heterostructure is constructed by individual pristine graphene and MoS_2 layer sheet separated by a 0.335 nm space based on experimental and theoretical analysis[231, 232]. The length and width of the computational modeling are l=11.2 nm and w=3.71 nm, respectively. Two ends were fixed to prevent atoms from sublimating. The interaction between

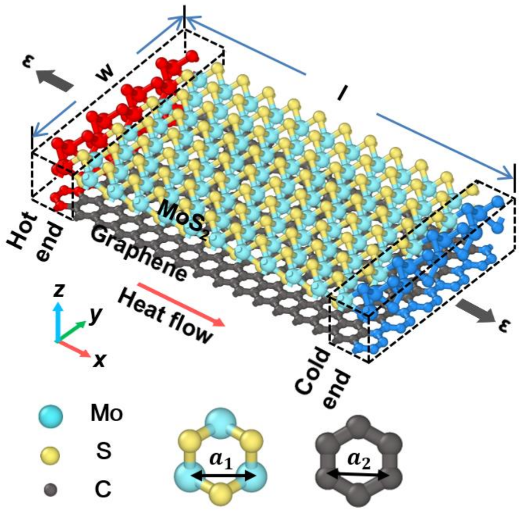

Figure 4.1. Computational model of the bilayer graphene-MoS$_2$ heterostructure (a) Molecular modeling of the graphene-MoS$_2$ heterostructure. Heat flow is achieved along the *x*-direction, in parallel to the interface of the heterostructure, and a uniaxial tensile strain ε is applied in the *x*-direction. The ends are set to the hot and cold region, respectively and are fixed in simulations. A periodic boundary condition is applied to the *y*-direction and other two directions (i.e. *x*- and *z*-directions) are non-periodic boundary conditions.

carbon atoms in graphene was described by AIREBO potential[178] and the interatomic interaction in MoS$_2$ layer was described by Stillinger-Weber potential[233]. The van der Waals interaction between two layers was modeled by Lennard-Jones potential[231], and the cut-off radius was set as 1 nm. A periodic boundary condition was used in the *y*-direction and non-periodic boundary conditions were used in the *x*- and *z*- direction.

The heterostructure was first equilibrated in canonical ensemble (NVT ensemble) at 300 K for 0.4 ns, and the temperature was maintained by Nose-Hoover thermostat. Next, the whole structure was uniformly stretched in NVT ensemble along the *x*-direction under a quasi-static displacement loading to introduce an external strain ε with a desirable magnitude. Afterward, the structure was relaxed in NVT ensemble for another 0.2 ns.

To extract the thermal conductivity of the structures in tension, the simulation box was divided into 40 slabs in the *x*-direction. The five slabs that are closest to the ends were selected as the hot and cold reservoir and controlled by Langevin thermostats at 320 K and 280 K,

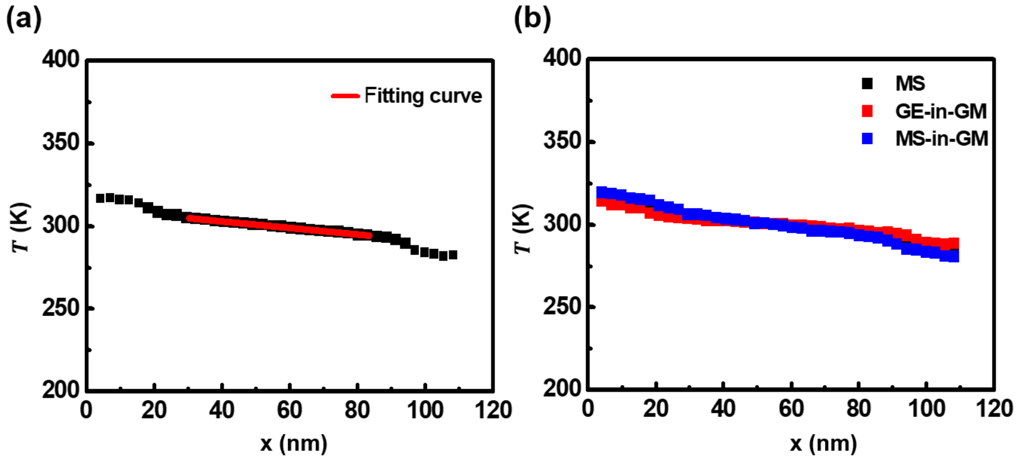

Figure 4.2. Temperature profiles in the graphene-MoS$_2$ heterostructure and individual layer components. (a) The temperature profile in the graphene-MoS$_2$ heterostructure, where the cold and hot ends are set to the ends of the heterostructure, respectively and controlled by Langevin thermostats. The linear region is employed to extract the temperature gradient for use in the determination of thermal conductivity. **(b)** Comparison of temperature profiles of individual layers of graphene (GE-in-GM), and MoS$_2$ (MS-in-GM) in heterostructure and graphene-MoS$_2$ heterostructure (GM). The temperature profiles of individual layer components are obtained by assigning the hot and cold reservoir separately to graphene and MoS$_2$ layers.

respectively. It took 0.5 ns to reach a steady temperature gradient (**Figure 4.2a**) and the simulation data in the following 2.0 ns were recorded in the calculation of thermal conductivity. The difference between temperature gradient of graphene and MoS$_2$ could be neglected (**Figure 4.2b**). The same temperature gradient could be reached when the hot and cold reservoir is assigned separately to graphene and MoS$_2$ layers in heterostructures. This settings of thermostats to individual layers allow to record the heat flow passing through each layer, respectively.[150] All simulations were performed using LAMMPS[177].

The phonon spectra were calculated via $G(\omega) = \int_0^\infty e^{-i\omega t} \frac{<v(t)\cdot v(0)>}{<v(t)\cdot v(0)>} dt$, where, ω is the frequency, $v(t)$ is the atomic velocity vector and $\cdot$ denotes the average over atoms in layer components. In the calculation of in-plane and out-of-plane phonon spectra, $v(t)$ was replaced by the in-plane and out-of-plane velocity vector $v_i(t)$ and $v_o(t)$.

4.2.2 Mechanical Properties: Mitigation of Lattice Mismatch Deformation by Strain

Figure 4.3a shows the nominal stress-strain curves of the graphene-MoS_2 heterostructure, bilayer graphene and bilayer MoS_2. For the bilayer graphene, the stress increases linearly at a small strain, followed by a nonlinear variation till to a sudden drop that corresponds to the failure of carbon-carbon bonds, which is similar to that of single layer graphene under uniaxial

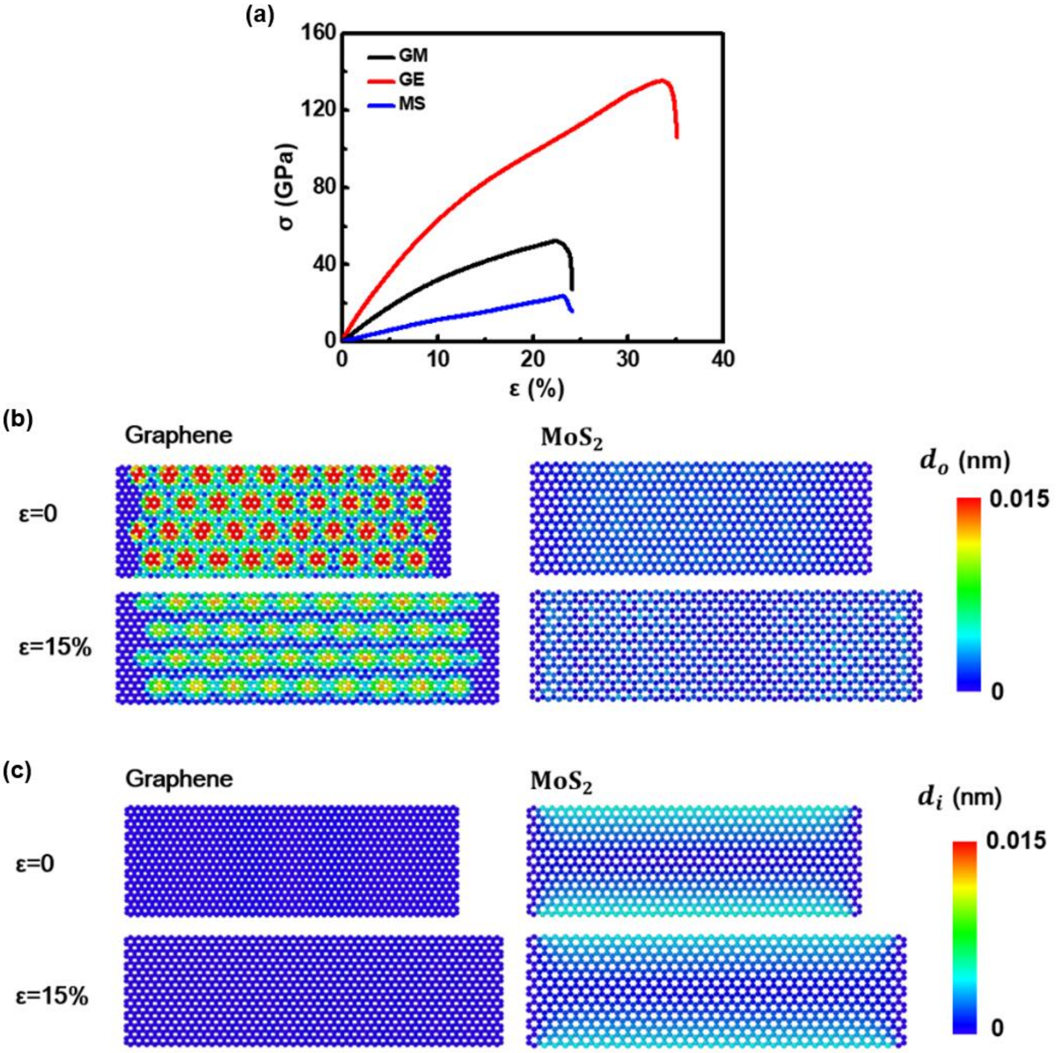

Figure 4.3. Mechanical properties of the Graphene-MoS2 bilayer heterostructure. (b) Nominal stress-strain curve of the graphene-MoS_2 heterostructure, bilayer graphene and bilayer MoS_2. **(c)** Lattice mismatch-induced out-of-plane displacement, d_o, of atomic positions in graphene and MoS_2 layer in the heterostructure at equilibrium under the tensile strain of 0% and 15%, and it is calculated by comparing positions of atoms in heterostructures and their corresponding bilayer structures.

tension[83]. As for the bilayer MoS_2, the stress increases almost linearly until the failure of the structure occurs, which is analogous to that of a single layer MoS_2[230, 234]. At the same strain, the stress of the graphene-MoS_2 heterostructure is higher than that of bilayer MoS_2 but lower than that of bilayer graphene. The failure strain is almost the same as the bilayer MoS_2, demonstrating that the deformation of heterostructure is dominated by the MoS_2 layer with weaker stretchability[230].

To reveal the effect of the applied tensile strain on lattice mismatch-induced layer deformation, the variation in the positions of carbon and molybdenum disulfide atoms in graphene-MoS_2 heterostructure at equilibrium in comparison to their individual bilayer structures are extracted. **Figure 4.3b** shows the out-of-plane displacement for both graphene and MoS_2 layer components, d_o. An obvious out-of-plane deformation in the graphene sheet is observed, and the periodic pattern is attributed to the non-centrosymmetric atomistic structure of MoS_2. Besides, in contrast to the planar carbon ring structure in graphene layer, since the distribution of molybdenum and sulfur atoms in the MoS_2 layer show a trigonal structure with a relatively high thickness, the lattice mismatch leads to a weak influence[235], and a very small displacement to MoS_2 layer is observed. When an external strain ε is applied, it will stretch the carbon-carbon bonds and constrain the out-of-plane deformation, leading to a decreased out-of-plane displacement. The similar reduction to the deformation on MoS_2 layer is also observed. Different from the obvious out-of-plane displacement, the lattice mismatch causes a relatively small displacement to the in-plane displacement, d_i, in graphene layer owing to the high in-plane stiffness of graphene (**Figure 4.3c**)[36]. Note that the in-plane displacement of MoS_2 is greater than that of graphene due to the inherent 3D atomistic structure that facilitates the in-plane displacement. Besides, in comparison to the obvious mitigation to out-of-plane deformation by the applied tension, the effect of tensile strain on the in-plane displacement is small.

4.2.3 Thermal Transport Properties of Bilayer Heterostructure Subjected to Tension

Figure 4.4a shows the thermal conductivity of graphene-MoS_2 heterostructure, κ_H, bilayer graphene, κ_{BGE} and bilayer MoS_2, κ_{BMS}. In the absence of the applied tensile strain, κ_{BGE}, κ_{BMS} and κ_H are 100.79, 8.50 and 34.05 W/mK, respectively, consistent with previous reports[150, 231, 235, 236]. As ε increases, they all decrease monotonously, and κ_H is in between κ_{BGE} and κ_{BMS}, which remains with the increase of the strain ε, similar to that observed in the stress-strain curve in Figure 4.3a.

To understand the effect of the lattice mismatch, we calculate the thermal conductivity of individual graphene and MoS_2 layers in the heterostructure by monitoring the heat flow in each layer (see method section for computational settings). Their variations with the applied strain are plotted in **Figure 4.4b**. It shows that the thermal conductivity of graphene in heterostructure $\kappa_{GE-in-GM}$ is lower than that of bilayer graphene structure κ_{BGE} (Figure 4.4a); while the thermal conductivity of MoS_2 in heterostructure $\kappa_{MS-in-GM}$ is close to that of bilayer MoS_2 structure k_{BMS} (Figure 4.4a), implying that the thermal conductivity of MoS_2 is barely affected by interaction in its cross-plane direction, consistent with the fact that thermal conductivity of MoS_2 is independent of layer numbers[237]. Similar to κ_{BGE} and κ_{BMS}, both $\kappa_{GE-in-GM}$ and $\kappa_{MS-in-GM}$ decrease monotonously with the increase of ε. Consider the equivalence of the total heat flow, we have $J_H = J_{GE-in-GM} + J_{MS-in-GM}$, where J_H is the heat flow through the entire heterostructure, and $J_{GE-in-GM}$ and $J_{MS-in-GM}$ are the heat flow passing through individual graphene and MoS_2 layer, respectively. Since the temperature gradient is approximately the same (Figure 4.2b), based on Fourier's Law, we have

$$\kappa_H = (\kappa_{GE-in-GM} t_{GE} + \kappa_{MS-in-GM} t_{MS})/t_H, \tag{4.1}$$

where t_{GE} and t_{MS} are the thickness of graphene and MoS_2 layer in heterostructure, respectively and are approximately equal to the thickness of a single graphene and MoS_2

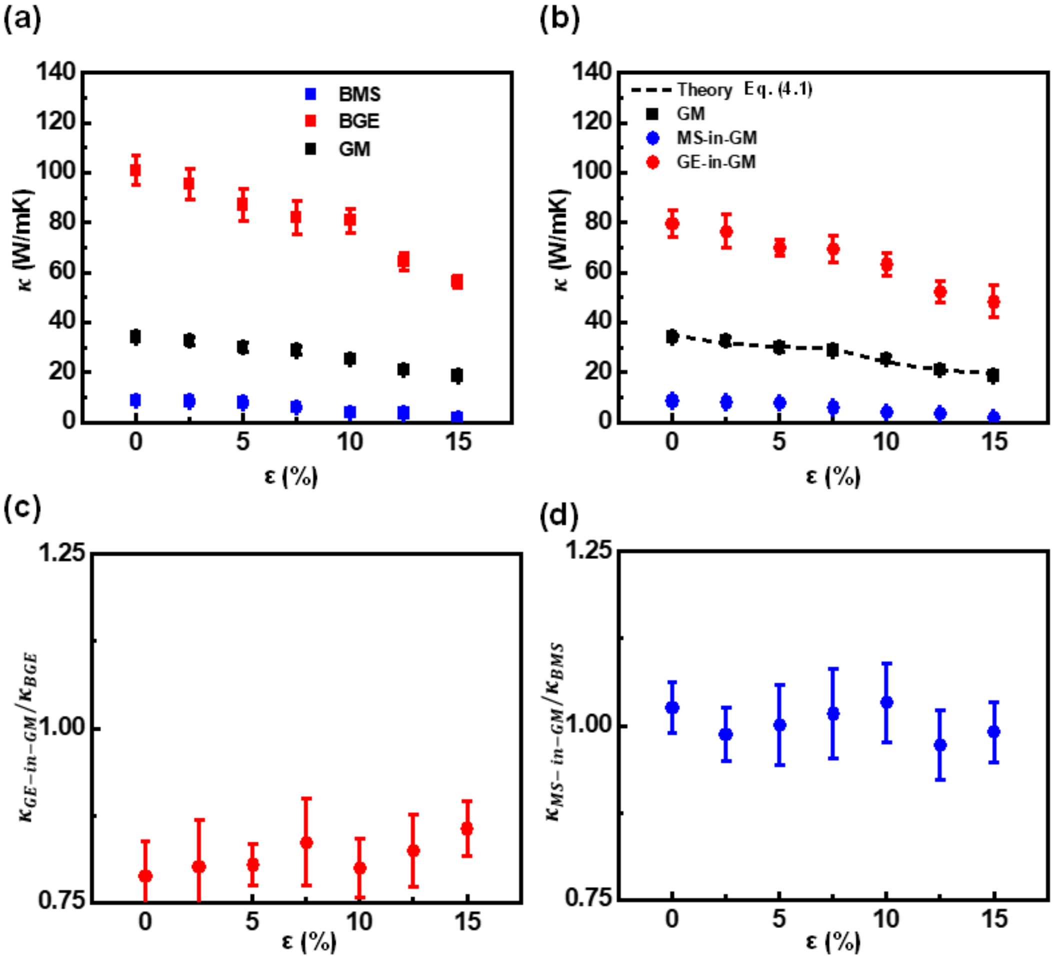

Figure 4.4. The thermal conductivity of the graphene-MoS_2 heterostructure. **(a)** The thermal conductivity of the graphene-MoS_2 (GM) heterostructure, bilayer graphene (BGE) and bilayer MoS_2 (BMS) as a function of the applied tensile strain ε. **(b)** The thermal conductivity of individual graphene (GE-in-GM) and MoS_2 (MS-in-GM) components in the heterostructure, and comparison of thermal conductivity under different tensile strains between the theoretical predictions **(c)** The ratio of thermal conductivity of graphene in the heterostructure to that in bilayer graphene in tension, $\kappa_{GE-in-GM}$. **(d)** The ratio of thermal conductivity of MoS_2 in the heterostructure to that in bilayer MoS_2 in tension, $\kappa_{MS-in-GM}$. The error bar arises from the small uncertainty of determining the temperature gradient by fitting the linear region of temperature profiles.

layer[150, 230]. t_H is the thickness of heterostructure, and $t_H = t_{GE} + t_{MS}150$. Taking t_{GE}=0.335 nm, and t_{MS}=0.609 nm[230], we can calculate k_H, as shown in Figure 4.4b (dash line), and they show good agreement with MD results that are extracted from graphene-MoS_2 heterostructure as an entire structure.

To clarify the effect of the lattice mismatch in heterostructure and the tensile strain on k_H, the thermal conductivity of individual graphene and MoS_2 layer in the heterostructrue is normalized by their corresponding bilayer structures, and is plotted in **Figure 4.4c** and **d**, respectively. For the graphene layer, $\kappa_{GE-in-GM}/\kappa_{BGE}$is 0.788 (< 1.0) at ε=0, indicating that $\kappa_{GE-in-GM}$ is reduced by the presence of MoS_2 layer that causes the out-of-plane displacement intrigued by the lattice mismatch (Figure 4.3b). With the increase of ε, $\kappa_{GE-in-GM}/\kappa_{BGE}$ increases, implying that the restriction on thermal transport by the lattice mismatch is weakened by the tensile strain. The alleviated effect agrees well with the decreased out-of-plane mismatch displacement under a tensile strain (Figure 4.3b). In contrast to an increased $\kappa_{GE-in-GM}/\kappa_{BGE}$ with the applied strain in graphene, $\kappa_{MS-in-GM}/\kappa_{BMS}$ remains to be near 1, demonstrating that the thermal transport across MoS_2 is barely affected by the lattice mismatch, independent of the applied tensile strain, which is also in good agreement with the very small out-of-plane and in-plane displacement in MoS_2 layer (Figure 4.3b and c).

4.2.4 Phonon Mechanisms of Bilayer Heterostructure Subjected to Tension

To further probe the atomic mechanism of heat conduction and the effect of tensile strain and mismatch-induced displacement in the graphene-MoS_2 heterostructure, the most popular phonon frequency spectrum $G(\omega)$ is investigated. **Figure 4.5a** shows the total phonon spectrum of graphene in graphene-MoS_2 heterostructure without and with tensile strain. Two main peaks are observed. One is located within high frequency range at around 53 THz, and is dominated by the in-plane phonon mode (**Figure 4.5b**), the other is located within low frequency range at about 17 THz, and is dominated by the out-of-plane phonon mode (**Figure 4.5c**). As the tensile strain increases, the high frequency mode shifts to a low one, which indicates a softened phonon transport and lattice anharmonicity[16, 238]. The low frequency mode remains without an obvious shift, suggesting the dominant role of in-plane phonon mode in the graphene layer. The shift of high frequency phonon model that leads to softening of phonon mode impedes phonon thermal transport and reduces thermal conductivity (Figure 4.4a). Different from spectrum in graphene, **Figure 4.5d** show that peaks of phonon spectrum in MoS_2 layer only occur at relatively low frequency. Further decoupling analysis of phonon spectrum (**Figure 4.5 e** and **f**) indicates that both in-plane and out-of-plane phonon spectra play a significant role in thermal transports in response to the applied tensile strain. This joint contribution is attributed to the trigonal atomistic structure of MoS_2 layer. Similar to the

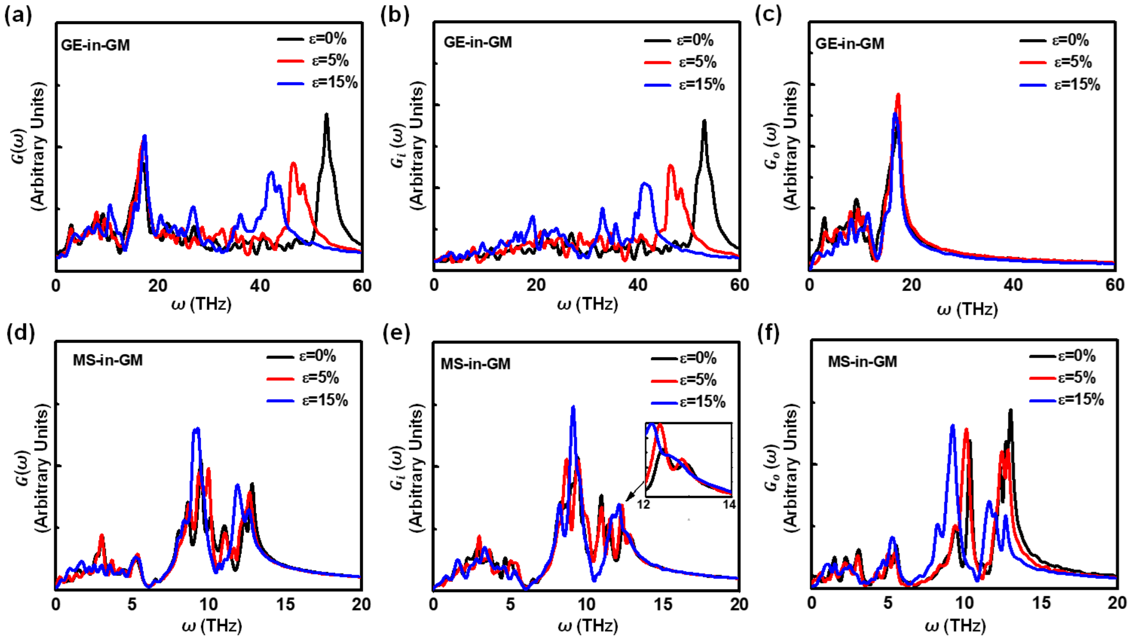

Figure 4.5. Total, in-plane and out-of-plane phonon spectra of (a)-(c) graphene and **(d)-(f)** MoS2 at tensile strain of 0, 5% and 15%

frequency shift phenomena observed in graphene, as the tensile strain increases, the peaks at such as 12 THz, 10 THz, and 9 THz shift to lower frequencies, indicating similar softening phenomena in MoS_2 layer with that of graphene on phonon modes and lattice anharmonicity, thus leading to a decrease of thermal conductivity in tension (Figure 4.4a and b).

To investigate the influence of the lattice mismatch on phonon activity, **Figure 4.6a** shows the in-plane phonon spectrum, $G_i\ (\omega)$, of graphene in graphene-MoS_2 heterostructure and bilayer graphene under no tensile strain. The comparison shows an obvious decrease in the peak of the phonon spectrum of graphene near high frequency modes in the heterostructure. The reduction is expected to result from the enhanced phonon scattering and impedance to

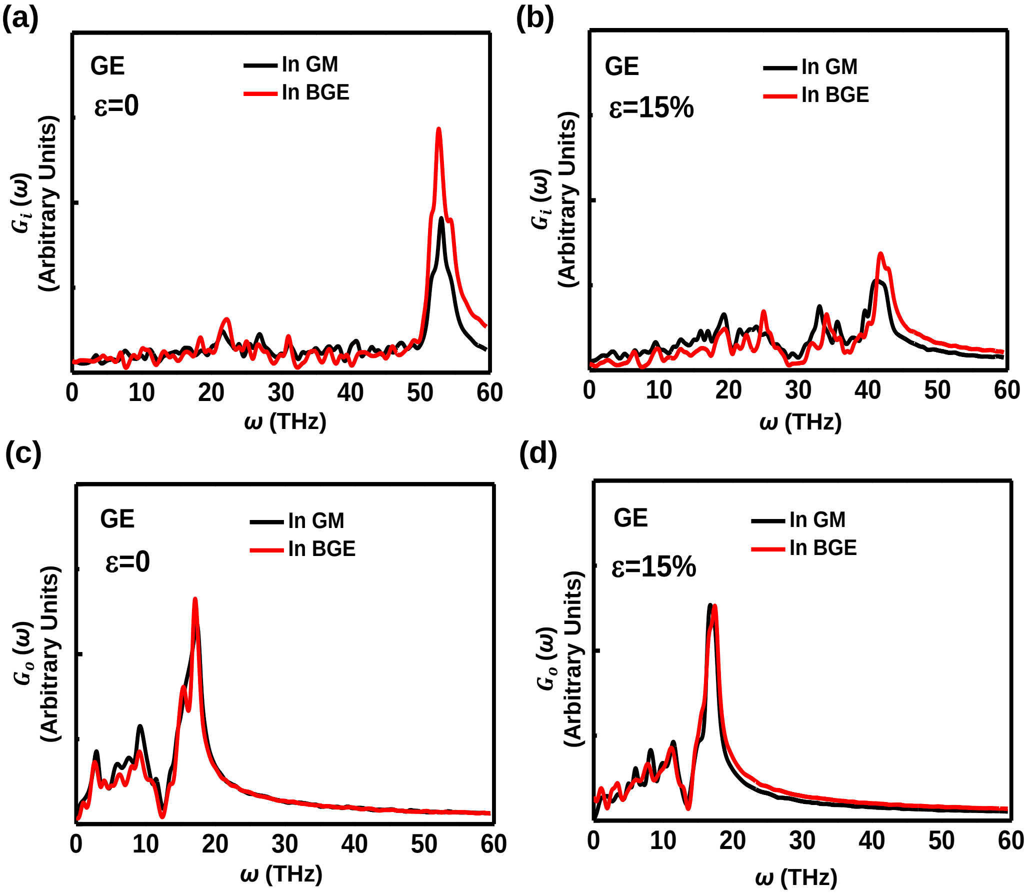

Figure 4.6. (**a**) and (**b**) Comparison of in-plane phonon spectrum $G_i\ (\omega)$ of graphene in heterostructure and in bilayer graphene at the tensile strain of 0 and 15%. (**c**) and (**d**) Comparison of out-of-plane phonon spectrum $G_o\ (\omega)$ of graphene in heterostructure and in bilayer graphene at the tensile strain of 0 and 15%.

phonon thermal transport. As the tensile strain increases to 15% as shown in **Figure 4.6b**, the peak difference of phonon spectra from graphene in heterostructure and bilayer graphene decreases, suggesting that the tensile strain mitigates the out-of-plane displacement and attenuates the effect of out-of-plane displacement on in-plane phonon activity. However, since the out-of-plane displacement does not change the mechanical confinement of atoms in the out-of-plane direction, the out-of-plane phonon activity is expected not to vary and the in-plane phonon spectrum at low frequency shows almost the same in both heterostructure and bilayer graphene, as shown in **Figure 4.6c and d,** consistent with independent in-plane phonon activity of out-of-plane deformation in graphene[161]. The high frequency phonons associated with out-

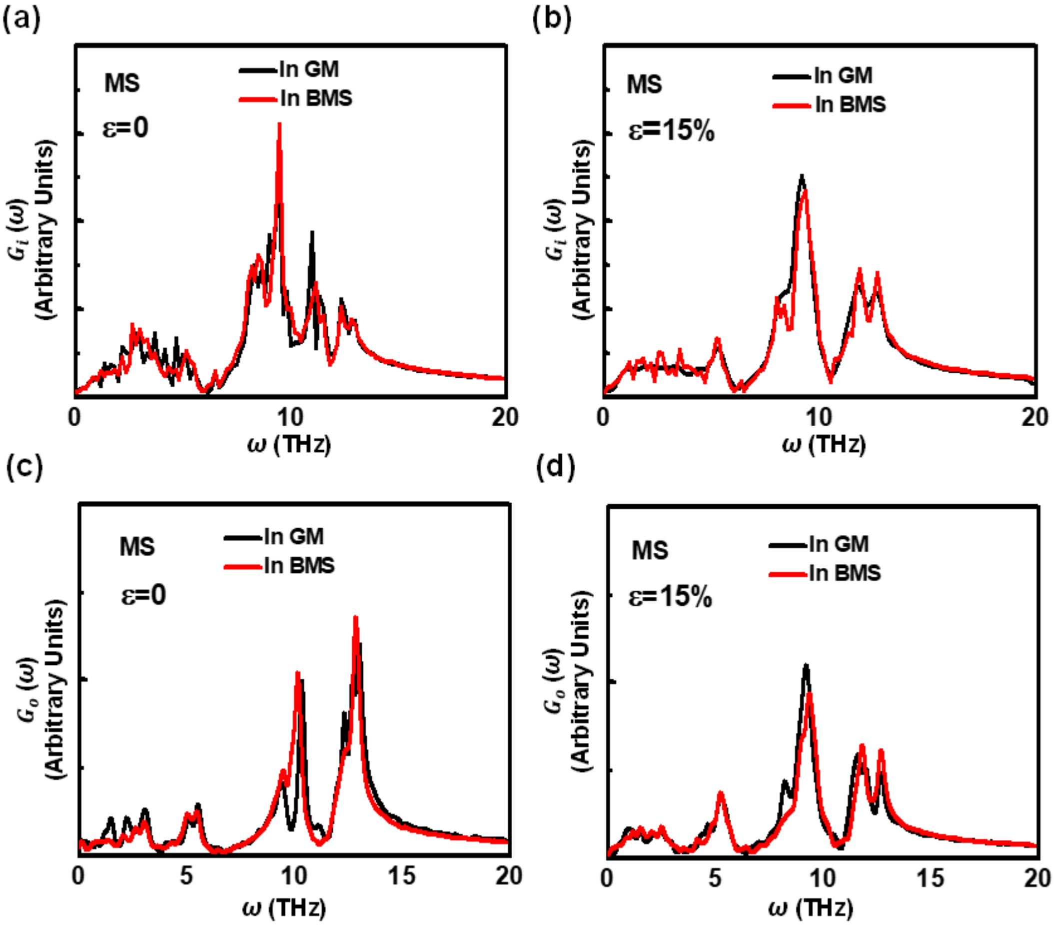

Figure 4.7. (**a**) and (**b**) Comparison of in-plane phonon spectrum $G_i\,(\omega)$ of MoS_2 in heterostructure and in bilayer MoS_2 at the tensile strain of 0 and 15%. (**c**) and (**d**) Comparison of out-of-plane phonon spectrum $G_o\,(\omega)$ of MoS_2 in heterostructure and in bilayer MoS_2 at the tensile strain of 0 and 15%.

of-plane deformation dominates thermal transport in graphene, and the effect of the lattice mismatch on thermal conductivity is reduced, consistent with Figure 4.4c. In contrast to the significant changes of phonon models for graphene in the bilayer graphene and heterostructure, **Figure 4.7a** shows that there is almost no difference between the in-plane phonon spectra of MoS_2 in heterostructure and bilayer MoS_2. Besides, as the tensile strain increases (**Figure 4.7b**), no change is found. The similar no difference is also found in the out-of-plane phonon spectra (**Figure 4.7 c and d**). The nearly same phonon activity indicates that the lattice mismatch does not affect the thermal conductivity of MoS_2, indicating good agreement with the approximate constant $\kappa_{MS-in-GM}/\kappa_{BMS}$ with the increase of the applied strain in Figure 4.4d.

4.2.5 Unified Theory and Verification

From the classical lattice thermal transport theory, we know $k = Cvl$, where C,v and l are the specific heat, phonon group velocity and phonon mean free path, respectively. Since no obvious softening or stiffing on modes with frequency shifts is observed in phonon spectra of graphene in heterostructure in comparison to that in the bilayer graphene (Figure 4.6 a and b), C and v are considered not to change[163, 239]. Based on Matthiessen rule on the phonon mean free path $l192$, for the phonon mean free path in bilayer graphene, l_{BGE}, we have $\frac{1}{l_{BGE}} = \frac{1}{l_{ph-ph}} + \frac{1}{l_{ph-b}}$, where $l_{ph-ph}$is the phonon-phonon scattering length and $l_{ph-b}$is the phonon-boundary scattering length and represents the phonon scattering at the interface[187]. For the graphene in heterostructure, the mean free path $l_{GE-in-GM}$ can be written as $\frac{1}{l_{GE-in-GM}} = \frac{1}{l_{BGE}} + \frac{1}{l_{mismatch}}$, where $l_{mismath}$ reflects the scattering length associated with the lattice mismatch. When a tensile strain is applied, it reduces the out-of-plane displacement and attenuates the limitation of phonon mean free path. $l_{mismatch}$ can be approximately estimated by $l_{mismatch} = \frac{1}{\lambda}(1+\epsilon)l_{BGE}$, and it corresponds to a longer length than l_{ph-b}, which agrees with the dominant role of phonon boundary scattering.[240, 241] When there is no lattice mismatch, λ=0, $l_{mismatch}$ is infinite and will not affect the phonon mean free path, and $l_{GE-in-GM}$ reduces to l_{BGE}. Hence we have $\kappa_{GE-in-GM} = \kappa_{BGE}\frac{1+\epsilon}{1+\epsilon+\lambda}$. Different from graphnene in heterostructure, since the lattice mismatch does not lead to an obvious change in the thermal conductivity of MoS$_2$, we have $l_{MS-in-GM} = l_{BMS}$, and thus $k_{MS-in-GM} = k_{BMS}$. Therefore, the thermal conductivity of graphene-MoS$_2$ heterostructure

$$\kappa_H = (\kappa_{BGE}\frac{1+\epsilon}{1+\epsilon+\lambda}t_{GE} + \kappa_{MS-in-GM}t_{MS})/t_H. \quad (4.2)$$

Using the thermal conductivity of bilayer graphene and MoS$_2$ structure without tension (Figure 2a), we can estimate κ_H under different ε. **Figure 4.8** shows that the theoretical estimations are well consistent with MD simulations.

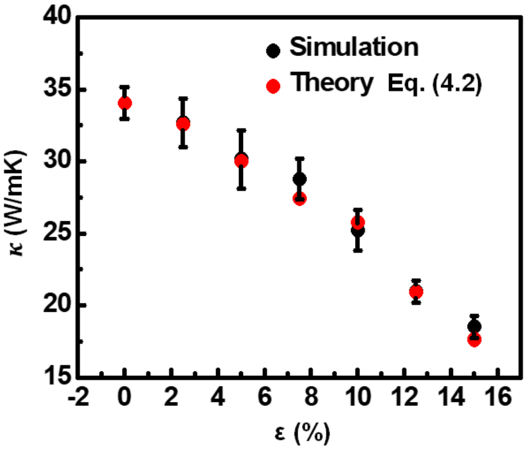

Figure 4.8. Comparison of theoretical predictions with simulations on the thermal conductivity in the graphene-MoS$_2$ heterostructure in tension. The error bar arises from the small uncertainty of determining the temperature gradient by fitting the linear region of temperature profiles.

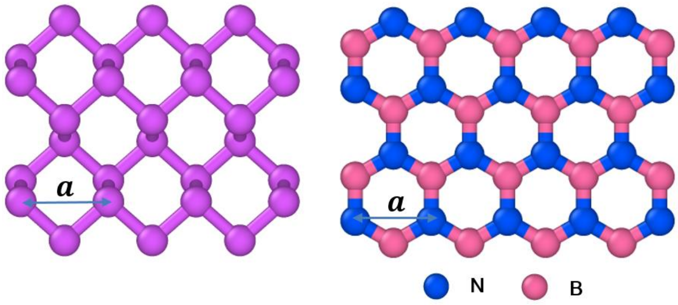

Figure 4.9. Molecular structures of 2D materials black phosphorus (BP) (left) and hexagonal boron nitride (hBN) (right). The first lattice constant of black phosphorus and hexagonal boron nitride is used to define the lattice mismatch when they are stacked with other 2D materials in heterostructures, and is 0.331 nm and 0.251 nm, respectively.

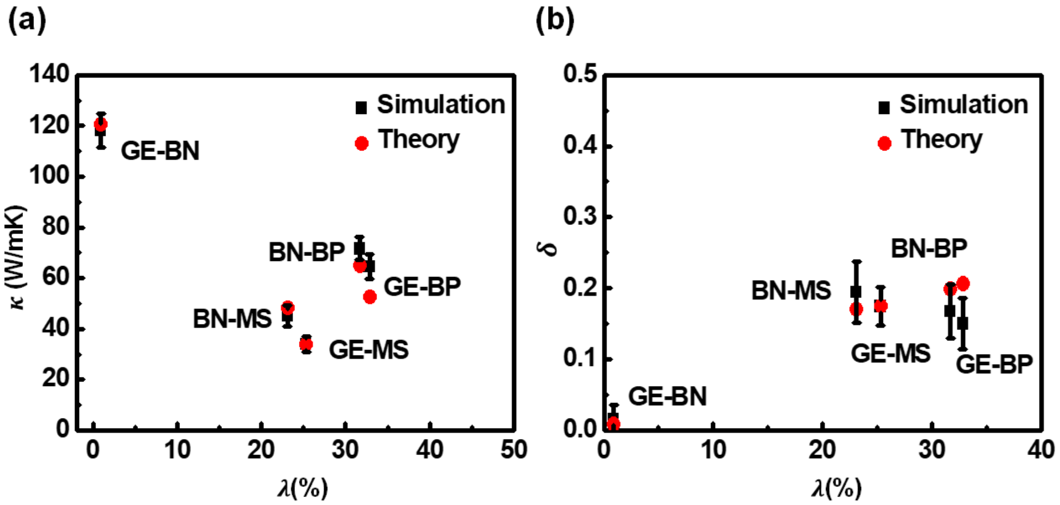

Figure 4.10. Verification of the lattice mismatch-integrated thermal theory on bilayer heterostructures. (a) Comparison of theoretical predictions and simulations on thermal conductivity of five bilayer heterostructures (graphene-hBN, hBN-black phosphorus (BP), hBN-MoS_2, graphene-MoS_2 and graphene-black phosphorus (BP) heterostructures) with different lattice mismatch parameters. **(b)** Variation of the ratio of thermal conductivity δ with the lattice mismatch.

To verify the robustness of this lattice mismatch-integrated thermal theory, we consider two more 2D materials: hexagonal boron nitride (hBN) and black phosphorous (BP) (**Figure 4.9**) and performed similar simulations on four other bilayer heterostructures (graphene-hBN, hBN-BP, hBN-MoS_2, and graphene-BP). The calculations of the lattice mismatch λ follow the same definition as graphene-MoS_2 heterostructure. **Figure 4.10a** shows the comparison of thermal conductivity from theoretical prediction and MD simulations. Good agreement is observed. To highlight the effect of the lattice mismatch, we define a ratio of thermal conductivity as $\delta = (\kappa_{Im} - \kappa_H)/\kappa_{Im}$, where $\kappa_{Im} = (\kappa_{B1}t_{B1} + \kappa_{B2}t_{B2})/(t_{B1}+t_{B2})$ is an imaginary thermal conductivity that is obtained by eliminating the lattice mismatch effect between two layers, and κ_{B1} and κ_{B2} are thermal conductivity values of bilayer structures of 2D materials 1 and 2 accordingly and t_{B1} and t_{B2} are the thickness of 2D materials 1 and 2 in their heterostructures. The variation of δ with λ is plotted in **Figure 4.10b**. With the increase of λ, δ increases, indicating that a higher lattice mismatch will lead to a stronger restriction to thermal transport of the heterostructures.

4.2.6 Summary

In summary, we have systematically investigated the thermal conductivity of the graphene-MoS2 bilayer heterostructure by performing extensive nonequilibrium molecular dynamics simulations and theoretical analysis, and probe the effect of the inherent lattice mismatch between layers. The simulations show clear evidence that the lattice mismatch has softened the phonon mode and leads to a reduction in the thermal conductivity of the graphene in the heterostructure due to the resultant out-of-plane displacement, while hardly changes the thermal conductivity of MoS2 due to a weak effect on the MoS2 layer. We also demonstrate that the effect of the lattice mismatch can be alleviated by applying an external tensile strain along the heat flow direction. The tensile strain decreases the lattice mismatch-induced out-of-plane deformation and causes shifts of frequency phonon from high to low modes, leading to a decreased thermal conductivity. We propose a unified theory to quantitatively describe the role of the lattice mismatch and mitigation of the tensile strain on the thermal conductivity in the graphene-MoS2 heterostructures, and the theoretical predictions agree well with simulations. The robustness of the proposed theory is further verified on more bilayer heterostructures consisting of such as graphene-hexagonal boron nitride, and hexagonal boron nitride-MoS2, graphene-black phosphorus, hexagonal boron nitride-black phosphorus. Our findings are of immediate applications to guide the design of heterostructures-enabled thermal devices that can be continuously regulated by an external mechanical strain and can also serve as a foundation for future explorations of the heterostructures with unprecedented functions by the lattice mismatch.

4.3 Interfacial Thermal Transport in Bilayer Graphene Kirigami Heterostructures Subjected to Tensile Loading

4.3.1 Computational Modeling and Method

Figure 4.11a depicts the computational modeling of heterostructures composed of bilayer graphene kirigami. The dimension was chosen as l=27.55 nm in length and w=30.67 nm in width after extensive study and confirmation on the size effect on mechanical properties[183, 242]. The interlayer distance was set as 0.34 nm initially by referring to the van der Waals thickness of graphene[243], and changed dynamically during simulations to reproduce the natural geometry of the interface. An in-plane external tensile strain ε was applied in the *x*-direction to both layers, and an out-of-plane heat flow q was transferred from the upper layer to the lower one along the *z*-direction. This simulation modeling is analogous with the optical-based setups in non-contact thermal measurement through thermoreflectance in experiments,[244] where the temperature gradient is generated across the van der Waals interface by optical sources. Two most popular structures with U and I cut shapes of graphene kirigami reported in experiments[124, 245] were employed, and their unit structures are shown in **Figure 4.11b**, where the length and

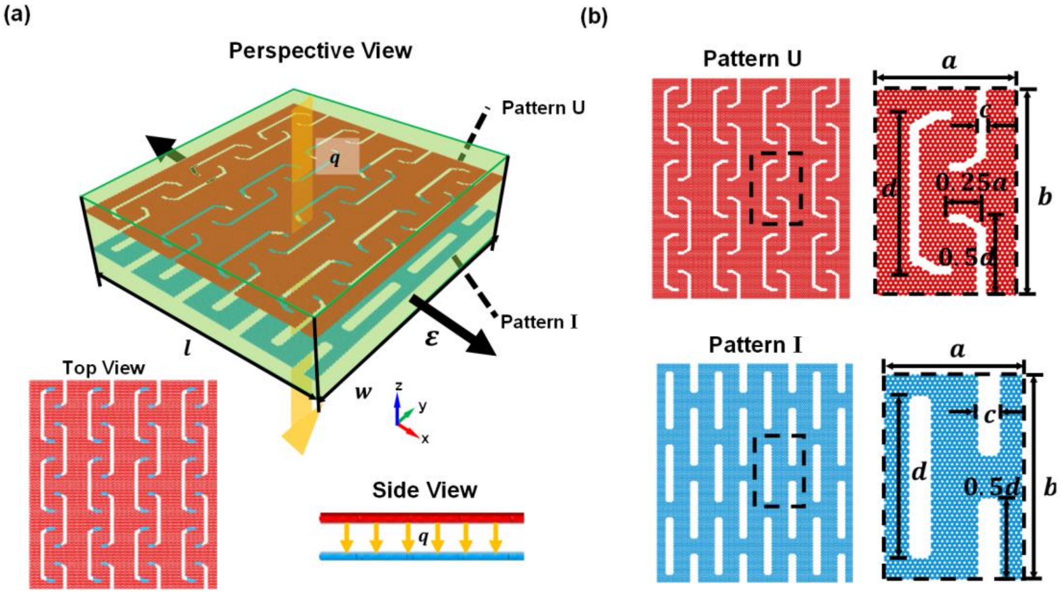

Figure 4.11. Modeling of van der Waals graphene kirigami heterostructure. (**a**) Atomistic modeling of graphene kirigami bilayer heterostructure (left) and individual kirigami layer components with U and I cut patterns (right). In the heterostructure, its dimension size is l=27.55 nm in length and w=30.67 nm in width. The external tensile strain ε is applied in the x-direction on both layers as marked in the black arrows, and the heat flow q is transferred from the upper layer to the lower layer along the z-direction as marked in the yellow arrow. (**b**) The individual kirigami layer unit. The length and width are a=6.89 nm and b=10.22 nm, respectively, the cut length is d=8.09 nm and the cut width c changes with cut patterns.

width of unit structures are a=6.89 nm and b=10.22 nm, respectively, and the dangling atoms of atoms at cuts were not functionalized so as to keep their natural mechanical modes as experiments.[124, 245]. Through the regulation to the cut width c meanwhile keeping the cut length d=8.09 nm,[183, 246, 247] six different kirigami derivatives (**Table 4.1**) were created and utilized to construct van der Waals kirigami bilayer heterostructures, denoted as "Up/Iq", "Up/Uq" or "Ip/Iq", where p and q reflect the variation of cut patterns in upper and lower kirigami layers respectively by changing the cut width c. In particular, when the heterostructure is composed of the same upper and lower layer-cut patterns, it is termed as homobilayers, and otherwise is termed as heterobilayers.

Table 4.1 Notation and Geometric Parameters of Kirigami Units. The length a, width b and cut length d of units are fixed as 6.89, 10.22 and 8.089 nm, respectively.

Notation	Cut Pattern (U or I)	Cut Width c (nm)	Porosity ϕ
U1	U	0.37	0.14
U2	U	0.62	0.21
U3	U	1.07	0.36
I1	I	0.98	0.26
I2	I	1.48	0.37
I3	I	1.97	0.48

To obtain the thermal conductance of bilayer graphene kirigami, the structure under the tension was relaxed in NVT at 300 K for another 1.0 ns to ensure the energy minimization and the arrival of physically stable structures[248, 249]. After that, the thermal relaxation method which mimics the pump-probe approach in experiments[248] is employed, described as follows. A temperature difference ΔT=200 K was first created by setting the temperature of the upper layer at 500 K with velocity rescaling and maintained for 50 ps with separate thermostats. And then, the ensemble that governed the whole system shifted to the micro-canonical (NVE) ensemble. As a consequence, ΔT decreased with an exponential manner as $\Delta T = \Delta T_{t=0}\exp(-t/\tau)$, where the time constant τ is determined through an exponential fitting approach. According to the lumped heat capacity model,[249] the thermal conductance G is calculated *via* $G = C_V/(A\tau)$, where the effective constant volume heat capacity of graphene kirigami bilayer system C_V can be evaluated as $C_V = C_{V,upper}C_{V,lower}/(C_{V,upper} + C_{V,lower})$. $C_{V,upper}$ and $C_{V,lower}$ are the heat capacity of two graphene kirigami layers (upper and lower layers), and each of them can be calculated by $C_{V,upper\ or\ lower} = 3N_{atom}k_b \int_0^{\infty} \frac{PS(\omega)\left(\frac{h\omega}{k_BT}\right)^2 \exp\left(\frac{h\omega}{k_BT}\right)}{\left[\left(\frac{h\omega}{k_BT}\right)-1\right]^2}$, where N_{atom} is the number of atoms in the corresponding layer, k_B is the Boltzmann constant, T is the temperature and can be represented by the final equilibrium temperature (~400 K). The vibrational spectrum $PS(\omega)$ can be obtained by conducting fast Fourier transform on velocity autocorrelation function *via* $PS(\omega) = \frac{1}{\sqrt{2\pi}}\int_0^{\infty} e^{i\omega t} < \sum_{j=1}^{N_{atom}} v_j(t) \cdot v_j(0) > d\omega$.

4.3.2 Mechanical Properties and Thermal Transparency in Bilayer Graphene Kirigami Heterostructures

Figure 4.12a shows the nominal stress-strain curves of heterostructures. For the homobilayers with both pristine graphene layers (denoted as "Pristine/Pristine"). The stress increases linearly with strain till reaching ~13.6% and is similar to that of monolayer graphene[250, 251]. In contrast, the stress of kirigami homobilayers with cut pattern U (*e.g.* U1/U1, U2/U2 and U3/U3 correspond to c=0.37, 0.62 and 1.07 nm, respectively) remains nearly zero until the tensile strain reaches approximately 10%, followed by a slow increase until the failure of structures. Besides, as the width of cut c increases, the failure strain is enhanced to ~60%. When the kirigami homobilayers is the cut pattern I (*e.g.* I1/I1, I2/I2 and I3/I3 correspond to

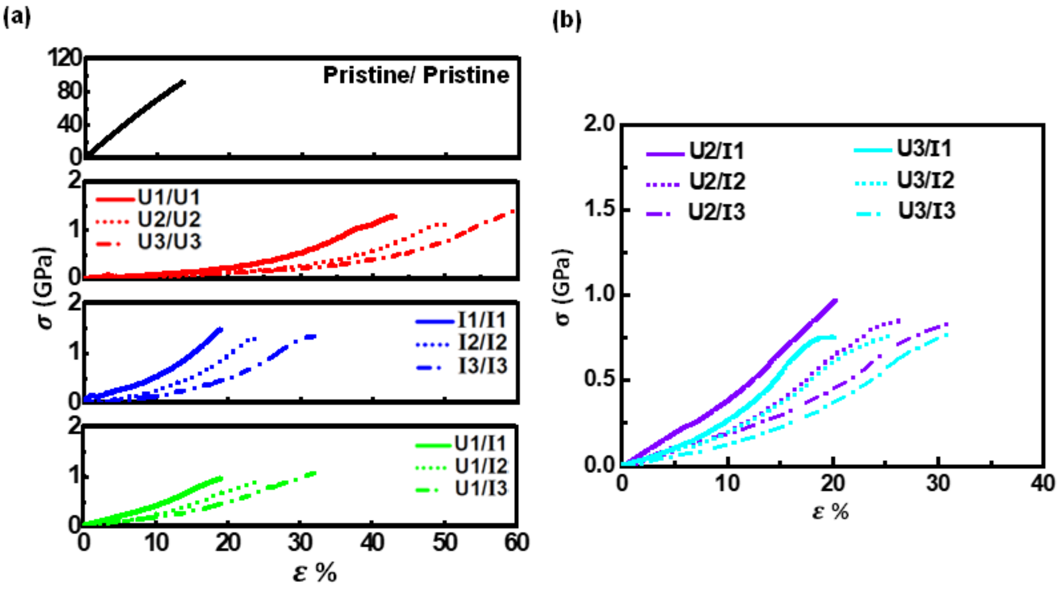

Figure 4.12. (a) and (b) Variations of nominal stress σ with tensile strain ε in graphene heterostructure, where homobilayers are composed of the same two pristine graphene, or kirigami layers U1, U2, U3, or I1, I2, I3, and heterobilayers are composed of one layer with cut pattern U (U1) and the other with cut pattern I (I1, I2 and I3).

c=0.98, 1.48 and 1.97 nm, respectively), similar variations of stress with strain is obtained, yet a lower failure strain in homobilayers with the cut pattern I due to a severer local stress concentration near cuts. When kirigami with pattern U and pattern I is mixed to assemble kirigami heterobilayers (*e.g.* U1/I1, U1/I2 and U1/I3), Figure 4.12a also plots their nominal stress-strain curves with variations of c. Given the same tensile strain, the overall nominal stress falls between its component kirigami layer, yet the failure strain depends on the smaller one, *i.e.*, kirigami layers with the pattern I in this example. Further simulations (**Figure 4.12b**) on heterobilayers with different combinations of cut sizes for both cut patterns were also performed and confirm these findings. In comparison with Pristine/Pristine homobilayers, both pattern U and pattern I enabled homobilayers and heterobilayers have much lower failure stress (~1 GPa), which can be negligible compared to the monolayer pristine graphene (~100 GPa). Generally, the cut expansion leads to a "bulk" motion of the graphene nanoribbons, and the deformation of inherent hexagonal lattices in graphene will be delayed.[243] As a consequence, an overall decreased stress and enhanced failure strain are observed in kirigami layers.

Figure 4.13a presents the variation of thermal conductance G of heterostructures as the applied external tensile strain. For the thermal conductance of homobilayers with the pristine graphene in the absence of tensile strain, the thermal conductance is 73.57 MW/Km^2, consistent with previous results.[252] Upon applying a tensile strain, G drops quickly, indicating a good correspondence with the immediate increase of stress in Figure 4.12. The reduction in G is expected to be led by the suppression of out-of-plane vibrations of carbon atoms when the in-plane carbon-carbon bonds are stretched by the strain. When the heterostructures are composed of graphene kirigami, because of a smaller lattice deformation and lower overall stress at the

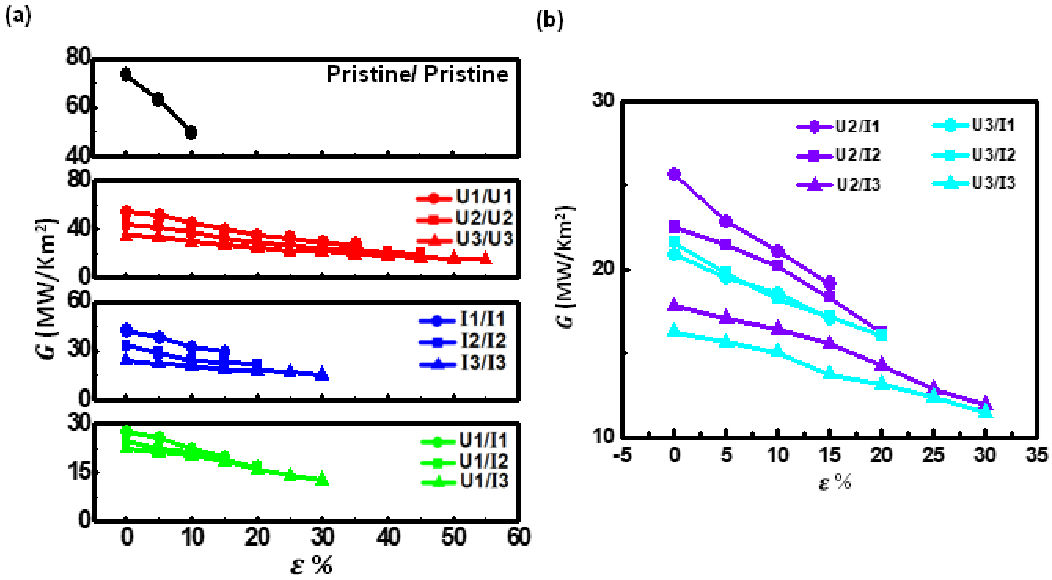

Figure 4.13. (a) and (b) Variations of thermal conductance G with tensile strain ε in graphene heterostructure.

same tensile strain in comparison with the pristine homobilayers, a smaller G with a slower decrease with strain is obtained for both homobilayers and heterobilayers considered in Figure 4.15. Similar results are also observed for further parameter studies in kirigami heterostructures in **Figure 4.13b**.

To quantitatively characterize the kirigami layer patterns and heterostructures, we define the porosity of the kirigami graphene layers as $\phi = A_{cut}/A$,[253] where A and A_{cut} are the planar area of graphene kirigami and cuts, respectively. A_{cut}=1- $\frac{A_{atom}N_{atom}}{A}$, where N_{atom} is the total number of carbon atoms in graphene kirigami, and A_{atom} is the planar area per carbon atom. Given the hexagonal lattice of graphene, $A_{atom} = \frac{3\sqrt{3}a_{graphene}^2}{4}$, and $a_{graphene}$(=0.246 nm) is the lattice parameter of graphene.[225] Table 4.1 gives ϕ for each graphene kirigami layer. Moreover, ϕ depends on the applied tensile strain ε. As the applied strain increases, the kirigami layers will deform along with the expansion of cuts, leading to a reduced number of density of atoms and hence a higher ϕ. Further, to correlate ϕ with the

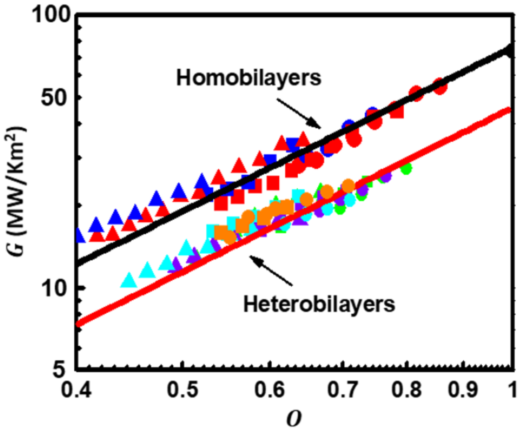

Figure 4.14. Generalized functions of thermal conductance G of kirigami heterostructure as thermal transparency $\boldsymbol{O}$. O=1 for bilayer pristine graphene, and O=$1-\phi$ and O=$\sqrt{(1-\phi_{upper})(1-\phi_{lower})}$ for homobilayers and heterobilayers, respectively. Homobilayers: U1/U1 (red circles), U2/U2 (red squares), U3/U3 (red triangles), I1/I1 (blue circles), I2/I2 (blue squares), I3/I3 (blue triangles); Heterobilayers: U1/I1 (green circles), U1/I2 (green squares), U1/I3 (green triangles), U2/I1 (cyan circles), U2/I2 (cyan squares), U2/I3 (cyan triangles), U3/I1 (purple circles), U3/I2 (purple squares), U3/I3 (purple triangles), U1/U3 (orange circles) and I1/I3 (orange squares).

thermal conductance across van der Waals interface, we define a thermal transparency factor O=$1-\phi$ for homobilayers, and O=$\sqrt{(1-\phi_{upper})(1-\phi_{lower})}$ for heterobilayers, where ϕ_{upper} and ϕ_{lower} represent the porosity of upper and lower kirigami layers in heterostructures, respectively. **Figure 4.14** presents the dependence of thermal conductance G on thermal transparency factor O. Linear variations for both homobilayers and heterobilayers are obtained in a log-log plot system. Besides, their slopes are the same. At the same O, compared to the homobilayers, the G of heterobilayers is lower due to a weaker atomic interaction per unit area.[166, 254] In addition, compared with a negligible lattice strain in graphene kirigami, the large mechanical strain leads to a significant suppression in vibration spectrum of pristine graphene (Section 2.2), and this generalized model of thermal transparency cannot describe the thermal conductance of pristine graphene-enabled heterostructures.

4.3.3 Density of Interactions and Distribution of Delocalized Phonon Energy

Figure 4.15a shows the vibration spectra $PS(\omega)$ at specific angular frequency ω of kirigami with the cut pattern I at different ϕ. With the increase of ϕ, both the high frequency peak at 55 THz and the low frequency peaks at 13 and 18 THz are slightly suppressed, indicating an amplified misfit of atom motions in the upper and lower kirigami layers because of the expanded cut size. A similar suppression is also observed in the spectra of kirigami with

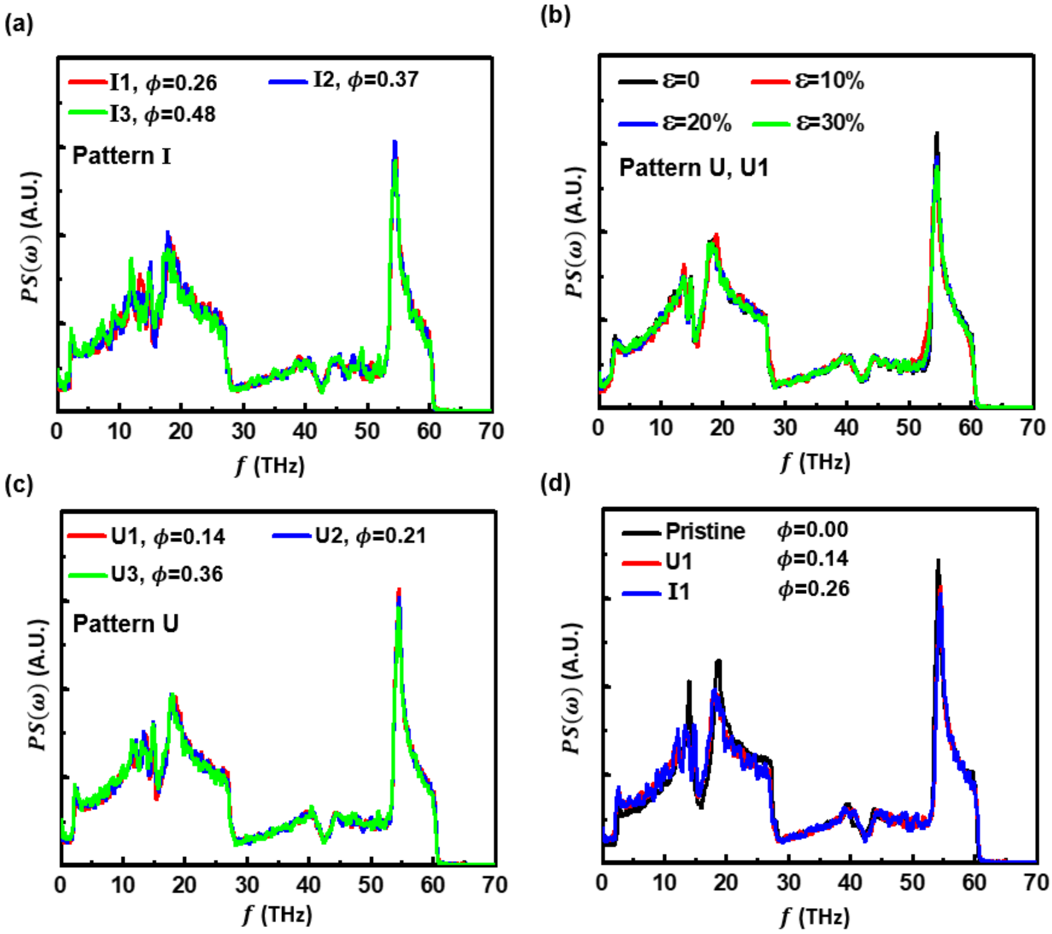

Figure 4.15. Vibrational spectra of graphene kirigami heterostructures. (**a**) Vibrational spectra $PS(\omega)$ of kirigami layer in the cut pattern I under different porosity ϕ. (**b**) Effect of tensile strain. As tensile strain ε increases, the cut expands, leading to lower thermal transparency. The high frequency peak at 55 THz and the low frequency peaks at 13 and 18 THz are slightly suppressed, indicating more inconsistent motion of atoms owing to the expanded cuts in the kirigami layer and a lower thermal conductance. The same conclusion can be drawn when increasing the size of cuts, as shown by (**c**). The same statement still holds true when making comparisons between different basic patterns, demonstrated by (**d**).

cut pattern U at different strain levels (**Figure 4.15b-d**). These decreased peaks in vibration spectra agree well with a lower thermal conductance at a higher tensile strain in Figure 4.13. Essentially, the thermal conductance across van der Waals junction is dominated by the effective atom pairs.[166, 254] Consider the theory of density of interactions, for each pair of atoms composed of atom i from one layer and atom j from the other layer with a separation distance of d_{ij}, the pairwise contribution to the thermal conductance across the van der Waals junction can be described as $n(d_{ij}) = \begin{cases} 1, & d_{ij} < r_m \\ 2(r_m/d_{ij})^6 - (r_m/d_{ij})^{12}, & r_m \le d_{ij} \le r_c \\ 0, & d_{ij} > r_c \end{cases}$ where r_m is the distance that corresponds the minimum potential and is equal to $2^{\frac{1}{6}}\sigma$, σ is the distance parameter in L-J potential employed in the simulations and r_c is the cut-off distance beyond which the pairwise contribution can be neglected and is set as 1 nm in all calculations.[166] When the distance d_{ij} between an atom pair is smaller than that of the minimum of potential, $d_{ij} < r_m$, the interaction of the atom pair is considered to be strong enough and will make a full contribution with n=1. On the other hand, the interaction is negligible when d_{ij} is larger than the cut-off distance r_c, $d_{ij} > r_c$, and the contribution n is

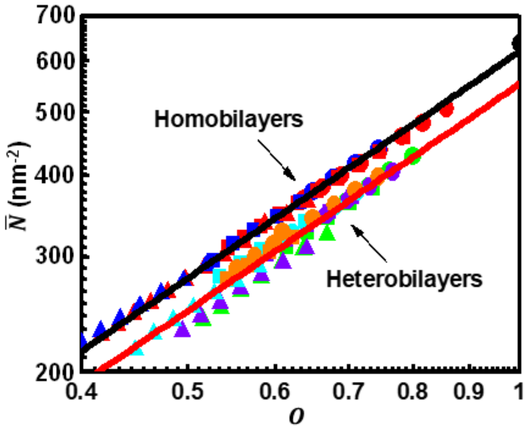

Figure 4.16 Unified relationship between density of interaction per unit area $\bar{N}$ and thermal transparency O. Same legends as those in Figure 4.14 are applied.

0. When $r_m \leq d_{ij} \leq r_c$, the contribution can be scaled by using the L-J potential.[166, 254] Further, the density of interaction is $\overline{N} = \frac{\sum_i \sum_j n(d_{ij})}{A}$. In our simulations, d_{ij} is not fixed and dynamically changes so as to take into account the local mechanical deformation of heterostructures. **Figure 4.16** shows a linear variation of $\overline{N}$ with O in a log-log coordinate system for both homobilayers and heterobilayers, which is consistent with the relationship between G and O in Figure 4.14. Besides, at the same thermal transparency O, the density of interaction $\overline{N}$ of heterobilayers is lower than that of homobilayers, indicating that the

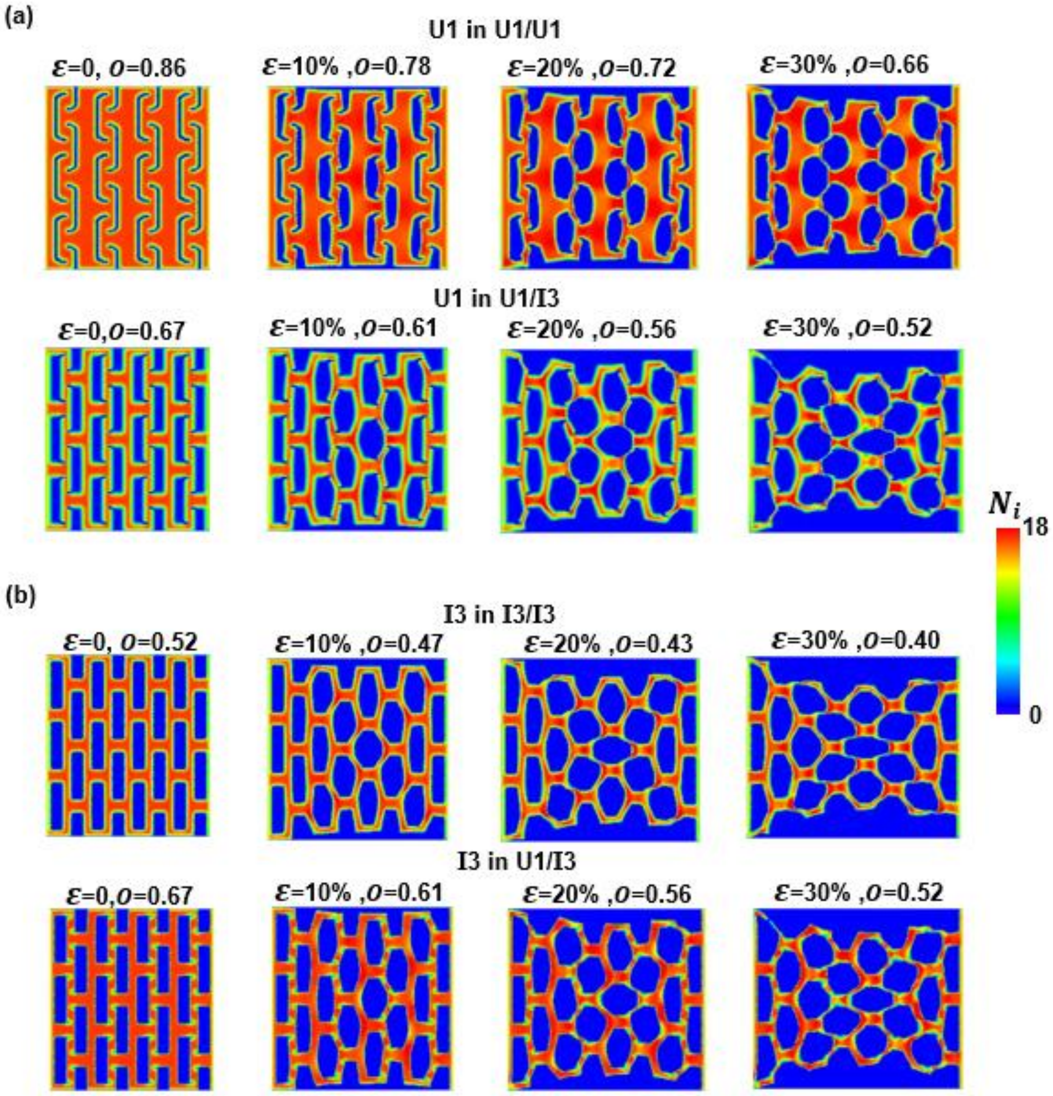

Figure 4.17 (**a**) Distribution of interaction N in kirigami layer with cut pattern U1 in homobilayers U1/U1 and heterobilayers U1/I3. (**b**) Distribution of interaction N in kirigami layer I3 in homobilayers I3/I3 and heterobilayers U1/I3.

geometric misfit between layers of heterobilayers reduces $\bar{N}$, and suppresses the thermal conductance G of heterobilayers.

As for the further understanding of this mechanism, we calculated the distribution of interaction N for each atom by $N = \sum_j n(d_{ij})$, where N=0 in the absence of atoms or interactions. Take kirigami U1 with ϕ=0.14 at $\varepsilon = 0$ as an example, **Figure 4.17a** shows the distribution of N of kirigami U1 in homobilayer U1/U1 and heterobilayer U1/I3. In homobilayer with O=0.86 at $\varepsilon = 0$, owing to the same geometry of both layers, N is approximately uniform except at the locations near cuts, where the interaction is weakened (in green) by the lack of atoms. As the tensile strain increases from 0 to 30%, the cuts are stretched with an evidence of expanded blue regions. Besides, N shows a slight decrease at the locations near cuts. This evidence indicates an overall decrease in the density of interactions at a larger ε and lower O, echoing well with results in Figures 4.16 and 4.14. In contrast, for heterobilayers U1/I3, where ϕ_{upper}=0.14, ϕ_{lower}=0.48 and O=0.67 at $\varepsilon = 0$. At $\varepsilon = 0$, compared to the same graphene kirigami in homobilayers, the reduction in density of interactions caused by the mismatch between the geometry of layers is evidenced by a larger area of blue and green regions, which indicates a weaker thermal contribution of the atoms and corresponds to the down shift of the linear variation of O with G. When ε increases, the cuts expand, leading to a lower density of interactions and thus a lower G, similar to that in homobilayers. The analysis on graphene kirigami with the cut pattern I (**Figure 4.17b**) further confirms this distribution of interaction. In addition, **Figure 4.18** plots the variation of G with $\bar{N}$ for homobilayers and heterobilayers. They feature the same linear behavior with that between G and O. In comparison with that of homobilayers, the downshift of G of

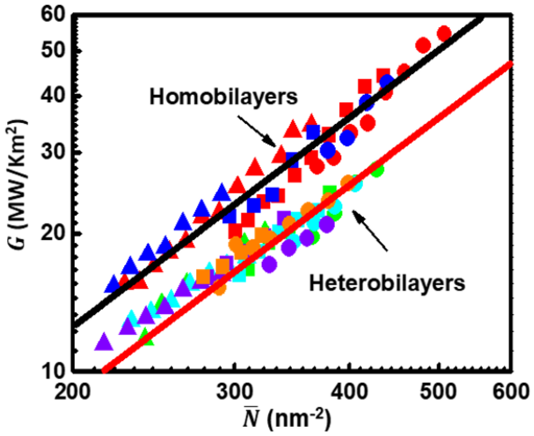

Figure 4.18. Thermal conductance G as functions of the density of interactions $\bar{N}$. While sharing the same slope with the linear function of homobilayers, the relationship between the thermal conductance and density of interactions is down shifted, which indicate the quality of each interaction is reduced in heterobilayers. Same legends as those in Figure 4.14 are applied.

heterobilayers indicates the critical role of the reduced density of interactions associated with geometry misfit between layer cut patterns.

Parallel to the density of pairwise interactions in heterobilayers, we further investigate the quality of pairwise interactions that could reflect the difference in the distribution of delocalized phonon modes. In order to identify delocalized phonon modes, the phonon participation ratio of each normal mode in the single unit of kirigami layers was calculated *via* $PPR = N_{atom} \sum_i \left(\sum_\beta \epsilon^*_{i\beta,\lambda} \epsilon_{i\beta,\lambda}\right)^2$, [228] where β is the polarization of interest (β= x, y or z), $\epsilon_{i\beta,\lambda}$ is the eigenvector component of the *i*th atom in the λth phonon mode in the β direction. The mode vectors and frequencies were obtained by performing lattice dynamics calculations, and in the calculations, GULP was employed by applying a periodic boundary and non-periodic boundary condition to the in-plane and out-of-plane direction, respectively.[227] In comparison with pristine graphene, **Figure 4.19a** shows that the presence of cuts leads to a reduction in PPR of normal modes in kirigami patterns U and I. As the porosity increases, PPR slightly decreases (**Figure 4.19b and c**). Because most of the phonon participation of modes in pristine

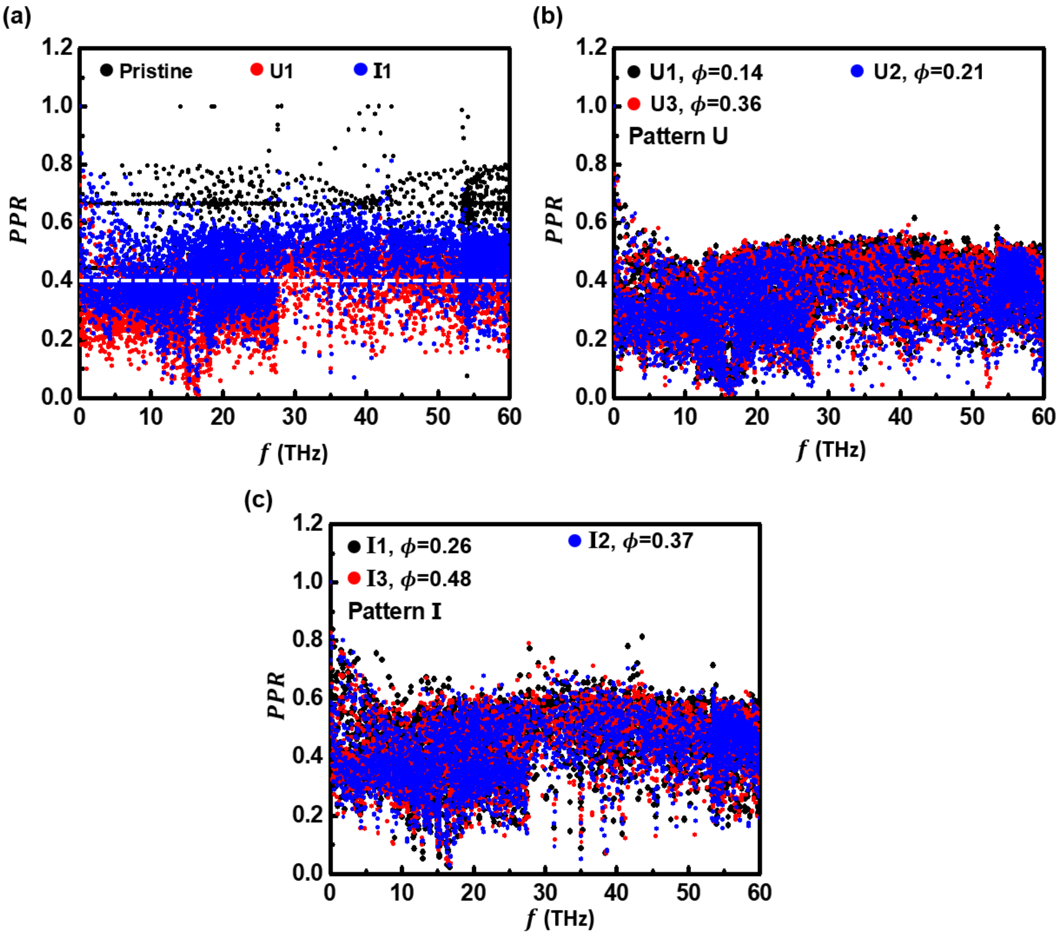

Figure 4.19. (**a**) Phonon participation ratio (PPR) of eigenmodes at different frequency f in pristine graphene, kirigami layers with cut patterns U1 and I1. As the sizes of cuts increase, the phonon participation ratio slightly reduces in pattern U (**b**) and pattern I (**c**).

graphene is larger than 0.4 (the white dash line), $PPR > 0.4$ is usually taken as the criterion for determining delocalized phonon modes.[214] Further, to calculate the distribution of delocalized phonon energy, at each location, the delocalized phonon energy can be represented by the accumulation in each atom, and is calculated *via* $E_{dp} = \sum_{\omega}\left(m+\frac{1}{2}\right)\hbar\omega De_i$, [228, 229] where $\hbar$ is the reduced Planck constant, ω is the angular frequency, m is the occupation number in the Bose-Einstein distribution, and D_i is the local vibrational density of states. More specifically, $De_i = \sum_{\lambda}\sum_{\beta}\epsilon^*_{i\beta,\lambda}\epsilon_{i\beta,\lambda}\delta(\omega-\omega_{\lambda})$, where δ denotes the Dirac delta function, and ω_{λ} is the angular frequency of the λ^{th} phonon mode. **Figure 4.20** presents the delocalized phonon energy at each atom (normalized by the largest one in the corresponding

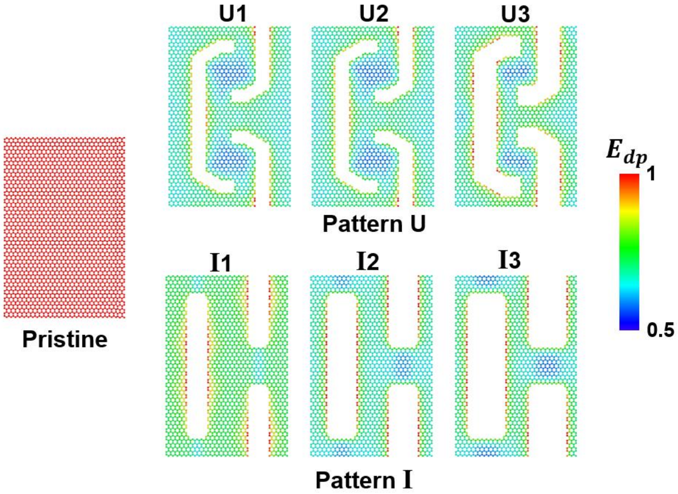

Figure 4.20. Distribution of normalized energy of delocalized phonon ($PPR > 0.4$) in the unit cell of pristine graphene, kirigami layer with cut patterns U1-3 and I1-3.

system) in the structures. For pristine graphene, E_{dp} is equal to 1 for each atom, and the existence of cuts in the single units of U1 (ϕ=0.14) and I1 (ϕ=0.26) reduces PPR of modes and leads to reduction in E_{dp} of atoms at different locations. The uneven distribution of E_{dp} remains in kirigami structures with different cut sizes. Next, we calculated the difference of delocalized phonon energy in the layers of heterobilayers *via* $D_i = |E_{dp,upper} - E_{dp,lower}|$ at each location, where $E_{dp,upper}$ and $E_{dp,lower}$ refer to the delocalized energy at the positions that share the same in-plane coordinates in upper and lower kirigami layers, respectively. At cuts, E_{dp} is considered to be 0 because of the absence of atoms. **Figure 4.21** shows the distribution of D_i in different heterostructures. For the homobilayers U1/U1 with ϕ=0.14 and O=0.86, the distribution of D_i is zero, confirming the absence of difference in distribution of delocalized phonon modes in homobilayers systems. Besides, such the difference holds in the heterobilayers, for example, heterobilayer composed of layers with different porosities but the same patterns (U1/U3 with ϕ_{upper}=0.14, ϕ_{lower}=0.36 and O=0.74), the same porosity but different patterns (U3/I2 with ϕ_{upper}=0.36, ϕ_{lower}=0.37 and O=0.64), or different porosity and patterns (U1/I1 ϕ_{upper}=0.14, ϕ_{lower}=0.26 and O=0.80). The different in-plane locations of delocalized modes in two layers will block the paths of heat transfer across the van der Waals junction and reduce the quality of pairwise contributions,[145, 214, 228] thus leading to an overestimation of G of heterobilayers by $\overline{N}$ and O (Figures 4.18 and 4.16). Similar phenomena are expected for heterostructures with mis-orientations or mis-alignments in geometry between two layers which are essentially equivalent to heterobilayers.

To quantitatively compare the degree of difference, an overall difference of coefficient is defined as $D = \frac{\sum D_i}{D_{max}}$, which is the summation of D_i over each location normalized by an imaginary scenario that includes a heterobilayer composed of pristine graphene and purely vacuum with the same size, D_{max}. **Figure 4.22** presents that the degree of the difference in the distribution of delocalized phonons is approximately the same for all heterobilayers, indicating an independence of O. As a result, although being depressed by such the difference, the G of

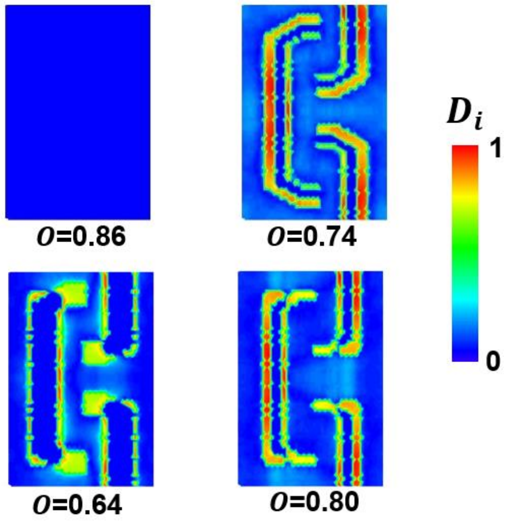

Figure 4.21. The difference in the distribution of delocalized phonon energy in four bilayer systems. Top left: homobilayers U1/U1 composed of layers with the same porosity $\phi = 0.14$ and the same cut pattern. Top right: heterobilayers U1/U3 composed of layers with different porosity $\phi_{upper} = 0.14$ and $\phi_{lower} = 0.36$ but the same cut pattern. Bottom left: heterobilayers U3/I2 composed of layers with different porosity $\phi_{upper} = 0.36$ and $\phi_{lower} = 0.37$ but the same cut pattern. Bottom right: homobilayers U1/I1 composed of layers with different porosity $\phi_{upper} = 0.14$ and $\phi_{lower} = 0.26$ but the same cut pattern.

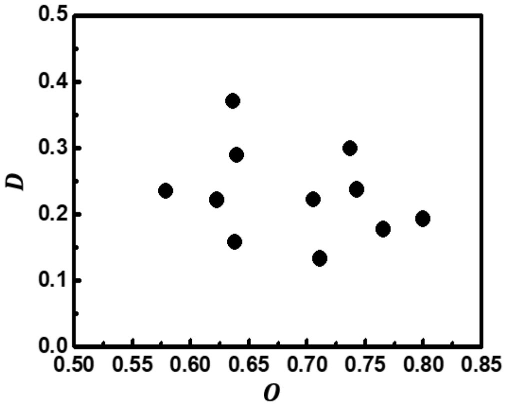

Figure 4.22. The overall difference of the coefficient D as a function of thermal transparency O

heterobilayers is still dominated by the density of interactions, which agrees with the down shift of linear G-O and G-$\overline{N}$ relationships as compared to those of homobilayers.

4.3.4 Tunable Thermal Transparency by Mechanical Strain

The elucidated correlation between thermal conductance G and thermal transparency O suggests that a higher failure strain and initial thermal transparency O_0 result in a larger maximum variance of thermal transport across the van der Waals interfaces under tensile strain (Figures 1d and S4). To characterize such the variance, we define $G_0/G_{\varepsilon_{max}}$ as the tuning ratio of thermal conductance and $\eta = \varepsilon_{max} O_0$ as the performance parameter, where G_0 and $G_{\varepsilon_{max}}$ are the thermal conductance without tensile strain and with the largest applied tensile strain ε_{max}, respectively. **Figure 4.23a** shows that the tuning ratio of all bilayer kirigami can be well predicted by η. With this tunable thermal transparency, a bilayer thermal unit that allows to manage heat flow is designed and illustrated in **Figure 4.23b**. Homobilayer U1/U1 (with O=0.86 in the absence of strain) is chosen as a demonstration example. **Figure 4.23c** presents the local density of interaction $\overline{N}_{local}$, where $\overline{N}_{local}$ is calculated by normalizing the atomic interaction of each atom N with the planar area A of the kirigami and $\overline{N}_{local} = \frac{N}{A}$. At $\varepsilon = 0$ and O=0.86, the heat flow could pass through the solid locations while being blocked

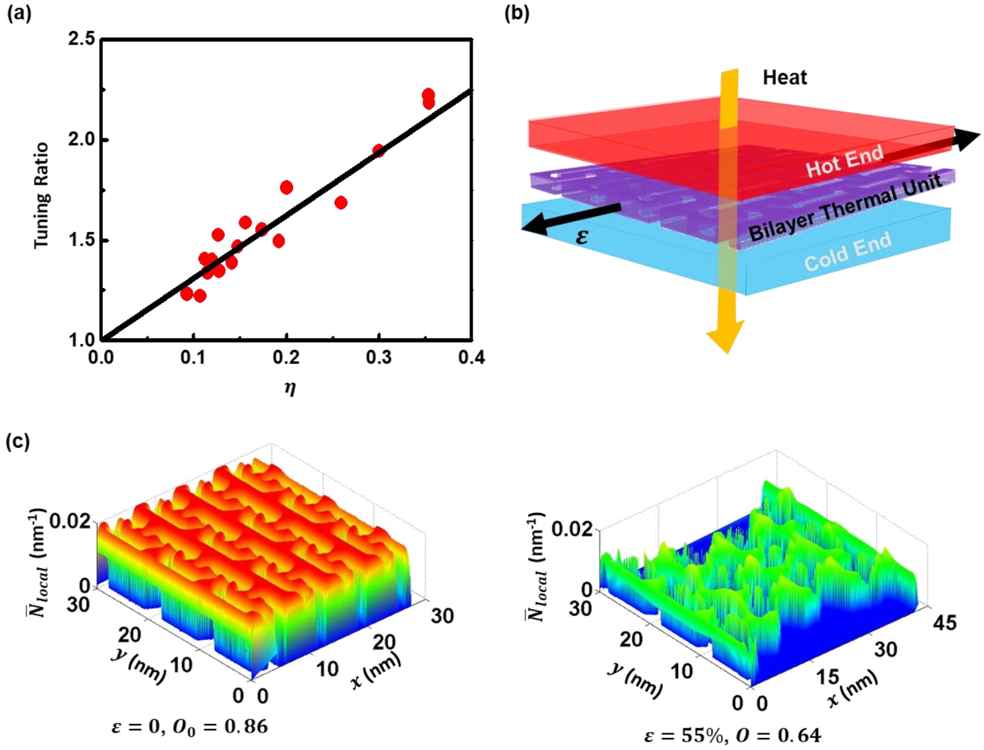

Figure 4.23. Application demonstration of strain-controlled heat flow in van der Waals graphene kirigami heterostructures. (**a**) The unified relationship between the tuning ratio of thermal conductance and performance governing coefficient η. (**b**) Schematic illustration of the bilayer van der Waals graphene kirigami system capable of being controlled in heat flow across the out-of-plane interface. (**c**) Distribution of local density of interaction $\bar{N}_{local}$ in the homobilayer at $\varepsilon = 0$ (left) and $\varepsilon = 55\%$ (right), indicating a clear change of thermal transparency O from initial O_0=0.86 (left) to O=0.64 (right).

at the cuts. When the tensile strain ε increases to 55%, the thermal transparency O decreases to 0.64, leading to a significant reduction of the local density of interaction and thus a decreased heat flow intensity, successfully demonstrating a feasibility of manipulating thermal flow across van der Waals interfaces by mechanical strain, where the regulatory capacity could be tuned by either magnitude of strain or layer structures.

4.3.5 Summary

We have presented a van der Waals bilayer heterostructure by assembling graphene kirigami that could sustain a large in-plane mechanical deformation through well-defined cut patterns, and systematically investigate its thermal conductance in response to an external mechanical tensile strain using non-equilibrium full-scale molecular dynamics simulations. Our results show that the thermal conductance monotonously decreases with tensile strain and can be quantitatively correlated with evolutions of cut patterns in each kirigami layer and their alignment misfit. Besides, the study reveals that the thermal transport across van der Waals interfaces in heterostructures is governed by the thermal transparency defined as the thermal flow intensity across the interface. A generalized model is proposed and confirmed by extensive simulations on the thermal conductance of graphene kirigami homobilayers and heterobilayers. Mechanical deformation, the density of interactions, and distribution of delocalized phonon energy in each kirigami layer are extracted and compared in detail to uncover the underpinned thermal transport mechanism and show that both density of interactions and distribution of delocalized phonon energy depress with the increase of mechanical deformation in kirigami layers and thermal transparency. These quantitative characterizations and understanding validate the mechanism of thermal transport across the van der Waals interfaces and more importantly agree well with the generalized model. Further, a thermal unit composed of graphene kirigami bilayer is constructed and demonstrates that its thermal flow in cross-plane direction can be continuously tuned by controlling mechanical strain and/or kirigami cut patterns, indicating a mechanically tunable capability of thermal transparency. It is expected that the mechanism of the proposed mechanically tunable thermal transparent in graphene kirigami structures could be applied to other heterostructures with cut patterns other than I and U shapes, functional groups or other 2D material components such as phosphorene and MoS_2 and could also be extended to relatively large dimensions close to experimental sizes. These findings are expected to facilitate the understanding of thermal transport across the van der Waals interfaces in heterostructures and provide a solution to thermal management, in particular, in response to mechanical strain. The concept of the state-of-the-art thermal transparency and its demonstrations will offer application guidance for the exploration of multifunctional devices by leveraging controllable thermal properties of heterostructures through strain engineering.

Chapter 5 1D-2D vdW Heterostructures as Pressure Sensors

5.1 Overview of the Chapter

In this chapter, we present a mixed-dimensional heterostructure by vertically stacking 1D and 2D materials through non-covalent vdW interactions and demonstrate that the thermal conductance can be generalized into a unified model by incorporating their mechanical properties and geometric features. Simulation analyses further reveal the strong dependence of thermal conductance on the location and magnitude of an external pressure loading applied to the local vdW heterojunctions. The underlying thermal transport mechanism is uncovered through the elucidation of the mechanical deformation, curvature morphology and density of atomic interactions at the heterojunctions. A proof-of-conceptual design of such a heterostructure-enabled pressure sensor is explored by utilizing the unique response of thermal transport to mechanical deformation at heterojunctions. These designs and models are expected to broaden the applications and functionalities of mixed-dimensional heterostructures and will also offer an alternative strategy to leverage thermal transport mechanisms in the design of high-performance vdW heterostructure-enabled sensors.

5.2 Computational Modeling and Methodology

Figure 5.1 depicts the computational modeling of the 1D-2D heterostructure with 2D materials -graphene sandwiched by two 1D carbon nanotubes (CNTs). The dimension of 2D layers is taken as l_{2D}=14.51 nm in length and w=14.77 nm in width while the number of the inserted layer can be variable; the length of both CNTs are the same and taken as l_{CNT}=19.70 nm, whereas their diameters d will vary from 0.678 to 3.254 nm. To generate the temperature gradient across the 2D layers, the hot and cold reservoirs are set up at two CNTs, guiding the heat flow across top and down heterojunctions between CNT and graphene in the z-direction.

All MD simulations were performed with LAMMPS.[177] In the computational modeling of 1D-2D heterostructures, the carbon interactions in CNTs and graphene layers were modeled by AIREBO potential[178]. The atomic interaction in boron nitride, black phosphorus and molybdenum disulfide were described by Tersoff,[207] Stillinger-Weber[255] and REBO[256] potentials, respectively. The non-bonded van der Waals interactions were modeled by Lennard-Jones (LJ) potential[257, 258] . The cutoff distance in LJ potential was taken as r_c=1 nm and is widely used in the studies of thermal transport.[166, 248, 259] A non-periodic boundary condition was applied in all directions. The boundary atoms in *x*-direction of the lower CNT were fixed in all directions to prevent its random motion, and the boundary atoms in the *x*-direction of 2D layers and the upper CNT were fixed in *x* and *y*-directions but free in the z-direction to

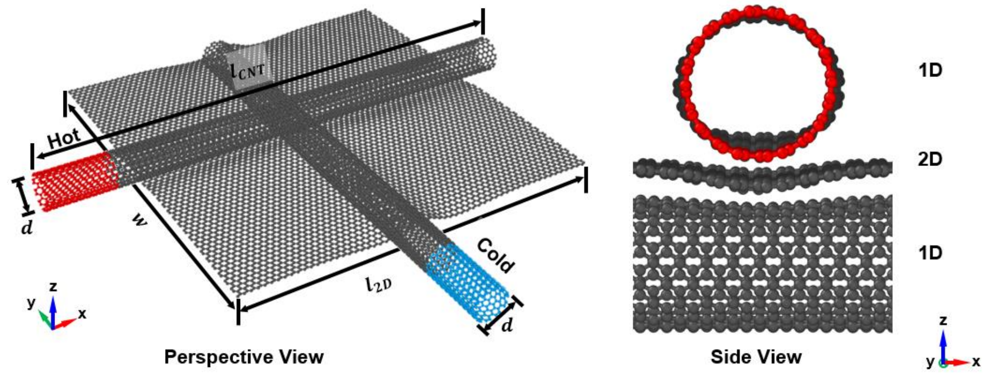

Figure 5.1. Computational model of 1D-2D van der Waals (vdW) heterostructures Molecular modeling of the 1D-2D heterostructure with a monolayer 2D materials (left: perspective view; right: side view). The 2D layer is sandwiched between the same two orthotropic 1D carbon nanotubes (CNTs), forming a 1D-2D heterostructure through non-covalent vdW interactions. Hot and cold reservoirs are assigned to the two ends of upper and lower nanotubes, generating a heat flow across the heterojunctions.

reproduce the natural and stable geometry of the van der Waals junctions. These boundary settings also help reach stable heterojunctions during simulations and no drifting or shifting is observed. The time step was set as 0.5 fs.

The heterostructures were first relaxed in the canonical (NVT) ensemble for 1 ns with a system temperature of 300 K controlled by Nosé-Hoover thermostat. To measure the thermal conductance, the atoms within 3 nm from the end of upper and lower CNTs were selected as hot and cold reservoirs, respectively. In micro-canonical (NVE) ensemble, at each time step, a constant amount of kinetic energy was added to/subtracted from the atoms in hot/cold reservoirs to introduce a constant heat flow of 10-60 nW for different systems from top to bottom of the heterostructures in the z-direction. After 0.5 ns, the temperature of each part of the system reached a stable state and became time independent. As a consequence, a temperature difference of ~100 K between hot end and cold end were created. This temperature difference is considered to minimize both non-linear effect and statistical uncertainties,[260] and has been applied to investigate thermal transport across different junctions in computations.[261, 262] Afterwards, the temperature data in next 2 ns were taken to calculate the thermal conductance via $G = \frac{J}{\bar{T}_{up} - \bar{T}_{lo}}$, where J is the heat flow, and $\bar{T}_{up}$ and $\bar{T}_{lo}$ are the average temperature of the upper and lower CNTs, respectively.

To introduce external pressure to the local heterojunction, an external yet equal force in the negative z-direction was applied to each atom in the region of upper CNT, marked in the schematics. The projection of the region in the x-y plane is in a square shape with the side length equal to the diameter of the upper CNT d_{up}. Once the heterostructures arrive at the new equilibrium subjected to the local pressure, the temperature difference will be created through the upper and lower CNTs to study the effect of pressure on thermal conductance.

5.3 Generalized Model of Thermal Conductance

Due to the curvature difference of 1D CNTs and 2D graphene and orientation setup of these two CNTs, a slight local deformation in the 2D graphene at the heterojunction is observed at the equilibrium. Generally, this local mechanical deformation depends on the bending stiffness of CNTs and 2D materials.[263] A smaller bending stiffness of 2D layers or a larger bending stiffness of CNTs will lead to a stronger atomic interaction in the heterojunction and thus a larger deformation in 2D materials. **Figure 5.2a** shows the thermal conductance G of the heterostructures as a function of the relative bending stiffness B_{CNT}/B_{2D}, where B_{CNT} and B_{2D} are the bending stiffness of CNTs and 2D layers, respectively. A higher B_{CNT}/B_{2D} will lead to a larger deformation of 2D layer at heterojunctions, and results in a higher G. This enhanced G holds true for various materials including monolayer graphene, hBN, BP, MoS_2

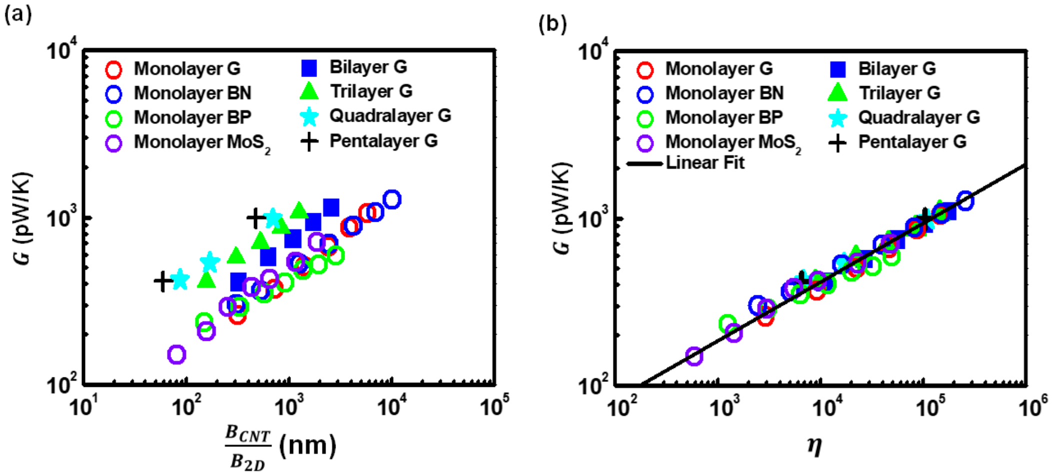

Figure 5.2. Thermal conductance of 1D-2D vdW heterostructures (a) Thermal conductance of heterostructures G as a function of relative bending stiffness between 1D and 2D materials B_{CNT}/B_{2D} for monolayer and multiple layer 2D materials. G: graphene, hBN: hexagonal boron nitride, BP: black phosphorus (BP), and MoS_2: molybdenum disulfide. **(b)** Thermal conductance of heterostructures G as a function of the proposed dimensionless coefficient η ($=\frac{B_{CNT}}{B_{2D}} \cdot \frac{d}{a_{2D}} \cdot \frac{1}{l} \cdot N^2$)

and multilayer graphene, suggesting that the out-of-plane local deformation promote the thermal transport across the heterojunctions associated with vdW interaction. We should note that the bending stiffness of multilayer graphene B_{2D} cannot be calculated by multiplying the layer number with the bending stiffness of monolayer due to the sliding between each layer, and is obtained separately from the square-power law confirmed in experiments.[264] Besides, the correlation between G and B_{CNT}/B_{2D} for all monolayer 2D materials follow the same linear behavior in the log-log coordinate system, but will change when multiple-layer 2D materials are employed.

In essence, the thermal transport based on the vdW interactions in heterostructures with multiple layers will rely on the number of pairwise atomic interactions near the heterojunctions.[12, 262, 265, 266] Therefore, in addition to the mechanical deformation, the thermal conductance of heterostructures will also change with the lattice structures of 2D materials, the layer number of 2D materials and the spatial distance between CNT and 2D layers. To consider all these factors, we here define a dimensionless coefficient η, $\eta = \frac{B_{CNT}}{B_{2D}} \cdot \frac{d}{a_{2D}} \cdot \frac{1}{l} \cdot N^2$, where d is the diameter of CNTs and a_{2D} is the lattice constant of 2D layers.[230, 267, 268] d/a_{2D} reflects the atomistic alignment between CNTs and 2D materials, and a larger d/a_{2D} will lead to a stronger atomic interaction. l is the effective distance of atomic interactions between the CNT and the center of the 2D layers and can be estimated as $l = 0.5(\sigma_{CC} + t)$, where σ_{CC} and t are the vdW thickness of CNTs [192] and 2D layers,[230, 269-271] respectively. N is the layer number of 2D materials, and the 2nd order reflects powered atomistic interactions in both upper and lower junctions. **Tables 5.1 and 5.2** in the supporting material summarize these parameters from literature. **Figure 5.2b** presents the thermal conductance G of heterostructures for all employed monolayer 2D materials (i.e. graphene, hBN, BP, MoS_2) and multiple-layered graphene. The variation of G with η for all these materials and layers can be featured as a unified linear function in the log-log coordination system. The unified thermal transport behavior of 1D-2D heterostructures indicates a one-to-one correspondence between G and η.

Table 5.1. Summary of the parameters of CNTs used in the calculations of η

Chirality	**(5,5)**	**(6,6)**	**(8,8)**	**(10,10)**	**(12,12)**
d **(nm)**	0.678	0.814	1.085	1.356	1.627
B_{CNT} **(eVnm)**[263]	263.91	456.70	1081.56	2111.25	3646.90
Chirality	**(14,14)**	**(16,16)**	**(18,18)**	**(20,20)**	**(24,24)**
d **(nm)**	1.898	2.17	2.441	2.712	3.254
B_{CNT} **(eVnm)**[263]	5789.62	8652.48	12315.87	16890.04	29175.23

Table 5.2. Summary of the parameters of 2D materials used in the calculations of η

2D layer	**Graphene**	**Boron Nitride (hBN)**	**Black Phosphorus* (BP)**	**MoS_2**
a_{2D} **(nm)**	0.249[230]	0.251[267]	0.331[268]	0.312[230]
B_{2D} **(eV)**	1.5[272]	0.86[54]	4.8 (A), 8.0 (Z)[55]	13.4[56]
t **(nm)**	0.34[269]	0.334[271]	0.555[270]	0.609[230]
2D layer	**Bilayer Graphene**	**Trilayer Graphene**	**Quadralayer Graphene**	**Pentalayer Graphene**
a_{2D} **(nm)**	0.249	0.249	0.249	0.249
B_{2D} **(eV)**	3.35[264]	6.92[264]	12.50[264]	18.10[264]
t **(nm)**	0.68	1.02	1.36	1.70

* For black phosphorus (BP), the average of B_{2D} from zigzag and armchair directions is used and a_{2D} is taken as its first lattice constant.

5.4 Gaussian Curvature in 2D Layers

The out-of-plane mechanical deformation of 2D materials at the heterojunctions mainly results from the curvature difference of 1D CNT and 2D materials and also is associated with the small bending stiffness of 2D materials in comparison with CNTs. This local mechanical deformation will allow conformal atomic interactions between CNTs and 2D materials. As a consequence, the effective "contact" interactive region between CNTs and 2D materials increases, leading to stronger atomic interactions and thus enhancing the thermal conductance. Mechanically, this local deformation and geometric feature near the heterojunctions can be indicated by the non-zero absolute value of Gaussian curvature in 2D layers. For heterostructure systems with different CNT diameters, 2D layer materials and 2D layer numbers, **Figure 5.3** shows comparisons of their out-of-plane deformation (d_o) and the absolute value of spatial Gaussian curvature distribution of 2D layers (|g|). For the monolayer 2D materials in heterostructures, the lager CNT diameter or lower bending stiffness of 2D materials leads to a larger absolute Gaussian curvature, being consistent with a higher thermal conductance in Figure 5.2b. By contrast, for multiple layered 2D materials in heterostructures, a larger layer number of 2D materials results in smaller mechanical deformation because of larger overall bending stiffness. The local maximum $|g|$ at the heterojunction decreases to approximately zero as the number of layer increases to five but leads to larger G than that

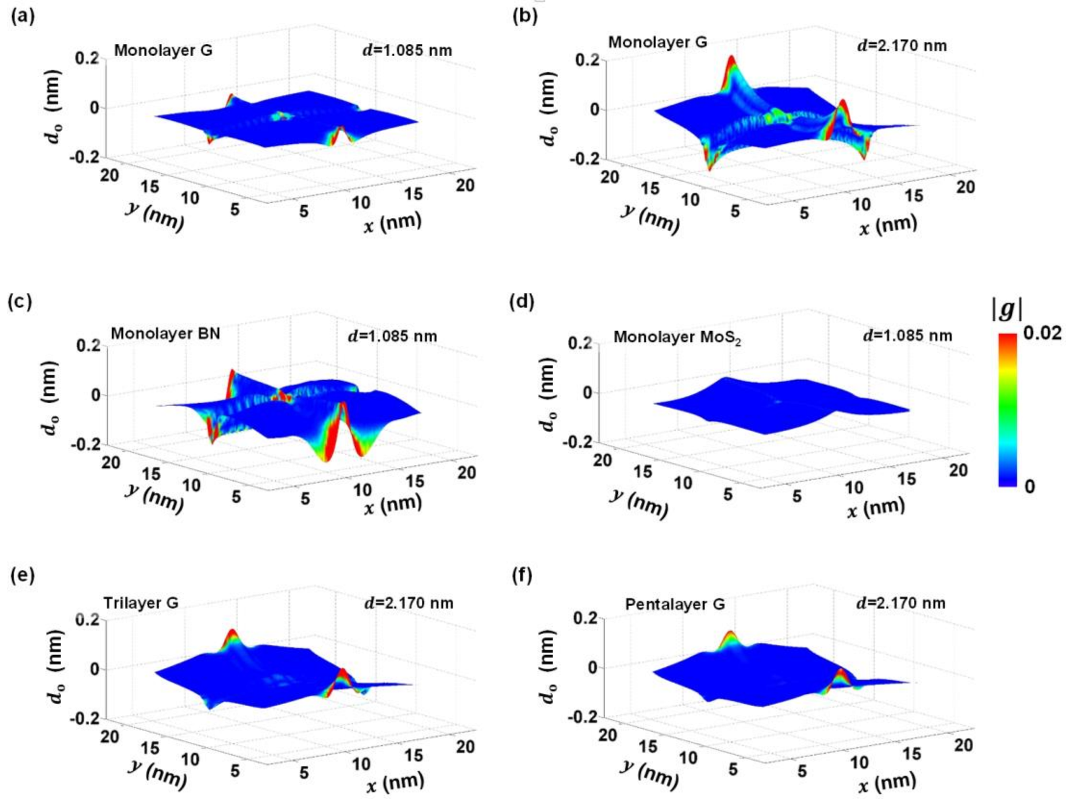

Figure 5.3. Out-of-plane mechanical deformation (d_o) and Gaussian curvature (g) distribution in 2D layers in heterostructures. (**a**) Monolayer graphene (G) with CNTs of 1.085 nm in diameter. (**b**) Monolayer graphene (G) with CNTs of 2.170 nm in diameter. (**c**) Monolayer boron nitride (BN) with CNTs of 1.085 nm in diameter. (**d**) Monolayer molybdenum disulfide (MoS_2) with CNTs of 1.085 nm in diameter. (**e**) Trilayer graphene (G) with CNTs of 2.170 nm in diameter. (**f**) Pentalayer graphene (G) with CNTs of 2.170 nm in diameter.

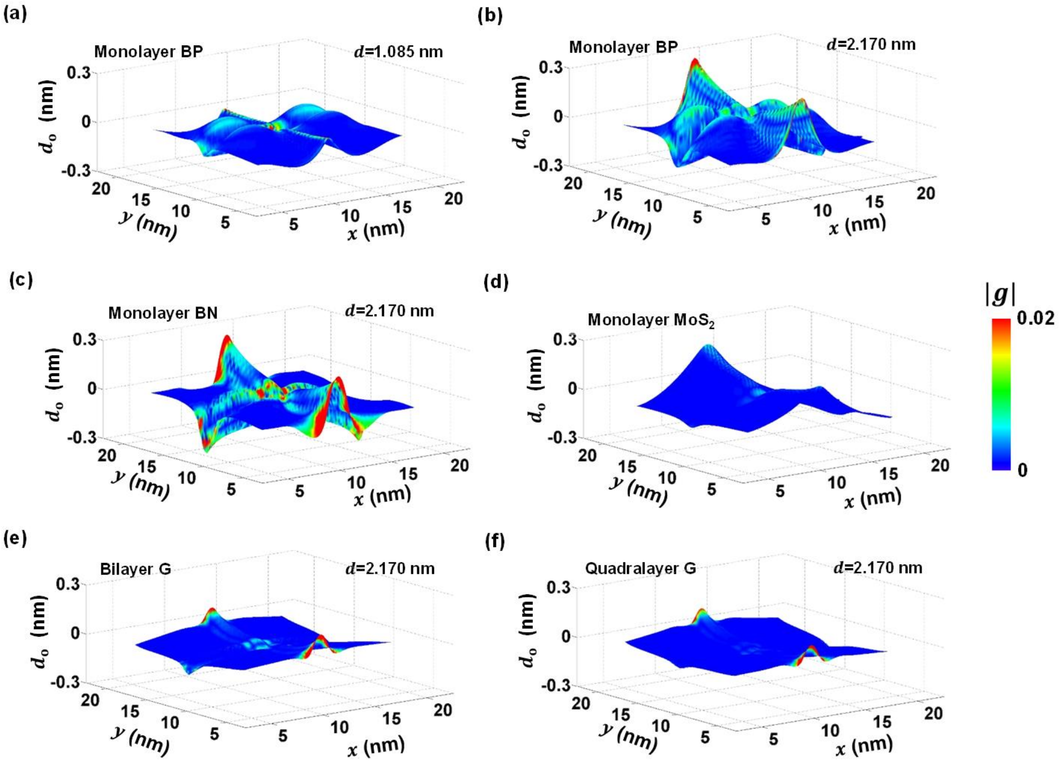

Figure 5.4. Out-of-plane mechanical deformation (d_o) and Gaussian curvature (g) distribution in 2D layers in heterostructures. 2D monolayer black phosphorus (BP) in heterostructures with CNT in diameter of (**a**) 1.085 nm and (**b**) 2.170 nm. 2D monolayer (**c**) hexagonal boron nitride (hBN) and (**d**) molybdenum disulfide (MoS_2) in heterostructures. The diameter of CNT is 2.170 nm. (**e**) bilayer graphene and (**f**) quadralayer graphene in heterostructures. The diameter of CNT is 2.170 nm.

expected in Figure 5.4b because of the absence of material and geometric features in B_{CNT}/B_{2D}. For the layer number of 2D materials (N>1), the out-of-plane deformation and Gaussian curvature $|g|$ in profiles were obtained by averaging the out-of-plane deformation in each layer at each location in the x-y-plane. The calculations on 2D material BP, effects of CNT diameter and layer numbers have further confirmed these results, as given in **Figure 5.4a-f**. The higher Gaussian curvature $|g|$ at both edges and heterojunction enhances the atomic interactions and promotes the thermal transport, which agrees with an enhanced thermal conductance in Figure 5.2.

5.5 Density of Atomic Interactions

The thermal transport across the vdW heterojunction is essentially contributed by each atom pair via vdW atomic interactions, and the theory of atomic interaction density can be employed to probe the underlying mechanism. The effective pairwise contribution n of atom

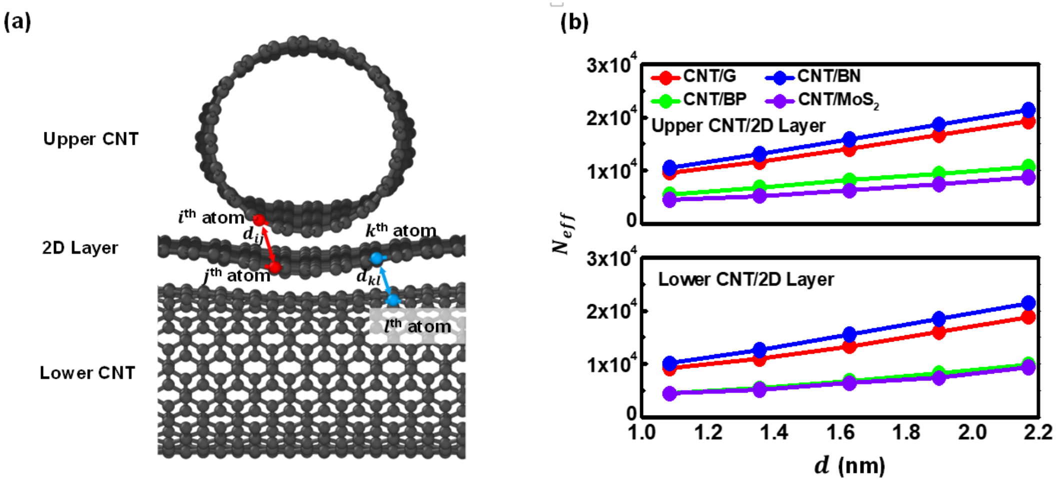

Figure 5.5. (**a**) Schematic illustration of atom pairs at two heterojunctions in 1D-2D heterostructure. i, j, k and l illustrate the atomic positions in the upper CNT, 2D layer, and lower CNT at the heterojunctions, respectively and form two atom pairs (i, j) and (k, *l*), and d_{ij} and d_{kl} are the equilibrium distance of atoms for the atom pairs (i, j) and (k, *l*). (**b**) The effective contribution of the cumulated pairwise interactions N_{eff} at upper and lower interfaces in heterostructures as a function of CNT diameter d.

pairs, which comprise of the i^{th} atom in the upper CNT and the j^{th} atom in the 2D layer at upper interface and the k^{th} atom in the 2D layer and the l^{th} atom in the lower CNT at lower interface, separated by the distance of d_{ij} and d_{kl}, respectively (**Figure 5.5a**), can be defined via Lennard-Jones potential as[166]

$$n(d_{\mathrm{ij}}) = \begin{cases} 1, & d_{ij} < r_m \\ 2\left(r_m/d_{ij}\right)^6 - \left(r_m/d_{ij}\right)^{12}, & r_m \le d_{ij} \le r_c \\ 0, & d_{ij} > r_c \end{cases}$$

and

$$n(d_{\mathrm{kl}}) = \begin{cases} 1, & d_{kl} < r_m \\ 2(r_m/d_{kl})^6 - (r_m/d_{kl})^{12}, & r_m \le d_{kl} \le r_c \\ 0, & d_{kl} > r_c \end{cases},$$

where r_{m} is the separation distance that corresponds to the minimum of the potential and is equal to $2^{\frac{1}{6}}\sigma$, σ is the distance parameter in L-J potential and r_c is the cut-off distance beyond which the pairwise contribution can be neglected and is set as 1 nm in all calculations.[166, 259] When the distance r between an atom pair is smaller than that corresponding to the minimum of potential, the interaction of the atom pair is considered to be strong enough and the contribution *n* is equal to 1. On the other hand, the interaction is considered to be negligible when r is larger than the cut-off distance r_c, and the contribution *n* is hence 0. When r falls in between the cut-off distance and the distance at the minimum potential, the contribution can be scaled by using the LJ potential that was employed to describe the non-bonded vdW interactions among atoms in the modeling. Accordingly, the effective contribution of cumulated pairwise interactions at upper and lower interfaces can be obtained via $N_{eff\_up} = \sum_i \sum_j n(d_{ij})$ and $N_{eff\_low} = \sum_k \sum_l n(d_{kl})$, respectively, which represent the effective number of atom pairs formed by atoms in both CNTs and 2D layers.[166] **Figure 5.5b** shows N_{eff_up} and N_{eff_low} as functions of CNT diameter for different 2D monolayers. We should note that both N_{eff_up} and N_{eff_low} are obtained from the deformed heterojunctions and thus can capture all features of mechanical, material and geometric behaviors. Both N_{eff_up} and N_{eff_low} at two interfaces increase with the increase of the diameter of CNTs, which indicates that larger CNTs introduce larger deformation at heterojunctions and more atom interactions, corresponding with the findings in mechanical deformation in Figure 5.3a and b. Besides, given the same diameter of CNTs, 2D monolayer materials with a lower bending stiffness in the heterostructure show a higher N_{eff_up} and N_{eff_low}, indicating that a smaller bending stiffness of 2D layers will lead to a stronger interaction, which also agrees well with a larger absolute Gaussian curvature in Figure 5.4a, c and d.

To incorporate N_{eff_up} and N_{eff_low} with the thermal conductance of heterostructures, we further define a contribution factor via $C = N_{eff\_up} N_{eff\_low}$, which reflects the total number of atomic routes for heat transfer across these top and bottom heterojunctions. For heterostructures consisting of multilayer 2D materials, our calculations show the temperature gradient between individual 2D layers is negligible, and the calculation of C can be obtained

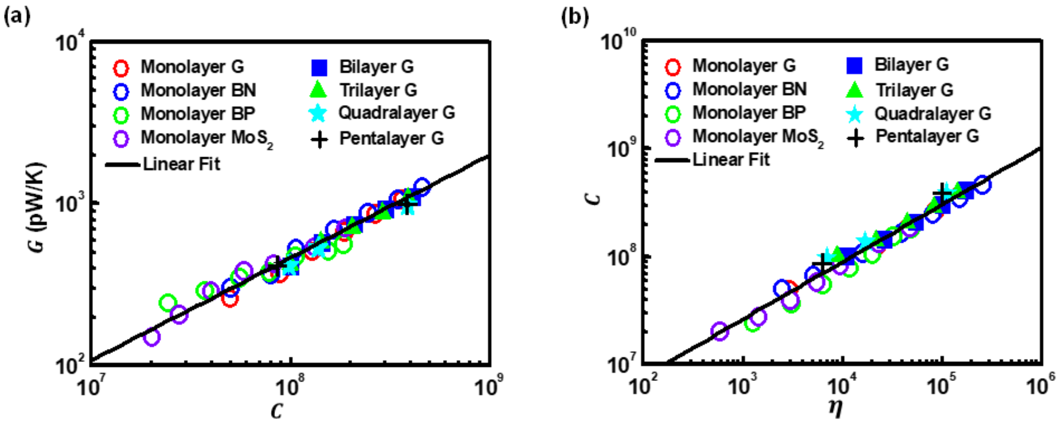

Figure 5.6. (**a**) Thermal conductance G as a function of the pairwise interaction contribution factor of atoms at heterojunctions C ($= N_{eff\_up}N_{eff\_low}$). (**b**) Contribution factor C as a function of the proposed dimensionless coefficient η

by considering the total thickness of 2D layer. **Figure 5.6a** shows a relationship between C and G and a linear variation is observed in the log-log plot, independent of 2D materials and layer numbers. **Figure 5.6b** further shows the variation of η with C in a log-log plot, and a linear relationship is also observed. Both one-to-one correspondences of C with G and η with C suggest that η should reflect the atomic interactions at the heterojunctions and can be used to determine the thermal conductance, which is consistent with Figure 5.2b. In comparison with bonded atomic interaction, phonon frequencies of the intralayer phonon modes in vdW heterostructures are usually an order of magnitude higher than those of interlayer modes, suppressing the contribution of intralayer phonon modes to thermal conductance across vdW heterojunction[82, 273, 274]. Instead, the contribution factor C that represents the density of atomic interactions can be utilized for understanding the underlying thermal transport mechanism in vdW heterostructures.

5.6 1D-2D Heterostructures for Pressure Sensors

Given the thermal conductance of 1D-2D heterostructure is closely associated with the density of atomic interactions at vdW heterojunctions, the heterojunctions are expected to be highly sensitive to an external loading such as pressure that could lead to mechanical deformation of 2D materials and density of atomic interactions, holding great potential for designing a pressure sensor. **Figure 5.7a** illustrates the 1D CNTs-2D graphene heterostructure subjected to a pressure P on the heterojunction. We should mention that, although the pressure is on the order of GPa because of the nanosized contact area (~1 nm^2) at heterojunctions between CNTs and 2D materials, the applied force was on the order of ~1 nN, which is comparable to experiments.[275, 276] As P increases, an approximately linear monotonous

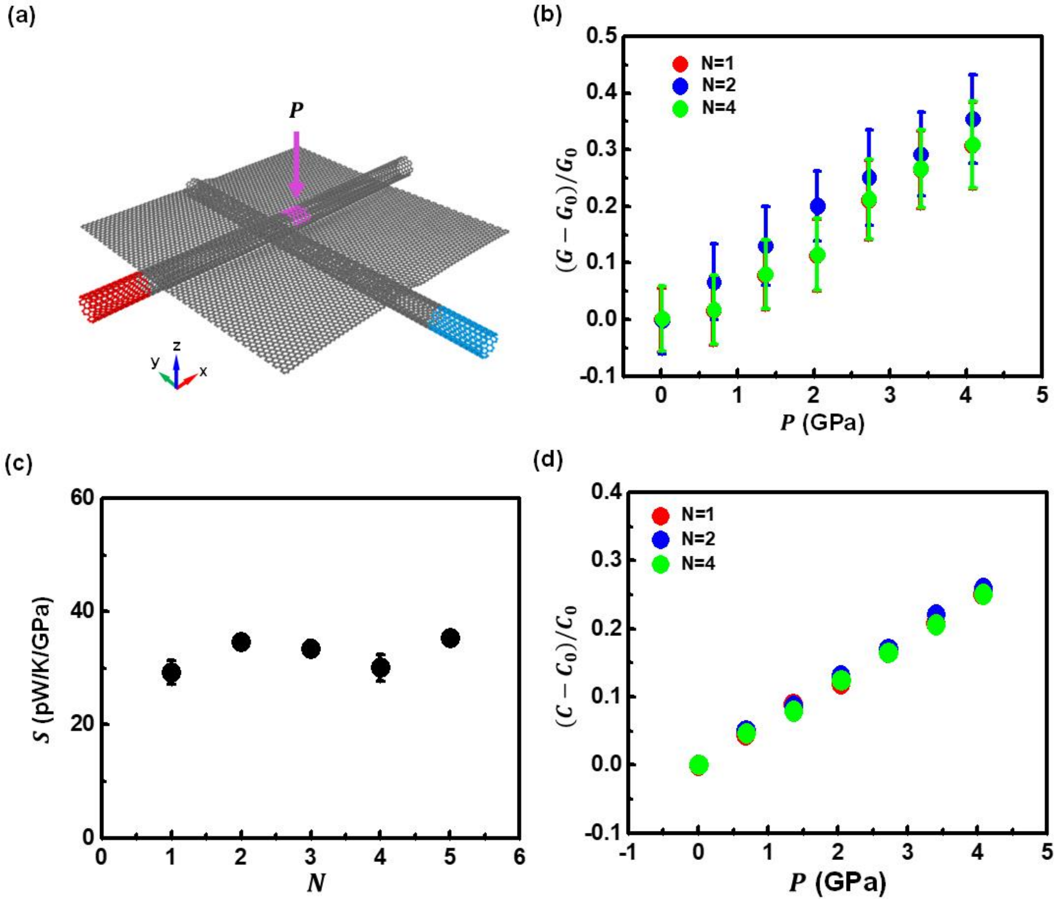

Figure 5.7. Thermal response of 1D-2D heterostructures to external pressure. (**a**) Schematic illustration of a 1D-2D heterostructure subjected to external pressure (P) at the heterojunction via the upper CNT. (**b**) Normalized thermal conductance $(G - G_0)/G_0$ of heterostructures composed of multilayer graphene as a function of external pressure P**.** G_0 is the thermal conductance at P=0. (**c**) Response sensitivity S of the heterostructure with multilayered graphene (layer number: N) to the pressure P. (**d**) Normalized pairwise interaction contribution factor of atoms $(C - C_0)/C_0$ at heterojunctions in heterostructures with multilayer graphene.

increase of thermal conductance G is obtained, as shown in **Figure 5.7b**. Taking the slope of a G-P curve as the sensitivity of the thermal transport of the heterostructure to external pressure, referred to as S, **Figure 5.7c** shows that S is independent of the layer numbers of graphene sandwiched between two CNTs. Mechanically, an external pressure will decrease the equilibrium distance between CNT and 2D layers, resulting in a stronger atomic interaction and larger C, and thus an enhanced G. Therefore, the minimum force/pressure detected by such designed sensor depends on the capability that can alter the density of atomic interactions at heterojunctions and is associated with the equilibrium distance between CNT and 2D layers. Besides, the weaker vdW interaction and/or small thickness of 2D materials, the easier deformation that can be tuned, and the higher sensitivity can be obtained. **Figure 5.7d** shows an obvious enhancement of the relative overall contribution factor $(C-C_0)/C_0$ at a larger P, where C_0 corresponds to P=0. This linear monotonous increase of $(C-C_0)/C_0$ also agrees with that of $(G-G_0)/G_0$ in Figure 5.7b. In addition, when an external pressure is applied to the heterojunction, the resulting distribution of stress change in the loading direction (*z*-direction) can be monitored and is given in **Figure 5.8a and b.** By comparing with that in the

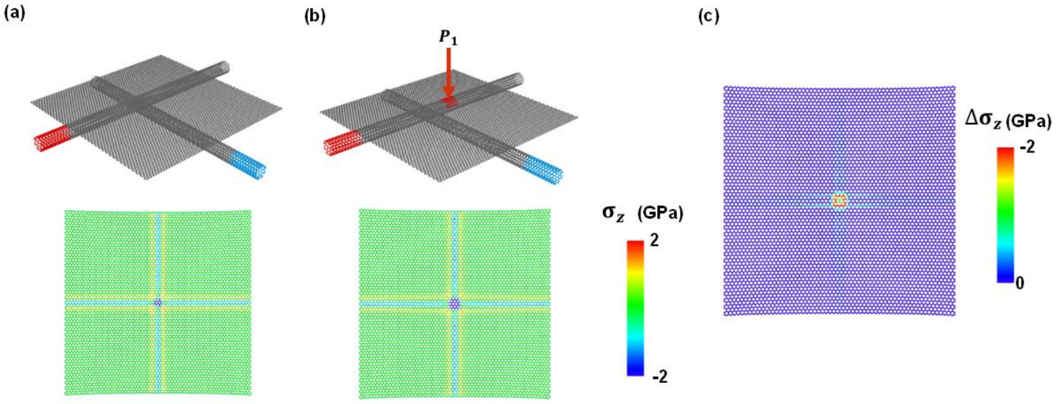

Figure 5.8. Stress distribution in graphene (a) in the absence of external pressure **(b)** at the pressure P_1=2GPa. (**c**) Stress change in monolayer graphene in the heterostructure at P=2 GPa in comparison with that of in absence of pressure

absence of the pressure loading, **Figure 5.8c** demonstrates a clear increase in the monolayer graphene at P=2 GPa. More importantly, the position of the pressure loading can be accurately located, suggesting that both the magnitude and location of the applied pressure could be determined through the measured thermal properties of 1D-2D heterostructures.

With the same mechanism, to further demonstrate the application of the thermal properties of 1D-2D heterostructures in pressure sensing, a pressure sensor consisting of an array of heterojunctions though multiple CNTs can be designed for pressure mapping. **Figure 5.9a** shows the illustrative schematics of the pressure sensor. Single layer graphene with the size of 29.27 nm in length and 31.78 nm in width is sandwiched between three pairs of CNTs with the same length of 36.03 nm to construct an array of nine heterojunctions, and the diameters of

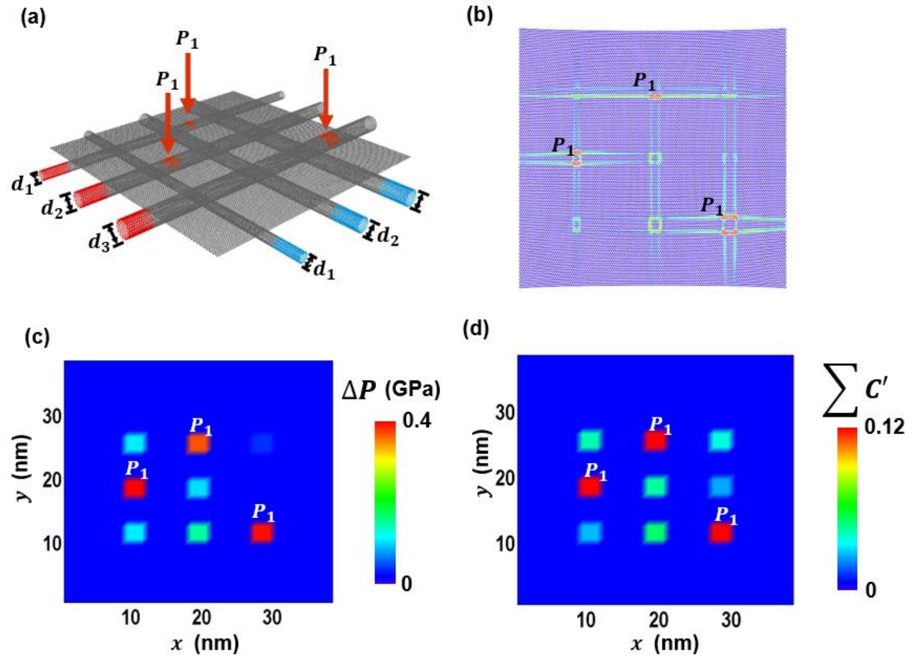

Figure 5.9. Conceptual design and demonstration application of 1D-2D heterostructure enabled pressure sensor. (**a**) Schematic illustrations of the heterostructure-pressure sensor array with monolayer graphene sandwiched between three pairs of CNTs with the same length but different diameters. The applied external pressure loadings are P_1=2GPa. (**b**) The stress change in graphene layers due to the external pressure loading. (**c**) Pressure change in graphene in the heterostructure-pressure sensor. (**d**) Pressure mapping demonstration through the total local pairwise interaction contribution factor of atoms at heterojunctions $\sum C'$ in heterostructures.

these three CNTs are d_1=1.085 nm, d_2=1.356 nm and d_3=1.898 nm, respectively. Local pressure with the same magnitude P_1=2 GPa is applied to three different heterojunctions via the top CNTs, as illustrated in Figure 5.9a. Similar to that Figure 5.8c, the resultant stress variation in graphene in comparison without the external pressure can be obtained and is shown in **Figure 5.9b**. Although the heterojunction area associated with different diameters of CNTs, the stress distribution in these three positions where the external applied is applied shows a good similarity, in particular, the maximum stress. As references, the pressure change at each heterojunction is the same as shown in **Figure 5.9c**. To reflect the thermal conductance through each heterojunction, we define a local contribution factor at each location in the 2D layer $C_{local} = N_{eff\_up\_i} N_{eff\_low\_i}$, where i represents the i^{th} atom in the 2D layer. Further, define the relative local contribution factor by considering the geometric size of upper CNTs and 2D layer, $C' = \frac{C_{local} - C_{local\_0}}{C_{local\_0}} \cdot \frac{a_{2d}}{d_{up}}$, where C_{local_0} represents the local contribution factor in the absence of external applied loadings. **Figure 5.9d** shows the summation of the variation of thermal conductance $\sum C'$at each heterojunction. A clear difference at the regions with and without external pressure can be identified. More importantly, these three regions with the external pressure show the same magnitude of variation of thermal conductance, being consistent with the same magnitude of applied pressure (P_1=2GPa), demonstrating the success of sensing the external pressure through the measurement of thermal conductance at local heterojunctions.

To further examine the functionality and sensitivity of the pressure sensor, three different pressures P_2=1.5 GPa, P_3=1 GPa and P_4= 0.67 GPa but in the same locations with that P_1 are applied, as illustrated in **Figure 5.10a**. **Figure 5.10b** shows the stress change in graphene

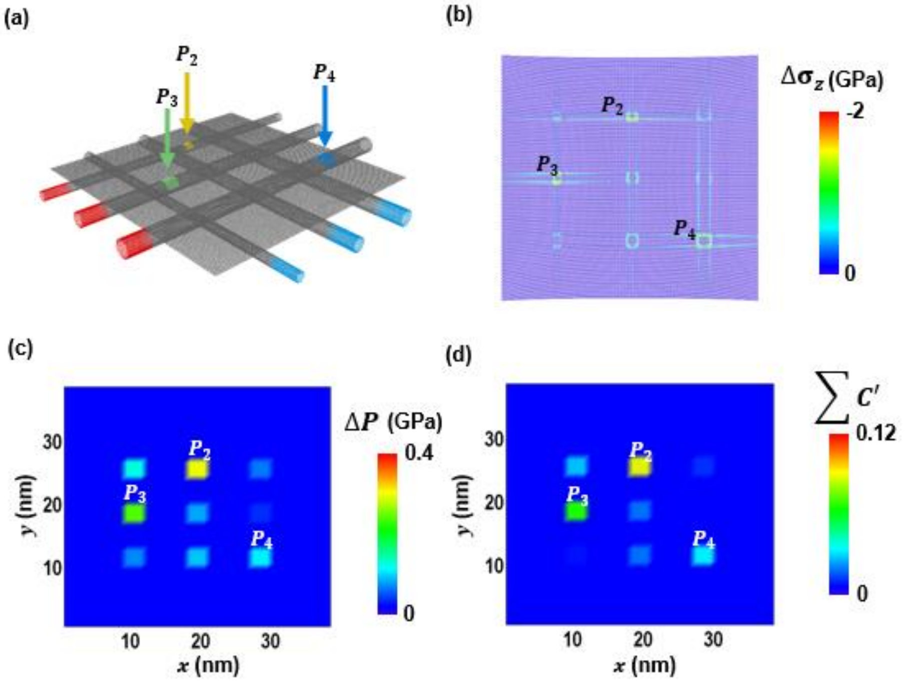

Figure 5.10. Conceptual design and demonstration application of 1D-2D heterostructure enabled pressure sensor. (**a**) Schematic illustrations of the heterostructure-pressure sensor array with monolayer graphene sandwiched between three pairs of CNTs with the same length but different diameters. The applied external pressure loadings are P_2=1.5 GPa, P_3=1 GPa and P_4= 0.67 GPa. (**b**) The stress change in graphene layers due to the external pressure loading. (**c**) Pressure change in graphene in the heterostructure-pressure sensor. (**d**) Pressure mapping demonstration through the total local pairwise interaction contribution factor of atoms at heterojunctions $\sum C'$ in heterostructures.

by comparing the stress distribution with and without external pressures. The pressure change at each heterojunction is the same as shown in **Figure 5.10c**. Lower external pressure results in a lower stress increase in corresponding loading locations. Besides, **Figure 5.10d** shows that the summation of variation of thermal conductance $\sum C'$ in these three regions is different. A lower pressure corresponds to a lower $\sum C'$, which is also consistent with the magnitude of applied pressures. Therefore, the 1D-2D heterostructures array can be used to identify both the magnitude and location of the applied pressures by extracting the local thermal properties and successfully demonstrates the performance of pressure sensing. We should note that the small increase of stress in Figures 5.9b and 5.10b and local contribution factor in Figures 5.9c and

5.10c in the heterojunction without external pressures is led by the overall displacement of CNTs and can be neglected in comparison with those in heterojunctions with pressure applied.

5.7 Summary

The thermal conductance will not only depend on local mechanical deformation of 2D materials at the heterojunction associated with bending stiffness, but will also rely on spatial equilibrium distance at heterojunction, and lattice structures and layer number of 2D materials, and can be described through a unified model by integrating both contributions. Both mechanical deformation of 2D materials and the density of atomic interaction at the heterojunctions are studied to reveal the underlying unique thermal transport mechanism and are in good agreement with the generalized unique model. Besides, when an external pressure is applied to the heterojunctions, the thermal conductance shows a monotonous variation and the variation sensitivity is independent of layer numbers. By utilizing the one-to-one correspondence between thermal conductance of heterostructures and the local pressure applied at heterojunctions, we put forward a conceptual design of a pressure sensor enabled by 1D-2D heterostructure and successfully demonstrate its capability of sensing to external pressures with high accuracy. These designs and findings are expected to lay a foundation for understanding thermal transport, mechanical deformation and their couplings in mixed-dimensional vertical heterostructures, and they are also expected to provide immediate application guidance for designing mechanical sensor such as pressure sensor by using mix-dimensional heterostructures underpinned by thermal transport mechanisms.

Chapter 6 Graphene Oxide-Water Heterostructures for Mechanical Load Sensing and Mode Differentiating

6.1 Overview of the Chapter

In this chapter, we present a heterostructure composed of bilayer graphene oxides and confined water as a mechanical sensor that enables the detection and differentiation of tension, compression, pressure and bending. Guided by molecular simulations, we demonstrate that the thermal transport across solid-liquid interfaces is sensitive to loading modes owing to the reversible response of hydrogen bonding networks between confined water molecules and graphene oxides, and quantitatively elucidate the thermal transport mechanism by correlating thermal conductance, number and distribution of hydrogen bonds and interfacial energy with mechanical loadings. Such structure-enabled mechanical sensor with contrasting thermal response to different loading modes is devised to exemplify robustness of sensing functions. These results lay a foundation for rational designs of mechanical sensors that leverage the thermal response of solid-liquid systems, beyond the current strategy relying on electrical properties of sole solids.

6.2 Computational Modeling and Methodology

Figure 6.1 depicts the schematic of the graphene oxide (GO)-confined water heterostructure. The dimension was $l =$ 6.15 nm in length and $w =$ 6.39 nm in width. The two GO layers were decorated with equal numbers of randomly distributed epoxy and hydroxyl functional groups.[277] This surface functionalization led to two different degrees of oxidation p

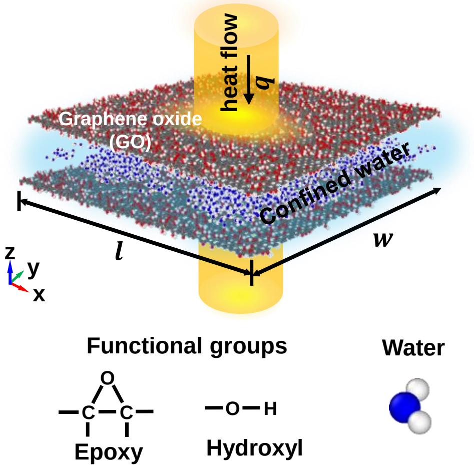

Figure 6.1. Atomistic modeling of the graphene oxide (GO)-confined water heterostructures with the size of $l =$ 6.15 nm and $w =$ 6.39 nm. The surface of both GO layers that is decorated with epoxy and hydroxyl functional groups reflects the oxidation. The heat is transferred from upper graphene oxide to the lower one.

(=0.4 and 0.5), which is defined as the ratio of the number of functional groups to the number of carbon atoms in a GO layer. Various numbers of water molecules are confined between these two GO layers, and is represented by the weight ratio, $wt = m_{water}/m_{GO}$, where m_{water} and m_{GO} are the mass of water molecules and a single graphene oxide layer, respectively, and wt usually changes from 0 to 25%.

All the molecular dynamics computations were carried out with LAMMPS package.[177] The time step was set as 0.5 fs. As for modeling, the bonded interactions within graphene oxide was described by OPLS-AA force field[278] that proves to reproduce both mechanical[279] and thermal transport properties[280] of graphene oxide. The widely adopted SPC/E model[281] was utilized to describe the behavior of water molecules. The non-bonded van der Waals interactions were modeled by Lennard-Jones potential,[278] and the particle-particle-particle-mesh (PPPM) with a root mean of 0.0001 was applied to evaluate the Coulomb interactions between charged atoms. The GO-water heterostructure was set between hot and cold substrates which are represented by GO layers with the same degree of oxidation. The periodic condition was applied in the in-plane direction of graphene oxide (x and y-direction) and non-periodic boundary conditions were applied in the cross-plane direction (z-direction).

The system was first relaxed in the NPT ensemble at a constant temperature of 300 K maintained by Nose-Hoover method for 1 ns. Next, NVT ensemble was applied to further optimize the heterostructure at 300K for another 1 ns. To calculate the thermal conductance, the reverse nonequilibrium molecular dynamics was applied. A specific amount of kinetic energy was added to/subtracted from the GO layer as hot and cold substrates at each time step to generate a constant heat flow q ranging from 0.5 to 0.7 nW that corresponded to a typical temperature difference between GO layers in the heterostructure $\Delta T_0 = 60$ K. This process continued for 4 ns and the thermal conductance was calculated $via\ G = q/\Delta T$ from the temperature data obtained during the last 2 ns.

To apply an external tensile or compressive strain, a uniform displacement at a strain rate $\dot{\varepsilon_x} = \pm 0.5$ ns^{-1} which can be approximately considered as a quasistatic manner was introduced to the system every 1000 time steps by remapping the x coordinates of atoms. To introduce external pressure to the system, an external yet equal force in z-direction was applied to the carbon atoms in the substrate. To apply a bending deformation, non-periodic boundary condition was applied to replace the periodic one in the x-direction. A neutral plane was assumed to exist between the GO layers of the heterostructure,[282] and the deformed structure at a specific bending curvature could be predicted by continuum mechanics, often referred to targeted molecular mechanics (TMM) method.[56]

The thermal transport could be decoupled by calculating the power exchange in the lower graphene oxide with upper graphene oxide as well as water molecules according to $q_{GO-GO} = 0.5(\sum_{i\in upperGO, j\in lowerGO} F_{ij} \cdot v_j - \sum_{i\in upperGO, j\in lowerGO} F_{ji} \cdot v_i)$,[283] where F_{ij} denotes the force vector exerted on atom j by atom i, and v_j represents the velocity vector of atom j. Similarly, $q_{GO-W} = 0.5(\sum_{i\in water, j\in lowerGO} F_{ij} \cdot v_j - \sum_{i\in water, j\in lowerGO} F_{ji} \cdot v_i)$ can be obtained. Their contributions to the thermal conductance can be further obtained by $G_{\mathrm{GO-GO}} = q_{\mathrm{GO-GO}}/\Delta T$ and $G_{\mathrm{GO-W}} = q_{\mathrm{GO-W}}/\Delta T$.

The phonon spectra were obtained by performing fast Fourier transform on the velocity autocorrelation function according to $PS(\omega) = 1/\sqrt{2\pi}\int_0^\infty e^{-i\omega t}\frac{<v(t)\cdot v(0)>}{<v(0)\cdot v(0)>}\mathrm{d}\omega$, where ω is the angular frequency and $v(t)$ is the atomic velocity vector at time t. The symbol $<>$ represents the average over atoms being concerned.

The hydrogen bonds in the system were identified according to two criteria associated with the geometry of the donor and acceptor. First, the H⋯O distance should not exceed 0.24 nm. Second, the H-O⋯O angle should be less than 30 degrees, which are usually applied to identify H-bonds in the systems enabled by GO and water molecules.[284] The number of H-bonds in a specific system was obtained by calculating the number of H-bonds in 100 frames in the last 1 ns during the simulations.

6.3 Thermal Conductance of Bilayer Graphene Oxide (GO)-Confined Water Heterostructures and its Response to Mechanical Loading

Figure 6.2 presents the thermal conductance G of heterostructures as a function of water content. In the absence of confined water, G is 10.24 pW/K for the heterostructure with $p = 0.5$, which is higher than the conductance 7.71 pW/K of the heterostructure with $p = 0.4$. This

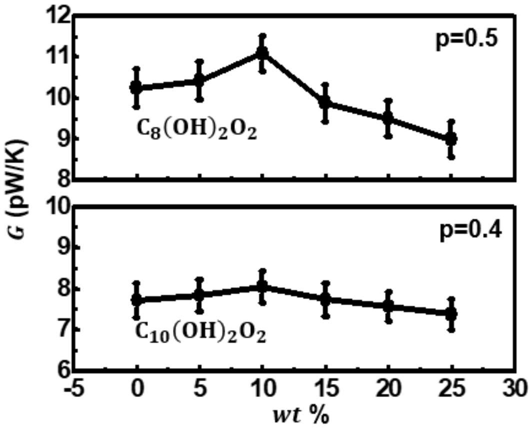

Figure 6.2. Thermal conductance G of the heterostructures with degrees of oxidation p =0.4 and 0.5 as functions of confined water content.

relative higher G with $p =$ 0.5 remains when wt increases to 25% due to the stronger atomic interactions provided by more functional groups at molecular junctions.[254] As the water content increases, G shows an increase until wt reaches 10%, followed by a decrease as the water content continuously increases. Such variation is more obvious at a higher p (= 0.5) due to more functional groups in GO layers, which will potentially benefit the formation of GO-water hydrogen (H)-bonds as both donors and acceptors.[285] For the heterostructure, two types of H-bonds will be formed in the interlayer. One results from the interactions of the functional

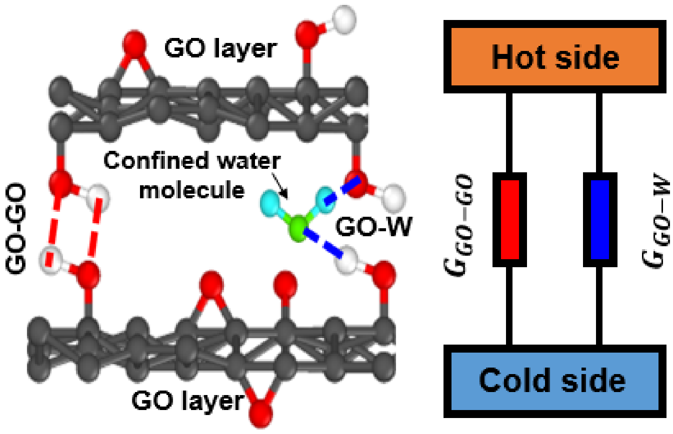

Figure 6.3. Schematic of the hydrogen bonds-featured interactions between graphene oxide layers (GO-GO) and between graphene oxide and water molecules (GO-W) (left) and their correspondence to a circuit model consisting of the two heat transfer paths with thermal conductance of $G_{\mathrm{GO-GO}}$ and $G_{\mathrm{GO-W}}$, respectively (right).

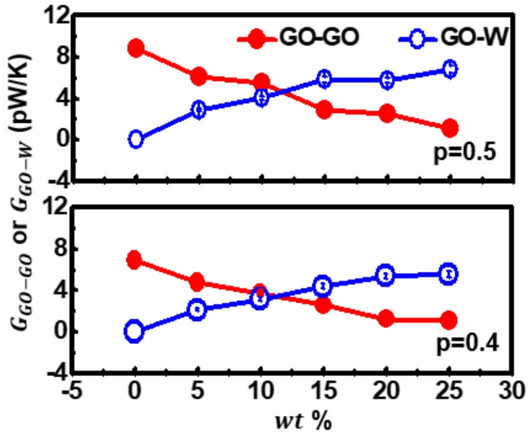

Figure 6.4. Variation of $G_{\mathrm{GO-GO}}$ and $G_{\mathrm{GO-W}}$ as functions of water content in the heterostructure with degrees of oxidation $p =$ 0.4 and 0.5.

groups between GO layers, referred to as GO-GO H-bonds, as marked in red dash lines in the atomic schematics in **Figure 6.3,** and the other governs the coordination between GO and confined water molecules, referred to as GO-W H-bonds, marked by the blue dash lines in Figure 6.3. Further analysis shows that the contribution of van der Waals interaction associated with these two types of H-bonds to thermal transport is >90% and the effect of electrostatic interaction on thermal transport can be neglected. As a consequence, the interactions associated with these two H-bonds can be considered to serve as two dominant paths of thermal transport across the interface, analogical to a circuit model, as illustrated in Figure 6.3. By decoupling the heat flow, **Figure 6.4** gives the contribution of thermal transport along these two corresponding transfer routes, where $G_{GO-\mathrm{GO}}$ and $G_{GO-\mathrm{W}}$ represent the thermal conductance with the transport path from upper GO to lower GO via GO-GO H-bonds and from upper GO to water molecules and then to lower GO via GO-W H-bonds, respectively. With the increasing of the confined water molecules between GO layers, the equilibrium distance between two GO layers increases, weakening firsthand interactions between GO layers, and leading to a reduction of GO-GO H-bonds and thus a lower $G_{GO-\mathrm{GO}}$, as observed in Figure 6.4. By contrast, the interaction between GO and water molecules is enhanced through GO-W H-bonds, thus promoting G_{GO-W}.

Given the stronger ability to form H-bonds in the heterostructure with $p = 0.5$, we will take it as a material design platform to exemplify the response of thermal transport to external applied mechanical loadings. Four typical mechanical loading modes of in-plane tension and compression and out-of-plane pressure and bending will be investigated and their realization in atomistic modeling can be found in Materials and Methods section. **Figure 6.5a** presents the effect of in-plane external tensile loading ε_t on relative thermal conductance $(G - G_0)/G_0$,

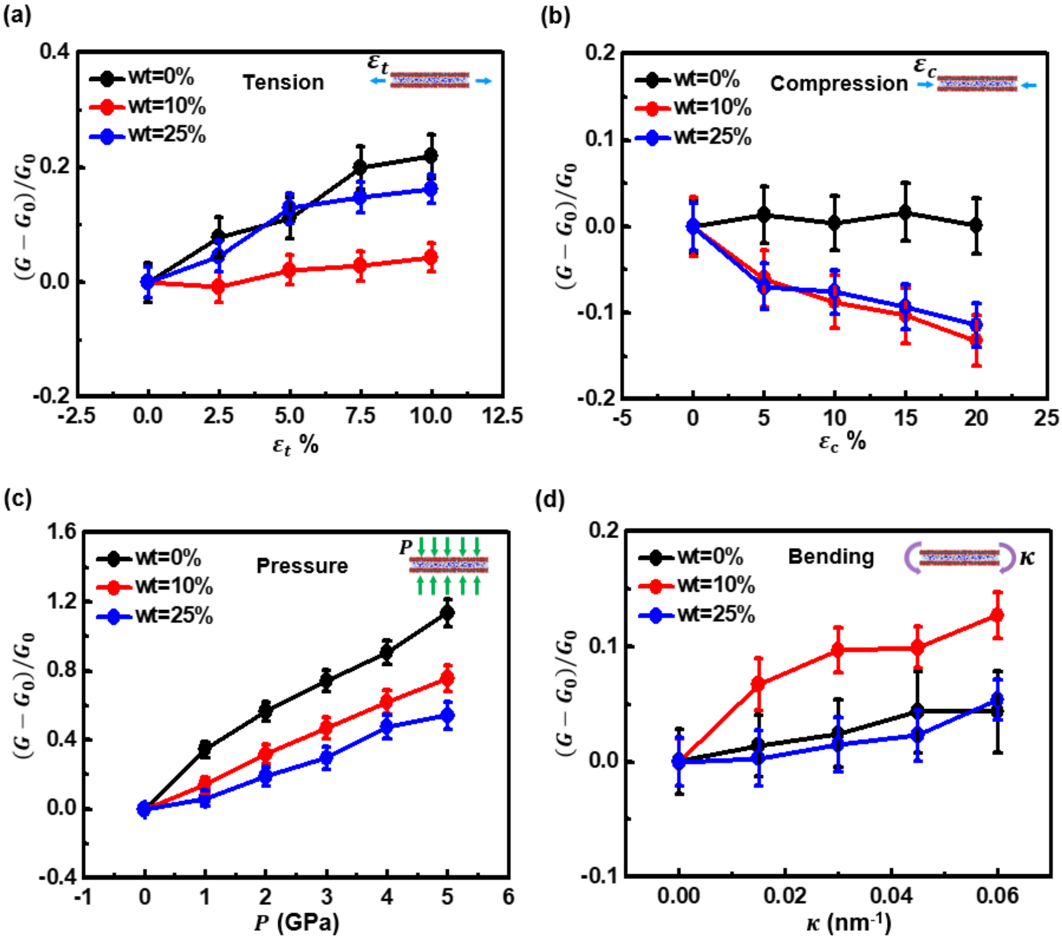

Figure 6.5. Responses of thermal conductance in graphene oxide (GO)-confined water heterostructures to different mechanical loading modes. The thermal conductance G in the heterostructure with degree of oxidation $\mathrm{p} = 0.5$ and water content of 0, 10% and 25% as functions of (**a**) in-plane tensile strain ε_{t}, (**b**) in-plane compressive strain ε_{c}, (**c**) cross-plane pressure P and (**d**) cross-plane bending curvature κ.

where G_0 is the thermal conductance of heterostructures in the absence of mechanical loadings. Without water molecules ($wt = 0$), G increases by ~20% by 10% of ε_t. As the water content reaches 10%, G slightly increases with tensile strain, and shows a similar enhancement with the one at $wt = 0$ at the water content of 25%. **Figure 6.5b** shows the relationship between G and the in-plane compressive strain ε_c. Without water molecules confined, G is approximately independent of ε_c. By contrast, at $wt = 10\%$ and 25%, the thermal conductance decreases with the increase of compressive strain, to approximately 90% of its initial value at ε_c 20%. When a cross-plane pressure loading P is exerted on the GO layers, the heterostructure shows an enhanced thermal conductance G, as obtained in **Figure 6.5c**. As the water content increases, the enhancement remains but with a smaller ratio. With a cross-plane bending curvature κ applied to the heterostructure, **Figure 6.5d** shows that the thermal conductance without water molecules is slightly enhanced. When the water content increases to 10%, G increases by 10% at $\kappa = 0.06$/nm; at $wt = 25\%$, the increase of G with bending curvature is significantly suppressed, leading to similar behavior to that of GO heterostructures without the confinement of water molecules.

6.4 Mechanism and Generalized Correlation Between Thermal Conductance and H-bonds

To understand the underlying mechanism of the thermal response to mechanical loadings, we first examine the atomic vibration features by investigating the phonon spectra. Under different mechanical loadings, **Figure 6.6** shows no significant change in the phonon spectra of heterostructures, indicating negligible lattice deformation in the heterostructures, and thus phonon properties are barely changed.[286] This non-change of phonon spectra of

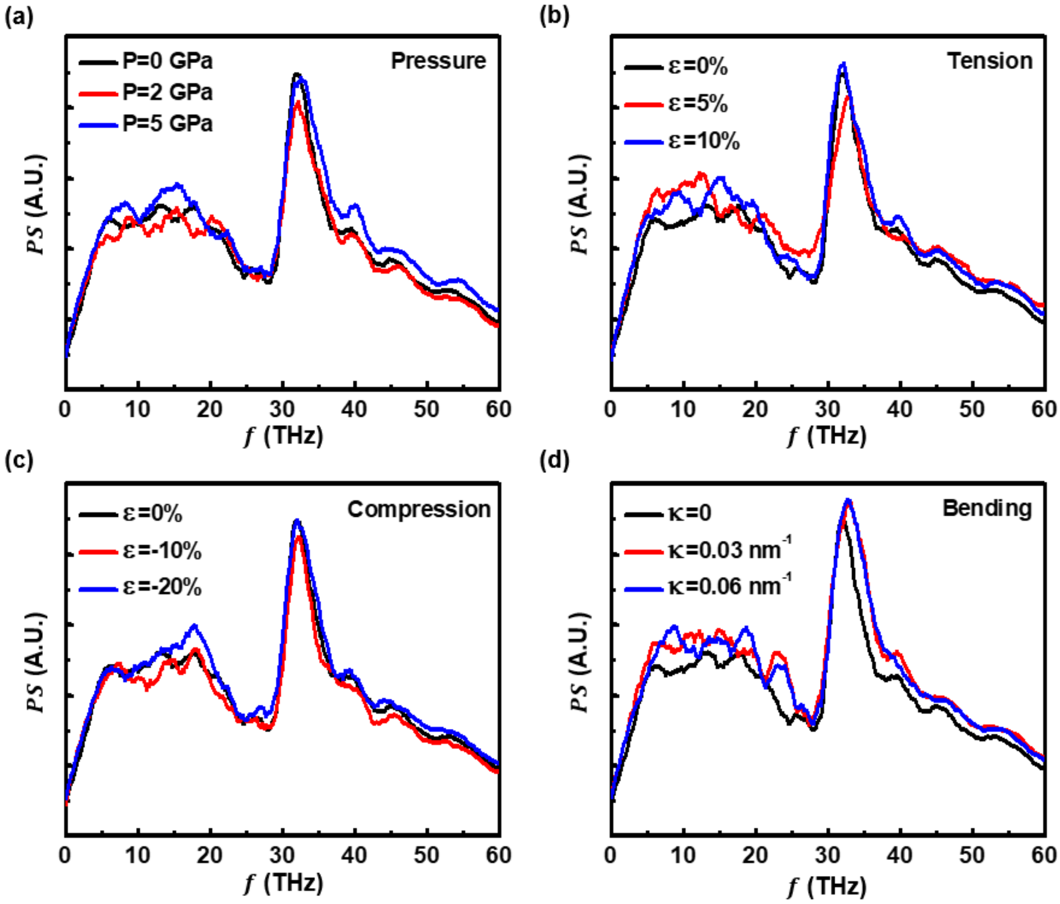

Figure 6.6. Phonon spectra of graphene oxide under mechanical loadings. No obvious difference is observed under the influence of (**a**) tensile strain ε_{t}, (**b**) compressive strain ε_{c}, (**c**) pressure P and (**d**) bending curvature κ.

heterostructures is further confirmed under different loading levels with these four loading modes.

The strength of atomic interactions, as another physical parameter that is usually employed to understand the thermal transport at non-bonded molecular junctions,[254, 287] are then extracted and characterized by the interfacial interaction energy E_{int}. **Figure 6.7a** plots the variation of thermal conductance G with E_{int}. When there are no confined water molecules, a generalized linear relationship between G and E_{int} independent of mechanical loading magnitude and modes, can be obtained, consistent with thermal transport across interfaces of bulk-bulk materials.[283, 288] When water molecules are introduced to the interlayer, although a higher E_{int}

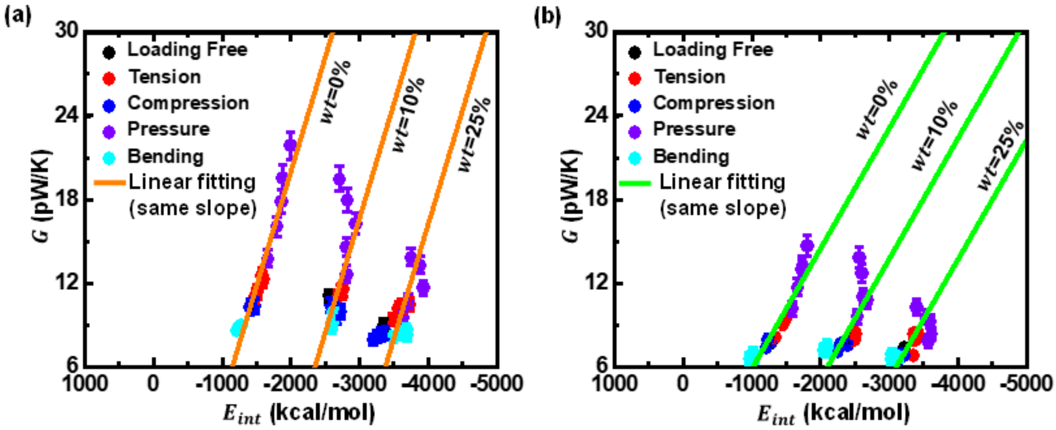

Figure 6.7. Thermal conductance G versus interfacial interaction energyE_{int} at (**a**) $\mathrm{p} = 0.5$ and (**b**) $\mathrm{p} = 0.4$. Compared to the $G - E_{\mathrm{int}}$ relationships obtained at $\mathrm{p} = 0.5$, the slopes of linear fittings decrease due to the reduction in the number of functional groups and atomic density at the solid-liquid interface.

is obtained, the generalized linear relationship with the same slope between G and E_{int} remains with a small deviation. This deviation becomes a little large at a high pressure loading and/or water content (25%) and is expected to be caused by the breaking of partial GO-GO interaction featured by functional groups and enhanced GO-water interactions, where the GO-water interactions suppress the thermal transport with Kapitza resistance by the contrasting vibration nature of atoms in GO and water.[289] Similar results can be obtained in heterostructures with $p = 0.4$ (**Figure 6.7b**).

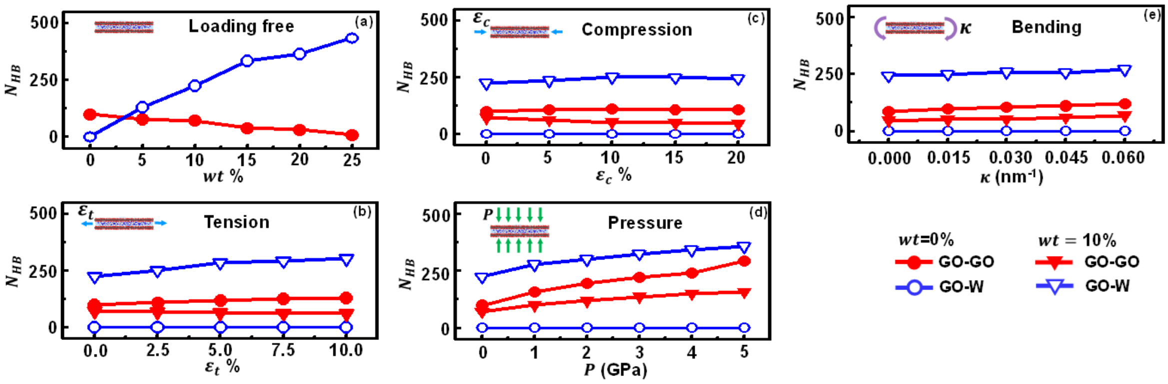

Figure 6.8. The number of hydrogen (H)-bonds between graphene oxides (GO-GO H-bonds) and graphene oxides and water (GO-W H-bonds) as functions of (**a**) water content, (**b**) tensile strain ε_{t}, (**c**) compressive strain ε_{c}, (**d**) external pressure P, and (**e**) bending curvature κ.

Since the atomic interaction and interaction energy at non-bonded interfaces are essentially associated with H-bonds,[283] the variation in the number of GO-GO and GO-W H-bonds are further investigated, as shown in the **Figure 6.8a-e.** As the number of the confined water molecules increases, the number of GO-GO H-bonds decreases and the number of GO-W H-bonds increases (Figure 6.8a), consistent with the thermal contributions to their corresponding $G_{GO-\mathrm{GO}}$ and $G_{GO-\mathrm{W}}$ in Figure 6.4. With the increase of in-plane tensile strain ε_t, the number of GO-GO H-bonds increases at $wt =$ 0%, but decreases with an increase of GO-W H-bonds at $wt =$10%, which echoes with that of $G_{GO-\mathrm{GO}}$ and $G_{GO-\mathrm{W}}$ with ε_t in **Figure 6.9a**. At an

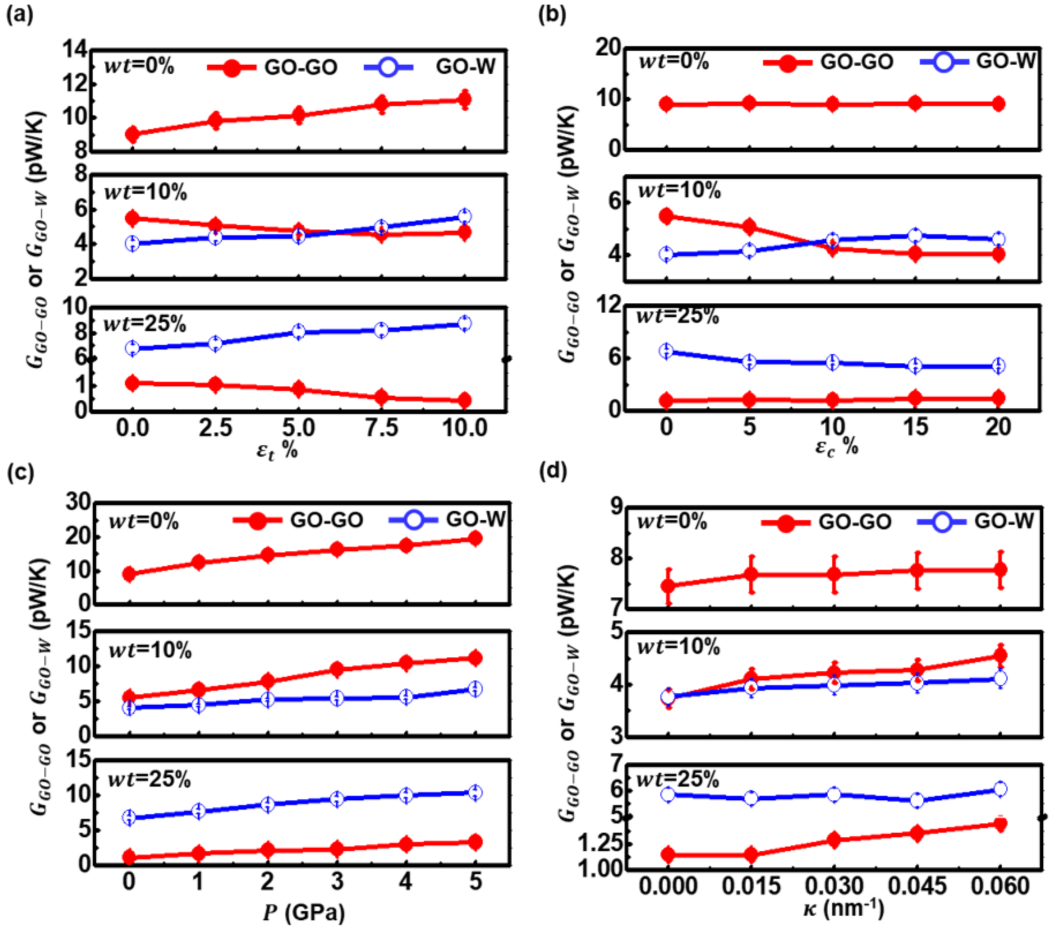

Figure 6.9. Decoupled thermal conductance along two heat transfer paths. The partial contribution to the thermal conductance from the interaction between graphene oxide layers $G_{\mathrm{GO-GO}}$ and the interaction between graphene oxide and water molecule $G_{\mathrm{GO-W}}$ at different water weight ratio $wt =$ 0, 10% and 25%. Partial contributions as functions of (**a**) tensile strain ε_t, (**b**) compressive strain ε_c, (**c**) pressure P and (**d**) bending curvature κ.

in-plane compressive strain ε_{c}, the total number of H-bonds barely changes when there is no confined water molecules in the heterostructures (Figure 6.8b). On the other hand, at the water content of 10%, ε_{c} will lead to an increase of GO-W H-bonds and a decrease of GO-GO H-bonds (Figure 6.8c), which also agrees with that of $G_{GO-\mathrm{GO}}$ and $G_{GO-\mathrm{W}}$ with ε_{c} in **Figure 6.9b**. By contrast, when an out-of-plane pressure P is applied (Figure 6.8d), the number of both GO-GO and GO-W H-bonds at $wt =$ 0 and 10% will increase, corresponding to the increasing of $G_{GO-\mathrm{GO}}$ and $G_{GO-\mathrm{W}}$ in **Figure 6.9c**. The effect of bending curvature κ on H-bonds (Figure 6.8e) indicates that larger κ lead to higher GO-GO and GO-W H-bonds. This increase will be larger at a higher wt, which is also confirmed by the thermal conductance in **Figure 6.9d**. **Figure 6.10a** shows a generalized relationship between G and the number of H-bonds by considering water content wt as well as magnitudes and modes of mechanical loadings. A linear variation for both GO-GO and GO-W H-bonds is obtained but with a clearly different slope. The larger slope for GO-GO H-bonds indicates its higher contributions to

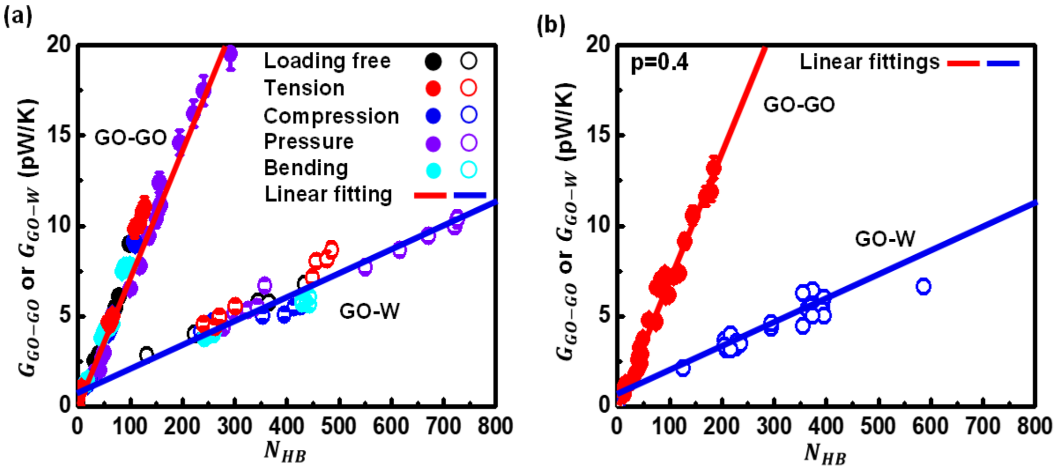

Figure 6.10. Decoupled contribution of GO-GO H-bonds to thermal conductance $G_{\mathrm{GO-GO}}$ and GO-W H-bonds to thermal conductance $G_{\mathrm{GO-W}}$ at (**a**) $\mathrm{p} = 0.5$ and (**b**) $\mathrm{p} = 0.4$.

thermal transport of heterostructures. The same generalized relationship is also obtained in the heterostructures with $p = 0.4$ (**Figure 6.10b**).

Afterward, to elucidate the role of H-bonds, **Figure 6.11a-e** shows the density distribution of H-bonds ρ_{HB} in the heterostructures with 10% of water ratio. Compared with the loading free condition in the heterostructure in Figure 6.11a, Figure 6.11b shows that an increase of

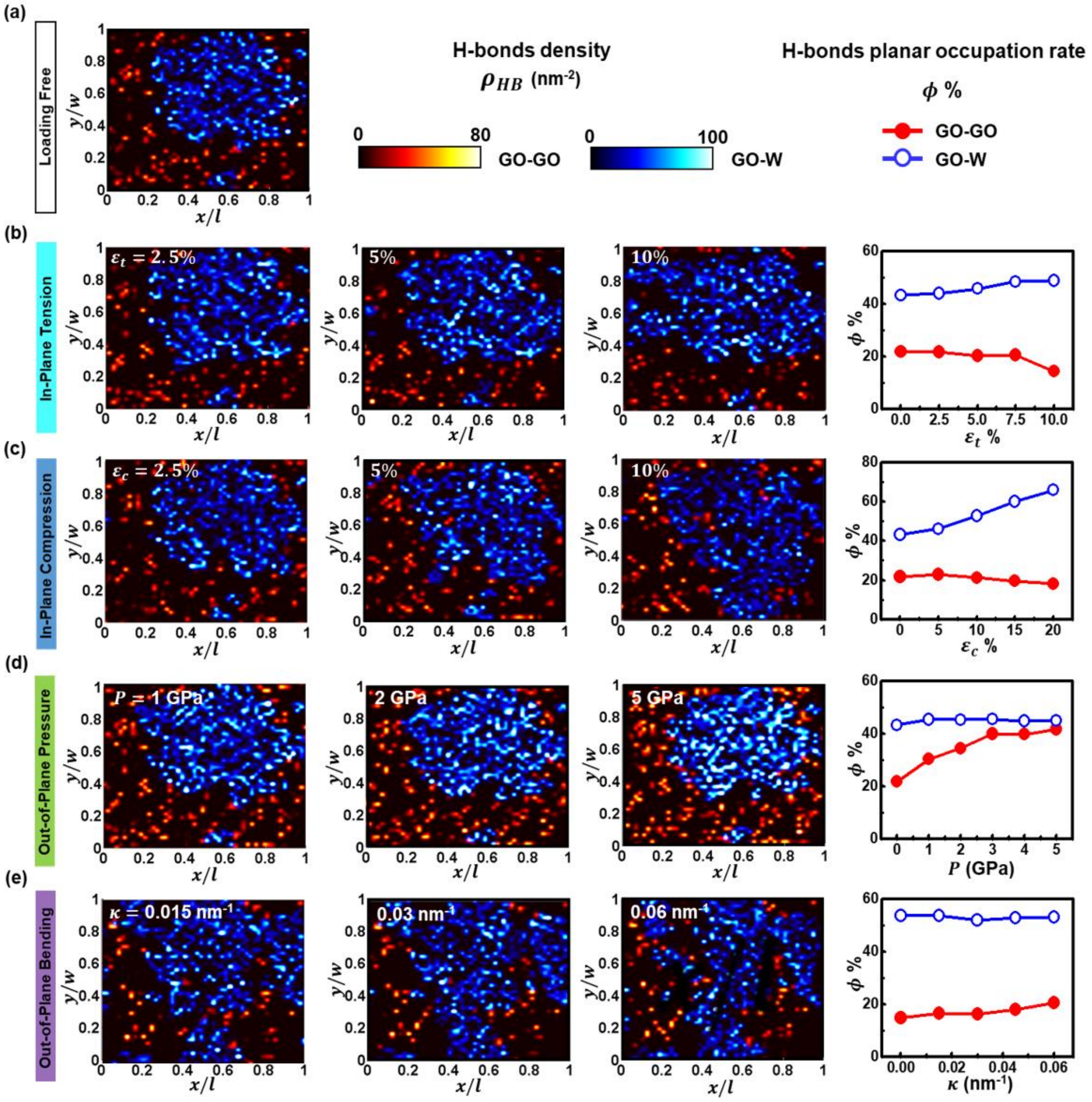

Figure 6.11. Planar distribution and occupation of hydrogen (H)-bonds in the interlayer of confined water and graphene oxides. The density ρ_{HB} and planar occupation rate ϕ of hydrogen bonds in the interlayer of heterostructures with degree of oxidation $p = 0.5$ and water weight ratio $wt = 10\%$ (**a**) in the absence of loading, under (**b**) tensile strain ε_{t}, (**c**) compressive strain ε_{c}, (**d**) external pressure P, and (**e**) bending curvature κ. The H-bonds formed between graphene oxide layers (GO-GO) and between graphene oxide and water molecules (GO-W) are represented by red and blue dots, respectively.

tensile loading from 2.5% to 10% constrains the out-of-plane displacement of GO layers (**Figure 6.12a-b**), strengthening the confinement effect of water molecules and thus facilitating the formation and in-plane spread of GO-W H-bonds, yet leading to a slight reduction of GO-GO H-bonds. This distribution can be further confirmed from the planar area occupation rate

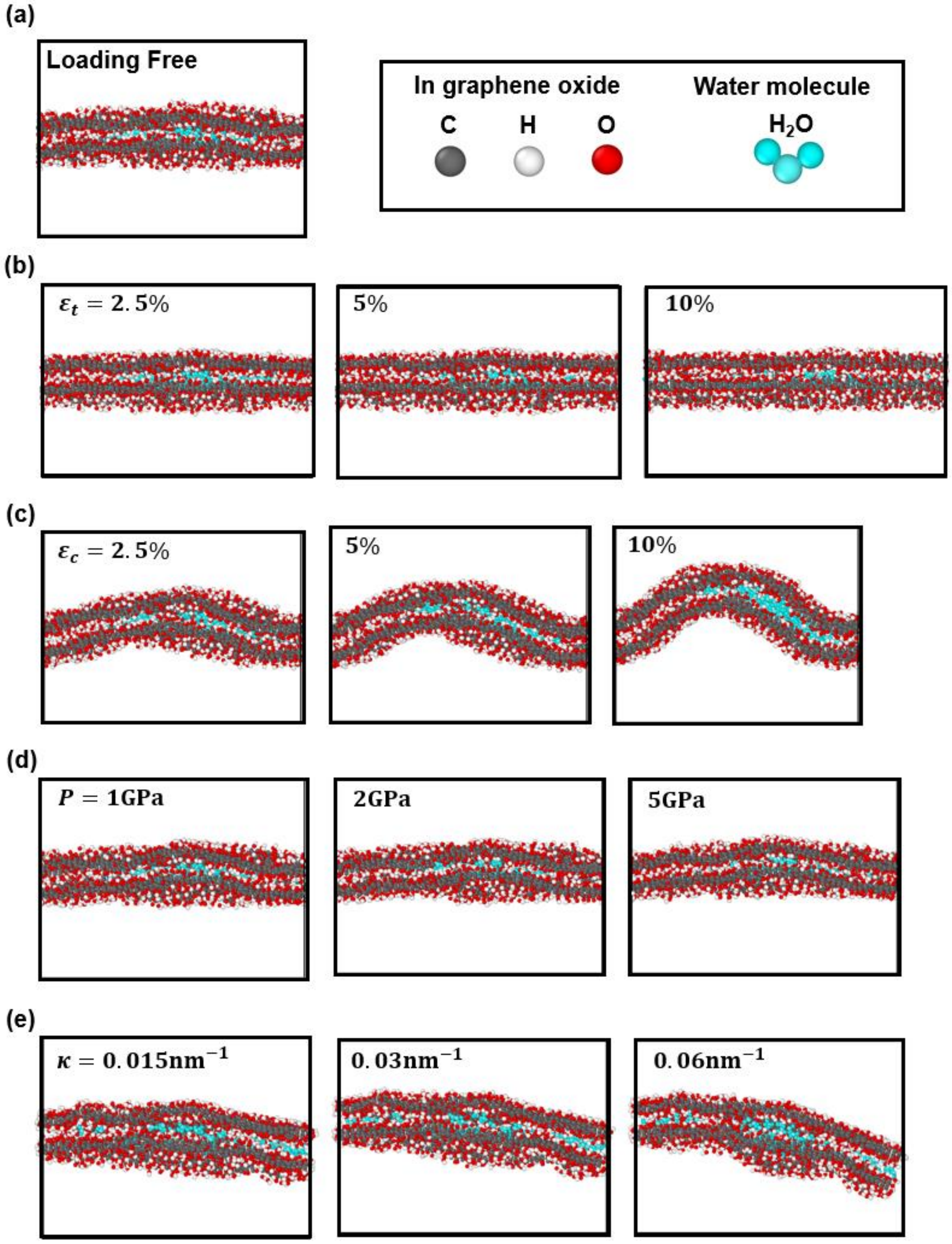

Figure 6.12. Deformation snapshots of the heterostructure with $p = 0.5$ and $wt = 10\%$ (**a**) tensile strain ε_t, (**b**) compressive strain ε_c, (**c**) pressure P and (**d**) bending curvature κ.

ϕ of GO-W and GO-GO H-bonds, where ϕ is defined as the ratio of the total planar area covered by GO-W or GO-GO H-bonds to the total interlayer area of the heterostructure. A specific area of a single hydrogen bond can be calculated via πr_{HB}^2 ($r_{\mathrm{HB}} =$ 0.24 nm is the length of H-bonds[284]). At a compressive strain (Figure 6.11c), the formed GO-W H-bonds spread in the y-direction, leading to a larger region of GO-W H-bonds with the destruction of GO-GO H-bonds, which can be seen clearly in the plot of ϕ. Different from the constraint to the out-of-plane deformation under the tensile loading, the compression loading will promote an out-of-plane displacement and prevents the effective contact of GO-GO layers and GO layer-water (**Figure 6.12c**), which decreases the number of GO-GO H-bonds and also impedes the formation of GO-W H-bonds, leading to a smaller thermal conductance, as shown in Figure 6.5b. When an external pressure P is applied to the heterostructure, the interlay distance between GO layers will decrease (**Figure 6.12d**), leading to enhanced interactions including enhanced confinement effect of water molecules. Consequently, an increase in both GO-GO and GO-W H-bonding density is observed (Figure 6.11d). However, the formation of more GO-GO H-bonds leads to a higher ϕ meanwhile the ϕ of GO-W H-bonds remains, which indicates the external pressure does not spread the water in planar directions. The increase of both H-bonds becomes more obvious at a higher pressure, leading to an enhanced thermal conductance, as shown in Figure 6.5c. When the heterostructure is subjected to a mechanical bending, the interactions among water molecules will be weakened because of their interrupted (even discontinuous) distributions by bending deformation (**Figure 6.12e**), and GO-GO H-bonds will form, corresponding to the increasing ϕ of GO-GO H-bonds (Figure 6.11e) and thus leading to a larger increase in thermal conductance (Figure 6.5d). As wt changes (*e.g.* 0

and 25%), the distribution and occupation rate ϕ of H-bonds with mechanical loadings will change correspondingly.

6.5 Application of Mechanical Sensor Design and Demonstrations for Multiple Mechanical Loading Sensing and Mode Differentiation

The thermal transport response of GO-water heterostructures to multiple mechanical loadings can be utilized as a sensor platform to distinguish mechanical modes that are commonly required in sensor design for applications in human-machine interfaces and smart

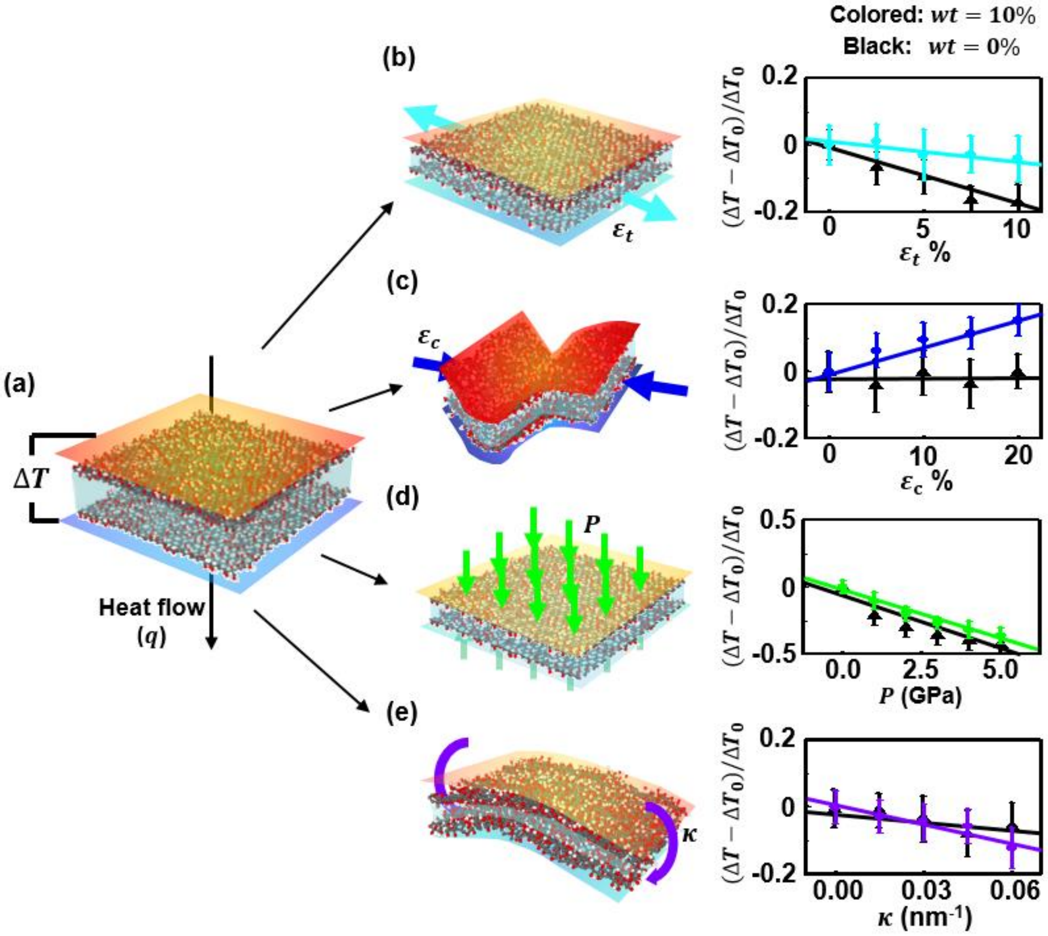

Figure 6.13. Design and demonstration application of mechanical sensor enabled by graphene oxide-confined water heterostructure. (a) Schematic of mechanical sensor design, where a constant heat flow q is applied to generate a temperature difference ΔT between the graphene oxides in the heterostructure. Measurement of relative temperature $(\Delta T - \Delta T_0)/T_0$ with respect to external mechanical loading of (**b**) tension ε_t, (**c**) compression ε_c, (**d**) pressure P and (**e**) bending curvature κ. ΔT (~60 K) is the temperature difference in the absence of mechanical loading.

e-skins. As demonstration, a constant heat flow q is introduced to generate a temperature difference across the interface in the GO-water heterostructure with water content of 10%, as illustrated in **Figure 6.13a**. Four typical mechanical loading modes, in-plane tension and compression and out-of-plane pressure and bending, are studied. The temperature difference between upper and lower graphene oxide layers ΔT will be measured as a parameter characterization for mechanical loading sensing and loading mode differentiation. For instance, with a tensile loading to the heterostructure, **Figure 6.13b** shows a continuous decrease of $(\Delta T - \Delta T_0)/\Delta T_0$, where ΔT_0 is the temperature difference in the absence of mechanical loading. By contrast, if the mechanical loading is an in-plane compression, $(\Delta T - \Delta T_0)/\Delta T_0$ shows a continuous increase (**Figure 6.13c**). The contrasting variation of temperature indicates that the in-plane tension and compression modes can be determined from the decreasing and increasing trend of temperature, respectively. Besides, the strain range can be as high as 10%, much higher than that of conventional strain sensors (usually less than 3% [4]), and can be used to sense a large mechanical strain. By analogy with electrical resistance-based strain sensors, we further define the gauge factor of this thermal property-based strain sensor via $GF = \frac{\Delta T - \Delta T_0}{\Delta T_0}/\varepsilon$, where ε is the applied in-plane strain, and GF is ~1 for both tension and compression, which is comparable with that of conventional strain sensors.[290, 291] It is expected that both the gauge factor and sensing range can be enhanced by programming the GO layers into meshed or kirigami structures. [286] When an out-of-plane pressure or bending is applied, **Figure 6.13d and e** shows a continuous decrease of $(\Delta T - \Delta T_0)/\Delta T_0$ as the increasing of the pressure and bending curve, respectively, which is similar to that at tension. The bending deformation leads to the fastest drop of temperature, and there is the slowest one for the tension, which can be used to identify the mechanical mode among tension, pressure and bending. For comparison, we designed a mechanical sensor enabled by heterostructure without water confined (i.e. $wt = 0$) and performed the calculations. Similar change of temperature with that in the presence of confined water is observed to tensile, compression and bending modes, but the temperature remains unchanged to compression loading. This independence indicates that the compression loading mode cannot be sensed and results from unchanged number of H-bonds (Figure 6.5c) due to the conformal attachment between GO layers under compression, which in turn confirms the critical role of confined water in the mechanical model differentiation. In addition, extensive simulations on the sensor enabled by GO-water

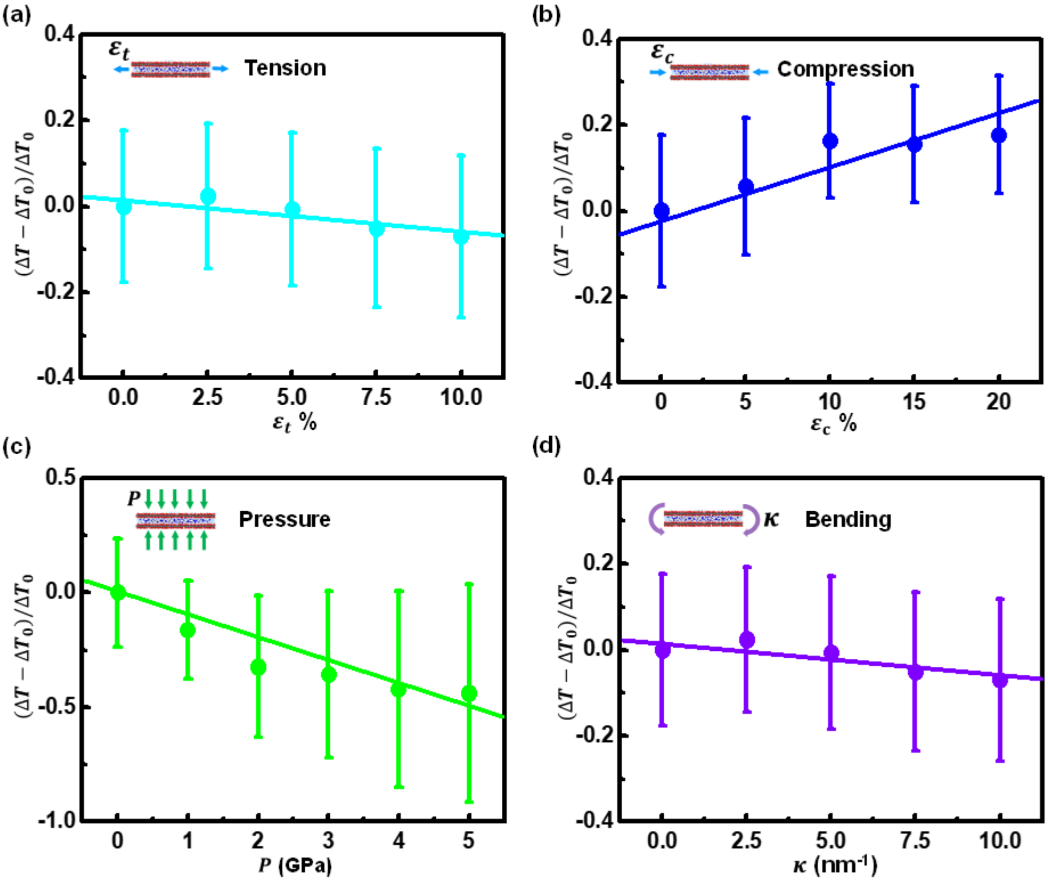

Figure 6.14. Measurement of relative temperature $(\Delta T-\Delta T_0)/\Delta T_0$ with respect to external mechanical loading of (**a**) tensile strain ε_t, (**b**) compressive strain ε_c, (**c**) pressure P and (**d**) bending curvature κ. ΔT_0 (~30 K) is the temperature difference in the absence of mechanical loading.

heterostructure under a small temperature drop ΔT_0 further confirm the robustness and sensitivity of sensing and differentiating these mechanical loading modes (**Figure 6.14a-d**).

6.6 Summary

Mechanically flexible, structurally simple and functionally multiple sensors whose sensing mechanism is not limited to the changes in electrical properties of material components in response to external mechanical loadings are in the development of sensor structures to reduce the effects of temperature variations and/or physical couplings with inputs of electrical power information through measurement of their unprecedented properties and loading mode sensitive responses meanwhile possessing the comparable sensitivity.. We here provide a possibility by constructing a bilayer graphene oxide heterostructure with liquid confined in the interlayer and report its unique thermal response to mechanical loading magnitudes and modes. Extensive atomistic modeling and comprehensive mechanism analysis elucidate the fundamental principle of solid-liquid interaction in the confined interlayer spaces associated with dynamically reversible hydrogen bonding networks. The application demonstration of such solid-confined liquid heterostructures based mechanical sensors confirms that the mechanical loading sensing and mode differentiation to four typical mechanical modes, tension, compression, pressure, and bending can be realized from the measurement of the temperature difference in the sensor. The results and findings extend a design solution of mechanical sensors from electrical resistance based to thermal transport based responses. The employment of confined liquid and the resultant dynamic interactions with solid components in response to external environments and stimuli foster the opportunities for designing devices that rely on solid materials only.

Chapter 7 Conclusions and Future Work

7.1 Concluding Remarks

In this dissertation, we investigated the mechanically responsive thermal transport in 2D materials and heterostructures to establish the quantitative relationship between mechanical deformation and thermal properties. Furthermore, we propose multifunctional mechanical sensors relying on unique thermal responses to mechanical stimuli and demonstrate their functionalities with atomistic simulations.

We start with graphene nanoribbons with serpentine geometries, named as “serpentine graphene nanoribbons” (SGNRs) and show that the thermal conductivity of SGNRs increases with the increase of tensile strain till to a significant appearance of localized stress in the structures. During tension, the stress in SGNRs remains an approximate zero until the tensile strain reaches a critical value, referred to “mechanical stretchability”, and this large deformation without an increase in localized stress is dominated by the alignment effect of serrated-edges to the direction of the tensile strain. This straightening deformation mechanism of SGNRs in tension extensively extends the effective length of thermal transport and enhances the thermal conductivity. Beyond the mechanical stretchability, the carbon-carbon bonds will experience stretching deformation, which leads to elastic deformation of SGNRs till to the failure of structures with a sudden drop in stress. The localized elastic deformation softens the phonon modes, leading to a reduced thermal conductivity. The unusual thermal behavior depends on the mechanical stretchability of SGNRs, and a large stretchability will promote the unusual thermal behavior in tension.

Then, we create auxetic graphene (AG) and contractile graphene (CG) and illustrate that the responses Poisson’s ratio, as well as the thermal conductivity of the heterostructures enabled by their single units can be regulated by patterning unit cells with different interface properties. Analyses of both mechanical deformation and vibrational spectra indicate that the thermal transport properties of graphene heterostructures are highly dependent on their stress distribution, and also rely on the interfaces that are parallel with the directions of mechanical loadings. Theoretical models are developed to quantitatively describe the thermal conductivity of graphene heterostructures in a uniaxial tensile loading and their robustness is verified by extensive simulations. These findings and models are expected to lay the groundwork for designing and manufacturing 2D materials-based interface-mediated functional devices with mechanically tunable thermal performance.

Next, we move to the thermal transport in covalently bonded heterostructures. Using non-equilibrium molecular dynamics (NEMD) simulation, we show that the asymmetric heat transport (thermal rectification) in graphene-boron nitride (GBN) heterostructure can be laid down by the introduction of junction defects, yet possessing a non-monotonous variation with mechanical tensile loading perpendicular to the GBN heterojunction, which is probed through the stress analysis, vibrational spectra, phonon participation ratio, and heat flow distribution. At a small tensile strain, the thermal rectification is dominated by out-of-plane phonon mode resonance and localization, and with the increase of tensile strain, the mechanical stress concentration at the interface plays a dominant role. We put forward two conceptual designs of controllable thermal transport heterostructure systems, in which heat can also be controlled to transfer along the desired path through careful design and selection of junction interfaces.

Using molecular dynamics simulations, we show that the lattice mismatch in graphene-MoS_2 bilayer van der Waals heterostructure can soften phonon modes and lead to reduction of the thermal conductivity of the graphene in the heterostructure by intriguing out-of-plane displacement, while hardly changes the thermal conductivity of MoS2 due to a weak vdW effect on the MoS2 layer with trilayer atomic structure. The effect of the lattice mismatch can be mitigated by an external tensile strain along the heat flow direction by restricting out-of-plane deformation. However, the shifts of frequency phonon from high to low modes lead to decreased thermal conductivity. We propose a unified theory to quantitatively describe the role of the lattice mismatch and mitigation of the tensile strain on the thermal conductivity in bilayer vdW heterostructures, with robustness verified on multiple heterostructures consisting of graphene-hexagonal boron nitride, hexagonal boron nitride-MoS2, graphene-black phosphorus, and hexagonal boron nitride-black phosphorus.

Next, we demonstrate that bilayer graphene kirigami van der Waals heterostructures can sustain a large in-plane mechanical deformation through well-defined cut patterns, and their thermal conductance monotonously decreases with tensile strain and can be quantitatively correlated with evolutions of cut patterns in each kirigami layer and their alignment misfit. A generalized model of thermal transparency is proposed and confirmed by extensive simulations. Further, a thermal unit composed of graphene kirigami bilayer is constructed and demonstrates that its thermal flow in cross-plane direction can be continuously tuned by controlling mechanical strain and/or kirigami cut patterns, indicating a mechanically tunable capability of thermal transparency.

We elucidate that the thermal conductance in 1D CNT-2D layer vdW heterostructure depends on local mechanical deformation of 2D materials at the heterojunction associated with bending stiffness as well as the spatial equilibrium distance at heterojunction, and lattice structures and layer number of 2D materials, which can be generalized by a unified model by integrating both contributions. When an external pressure loading is applied to the heterojunctions, the thermal conductance shows a monotonous increase with a sensitivity independent of layer numbers, base on which we put forward a conceptual design of a pressure sensor enabled by 1D-2D heterostructure and successfully demonstrate its capability of sensing to external pressures with high accuracy.

Finally, We construct a bilayer graphene oxide heterostructure with liquid confined in the interlayer and report its unique thermal response to mechanical loading magnitudes and modes. By extensive calculations and analyses, mehcanically responsive thermal transport across solid-liquid interaction is found to be associated with the dynamically reversible hydrogen bonding networks. The application demonstration of such solid-confined liquid heterostructures based mechanical sensors confirms that the mechanical loading sensing and mode differentiation to four typical mechanical modes, tension, compression, pressure and bending can be realized from the measurement of the temperature difference in the sensor.

7.2 Recommandations for Future Works

As for wearable and flexible electronics, mechanical durability and stretchability have always been the top concern. In addition to the 2D materials being focused in the current thesis, soft materials such as semiconducting polymers that can maintain high charge-carrier mobility at a 100% tensile strain[292] with self-healing functions based on the restoration of either covalent bonding or hydrogen bonding[293] are desirable for wearable electronics, which is expected to lead to broad applications in the future. In this thesis, we demonstrate that the thermal properties in heterostructures are dominated by the heterojunction. Analogically, it is the orientation and orderliness that govern the thermal conductivity of polymers[294]. What is the orientation that maximizes thermal transport? How to arrange polymer chains in order to achieve mechanically responsive thermal transport, which further varies with different loading modes like tension, compression, and bending? Exploring the thermal transport properties in soft polymers subjected to extreme loadings and similar mechanics-thermal coupling effects will be meaningful to the thermal management issues in the next-generation polymer based wearable electronic devices.

In the current research, we have demonstrated the thermal transport sensitivity and explained its magnitude with material, mechanical and geometric factors, how to precisely control it with material and structural design remains questionable. While an exhaustive test on all the combinations of structures and materials with theoretical explanations seems to be impractical, current research, with the help of machine learning (ML) based on neural network, searching for the kirigami structures with the best stretchability can be very inspiring[295]. The artificial intelligence (AI) methods can also be utilized to control the mechanics-thermal coupling. In this case, how to transfer the geometric, material, thermal and mechanical features into the parameters of a machine learning model would be the main focus. Specifically, the input layer in the model of neural network can consist of several independent features of materials such as Young’s modulus, bending stiffness, porosity, and digitalized geometric shape while the output layer should contain target properties like thermal transport, tensile strain, mechanical strength and stretchability. By training the parameters in the hidden layer with regression methods, the relationship between input and output layers can be established, based on which the ideal candidates with desirable thermal and mechanical properties can be found. Successful development of the AI design techniques may directly answer a broad range of questions associated with designs and applications. For examples: How to design structures with high thermal sensitivity/gauge factor to strain or pressure? Which structure possess the highest mechanical strength, thermal conductivity at the same time? How to select materials to minimize the substrate effect?

Last but not least, as discussed in Section 3.2, the mechanics-thermal coupling can be used to design other thermal devices such as thermal diodes, which directly offer solutions to thermal management. Actually, in addition to mechanical sensors, other devices in the fields of thermal energy storage, thermal-based calculation and thermoelectric materials can be developed.

Bibliography

1. Heikenfeld, J.; Jajack, A.; Rogers, J.; Gutruf, P.; Tian, L.; Pan, T.; Li, R.; Khine, M.; Kim, J.; Wang, J., Wearable Sensors: Modalities, Challenges, and Prospects. *Lab on a Chip* **2018**, 18, 217-248.
2. Heikenfeld, J., Non‐Invasive Analyte Access and Sensing through Eccrine Sweat: Challenges and Outlook Circa 2016. *Electroanalysis* **2016**, 28, 1242-1249.
3. Kim, J.; Banks, A.; Xie, Z.; Heo, S. Y.; Gutruf, P.; Lee, J. W.; Xu, S.; Jang, K. I.; Liu, F.; Brown, G., Miniaturized Flexible Electronic Systems with Wireless Power and near‐Field Communication Capabilities. *Adv. Funct. Mater.* **2015**, 25, 4761-4767.
4. Kang, D.; Pikhitsa, P. V.; Choi, Y. W.; Lee, C.; Shin, S. S.; Piao, L.; Park, B.; Suh, K.-Y.; Kim, T.-i.; Choi, M., Ultrasensitive Mechanical Crack-Based Sensor Inspired by the Spider Sensory System. *Nature* **2014**, 516, 222.
5. Thomas, J. A.; Iutzi, R. M.; McGaughey, A. J., Thermal Conductivity and Phonon Transport in Empty and Water-Filled Carbon Nanotubes. *Physical Review B* **2010**, 81, 045413.
6. Li, H.; Liang, Y.; Yin, G.; Wei, X.; Xu, Z., Template-Free Fabrication of Fullerene (C60, C70) Nanometer-Sized Hollow Spheres under Solvothermal Conditions. *Carbon* **2008**, 46, 1736-1740.
7. Shi, J.; Dong, Y.; Fisher, T.; Ruan, X., Thermal Transport across Carbon Nanotube-Graphene Covalent and Van Der Waals Junctions. *Journal of Applied Physics* **2015**, 118, 044302.
8. Siegal, M. P.; Overmyer, D. L.; Provencio, P. P.; Tallant, D. R., Linear Behavior of Carbon Nanotube Diameters with Growth Temperature. *The Journal of Physical Chemistry C* **2010**, 114, 14864-14867.
9. Yang, X.; Yu, D.; Cao, B., Giant Thermal Rectification from Single-Carbon Nanotube–Graphene Junction. *ACS Appl. Mater. Interfaces* **2017**, 9, 24078-24084.
10. Allison, G., Trunk Muscle Onset Detection Technique for Emg Signals with Ecg Artefact. *Journal of Electromyography and Kinesiology* **2003**, 13, 209-216.
11. Fujita, J.-i.; Hiyama, T.; Hirukawa, A.; Kondo, T.; Nakamura, J.; Ito, S.-i.; Araki, R.; Ito, Y.; Takeguchi, M.; Pai, W. W., Near Room Temperature Chemical Vapor Deposition of Graphene with Diluted Methane and Molten Gallium Catalyst. *Sci. Rep.* **2017**, 7, 12371.
12. Liu, F.; Liu, X.; Hu, N.; Ning, H.; Atobe, S.; Yan, C.; Mo, F.; Fu, S.; Zhang, J.; Wang, Y., Investigation of Thermal Energy Transport Interface of Hybrid Graphene-Carbon Nanotube/Polyethylene Nanocomposites. *Sci. Rep.* **2017**, 7, 14700.
13. Liao, A. D.; Wu, J. Z.; Wang, X.; Tahy, K.; Jena, D.; Dai, H.; Pop, E., Thermally Limited Current Carrying Ability of Graphene Nanoribbons. *Phys. Rev. Lett.* **2011**, 106, 256801.
14. Meng, Y.; Zhao, Y.; Hu, C.; Cheng, H.; Hu, Y.; Zhang, Z.; Shi, G.; Qu, L., All‐Graphene Core‐Sheath Microfibers for All‐Solid‐State, Stretchable Fibriform Supercapacitors and Wearable Electronic Textiles. *Adv. Mater.* **2013**, 25, 2326-2331.
15. Fu, Y.; Cai, X.; Wu, H.; Lv, Z.; Hou, S.; Peng, M.; Yu, X.; Zou, D., Fiber Supercapacitors Utilizing Pen Ink for Flexible/Wearable Energy Storage. *Adv. Mater.* **2012**, 24, 5713-5718.

16. Picu, R. C.; Borca-Tasciuc, T.; Pavel, M. C., Strain and Size Effects on Heat Transport in Nanostructures. *Journal of Applied Physics* **2003**, 93, 3535-3539.
17. Li, X.; Maute, K.; Dunn, M. L.; Yang, R., Strain Effects on the Thermal Conductivity of Nanostructures. *Phys. Rev. B* **2010**, 81, 245318.
18. Lorwongtragool, P.; Sowade, E.; Watthanawisuth, N.; Baumann, R. R.; Kerdcharoen, T., A Novel Wearable Electronic Nose for Healthcare Based on Flexible Printed Chemical Sensor Array. *Sensors* **2014**, 14, 19700-19712.
19. Zhao, X.; Hua, Q.; Yu, R.; Zhang, Y.; Pan, C., Flexible, Stretchable and Wearable Multifunctional Sensor Array as Artificial Electronic Skin for Static and Dynamic Strain Mapping. *Advanced Electronic Materials* **2015**, 1.
20. Cheng, Y.; Wang, R.; Sun, J.; Gao, L., A Stretchable and Highly Sensitive Graphene ‐ Based Fiber for Sensing Tensile Strain, Bending, and Torsion. *Adv. Mater.* **2015**, 27, 7365-7371.
21. Shim, B. S.; Chen, W.; Doty, C.; Xu, C.; Kotov, N. A., Smart Electronic Yarns and Wearable Fabrics for Human Biomonitoring Made by Carbon Nanotube Coating with Polyelectrolytes. *Nano Lett.* **2008**, 8, 4151-4157.
22. Wang, Y.; Wang, L.; Yang, T.; Li, X.; Zang, X.; Zhu, M.; Wang, K.; Wu, D.; Zhu, H., Wearable and Highly Sensitive Graphene Strain Sensors for Human Motion Monitoring. *Adv. Funct. Mater.* **2014**, 24, 4666-4670.
23. Melzer, M.; Mönch, J. I.; Makarov, D.; Zabila, Y.; Cañón Bermúdez, G. S.; Karnaushenko, D.; Baunack, S.; Bahr, F.; Yan, C.; Kaltenbrunner, M., Wearable Magnetic Field Sensors for Flexible Electronics. *Adv. Mater.* **2015**, 27, 1274-1280.
24. Xu, B.; Akhtar, A.; Liu, Y.; Chen, H.; Yeo, W. H.; Park, S. I.; Boyce, B.; Kim, H.; Yu, J.; Lai, H. Y., An Epidermal Stimulation and Sensing Platform for Sensorimotor Prosthetic Control, Management of Lower Back Exertion, and Electrical Muscle Activation. *Adv. Mater.* **2016**, 28, 4462-4471.
25. Levin, M.; Stevenson, C. G., Regulation of Cell Behavior and Tissue Patterning by Bioelectrical Signals: Challenges and Opportunities for Biomedical Engineering. *Annual review of biomedical engineering* **2012**, 14.
26. Amon, C. H.; Murthy, J.; Yao, S.; Narumanchi, S.; Wu, C.-F.; Hsieh, C.-C., Mems-Enabled Thermal Management of High-Heat-Flux Devices Edifice: Embedded Droplet Impingement for Integrated Cooling of Electronics. *Exp. Therm Fluid Sci.* **2001**, 25, 231-242.
27. Krishnan, S.; Garimella, S. V.; Kang, S. S., A Novel Hybrid Heat Sink Using Phase Change Materials for Transient Thermal Management of Electronics. *IEEE Transactions on Components and Packaging Technologies* **2005**, 28, 281-289.
28. Pop, E., Energy Dissipation and Transport in Nanoscale Devices. *Nano Research* **2010**, 3, 147-169.
29. Cahill, D. G.; Braun, P. V.; Chen, G.; Clarke, D. R.; Fan, S.; Goodson, K. E.; Keblinski, P.; King, W. P.; Mahan, G. D.; Majumdar, A., Nanoscale Thermal Transport. Ii. 2003–2012. *Applied Physics Reviews* **2014**, 1, 011305.
30. Cahill, D. G.; Ford, W. K.; Goodson, K. E.; Mahan, G. D.; Majumdar, A.; Maris, H. J.; Merlin, R.; Phillpot, S. R., Nanoscale Thermal Transport. *Journal of applied physics* **2003**, 93, 793-818.

31. Jang, D.-W.; Lee, J.-H.; Kim, A.; Lee, S.-B.; Hong, S.-G., Self-Heating-Induced Deterioration of Electromechanical Performance in Polymer-Supported Metal Films for Flexible Electronics. *Sci. Rep.* **2017**, 7, 12506.
32. Balandin, A. A.; Nika, D. L., Phononics in Low-Dimensional Materials. *Mater. Today* **2012**, 15, 266-275.
33. Dresselhaus, M. S.; Chen, G.; Tang, M. Y.; Yang, R.; Lee, H.; Wang, D.; Ren, Z.; Fleurial, J. P.; Gogna, P., New Directions for Low‐Dimensional Thermoelectric Materials. *Adv. Mater.* **2007**, 19, 1043-1053.
34. Wang, Q. H.; Kalantar-Zadeh, K.; Kis, A.; Coleman, J. N.; Strano, M. S., Electronics and Optoelectronics of Two-Dimensional Transition Metal Dichalcogenides. *Nat. Nanotechnol.* **2012**, 7, 699.
35. Zhi, C.; Bando, Y.; Tang, C.; Kuwahara, H.; Golberg, D., Large-Scale Fabrication of Boron Nitride Nanosheets and Their Utilization in Polymeric Composites with Improved Thermal and Mechanical Properties. *Adv. Mater.* **2009**, 21, 2889-2893.
36. Lee, C.; Wei, X.; Kysar, J. W.; Hone, J., Measurement of the Elastic Properties and Intrinsic Strength of Monolayer Graphene. *Science* **2008**, 321, 385-388.
37. Castellanos-Gomez, A.; Poot, M.; Steele, G. A.; van der Zant, H. S. J.; Agraït, N.; Rubio-Bollinger, G., Elastic Properties of Freely Suspended Mos2 Nanosheets. *Adv. Mater.* **2012**, 24, 772-775.
38. Jiang, J.-W.; Park, H. S., Negative Poisson's Ratio in Single-Layer Black Phosphorus. *Nat Commun* **2014**, 5.
39. Li, L.; Yu, Y.; Ye, G. J.; Ge, Q.; Ou, X.; Wu, H.; Feng, D.; Chen, X. H.; Zhang, Y., Black Phosphorus Field-Effect Transistors. *Nat Nano* **2014**, 9, 372-377.
40. Bonaccorso, F.; Sun, Z.; Hasan, T.; Ferrari, A. C., Graphene Photonics and Optoelectronics. *Nat Photon* **2010**, 4, 611-622.
41. Novoselov, K. S.; Falko, V. I.; Colombo, L.; Gellert, P. R.; Schwab, M. G.; Kim, K., A Roadmap for Graphene. *Nature* **2012**, 490, 192-200.
42. Mak, K. F.; He, K.; Shan, J.; Heinz, T. F., Control of Valley Polarization in Monolayer Mos2 by Optical Helicity. *Nat Nano* **2012**, 7, 494-498.
43. Yu, W. J.; Liu, Y.; Zhou, H.; Yin, A.; Li, Z.; Huang, Y.; Duan, X., Highly Efficient Gate-Tunable Photocurrent Generation in Vertical Heterostructures of Layered Materials. *Nat Nano* **2013**, 8, 952-958.
44. Watanabe, K.; Taniguchi, T.; Kanda, H., Direct-Bandgap Properties and Evidence for Ultraviolet Lasing of Hexagonal Boron Nitride Single Crystal. *Nat Mater* **2004**, 3, 404-409.
45. Chen, S.; Wu, Q.; Mishra, C.; Kang, J.; Zhang, H.; Cho, K.; Cai, W.; Balandin, A. A.; Ruoff, R. S., Thermal Conductivity of Isotopically Modified graphene. *Nat Mater* **2012**, 11, 203-207.
46. Jo, I.; Pettes, M. T.; Kim, J.; Watanabe, K.; Taniguchi, T.; Yao, Z.; Shi, L., Thermal Conductivity and Phonon Transport in Suspended Few-Layer Hexagonal Boron Nitride. *Nano Letters* **2013**, 13, 550-554.
47. Yan, R.; Simpson, J. R.; Bertolazzi, S.; Brivio, J.; Watson, M.; Wu, X.; Kis, A.; Luo, T.; Hight Walker, A. R.; Xing, H. G., Thermal Conductivity of Monolayer Molybdenum Disulfide Obtained from Temperature-Dependent Raman Spectroscopy. *ACS Nano* **2014**, 8, 986-993.

48. Lemme, M. C.; Li, L.-J.; Palacios, T.; Schwierz, F., Two-Dimensional Materials for Electronic Applications. *Mrs Bulletin* **2014**, 39, 711-718.

49. Zhao, H.; Min, K.; Aluru, N., Size and Chirality Dependent Elastic Properties of Graphene Nanoribbons under Uniaxial Tension. *Nano letters* **2009**, 9, 3012-3015.

50. Wu, J.; Wang, B.; Wei, Y.; Yang, R.; Dresselhaus, M., Mechanics and Mechanically Tunable Band Gap in Single-Layer Hexagonal Boron-Nitride. *Materials Research Letters* **2013**, 1, 200-206.

51. Mrozek, A.; Burczyński, T., Examination of Mechanical Properties of Graphene Allotropes by Means of Computer Simulation. *Computer Assisted Methods in Engineering and Science* **2017**, 20, 309-323.

52. Coleman, J. N.; Khan, U.; Blau, W. J.; Gun'ko, Y. K., Small but Strong: A Review of the Mechanical Properties of Carbon Nanotube–Polymer Composites. *Carbon* **2006**, 44, 1624-1652.

53. Kudin, K. N.; Scuseria, G. E.; Yakobson, B. I., C 2 F, Bn, and C Nanoshell Elasticity from Ab Initio Computations. *Phys. Rev. B* **2001**, 64, 235406.

54. Singh, S. K.; Neek-Amal, M.; Costamagna, S.; Peeters, F., Thermomechanical Properties of a Single Hexagonal Boron Nitride Sheet. *Phys. Rev. B* **2013**, 87, 184106.

55. Zhang, H.-Y.; Jiang, J.-W., Elastic Bending Modulus for Single-Layer Black Phosphorus. *Journal of Physics D: Applied Physics* **2015**, 48, 455305.

56. Xiong, S.; Cao, G., Bending Response of Single Layer Mos2. *Nanotechnology* **2016**, 27, 105701.

57. Rogers, J.; Lagally, M.; Nuzzo, R., Synthesis, Assembly and Applications of Semiconductor Nanomembranes. *Nature* **2011**, 477, 45.

58. Zhong, J.; Zhang, Y.; Zhong, Q.; Hu, Q.; Hu, B.; Wang, Z. L.; Zhou, J., Fiber-Based Generator for Wearable Electronics and Mobile Medication. *ACS Nano* **2014**, 8, 6273-6280.

59. Cheng, R.; Li, D.; Zhou, H.; Wang, C.; Yin, A.; Jiang, S.; Liu, Y.; Chen, Y.; Huang, Y.; Duan, X., Electroluminescence and Photocurrent Generation from Atomically Sharp Wse2/Mos2 Heterojunction P–N Diodes. *Nano Letters* **2014**, 14, 5590-5597.

60. Ponomarenko, L. A.; Gorbachev, R. V.; Yu, G. L.; Elias, D. C.; Jalil, R.; Patel, A. A.; Mishchenko, A.; Mayorov, A. S.; Woods, C. R.; Wallbank, J. R.; Mucha-Kruczynski, M.; Piot, B. A.; Potemski, M.; Grigorieva, I. V.; Novoselov, K. S.; Guinea, F.; Fal/'ko, V. I.; Geim, A. K., Cloning of Dirac Fermions in Graphene Superlattices. *Nature* **2013**, 497, 594-597.

61. Lee, G.-H.; Yu, Y.-J.; Cui, X.; Petrone, N.; Lee, C.-H.; Choi, M. S.; Lee, D.-Y.; Lee, C.; Yoo, W. J.; Watanabe, K.; Taniguchi, T.; Nuckolls, C.; Kim, P.; Hone, J., Flexible and Transparent Mos2 Field-Effect Transistors on Hexagonal Boron Nitride-Graphene Heterostructures. *ACS Nano* **2013**, 7, 7931-7936.

62. Georgiou, T.; Jalil, R.; Belle, B. D.; Britnell, L.; Gorbachev, R. V.; Morozov, S. V.; Kim, Y.-J.; Gholinia, A.; Haigh, S. J.; Makarovsky, O.; Eaves, L.; Ponomarenko, L. A.; Geim, A. K.; Novoselov, K. S.; Mishchenko, A., Vertical Field-Effect Transistor Based on Graphene-Ws2 Heterostructures for Flexible and Transparent Electronics. *Nat Nano* **2013**, 8, 100-103.

63. Britnell, L.; Gorbachev, R. V.; Geim, A. K.; Ponomarenko, L. A.; Mishchenko, A.; Greenaway, M. T.; Fromhold, T. M.; Novoselov, K. S.; Eaves, L., Resonant Tunnelling and Negative Differential Conductance in Graphene Transistors. *Nat Commun* **2013**, 4, 1794.

64. Deng, Y.; Luo, Z.; Conrad, N. J.; Liu, H.; Gong, Y.; Najmaei, S.; Ajayan, P. M.; Lou, J.; Xu, X.; Ye, P. D., Black Phosphorus–Monolayer Mos2 Van Der Waals Heterojunction P–N Diode. *ACS Nano* **2014**, 8, 8292-8299.

65. Padilha, J. E.; Fazzio, A.; da Silva, A. J. R., Van Der Waals Heterostructure of Phosphorene and Graphene: Tuning the Schottky Barrier and Doping by Electrostatic Gating. *Phys. Rev. Lett.* **2015**, 114, 066803.

66. Gong, Y.; Lin, J.; Wang, X.; Shi, G.; Lei, S.; Lin, Z.; Zou, X.; Ye, G.; Vajtai, R.; Yakobson, B. I.; Terrones, H.; Terrones, M.; Tay, Beng K.; Lou, J.; Pantelides, S. T.; Liu, Z.; Zhou, W.; Ajayan, P. M., Vertical and in-Plane Heterostructures from Ws2/Mos2 Monolayers. *Nat Mater* **2014**, 13, 1135-1142.

67. Liu, Z.; Ma, L.; Shi, G.; Zhou, W.; Gong, Y.; Lei, S.; Yang, X.; Zhang, J.; Yu, J.; Hackenberg, K. P.; Babakhani, A.; Idrobo, J.-C.; Vajtai, R.; Lou, J.; Ajayan, P. M., In-Plane Heterostructures of Graphene and Hexagonal Boron Nitride with Controlled Domain Sizes. *Nat Nano* **2013**, 8, 119-124.

68. Chen, K.; Wan, X.; Xie, W.; Wen, J.; Kang, Z.; Zeng, X.; Chen, H.; Xu, J., Lateral Built-in Potential of Monolayer Mos2–Ws2 in-Plane Heterostructures by a Shortcut Growth Strategy. *Advanced Materials* **2015**, 27, 6431-6437.

69. Liu, Y.; Cheng, R.; Liao, L.; Zhou, H.; Bai, J.; Liu, G.; Liu, L.; Huang, Y.; Duan, X., Plasmon Resonance Enhanced Multicolour Photodetection by Graphene. *Nat Commun* **2011**, 2, 579.

70. Echtermeyer, T. J.; Britnell, L.; Jasnos, P. K.; Lombardo, A.; Gorbachev, R. V.; Grigorenko, A. N.; Geim, A. K.; Ferrari, A. C.; Novoselov, K. S., Strong Plasmonic Enhancement of Photovoltage in Graphene. *Nat Commun* **2011**, 2, 458.

71. Gannett, W.; Regan, W.; Watanabe, K.; Taniguchi, T.; Crommie, M. F.; Zettl, A., Boron Nitride Substrates for High Mobility Chemical Vapor Deposited Graphene. *Applied Physics Letters* **2011**, 98, 242105.

72. Jariwala, D.; Sangwan, V. K.; Wu, C.-C.; Prabhumirashi, P. L.; Geier, M. L.; Marks, T. J.; Lauhon, L. J.; Hersam, M. C., Gate-Tunable Carbon Nanotube–Mos2 Heterojunction Pn Diode. *Proceedings of the National Academy of Sciences* **2013**, 110, 18076-18080.

73. Wei, Y.; Wu, J.; Yin, H.; Shi, X.; Yang, R.; Dresselhaus, M., The Nature of Strength Enhancement and Weakening by Pentagon–Heptagon Defects In graphene. *Nat Mater* **2012**, 11, 759-763.

74. Liu, Y.; Zou, X.; Yakobson, B. I., Dislocations and Grain Boundaries in Two-Dimensional Boron Nitride. *ACS Nano* **2012**, 6, 7053-7058.

75. Gao, L., Flexible Device Applications of 2d Semiconductors. *Small* **2017**, 13, 1603994.

76. Pang, C.; Lee, G.-Y.; Kim, T.-i.; Kim, S. M.; Kim, H. N.; Ahn, S.-H.; Suh, K.-Y., A Flexible and Highly Sensitive Strain-Gauge Sensor Using Reversible Interlocking of Nanofibres. *Nat. Mater.* **2012**, 11, 795.

77. Zhang, K.; Yang, Y., Thermo‐Phototronic Effect Enhanced Inp/Zno Nanorod Heterojunction Solar Cells for Self‐Powered Wearable Electronics. *Adv. Funct. Mater.* **2017**, 27, 1703331.

78. Vu, Q. A.; Shin, Y. S.; Kim, Y. R.; Kang, W. T.; Kim, H.; Luong, D. H.; Lee, I. M.; Lee, K.; Ko, D.-S.; Heo, J., Two-Terminal Floating-Gate Memory with Van Der Waals Heterostructures for Ultrahigh on/Off Ratio. *Nat. Commun.* **2016**, 7, 12725.

79. Zhang, C.; Hao, X.-L.; Wang, C.-X.; Wei, N.; Rabczuk, T., Thermal Conductivity of Graphene Nanoribbons under Shear Deformation: A Molecular Dynamics Simulation. *Sci. Rep.* **2017**, 7, 41398.
80. Wei, N.; Xu, L.; Wang, H.-Q.; Zheng, J.-C., Strain Engineering of Thermal Conductivity in Graphene Sheets and Nanoribbons: A Demonstration of Magic Flexibility. *Nanotechnology* **2011**, 22, 105705.
81. Zhang, Y.-Y.; Pei, Q.-X.; Jiang, J.-W.; Wei, N.; Zhang, Y.-W., Thermal Conductivities of Single-and Multi-Layer Phosphorene: A Molecular Dynamics Study. *Nanoscale* **2016**, 8, 483-491.
82. Ding, Z.; Pei, Q.-X.; Jiang, J.-W.; Huang, W.; Zhang, Y.-W., Interfacial Thermal Conductance in Graphene/Mos 2 Heterostructures. *Carbon* **2016**, 96, 888-896.
83. Gao, Y.; Yang, W.; Xu, B., Unusual Thermal Conductivity Behavior of Serpentine Graphene Nanoribbons under Tensile Strain. *Carbon* **2016**, 96, 513-521.
84. Xu, Z., Heat Transport in Low-Dimensional Materials: A Review and Perspective. *Theoretical and Applied Mechanics Letters* **2016**, 6, 113-121.
85. Gustafsson, M. V.; Aref, T.; Kockum, A. F.; Ekström, M. K.; Johansson, G.; Delsing, P., Propagating Phonons Coupled to an Artificial Atom. *Science* **2014**, 346, 207-211.
86. Ren, J.; Zhu, J.-X., Heat Diode Effect and Negative Differential Thermal Conductance across Nanoscale Metal-Dielectric Interfaces. *Phys. Rev. B* **2013**, 87, 241412.
87. Yang, N.; Xu, X.; Zhang, G.; Li, B., Thermal Transport in Nanostructures. *Aip Advances* **2012**, 2, 041410.
88. Chang, C.-W.; Okawa, D.; Garcia, H.; Majumdar, A.; Zettl, A., Breakdown of Fourier's Law in Nanotube Thermal Conductors. *Phys. Rev. Lett.* **2008**, 101, 075903.
89. Ziman, J. M., *Electrons and Phonons: The Theory of Transport Phenomena in Solids*. Oxford university press: 2001.
90. Picu, R.; Borca-Tasciuc, T.; Pavel, M., Strain and Size Effects on Heat Transport in Nanostructures. *Journal of applied physics* **2003**, 93, 3535-3539.
91. Feng, T.; Ruan, X., Quantum Mechanical Prediction of Four-Phonon Scattering Rates and Reduced Thermal Conductivity of Solids. *Phys. Rev. B* **2016**, 93, 045202.
92. Broido, D.; Ward, A.; Mingo, N., Lattice Thermal Conductivity of Silicon from Empirical Interatomic Potentials. *Phys. Rev. B* **2005**, 72, 014308.
93. Balandin, A. A.; Ghosh, S.; Bao, W.; Calizo, I.; Teweldebrhan, D.; Miao, F.; Lau, C. N., Superior Thermal Conductivity of Single-Layer Graphene. *Nano Letters* **2008**, 8, 902-907.
94. Seol, J. H.; Jo, I.; Moore, A. L.; Lindsay, L.; Aitken, Z. H.; Pettes, M. T.; Li, X.; Yao, Z.; Huang, R.; Broido, D., Two-Dimensional Phonon Transport in Supported Graphene. *Science* **2010**, 328, 213-216.
95. Shao, C.; Yu, X.; Yang, N.; Yue, Y.; Bao, H., A Review of Thermal Transport in Low-Dimensional Materials under External Perturbation: Effect of Strain, Substrate, and Clustering. *Nanoscale and Microscale Thermophysical Engineering* **2017**, 21, 201-236.
96. Guo, Z.; Zhang, D.; Gong, X.-G., Thermal Conductivity of Graphene Nanoribbons. *Applied physics letters* **2009**, 95, 163103.
97. Hu, J.; Ruan, X.; Chen, Y. P., Thermal Conductivity and Thermal Rectification in Graphene Nanoribbons: A Molecular Dynamics Study. *Nano Letters* **2009**, 9, 2730-2735.

98. Zhong, W.-R.; Zhang, M.-P.; Ai, B.-Q.; Zheng, D.-Q., Chirality and Thickness-Dependent Thermal Conductivity of Few-Layer Graphene: A Molecular Dynamics Study. *Applied Physics Letters* **2011**, 98, 113107.

99. Hao, F.; Fang, D.; Xu, Z., Mechanical and Thermal Transport Properties of Graphene with Defects. *Applied physics letters* **2011**, 99, 041901.

100. Ng, T. Y.; Yeo, J. J.; Liu, Z., A Molecular Dynamics Study of the Thermal Conductivity of Graphene Nanoribbons Containing Dispersed Stone–Thrower–Wales Defects. *Carbon* **2012**, 50, 4887-4893.

101. Zhu, Y.; Murali, S.; Cai, W.; Li, X.; Suk, J. W.; Potts, J. R.; Ruoff, R. S., Graphene and Graphene Oxide: Synthesis, Properties, and Applications. *Adv. Mater.* **2010**, 22, 3906-3924.

102. Hu, J.; Schiffli, S.; Vallabhaneni, A.; Ruan, X.; Chen, Y. P., Tuning the Thermal Conductivity of Graphene Nanoribbons by Edge Passivation and Isotope Engineering: A Molecular Dynamics Study. *Applied Physics Letters* **2010**, 97, 133107.

103. Savin, A. V.; Kivshar, Y. S.; Hu, B., Suppression of Thermal Conductivity in Graphene Nanoribbons with Rough Edges. *Physical Review B* **2010**, 82, 195422.

104. Maruyama, S., A Molecular Dynamics Simulation of Heat Conduction of a Finite Length Single-Walled Carbon Nanotube. *Microscale Thermophys. Eng.* **2003**, 7, 41-50.

105. Li, B.; Wang, J., Anomalous Heat Conduction and Anomalous Diffusion in One-Dimensional Systems. *Phys. Rev. Lett.* **2003**, 91, 044301.

106. Liang, L.; Li, B., Size-Dependent Thermal Conductivity of Nanoscale Semiconducting Systems. *Phys. Rev. B* **2006**, 73, 153303.

107. Zhang, G.; Li, B., Thermal Conductivity of Nanotubes Revisited: Effects of Chirality, Isotope Impurity, Tube Length, and Temperature. *The Journal of chemical physics* **2005**, 123, 114714.

108. Yang, N.; Zhang, G.; Li, B., Ultralow Thermal Conductivity of Isotope-Doped Silicon Nanowires. *Nano Letters* **2008**, 8, 276-280.

109. Chen, J.; Zhang, G.; Li, B., Remarkable Reduction of Thermal Conductivity in Silicon Nanotubes. *Nano letters* **2010**, 10, 3978-3983.

110. Evans, W. J.; Hu, L.; Keblinski, P., Thermal Conductivity of Graphene Ribbons from Equilibrium Molecular Dynamics: Effect of Ribbon Width, Edge Roughness, and Hydrogen Termination. *Applied Physics Letters* **2010**, 96, 203112.

111. Xie, Z.-X.; Chen, K.-Q.; Duan, W., Thermal Transport by Phonons in Zigzag Graphene Nanoribbons with Structural Defects. *Journal of Physics: Condensed Matter* **2011**, 23, 315302.

112. Jiang, J.-W.; Lan, J.; Wang, J.-S.; Li, B., Isotopic Effects on the Thermal Conductivity of Graphene Nanoribbons: Localization Mechanism. *Journal of Applied Physics* **2010**, 107, 054314.

113. Xu, Y.; Chen, X.; Gu, B.-L.; Duan, W., Intrinsic Anisotropy of Thermal Conductance in Graphene Nanoribbons. *Applied Physics Letters* **2009**, 95, 233116.

114. Tabarraei, A., Thermal Conductivity of Monolayer Hexagonal Boron Nitride Nanoribbons. *Computational Materials Science* **2015**, 108, 66-71.

115. Jain, A.; McGaughey, A. J., Strongly Anisotropic in-Plane Thermal Transport in Single-Layer Black Phosphorene. *Sci. Rep.* **2015**, 5, 8501.

116. Liu, X.; Zhang, G.; Pei, Q.-X.; Zhang, Y.-W., Phonon Thermal Conductivity of Monolayer Mos2 Sheet and Nanoribbons. *Applied Physics Letters* **2013**, 103, 133113.

117. Zeraati, M.; Allaei, S. M. V.; Sarsari, I. A.; Pourfath, M.; Donadio, D., Highly Anisotropic Thermal Conductivity of Arsenene: An Ab Initio Study. *Phys. Rev. B* **2016**, 93, 085424.

118. Yang, K.; Chen, Y.; Xie, Y.; Ouyang, T.; Zhong, J., Resonant Splitting of Phonon Transport in Periodic T-Shaped Graphene Nanoribbons. *EPL (Europhysics Letters)* **2010**, 91, 46006.

119. Blom, P.; Wolf, R.; Cillessen, J.; Krijn, M., Ferroelectric Schottky Diode. *Phys. Rev. Lett.* **1994**, 73, 2107.

120. Wang, Y.; Vallabhaneni, A.; Hu, J.; Qiu, B.; Chen, Y. P.; Ruan, X., Phonon Lateral Confinement Enables Thermal Rectification in Asymmetric Single-Material Nanostructures. *Nano letters* **2014**, 14, 592-596.

121. Feng, T.; Ruan, X., Ultra-Low Thermal Conductivity in Graphene Nanomesh. *Carbon* **2016**, 101, 107-113.

122. Hu, S.; An, M.; Yang, N.; Li, B., A Series Circuit of Thermal Rectifiers: An Effective Way to Enhance Rectification Ratio. *small* **2017**, 13, 1602726.

123. Wang, H.; Hu, S.; Takahashi, K.; Zhang, X.; Takamatsu, H.; Chen, J., Experimental Study of Thermal Rectification in Suspended Monolayer Graphene. *Nat. Commun.* **2017**, 8, 15843.

124. Blees, M. K.; Barnard, A. W.; Rose, P. A.; Roberts, S. P.; McGill, K. L.; Huang, P. Y.; Ruyack, A. R.; Kevek, J. W.; Kobrin, B.; Muller, D. A.; McEuen, P. L., Graphene Kirigami. *Nature* **2015**, advance online publication.

125. Wei, N.; Chen, Y.; Cai, K.; Zhao, J.; Wang, H.-Q.; Zheng, J.-C., Thermal Conductivity of Graphene Kirigami: Ultralow and Strain Robustness. *Carbon* **2016**, 104, 203-213.

126. Vavro, J.; Llaguno, M. C.; Satishkumar, B.; Luzzi, D. E.; Fischer, J. E., Electrical and Thermal Properties of C 60-Filled Single-Wall Carbon Nanotubes. *Applied physics letters* **2002**, 80, 1450-1452.

127. Noya, E. G.; Srivastava, D.; Chernozatonskii, L. A.; Menon, M., Thermal Conductivity of Carbon Nanotube Peapods. *Phys. Rev. B* **2004**, 70, 115416.

128. Kodama, T.; Ohnishi, M.; Park, W.; Shiga, T.; Park, J.; Shimada, T.; Shinohara, H.; Shiomi, J.; Goodson, K. E., Modulation of Thermal and Thermoelectric Transport in Individual Carbon Nanotubes by Fullerene Encapsulation. *Nat. Mater.* **2017**, 16, 892.

129. Kandasamy, R.; Wang, X.-Q.; Mujumdar, A. S., Application of Phase Change Materials in Thermal Management of Electronics. *Appl. Therm. Eng.* **2007**, 27, 2822-2832.

130. Loh, G.; Baillargeat, D., A Boron Nitride Nanotube Peapod Thermal Rectifier. *Journal of Applied Physics* **2014**, 115, 243501.

131. Chen, J.; Zhang, G.; Li, B., Impacts of Atomistic Coating on Thermal Conductivity of Germanium Nanowires. *Nano letters* **2012**, 12, 2826-2832.

132. Chalopin, Y.; Esfarjani, K.; Henry, A.; Volz, S.; Chen, G., Thermal Interface Conductance in Si/Ge Superlattices by Equilibrium Molecular Dynamics. *Phys. Rev. B* **2012**, 85, 195302.

133. Hu, M.; Poulikakos, D., Si/Ge Superlattice Nanowires with Ultralow Thermal Conductivity. *Nano Letters* **2012**, 12, 5487-5494.

134. Lee, S.-M.; Cahill, D. G.; Venkatasubramanian, R., Thermal Conductivity of Si–Ge Superlattices. *Applied physics letters* **1997**, 70, 2957-2959.

135. Dames, C.; Chen, G., Theoretical Phonon Thermal Conductivity of Si/Ge Superlattice Nanowires. *Journal of Applied Physics* **2004**, 95, 682-693.

136. Luckyanova, M. N.; Garg, J.; Esfarjani, K.; Jandl, A.; Bulsara, M. T.; Schmidt, A. J.; Minnich, A. J.; Chen, S.; Dresselhaus, M. S.; Ren, Z., Coherent Phonon Heat Conduction in Superlattices. *Science* **2012**, 338, 936-939.

137. Li, T.; Tang, Z.; Huang, Z.; Yu, J., Interfacial Thermal Resistance of 2d and 1d Carbon/Hexagonal Boron Nitride Van Der Waals Heterostructures. *Carbon* **2016**, 105, 566-571.

138. An, Y.; Sun, Y.; Jiao, J.; Zhang, M.; Wang, K.; Chen, X.; Wu, D.; Wang, T.; Fu, Z.; Jiao, Z., The Rectifying Effect of Heterojunctions Composed of Carbon and Boron Nitride Nanotubes. *Org. Electron.* **2017**, 50, 43-47.

139. Varshney, V.; Patnaik, S. S.; Roy, A. K.; Froudakis, G.; Farmer, B. L., Modeling of Thermal Transport in Pillared-Graphene Architectures. *ACS Nano* **2010**, 4, 1153-1161.

140. Xu, L.; Wei, N.; Zheng, Y.; Fan, Z.; Wang, H.-Q.; Zheng, J.-C., Graphene-Nanotube 3d Networks: Intriguing Thermal and Mechanical Properties. *J. Mater. Chem.* **2012**, 22, 1435-1444.

141. Sakhavand, N.; Shahsavari, R., Dimensional Crossover of Thermal Transport in Hybrid Boron Nitride Nanostructures. *ACS Appl. Mater. Interfaces* **2015**, 7, 18312-18319.

142. Yang, X.; Yu, D.; Cao, B.; To, A. C., Ultrahigh Thermal Rectification in Pillared Graphene Structure with Carbon Nanotube–Graphene Intramolecular Junctions. *ACS Appl. Mater. Interfaces* **2016**, 9, 29-35.

143. Zhu, T.; Ertekin, E., Phonon Transport on Two-Dimensional Graphene/Boron Nitride Superlattices. *Phys. Rev. B* **2014**, 90, 195209.

144. Ong, Z.-Y.; Zhang, G., Efficient Approach for Modeling Phonon Transmission Probability in Nanoscale Interfacial Thermal Transport. *Phys. Rev. B* **2015**, 91, 174302.

145. Chen, X.-K.; Xie, Z.-X.; Zhou, W.-X.; Tang, L.-M.; Chen, K.-Q., Thermal Rectification and Negative Differential Thermal Resistance Behaviors in Graphene/Hexagonal Boron Nitride Heterojunction. *Carbon* **2016**, 100, 492-500.

146. Liu, X.; Gao, J.; Zhang, G.; Zhang, Y.-W., Mos 2-Graphene in-Plane Contact for High Interfacial Thermal Conduction. *Nano Research* **2017**, 10, 2944-2953.

147. Liu, B.; Baimova, J. A.; Reddy, C. D.; Dmitriev, S. V.; Law, W. K.; Feng, X. Q.; Zhou, K., Interface Thermal Conductance and Rectification in Hybrid Graphene/Silicene Monolayer. *Carbon* **2014**, 79, 236-244.

148. Song, J.; Medhekar, N. V., Thermal Transport in Lattice-Constrained 2d Hybrid Graphene Heterostructures. *Journal of Physics: Condensed Matter* **2013**, 25, 445007.

149. Lebedev, A. V.; Lebedeva, I. V.; Popov, A. M.; Knizhnik, A. A., Stacking in Incommensurate Graphene/Hexagonal-Boron-Nitride Heterostructures Based on Ab Initio Study of Interlayer Interaction. *Phys. Rev. B* **2017**, 96, 085432.

150. Liu, B.; Meng, F.; Reddy, C. D.; Baimova, J. A.; Srikanth, N.; Dmitriev, S. V.; Zhou, K., Thermal Transport in a Graphene-Mos2 Bilayer Heterostructure: A Molecular Dynamics Study. *RSC Advances* **2015**, 5, 29193-29200.

151. Srinivasan, S.; Balasubramanian, G., Reduced Thermal Transport in the Graphene/Mos2/Graphene Heterostructure: A Comparison with Freestanding Monolayers. *Langmuir* **2018**, 34, 3326-3335.

152. Zhang, J.; Hong, Y.; Wang, X.; Yue, Y.; Xie, D.; Jiang, J.; Xiong, Y.; Li, P., Phonon Thermal Properties of Transition-Metal Dichalcogenides Mos2 and Mose2 Heterostructure. *The Journal of Physical Chemistry C* **2017**, 121, 10336-10344.

153. Liang, T.; Zhang, P.; Yuan, P.; Zhai, S., In-Plane Thermal Transport in Black Phosphorene/Graphene Layered Heterostructures: A Molecular Dynamics Study. *Physical Chemistry Chemical Physics* **2018**, 20, 21151-21162.

154. Ding, Z.; Pei, Q.-X.; Jiang, J.-W.; Huang, W.; Zhang, Y.-W., Interfacial Thermal Conductance in Graphene/Mos2 Heterostructures. *Carbon* **2016**, 96, 888-896.

155. Chen, Y.; Zhang, Y.; Cai, K.; Jiang, J.; Zheng, J.-C.; Zhao, J.; Wei, N., Interfacial Thermal Conductance in Graphene/Black Phosphorus Heterogeneous Structures. *Carbon* **2017**, 117, 399-410.

156. Chen, C.-C.; Li, Z.; Shi, L.; Cronin, S. B., Thermal Interface Conductance across a Graphene/Hexagonal Boron Nitride Heterojunction. *Applied Physics Letters* **2014**, 104, 081908.

157. Ren, C.; Zhang, W.; Xu, Z.; Zhu, Z.; Huai, P., Thermal Conductivity of Single-Walled Carbon Nanotubes under Axial Stress. *The Journal of Physical Chemistry C* **2010**, 114, 5786-5791.

158. Xu, Z.; Buehler, M. J., Strain Controlled Thermomutability of Single-Walled Carbon Nanotubes. *Nanotechnology* **2009**, 20, 185701.

159. Volkov, A. N.; Shiga, T.; Nicholson, D.; Shiomi, J.; Zhigilei, L. V., Effect of Bending Buckling of Carbon Nanotubes on Thermal Conductivity of Carbon Nanotube Materials. *Journal of applied physics* **2012**, 111, 053501.

160. Khalkhali, M.; Khoeini, F.; Rajabpour, A., Thermal Transport in Silicene Nanotubes: Effects of Length, Grain Boundary and Strain. *Int. J. Heat Mass Transfer* **2019**, 134, 503-510.

161. Xu, L.; Zhang, X.; Zheng, Y., Local Strain Effect on the Thermal Transport of Graphene Nanoribbons: A Molecular Dynamics Investigation. *Physical Chemistry Chemical Physics* **2015**, 17, 12031-12040.

162. Ong, Z.-Y.; Cai, Y.; Zhang, G.; Zhang, Y.-W., Strong Thermal Transport Anisotropy and Strain Modulation in Single-Layer Phosphorene. *The Journal of Physical Chemistry C* **2014**, 118, 25272-25277.

163. Ding, Z.; Pei, Q.-X.; Jiang, J.-W.; Zhang, Y.-W., Manipulating the Thermal Conductivity of Monolayer Mos2 Via Lattice Defect and Strain Engineering. *The Journal of Physical Chemistry C* **2015**, 119, 16358-16365.

164. Ong, Z.-Y.; Zhang, G.; Zhang, Y.-W., Controlling the Thermal Conductance of Graphene/H− Bn Lateral Interface with Strain and Structure Engineering. *Phys. Rev. B* **2016**, 93, 075406.

165. Park, J.; Pena, P. In *Strain Effect on Thermal Transport in Carbon Nanotube-Graphene Junctions*, ASME 2018 International Mechanical Engineering Congress and Exposition, American Society of Mechanical Engineers: 2018; pp V08BT10A049-V08BT10A049.

166. Salaway, R. N.; Zhigilei, L. V., Thermal Conductance of Carbon Nanotube Contacts: Molecular Dynamics Simulations and General Description of the Contact Conductance. *Phys. Rev. B* **2016**, 94, 014308.

167. Zhang, W.; Fisher, T.; Mingo, N., Simulation of Interfacial Phonon Transport in Si–Ge Heterostructures Using an Atomistic Green's Function Method. *Journal of heat transfer* **2007**, 129, 483-491.

168. Alder, B. J.; Wainwright, T. E., Studies in Molecular Dynamics. I. General Method. *The Journal of Chemical Physics* **1959**, 31, 459-466.

169. Allen, M. P., Introduction to Molecular Dynamics Simulation. *Computational soft matter: from synthetic polymers to proteins* **2004**, 23, 1-28.

170. Werder, T.; Walther, J. H.; Jaffe, R. L.; Halicioglu, T.; Noca, F.; Koumoutsakos, P., Molecular Dynamics Simulation of Contact Angles of Water Droplets in Carbon Nanotubes. *Nano Letters* **2001**, 1, 697-702.

171. Shakouri, A.; Ng, T.; Lin, R., A New Rebo Potential Based Atomistic Structural Model for Graphene Sheets. *Nanotechnology* **2011**, 22, 295711.

172. Lindsay, L.; Broido, D., Optimized Tersoff and Brenner Empirical Potential Parameters for Lattice Dynamics and Phonon Thermal Transport in Carbon Nanotubes and Graphene. *Phys. Rev. B* **2010**, 81, 205441.

173. Hockney, R. W.; Eastwood, J. W., *Computer Simulation Using Particles*. crc Press: 1988.

174. Born, M.; von Kármán, T., On Fluctuations in Spatial Grids. *Physikalische Zeitschrift* **1912**, 13, 18.

175. Dove, M., Introduction to the Theory of Lattice Dynamics. *École thématique de la Société Française de la Neutronique* **2011**, 12, 123-159.

176. Vo, T. H.; Shekhirev, M.; Kunkel, D. A.; Morton, M. D.; Berglund, E.; Kong, L.; Wilson, P. M.; Dowben, P. A.; Enders, A.; Sinitskii, A., Large-Scale Solution Synthesis of Narrow Graphene Nanoribbons. *Nat. Commun.* **2014**, 5.

177. Plimpton, S., Fast Parallel Algorithms for Short-Range Molecular Dynamics. *J. Comput. Phys.* **1995**, 117, 1-19.

178. Stuart, S. J.; Tutein, A. B.; Harrison, J. A., A Reactive Potential for Hydrocarbons with Intermolecular Interactions. *The Journal of Chemical Physics* **2000**, 112, 6472-6486.

179. Kuang, S.; Gezelter, J. D., A Gentler Approach to Rnemd: Nonisotropic Velocity Scaling for Computing Thermal Conductivity and Shear Viscosity. *The Journal of chemical physics* **2010**, 133, 164101.

180. Müller-Plathe, F.; Bordat, P., Reverse Non-Equilibrium Molecular Dynamics. In *Novel Methods in Soft Matter Simulations*, Karttunen, M.; Lukkarinen, A.; Vattulainen, I., Eds. Springer Berlin Heidelberg: 2004; Vol. 640, pp 310-326.

181. Lu, Q.; Huang, R., Effect of Edge Structures on Elastic Modulus and Fracture of Graphene Nanoribbons under Uniaxial Tension. *arXiv preprint arXiv:1007.3298* **2010**.

182. Georgantzinos, S.; Giannopoulos, G.; Katsareas, D.; Kakavas, P.; Anifantis, N., Size-Dependent Non-Linear Mechanical Properties of Graphene Nanoribbons. *Computational Materials Science* **2011**, 50, 2057-2062.

183. Qi, Z.; Campbell, D. K.; Park, H. S., Atomistic Simulations of Tension-Induced Large Deformation and Stretchability in Graphene Kirigami. *Phys. Rev. B* **2014**, 90, 245437.

184. Zhu, S.; Huang, Y.; Li, T., Extremely Compliant and Highly Stretchable Patterned Graphene. *Applied Physics Letters* **2014**, 104, 173103.

185. Bets, K. V.; Yakobson, B. I., Spontaneous Twist and Intrinsic Instabilities of Pristine Graphene Nanoribbons. *Nano Research* **2009**, 2, 161-166.

186. Mazzamuto, F.; Saint-Martin, J.; Valentin, A.; Chassat, C.; Dollfus, P., Edge Shape Effect on Vibrational Modes in Graphene Nanoribbons: A Numerical Study. *Journal of Applied Physics* **2011**, 109, 064516.

187. Pop, E.; Varshney, V.; Roy, A. K., Thermal Properties of Graphene: Fundamentals and Applications. *MRS bulletin* **2012**, 37, 1273-1281.

188. Blees, M. K.; Barnard, A. W.; Rose, P. A.; Roberts, S. P.; McGill, K. L.; Huang, P. Y.; Ruyack, A. R.; Kevek, J. W.; Kobrin, B.; Muller, D. A.; McEuen, P. L., Graphene Kirigami. *Nature* **2015**, 524, 204-207.

189. Bezazi, A.; Scarpa, F.; Remillat, C., A Novel Centresymmetric Honeycomb Composite Structure. *Composite Structures* **2005**, 71, 356-364.

190. Rafsanjani, A.; Derome, D.; Guyer, R. A.; Carmeliet, J., Swelling of Cellular Solids: From Conventional to Re-Entrant Honeycombs. *Applied Physics Letters* **2013**, 102, 211907.

191. Scarpa, F.; Tomlin, P., On the Transverse Shear Modulus of Negative Poisson's Ratio Honeycomb Structures. *Fatigue & Fracture of Engineering Materials & Structures* **2000**, 23, 717-720.

192. Thomas, J. A.; Iutzi, R. M.; McGaughey, A. J. H., Thermal Conductivity and Phonon Transport in Empty and Water-Filled Carbon Nanotubes. *Phys. Rev. B* **2010**, 81, 045413.

193. Kim, D.-H.; Rogers, J. A., Stretchable Electronics: Materials Strategies and Devices. *Advanced Materials* **2008**, 20, 4887-4892.

194. Kim, D.-H.; Xiao, J.; Song, J.; Huang, Y.; Rogers, J. A., Stretchable, Curvilinear Electronics Based on Inorganic Materials. *Advanced Materials* **2010**, 22, 2108-2124.

195. Wan, H.; Ohtaki, H.; Kotosaka, S.; Hu, G., A Study of Negative Poisson's Ratios in Auxetic Honeycombs Based on a Large Deflection Model. *European Journal of Mechanics - A/Solids* **2004**, 23, 95-106.

196. Evans, K. E.; Alderson, K. L., Auxetic Materials: The Positive Side of Being Negative. *Engineering Science and Education Journal* **2000**, 9, 148-154.

197. Masters, I. G.; Evans, K. E., Models for the Elastic Deformation of Honeycombs. *Composite Structures* **1996**, 35, 403-422.

198. Frank, O.; Tsoukleri, G.; Parthenios, J.; Papagelis, K.; Riaz, I.; Jalil, R.; Novoselov, K. S.; Galiotis, C., Compression Behavior of Single-Layer Graphenes. *ACS Nano* **2010**, 4, 3131-3138.

199. Rogers, J. A.; Someya, T.; Huang, Y., Materials and Mechanics for Stretchable Electronics. *Science* **2010**, 327, 1603-1607.

200. Grima, J. N.; Oliveri, L.; Attard, D.; Ellul, B.; Gatt, R.; Cicala, G.; Recca, G., Hexagonal Honeycombs with Zero Poisson's Ratios and Enhanced Stiffness. *Advanced Engineering Materials* **2010**, 12, 855-862.

201. Zhao, H.; Min, K.; Aluru, N., Size and Chirality Dependent Elastic Properties of Graphene Nanoribbons under Uniaxial Tension. *Nano Lett* **2009**, 9, 3012-3015.

202. Nika, D. L.; Askerov, A. S.; Balandin, A. A., Anomalous Size Dependence of the Thermal Conductivity of Graphene Ribbons. *Nano letters* **2012**, 12, 3238-3244.

203. Yang, Y.; Murali, R., Impact of Size Effect on Graphene Nanoribbon Transport. *IEEE Electron Device Letters* **2010**, 31, 237-239.

204. Stone, A. J.; Wales, D. J., Theoretical Studies of Icosahedral C60 and Some Related Species. *Chem. Phys. Lett.* **1986**, 128, 501-503.

205. Lee, S.-M.; Kim, J.-H.; Ahn, J.-H., Graphene as a Flexible Electronic Material: Mechanical Limitations by Defect Formation and Efforts to Overcome. *Mater. Today* **2015**, 18, 336-344.

206. Kumar, N.; Moses, K.; Pramoda, K.; Shirodkar, S. N.; Mishra, A. K.; Waghmare, U. V.; Sundaresan, A.; Rao, C., Borocarbonitrides, Bxcynz. *J. Mater. Chem. A* **2013**, 1, 5806-5821.

207. Kınacı, A.; Haskins, J. B.; Sevik, C.; Çağın, T., Thermal Conductivity of Bn-C Nanostructures. *Phys. Rev. B* **2012**, 86, 115410.

208. Hong, Y.; Zhang, J.; Zeng, X. C., Thermal Contact Resistance across a Linear Heterojunction within a Hybrid Graphene/Hexagonal Boron Nitride Sheet. *Phys. Chem. Chem. Phys.* **2016**, 18, 24164-24170.

209. Liu, X.; Zhang, G.; Zhang, Y.-W., Topological Defects at the Graphene/H-Bn Interface Abnormally Enhance Its Thermal Conductance. *Nano Lett.* **2016**, 16, 4954-4959.

210. Bu, H.; Chen, Y.; Zou, M.; Yi, H.; Bi, K.; Ni, Z., Atomistic Simulations of Mechanical Properties of Graphene Nanoribbons. *Phys. Lett. A* **2009**, 373, 3359-3362.

211. Le, M.-Q., Size Effects in Mechanical Properties of Boron Nitride Nanoribbons. *J. Mech. Sci. Techno.* **2014**, 28, 4173-4178.

212. Wu, G.; Li, B., Thermal Rectification in Carbon Nanotube Intramolecular Junctions: Molecular Dynamics Calculations. *Phys. Rev. B* **2007**, 76, 085424.

213. Yang, N.; Zhang, G.; Li, B., Thermal Rectification in Asymmetric Graphene Ribbons0. *Appl. Phys. Lett.* **2009**, 95, 033107.

214. Wang, Y.; Vallabhaneni, A.; Hu, J.; Qiu, B.; Chen, Y. P.; Ruan, X., Phonon Lateral Confinement Enables Thermal Rectification in Asymmetric Single-Material Nanostructures. *Nano Lett.* **2014**, 14, 592-596.

215. Li, B.; Lan, J.; Wang, L., Interface Thermal Resistance between Dissimilar Anharmonic Lattices. *Phys. Rev. Lett.* **2005**, 95, 104302.

216. Sellan, D. P.; Landry, E. S.; Turney, J.; McGaughey, A. J.; Amon, C. H., Size Effects in Molecular Dynamics Thermal Conductivity Predictions. *Phys. Rev. B* **2010**, 81, 214305.

217. Maiti, A.; Mahan, G.; Pantelides, S., Dynamical Simulations of Nonequilibrium Processes—Heat Flow and the Kapitza Resistance across Grain Boundaries. *Solid State Commun.* **1997**, 102, 517-521.

218. Schelling, P. K.; Phillpot, S. R.; Keblinski, P., Comparison of Atomic-Level Simulation Methods for Computing Thermal Conductivity. *Phys. Rev. B* **2002**, 65, 144306.

219. Cepellotti, A.; Fugallo, G.; Paulatto, L.; Lazzeri, M.; Mauri, F.; Marzari, N., Phonon Hydrodynamics in Two-Dimensional Materials. *Nat. Commun.* **2015**, 6, 6400.

220. Zhang, G.; Zhang, Y.-W., Thermal Properties of Two-Dimensional Materials. *Chin. Phys. B* **2017**, 26, 034401.

221. Chen, R.; Cui, Y.; Tian, H.; Yao, R.; Liu, Z.; Shu, Y.; Li, C.; Yang, Y.; Ren, T.; Zhang, G.; Zou, R., Controllable Thermal Rectification Realized in Binary Phase Change Composites. *Sci. Rep.* **2015**, 5, 8884.

222. Wang, H.; Hu, S.; Takahashi, K.; Zhang, X.; Takamatsu, H.; Chen, J., Experimental Study of Thermal Rectification in Suspended Monolayer Graphene. *Nat. Commun.* **2017**, 8, 15843.

223. Topsakal, M.; Ciraci, S., Elastic and Plastic Deformation of Graphene, Silicene, and Boron Nitride Honeycomb Nanoribbons under Uniaxial Tension: A First-Principles Density-Functional Theory Study. *Phys. Rev. B* **2010**, 81, 024107.

224. Style, R. W.; Wettlaufer, J. S.; Dufresne, E. R., Surface Tension and the Mechanics of Liquid Inclusions in Compliant Solids. *Soft matter* **2015**, 11, 672-679.

225. Gao, Y.; Liu, Q.; Xu, B., Lattice Mismatch Dominant yet Mechanically Tunable Thermal Conductivity in Bilayer Heterostructures. *ACS Nano* **2016**, 10, 5431-5439.

226. Xu, Z., Heat Transport in Low-Dimensional Materials: A Review and Perspective. *Theor. Appl. Mech. Lett.* **2016**, 6, 113-121.

227. Gale, J. D.; Rohl, A. L., The General Utility Lattice Program (Gulp). *Mol. Simul.* **2003**, 29, 291-341.

228. Zhang, Z.; Chen, Y.; Xie, Y.; Zhang, S., Transition of Thermal Rectification in Silicon Nanocones. *Appl. Therm. Eng.* **2016**, 102, 1075-1080.

229. Chen, J.; Zhang, G.; Li, B., Remarkable Reduction of Thermal Conductivity in Silicon Nanotubes. *Nano Lett.* **2010**, 10, 3978-3983.

230. Jiang, J.-W.; Park, H. S., Mechanical Properties of Mos2/Graphene Heterostructures. *Applied Physics Letters* **2014**, 105, 033108.

231. Zhongwei, Z.; Yuee, X.; Qing, P.; Yuanping, C., Thermal Transport in Mos 2 /Graphene Hybrid Nanosheets. *Nanotechnology* **2015**, 26, 375402.

232. Ma, Y.; Dai, Y.; Guo, M.; Niu, C.; Huang, B., Graphene Adhesion on Mos2 Monolayer: An Ab Initio Study. *Nanoscale* **2011**, 3, 3883-3887.

233. Jiang, J.-W.; Park, H. S.; Rabczuk, T., Molecular Dynamics Simulations of Single-Layer Molybdenum Disulphide (Mos2): Stillinger-Weber Parametrization, Mechanical Properties, and Thermal Conductivity. *Journal of Applied Physics* **2013**, 114, 064307.

234. Elder, R. M.; Neupane, M. R.; Chantawansri, T. L., Stacking Order Dependent Mechanical Properties of Graphene/Mos2 Bilayer and Trilayer Heterostructures. *Applied Physics Letters* **2015**, 107, 073101.

235. Zhiwei, D.; Jin-Wu, J.; Qing-Xiang, P.; Yong-Wei, Z., In-Plane and Cross-Plane Thermal Conductivities of Molybdenum Disulfide. *Nanotechnology* **2015**, 26, 065703.

236. Rajabpour, A.; Vaez Allaei, S. M., Tuning Thermal Conductivity of Bilayer Graphene by Inter-Layer Sp3 Bonding: A Molecular Dynamics Study. *Applied Physics Letters* **2012**, 101, 053115.

237. Jiang, J.-W.; Park, H. S.; Rabczuk, T., Mos2 Nanoresonators: Intrinsically Better Than Graphene? *Nanoscale* **2014**, 6, 3618-3625.

238. He, J.; Sootsman, J. R.; Girard, S. N.; Zheng, J.-C.; Wen, J.; Zhu, Y.; Kanatzidis, M. G.; Dravid, V. P., On the Origin of Increased Phonon Scattering in Nanostructured Pbte Based Thermoelectric Materials. *J. Am. Chem. Soc.* **2010**, 132, 8669-8675.

239. Nika, D. L.; Ghosh, S.; Pokatilov, E. P.; Balandin, A. A., Lattice Thermal Conductivity of Graphene Flakes: Comparison with Bulk Graphite. *Applied Physics Letters* **2009**, 94, 203103.

240. Ghosh, S.; Bao, W.; Nika, D. L.; Subrina, S.; Pokatilov, E. P.; Lau, C. N.; Balandin, A. A., Dimensional Crossover of Thermal Transport in Few-Layer Graphene. *Nat Mater* **2010**, 9, 555-558.

241. Haskins, J. B.; Kınacı, A.; Sevik, C.; Çağın, T., Equilibrium Limit of Thermal Conduction and Boundary Scattering in Nanostructures. *The Journal of Chemical Physics* **2014**, 140, 244112.

242. Bahamon, D.; Qi, Z.; Park, H. S.; Pereira, V. M.; Campbell, D. K., Graphene Kirigami as a Platform for Stretchable and Tunable Quantum Dot Arrays. *Phys. Rev. B* **2016**, 93, 235408.

243. Gao, Y.; Yang, W.; Xu, B., Tailoring Auxetic and Contractile Graphene to Achieve Interface Structures with Fully Mechanically Controllable Thermal Transports. *Adv. Mater. Interfaces* **2017**, 4.

244. Hopkins, P. E.; Reinke, C. M.; Su, M. F.; Olsson, R. H.; Shaner, E. A.; Leseman, Z. C.; Serrano, J. R.; Phinney, L. M.; El-Kady, I., Reduction in the Thermal Conductivity of Single Crystalline Silicon by Phononic Crystal Patterning. *Nano Lett.* **2011**, 11, 107-112.

245. Shyu, T. C.; Damasceno, P. F.; Dodd, P. M.; Lamoureux, A.; Xu, L.; Shlian, M.; Shtein, M.; Glotzer, S. C.; Kotov, N. A., A Kirigami Approach to Engineering Elasticity in Nanocomposites through Patterned Defects. *Nat. Mater.* **2015**, 14, 785-789.

246. Hua, Z.; Zhao, Y.; Dong, S.; Yu, P.; Liu, Y.; Wei, N.; Zhao, J., Large Stretchability and Failure Mechanism of Graphene Kirigami under Tension. *Soft Matter* **2017**, 13, 8930-8939.

247. Mortazavi, B.; Lherbier, A.; Fan, Z.; Harju, A.; Rabczuk, T.; Charlier, J.-C., Thermal and Electronic Transport Characteristics of Highly Stretchable Graphene Kirigami. *Nanoscale* **2017**, 9, 16329-16341.

248. Liu, B.; Baimova, J. A.; Reddy, C. D.; Law, A. W.-K.; Dmitriev, S. V.; Wu, H.; Zhou, K., Interfacial Thermal Conductance of a Silicene/Graphene Bilayer Heterostructure and the Effect of Hydrogenation. *ACS Appl. Mater. Interfaces* **2014**, 6, 18180-18188.

249. Ong, Z.-Y.; Pop, E., Molecular Dynamics Simulation of Thermal Boundary Conductance between Carbon Nanotubes and Sio_2. *Phys. Rev. B* **2010**, 81, 155408.

250. Dewapriya, M.; Meguid, S., Atomistic Modeling of out-of-Plane Deformation of a Propagating Griffith Crack in Graphene. *Acta Mech.* **2017**, 228, 3063-3075.

251. Fan, N.; Ren, Z.; Jing, G.; Guo, J.; Peng, B.; Jiang, H., Numerical Investigation of the Fracture Mechanism of Defective Graphene Sheets. *Materials* **2017**, 10, 164.

252. Ni, Y.; Chalopin, Y.; Volz, S., Significant Thickness Dependence of the Thermal Resistance between Few-Layer Graphenes. *Appl. Phys. Lett.* **2013**, 103, 061906.

253. Yang, L.; Chen, J.; Yang, N.; Li, B., Significant Reduction of Graphene Thermal Conductivity by Phononic Crystal Structure. *Int. J. Heat Mass Transfer* **2015**, 91, 428-432.

254. Gao, Y.; Xu, B., On the Generalized Thermal Conductance Characterizations of Mixed One-Dimensional–Two-Dimensional Van Der Waals Heterostructures and Their Implication for Pressure Sensors. *ACS Appl. Mater. Interfaces* **2018**, 10, 14221-14229.

255. Jiang, J.-W., Parametrization of Stillinger–Weber Potential Based on Valence Force Field Model: Application to Single-Layer Mos2 and Black Phosphorus. *Nanotechnology* **2015**, 26, 315706.

256. Stewart, J. A.; Spearot, D., Atomistic Simulations of Nanoindentation on the Basal Plane of Crystalline Molybdenum Disulfide (Mos2). *Modell. Simul. Mater. Sci. Eng.* **2013**, 21, 045003.

257. Ye, Z.; Otero-De-La-Roza, A.; Johnson, E. R.; Martini, A., Oscillatory Motion in Layered Materials: Graphene, Boron Nitride, and Molybdenum Disulfide. *Nanotechnology* **2015**, 26, 165701.
258. Zhang, Y.-Y.; Pei, Q.-X.; Jiang, J.-W.; Wei, N.; Zhang, Y.-W., Thermal Conductivities of Single- and Multi-Layer Phosphorene: A Molecular Dynamics Study. *Nanoscale* **2016**, 8, 483-491.
259. Zhong, H.; Lukes, J. R., Interfacial Thermal Resistance between Carbon Nanotubes: Molecular Dynamics Simulations and Analytical Thermal Modeling. *Phys. Rev. B* **2006**, 74, 125403.
260. Chen, W.; Zhang, J.; Yue, Y., Molecular Dynamics Study on Thermal Transport at Carbon Nanotube Interface Junctions: Effects of Mechanical Force and Chemical Functionalization. *Int. J. Heat Mass Transfer* **2016**, 103, 1058-1064.
261. Liao, D.; Chen, W.; Zhang, J.; Yue, Y., Tuning Thermal Conductance of Cnt Interface Junction Via Stretching and Atomic Bonding. *J. Phys. D: Appl. Phys.* **2017**, 50, 475302.
262. Evans, W. J.; Shen, M.; Keblinski, P., Inter-Tube Thermal Conductance in Carbon Nanotubes Arrays and Bundles: Effects of Contact Area and Pressure. *Appl. Phys. Lett.* **2012**, 100, 261908.
263. Guo, X.; Zhang, T., A Study on the Bending Stiffness of Single-Walled Carbon Nanotubes and Related Issues. *J. Mech. Phys. Solids* **2010**, 58, 428-443.
264. Chen, X.; Yi, C.; Ke, C., Bending Stiffness and Interlayer Shear Modulus of Few-Layer Graphene. *Appl. Phys. Lett.* **2015**, 106, 101907.
265. Duda, J. C.; English, T. S.; Piekos, E. S.; Soffa, W. A.; Zhigilei, L. V.; Hopkins, P. E., Implications of Cross-Species Interactions on the Temperature Dependence of Kapitza Conductance. *Phys. Rev. B* **2011**, 84, 193301.
266. Hu, M.; Keblinski, P.; Schelling, P. K., Kapitza Conductance of Silicon–Amorphous Polyethylene Interfaces by Molecular Dynamics Simulations. *Phys. Rev. B* **2009**, 79, 104305.
267. Liu, L.; Feng, Y.; Shen, Z., Structural and Electronic Properties of H-Bn. *Phys. Rev. B* **2003**, 68, 104102.
268. Kaur, H.; Yadav, S.; Srivastava, A. K.; Singh, N.; Schneider, J. J.; Sinha, O. P.; Agrawal, V. V.; Srivastava, R., Large Area Fabrication of Semiconducting Phosphorene by Langmuir-Blodgett Assembly. *Sci. Rep.* **2016**, 6, 34095.
269. Yoo, E.; Kim, J.; Hosono, E.; Zhou, H.-s.; Kudo, T.; Honma, I., Large Reversible Li Storage of Graphene Nanosheet Families for Use in Rechargeable Lithium Ion Batteries. *Nano Lett.* **2008**, 8, 2277-2282.
270. Wei, Q.; Peng, X., Superior Mechanical Flexibility of Phosphorene and Few-Layer Black Phosphorus. *Applied Physics Letters* **2014**, 104, 251915.
271. Constantinescu, G.; Kuc, A.; Heine, T., Stacking in Bulk and Bilayer Hexagonal Boron Nitride. *Phys. Rev. Lett.* **2013**, 111, 036104.
272. Kudin, K. N.; Scuseria, G. E.; Yakobson, B. I., C_2f, Bn, and C Nanoshell Elasticity from Ab Initio Computations. *Phys. Rev. B* **2001**, 64, 235406.
273. Zhao, Y.; Luo, X.; Li, H.; Zhang, J.; Araujo, P. T.; Gan, C. K.; Wu, J.; Zhang, H.; Quek, S. Y.; Dresselhaus, M. S., Interlayer Breathing and Shear Modes in Few-Trilayer Mos2 and Wse2. *Nano Lett.* **2013**, 13, 1007-1015.

274. Zhang, L.; Keblinski, P.; Wang, J.-S.; Li, B., Interfacial Thermal Transport in Atomic Junctions. *Phys. Rev. B* **2011**, 83, 064303.

275. Grebikova, L.; Maroni, P.; Zhang, B.; Schlüter, A. D.; Borkovec, M., Single-Molecule Force Measurements by Nano-Handling of Individual Dendronized Polymers. *ACS Nano* **2014**, 8, 2237-2245.

276. Lee, J. S.; Song, J.; Kim, S. O.; Kim, S.; Lee, W.; Jackman, J. A.; Kim, D.; Cho, N.-J.; Lee, J., Multifunctional Hydrogel Nano-Probes for Atomic Force Microscopy. *Nat. Commun.* **2016**, 7, 11566.

277. Soler-Crespo, R. A.; Gao, W.; Mao, L.; Nguyen, H. T.; Roenbeck, M. R.; Paci, J. T.; Huang, J.; Nguyen, S. T.; Espinosa, H. D., The Role of Water in Mediating Interfacial Adhesion and Shear Strength in Graphene Oxide. *ACS Nano* **2018**.

278. Jorgensen, W. L.; Maxwell, D. S.; Tirado-Rives, J., Development and Testing of the Opls All-Atom Force Field on Conformational Energetics and Properties of Organic Liquids. *J. Am. Chem. Soc.* **1996**, 118, 11225-11236.

279. Wan, J.; Jiang, J.-W.; Park, H. S., Negative Poisson's Ratio in Graphene Oxide. *Nanoscale* **2017**, 9, 4007-4012.

280. Zhao, W.; Wang, Y.; Wu, Z.; Wang, W.; Bi, K.; Liang, Z.; Yang, J.; Chen, Y.; Xu, Z.; Ni, Z., Defect-Engineered Heat Transport in Graphene: A Route to High Efficient Thermal Rectification. *Sci. Rep.* **2015**, 5, 11962.

281. Mark, P.; Nilsson, L., Structure and Dynamics of the Tip3p, Spc, and Spc/E Water Models at 298 K. *J. Phys. Chem. A* **2001**, 105, 9954-9960.

282. Zhang, D.-B.; Akatyeva, E.; Dumitrică, T., Bending Ultrathin Graphene at the Margins of Continuum Mechanics. *Phys. Rev. Lett.* **2011**, 106, 255503.

283. Zhang, T.; Gans-Forrest, A. R.; Lee, E.; Zhang, X.; Qu, C.; Pang, Y.; Sun, F.; Luo, T., Role of Hydrogen Bonds in Thermal Transport across Hard/Soft Material Interfaces. *ACS Appl. Mater. Interfaces* **2016**, 8, 33326-33334.

284. Willcox, J. A.; Kim, H. J., Molecular Dynamics Study of Water Flow across Multiple Layers of Pristine, Oxidized, and Mixed Regions of Graphene Oxide. *ACS Nano* **2017**, 11, 2187-2193.

285. Medhekar, N. V.; Ramasubramaniam, A.; Ruoff, R. S.; Shenoy, V. B., Hydrogen Bond Networks in Graphene Oxide Composite Paper: Structure and Mechanical Properties. *ACS Nano* **2010**, 4, 2300-2306.

286. Gao, Y.; Yang, W.; Xu, B., Tailoring Auxetic and Contractile Graphene to Achieve Interface Structures with Fully Mechanically Controllable Thermal Transports. *Adv. Mater. Interfaces* **2017**, 4, 1700278.

287. Gao, Y.; Xu, B., Van Der Waals Graphene Kirigami Heterostructure for Strain-Controlled Thermal Transparency. *ACS Nano* **2018**.

288. Shenogina, N.; Godawat, R.; Keblinski, P.; Garde, S., How Wetting and Adhesion Affect Thermal Conductance of a Range of Hydrophobic to Hydrophilic Aqueous Interfaces. *Phys. Rev. Lett.* **2009**, 102, 156101.

289. Alexeev, D.; Chen, J.; Walther, J. H.; Giapis, K. P.; Angelikopoulos, P.; Koumoutsakos, P., Kapitza Resistance between Few-Layer Graphene and Water: Liquid Layering Effects. *Nano letters* **2015**, 15, 5744-5749.

290. Shin, U.-H.; Jeong, D.-W.; Park, S.-M.; Kim, S.-H.; Lee, H. W.; Kim, J.-M., Highly Stretchable Conductors and Piezocapacitive Strain Gauges Based on Simple Contact-Transfer Patterning of Carbon Nanotube Forests. *Carbon* **2014**, 80, 396-404.

291. Yao, S.; Zhu, Y., Wearable Multifunctional Sensors Using Printed Stretchable Conductors Made of Silver Nanowires. *Nanoscale* **2014**, 6, 2345-2352.

292. Oh, J. Y.; Rondeau-Gagné, S.; Chiu, Y.-C.; Chortos, A.; Lissel, F.; Wang, G.-J. N.; Schroeder, B. C.; Kurosawa, T.; Lopez, J.; Katsumata, T., Intrinsically Stretchable and Healable Semiconducting Polymer for Organic Transistors. *Nature* **2016**, 539, 411.

293. Kim, S. M.; Jeon, H.; Shin, S. H.; Park, S. A.; Jegal, J.; Hwang, S. Y.; Oh, D. X.; Park, J., Superior Toughness and Fast Self‐Healing at Room Temperature Engineered by Transparent Elastomers. *Adv. Mater.* **2018**, 30, 1705145.

294. Shi, W.; Shuai, Z.; Wang, D., Tuning Thermal Transport in Chain‐Oriented Conducting Polymers for Enhanced Thermoelectric Efficiency: A Computational Study. *Adv. Funct. Mater.* **2017**, 27, 1702847.

295. Hanakata, P. Z.; Cubuk, E. D.; Campbell, D. K.; Park, H. S., Accelerated Search and Design of Stretchable Graphene Kirigami Using Machine Learning. *Phys. Rev. Lett.* **2018**, 121, 255304.